ABSTRACT

BREWER, SCOTT HARMON. Solution and Surface Characterization of DNA and Proteins. (Under the direction of Stefan Franzen.)

A variety of experimental spectroscopic techniques complemented by theoretical calculations when appropriate were used to investigate DNA adlayers on surfaces and proteins in solution. The formation and characterization of DNA adlayers on gold and indium tin oxide surfaces were characterized along with subsequent surface DNA hybridization. Prior to the modification of indium tin oxide surfaces with DNA, the optical and electronic properties of this metal oxide, fluorine doped tin oxide and iridium oxide were investigated. The detection of DNA hybridization on indium tin oxide surfaces utilized gold nanoparticle labeled target ssDNA. Further work on gold surfaces was performed using infrared spectroscopy to detect sugar binding to a phenylboronic acid terminated self-assembled monolayer. The binding properties and stability of gold nanoparticles were investigated by characterizing citrate and bovine serum albumin binding to gold surfaces and the stability of particles stabilized by these molecules. The stability and folding kinetics of the three helix bundle protein, villin headpiece subdomain was also investigated in addition to a theoretical investigation of the vibrational Stark effect. Finally, a time resolved step scan FTIR spectrometer was implemented with five microsecond time resolution.

SOLUTION AND SURFACE CHARACTERIZATION OF DNA AND PROTEINS

by
SCOTT HARMON BREWER

A dissertation submitted to the Graduate Faculty of
North Carolina State University
in partial fulfillment of the
requirements for the Degree of
Doctor of Philosophy

CHEMISTRY

Raleigh, NC

2004

APPROVED BY:

_____
Dr. Stefan Franzen, Chair of Advisory Committee

_____ _____
Dr. Daniel L. Feldheim Dr. Edmond F. Bowden

_____
Dr. Jan Genzer,
Graduate School Representative

DEDICATION

This work is dedicated to my parents, Hobert and Margaret H. Brewer, my sister, Donna B. Petty, and my aunt, Katherine H. Heldreth.

BIOGRAPHY

Scott Harmon Brewer was born on October 21, 1977, into the family of Hobert and Margaret Brewer and sister Donna. After graduating from George Washington High School in Danville, Virginia, Scott began his undergraduate studies at James Madison University as a chemistry major in the fall of 1995. While at James Madison University, he performed undergraduate research in the lab of Dr. Gina MacDonald using difference FTIR spectroscopy to study nucleotide binding to the protein RecA. In the spring of 1999, Scott graduated *summa cum laude* with distinction in chemistry with a Bachelor of Science degree in chemistry. Scott graduated as one of JMU's class valedictorians with a 4.0 grade point average. Scott then gained research experience at Duke University in the lab of Dr. Richard Palmer using time resolved step scan FTIR spectrometry and at Xanthon, Inc. developing electrochemical detection strategies for DNA on indium tin oxide electrodes. In the fall of 2000, Scott entered the chemistry graduate program at North Carolina State University. His graduate work was performed in the lab of Dr. Stefan Franzen, his advisor. Scott's research focused on forming and characterizing DNA adlayers on metal and metal oxide surfaces and on studying protein folding and dynamics. His graduate research involved performing research experiments at a variety of other labs including Brookhaven National Laboratory (Upton, NY), National Institute of Science and Technology (Gaithersburg, MD), Los Alamos National Laboratory (Los Alamos, NM), Digilabs (Randolph, MA), Ecole Polytechnique (Palaiseau, France) and NTNU (Trondheim, Norway).

ACKNOWLEDGEMENTS

I first would like to acknowledge and thank my God through whom all things are possible and my family and friends. I especially would like to thank my parents, Hobert and Margaret H. Brewer, my sister, Donna B. Petty, my brother-in-law, Robert M. Petty, my aunt, Katherine H. Heldreth, and my grandmother, Edna Hylton, for their support and encouragement.

I would like to acknowledge the chemistry faculty at James Madison University, in particular my undergraduate research advisor, Dr. Gina MacDonald.

I especially would like to acknowledge and thank my graduate research advisor Dr. Stefan Franzen for making this research possible and for providing me with both educational and memorable research and teaching opportunities. I would like to thank the rest of my committee members Dr. Daniel Feldheim, Dr. Edmond Bowden and Dr. Jan Genzer. I would also like to acknowledge and thank the entire Franzen lab, both past and present group members. Finally, I would like to thank all those with whom I had the opportunity to conduct collaborative research.

TABLE OF CONTENTS

Page

LIST OF TABLES ……..xi

LIST OF FIGURES ……xv

LIST OF SCHEMES ……....xxxii

CHAPTER 1 INTRODUCTION ……1
Introduction ……...……1

CHAPTER 2 DETECTION OF DNA HYBRIDIZATION ON GOLD SURFACES BY POLARIZATION MODULATION INFRARED REFLECTION ABSORPTION SPECTROSCOPY ……6
Abstract ……..7
Introduction ……7
Methods and Materials ……..9
DNA Monolayer Formation ……..9
Polarization Modulation Infrared Reflection Absorption Spectroscopy (PM-IRRAS) ……...10
Density Functional Theory (DFT) Calculations ……..11
Results and Discussion ……11
Conclusions ……16
Acknowledgements ……..17
References ……17
Figures ……..22

CHAPTER 3 INFRARED DETECTION OF A PHENYLBORONIC ACID TERMINATED ALKANE THIOL MONOLAYER ON A GOLD SURFACE .....……27
Abstract ……28
Introduction ……..28
Materials and Methods ……..31
Chemicals and Substrates ……31
Synthesis of N-(3-dihydroxyborylphenyl)-11-mercaptoundecanamide) ……..31
Monolayer Formation on Gold Surfaces ……..32
Polarization Modulation Infrared Reflection Absorption Spectroscopy (PM-IRRAS) ……32
Infrared Reflection Absorption Spectroscopy (IRRAS) ……33
Single-Pass Attenuated Total Reflection Fourier

Transform Infrared (ATR-FTIR) Spectroscopy ……33
Vibrationally Resonant Sum Frequency
Generation (VR-SFG) Spectroscopy ……34
Density Functional Theory (DFT) Calculations ……....35
Results and Discussion ……35
IR spectra and DFT calculations of a
phenylboronic acid undecane thiol SAM ……..35
Isotopic shift in B-O stretching vibrations
observed by IR spectroscopy ……39
Spectroscopic studies of boronate ester formation ……40
Conclusion ……46
Acknowledgements ……...46
References ……47
Scheme ……..51
Table ……..52
Figures ……...53

CHAPTER 4 OPTICAL PROPERTIES OF INDIUM TIN OXIDE AND FLUORINE-DOPED TIN OXIDE SURFACES: CORRELATION OF REFLECTIVITY, SKIN DEPTH, AND PLASMON FREQUENCY WITH CONDUCTIVITY ……...59
Abstract ……..60
Introduction ……...60
Materials and Methods ……..62
ITO and SFO Electrodes ……62
Reflectance FTIR Spectroscopy ……62
X-ray Photoelectron Spectroscopy (XPS) ……63
Results ……...63
Discussion ……..66
Glass Substrate Mode Analysis ……..66
Fresnel Equations of Reflection at
a Single Dielectric Interface ……...67
Conclusion ……71
Acknowledgements ……72
References ……72
Figures ……74

CHAPTER 5 FORMATION OF THIOLATE AND PHOSPHONATE ADLAYERS ON INDIUM TIN OXIDE: OPTICAL AND ELECTRONIC CHARACTERIZATION ……...83
Abstract ……84
Introduction ……..84
Methods and Materials ……..86
Chemicals and Subtrates ……86

Deposition on ITO and SFO Electrodes ……86
Reflectance FTIR Spectroscopy ……87
X-ray Photoelectron Spectroscopy (XPS) ……..88
Density Functional Theory (DFT) Calculations ……88
Results ……..89
Reflectance FTIR Spectra of ITO ……..89
Deposition of Alkane Thiols, Phosphonates, and Sulfonates ……90
FTIR Characterization ……...90
XPS Characterization ……92
Modeling of 12-Phosphonododecanoic Acid Monolayer ……93
Modeling of Frequency Shifts Upon Adlayer Formation ……94
Modeling of Frequency Shifts Upon Adlayer Formation ……94
Sequential Electrode Immersions ……...96
Discussion ……..96
Conclusion ……...100
Acknowledgements ……..101
References ……101
Tables ……..104
Figures ……108

CHAPTER 6 INDIUM TIN OXIDE PLASMA FREQUENCY DEPENDENCE ON SHEET RESISTANCE AND SURFACE ADLAYERS DETERMINED BY REFLECTANCE FTIR SPECTROSCOPY …….120
Abstract ……121
Introduction ……..121
Materials and Methods ……123
ITO and SFO Electrodes ……123
Reflectance FTIR Spectroscopy ……...124
Theoretical Models ……..124
Drude Free-Electron Model ……124
Two-Phase Fresnel Equations for Reflectance ……125
Three-Phase Fresnel Equations for Reflectance ……...126
Results and Discussion ……128
Conclusion ……..134
Acknowledgements ……135
References ……...136
Tables ……..139
Figures ……140

CHAPTER 7 CALCULATION OF THE ELECTRONIC AND OPTICAL

PROPERTIES OF INDIUM TIN OXIDE BY DENSITY FUNCTIONAL THEORY ……149
Abstract ……150
Introduction ……150
Experimental Methods ……153
Computational Methods ……...153
Results and Discussion ……156
Conclusion ……...162
Acknowledgements ……..163
References ……164
Tables ……...168
Figures ……..171

CHAPTER 8 DETECTION OF DNA HYBRIDIZATION ON INDIUM TIN OXIDE SURFACES ……..179
Abstract ……180
Introduction ……180
Materials and Methods ……182
ssDNA Modification of ITO ……182
Preparation of the Gold Nanoparticle / Oligonucleotide Conjugates ……182
DNA Hybridization Conditions ……...183
X-ray Photoelectron Spectroscopy (XPS) ……...184
Infrared Reflection Absorption Spectroscopy (IRRAS) ……..184
Density Functional Theory (DFT) Calculations ……..184
Electrochemical Measurements ……...185
Thermographic Measurements ……....187
Atomic Force Microscopy (AFM) ……...187
Results and Discussion ……187
Characterization of ssDNA Modified ITO Surfaces ……...187
Detection of Hybridization by Au-Nanoparticle DNA Conjugates on ITO Surfaces ……..189
Conclusion ……..193
Acknowledgements ……194
References ……...195
Scheme ……198
Figures ……199

CHAPTER 9 INVESTIGATION OF THE ELECTRICAL AND OPTICAL PROPERTIES OF IRIDIUM OXIDE BY REFLECTANCE FTIR SPECTROSCOPY AND DENSITY FUNCTIONAL THEORY CALCULATIONS ……208
Abstract ……209

Introduction ……209
Materials and Methods ……211
Iridium Oxide Thin Films ……211
Reflectance FTIR Spectroscopy ……211
Computational Methods ……212
Drude Free-Electron Model ……212
Two-Phase Fresnel Equations for Reflectance ……213
Density Functional Theory Calculations ……213
Results and Discussion ……215
Reflectance FTIR Spectroscopy of Iridium Oxide Thin Films ……216
DFT Calculated Optical and Electronic Properties of Iridium Oxide ……217
Conclusion ……221
Acknowledgements ……223
References ……223
Table ……226
Figures ……227

CHAPTER 10 A QUANTITATIVE THEORY AND COMPUTATIONAL APPROACH FOR THE VIBRATIONAL STARK EFFECT ……232
Abstract ……233
Introduction ……233
Methods ……236
Results and Discussion ……242
Conclusion ……248
Acknowledgements ……249
References ……249
Tables ……252
Figures ……256

CHAPTER 11 BSA BINDING TO CITRATE COATED GOLD NANOPARTICLES AND SURFACES ……260
Acknowledgements ……268
References ……268
Figures ……271

CHAPTER 12 INFRARED TEMPERATURE JUMP INVESTIGATION OF THE FOLDING KINETICS OF THE VILLIN HEADPIECE SUBDOMAIN ……274
Abstract ……275
Introduction ……275
Materials and Methods ……278
Protein Sample Preparation ……278

Equilibrium FTIR Temperature Dependent Measurements ……278
Time-Resolved Temperature Jump (T-Jump) IR Kinetic Measurements ……279
Analysis of Equilibrium and Kinetic Data ……..280
Results and Discussion ……282
Structure of the Villin Headpiece Subdomain (PDB 1VII) ……..282
Equilibrium FTIR Spectroscopy ……..282
HP36 ……283
HP36F4751L ……....289
Time Resolved T-Jump IR Spectroscopy ……291
Conclusion ……...296
Acknowledgements ……297
References ……298
Tables ……..301
Figures ……305

CHAPTER 13 TIME-RESOLVED STEP-SCAN FTIR SPECTROSCOPY ……313
Abstract ……...314
Introduction ……314
Materials and Methods ……315
Protein Sample Preparation ……315
Time-Resolved Step-Scan FTIR Spectroscopy ……315
Results and Discussion ……317
Conclusion ……..319
Acknowledgements ……320
References ……...320
Figures ……323

APPENDIX 1 SUPPLEMENTARY MATERIAL FOR CHAPTER 2 ……326
Supplementary Material ……..327

APPENDIX 2 SUPPORTING INFORMATION FOR CHAPTER 3 ……...353
Supporting Information ……...354

APPENDIX 3 SUPPLEMENTARY INFORMATION FOR CHAPTER 6 ……359
Supplementary Information ……360

APPENDIX 4 SUPPORTING INFORMATION FOR CHAPTER 10 ……362
Supporting Information ……..363

APPENDIX 5 SUPPORTING INFORMATION FOR CHAPTER 12 ……...393
Supporting Information ……..394

LIST OF TABLES

Page

CHAPTER 3

Table 1. Partial list of vibrational modes and mode assignments corresponding to PBA on a gold surface ((PM)-IRRAS), in solution (single-pass ATR-FTIR) and calculated by DFT. ……....52

CHAPTER 5

Table 1. Normal mode frequencies of neat 1-hexadecanethiol and frequencies corresponding to a monolayer of 1-hexadecanethiol on ITO and SFO respectively at an incidence angle of 70 degrees with p-polarized light. ……..…….104

Table 2. Solid and solution values corresponding to normal mode frequencies of 12-phosphonododecanoic acid and the frequencies of the corresponding monolayer or partial monolayer of the same material on ITO and SFO respectively at an incidence angle of 70 degrees with p- polarized light. …….105

Table 3. In $3d_{5/2,3/2}$ (445.1, 452.7 eV), Sn $3d_{5/2,3/2}$ (487.2, 495.7 eV), and C 1s (285.2 eV) XPS intensities and percentage differences from bare ITO reference. ……...106

Table 4. Calculated frequencies for polymethylene (12 methylene groups per box) using PBC with two different box dimensions. The box angles were 60 degrees. (Length a is parallel to the molecular axis of the molecule while b and c are perpendicular to a). ……107

CHAPTER 6

Table 1. The electronic scattering time and plasma frequency of three different ITO electrodes with different sheet resistances as determined from fitting the experimental reflectance data using the Drude free-electron model with a constant value of 3.8 for the high frequency dielectric value to determine the dielectric function of the ITO thin film and the two-phase (air/ITO) (A) or the three-phase (air/ITO/glass) (B) Fresnel equations for reflection. ……..139

CHAPTER 7

Table 1A. Calculated effective free electron mass (fraction of the free electron mass, m_e) for indium oxide and indium tin oxide. ….168

Table 1B. Calculated effective free electron mass (fraction of the free electron mass, m_e) for $In_{28}Sn_4O_{48}$ as a function of the cubic lattice parameter. …….168

Table 2A. Calculated plasma frequencies (cm^{-1}) for indium oxide and indium tin oxide. …….169

Table 2B. Calculated plasma frequencies (cm^{-1}) for $In_{28}Sn_4O_{48}$ as a function of the cubic lattice parameter. ……..169

Table 3. Properties of $In_{28}Sn_4O_{48}$ calculated at room temperature (300K). ……170

CHAPTER 9

Table 1. DFT calculated values of the charge carrier concentration and plasma frequency of oxygen deficient iridium oxide models. ……..226

CHAPTER 10

Table 1. Experimental (recorded at liquid nitrogen temperatures) and calculated values of the CN or CO stretching frequency, cubic anharmonicity, bond length and ground state dipole moment in zero applied electric field. ……..252

Table 2. Calculated Stark tuning rates using the anharmonic and geometry distortion approaches compared with the experimentally measured values. ……...253

Table 3. Calculated transition moment polarizabilities compared to experimental values. ……254

Table 4. Calculated difference polarizabilities compared to experimental values. …….255

CHAPTER 12

Table 1A. Thermodynamic parameters for the unfolding of HP36 and HP36F4751L as determined from the SVD analysis of the temperature dependent equilibrium FTIR spectra based on a two-state model of unfolding. ……301

Table 1B. Thermodynamic parameters for the unfolding of HP36 as determined from the Gaussian global fitting analysis of the temperature dependent equilibrium FTIR difference spectra based on a two-state model of unfolding. ……..301

Table 2. Representative relaxation rates, times and percent amplitudes of the total amplitude at a given temperature (T_f) after a T-jump determined from a bi-exponential fit to the measured kinetic relaxation traces. ……...302

Table 3. Kinetic activation (‡) thermodynamic parameters obtained from a two-state model of folding for HP36 determined from the dependence of the microscopic folding and unfolding rates as a function of temperature. The microscopic rates were determined using the equilibrium constants obtained from the dependence of the second spectral component determined by SVD from the equilibrium melt of this protein. ……...303

Table 4. The slow (microsecond) observed relaxation rate with the corresponding microscopic folding and unfolding rates for HP36 and HP36F4751L at 45.6 and 49.9°C, respectively using the equilibrium values determined from the SVD analysis of the temperature dependent equilibrium FTIR data for each protein. ……..304

APPENDIX 4

Table 1. Calculated average anharmonicity values of nitrile and carbonyl functional groups for a variety of molecules. ……363

Table 2. Calculated electric field effect on the frequency, bond length, and dipole magnitude of nitrile and carbonyl functional groups of a variety of molecules. Values were calculated by allowing the molecules to optimize in the applied electric. ……364

Table 3. Calculated electric field effect on the frequency and dipole magnitude of nitrile and carbonyl functional groups of a

variety of molecules. These parameters were calculated using the optimized coordinates obtained in the absence of an applied electric field. ……367

Table 4. Experimental and calculated wavenumbers for nitrile and carbonyl stretches for a variety of molecules. ……...370

Table 5. Literature difference dipole moment values for a variety of nitrile and carbonyl containing molecules. ……...371

Table 6. PES polynomial coefficients for the nitrile or carbonyl stretching normal mode at zero applied electric field. …….372

Table 7. PES polynomial coefficients for the nitrile or carbonyl stretching normal mode at 5.14257 MV/cm applied electric field. ……..373

Table 8. Difference in the PES polynomial coefficients for the nitrile or carbonyl stretching normal mode between zero and 5.14257 MV/cm applied electric field. …….374

Table 9. Single point energies of the nitriles or carbonyls at –5.14257, 0.0, and 5.14257 MV/cm applied electric fields. ……375

Table 10. Coefficients for the anharmonic contributions to the transition moment at zero applied electric field. ……...376

Table 11. Coefficients for the anharmonic corrections to the transition moment for CO at -5.14257, 0 and 5.14257 MV/cm applied electric field. ……...377

Table 12. List of basis set used for carbonyl models. ……...378

Table 13. List of basis set used for the nitrile models. …….379

LIST OF FIGURES

Page

CHAPTER 2

Figure 1. PM-IRRAS spectra of a mixed monolayer of 6-mercapto-1-hexanol and single stranded DNA before (dashed spectrum) and after hybridization (solid spectrum) with the complementary single stranded DNA strand to obtain double stranded DNA with a hybridization temperature of 65°C (A) or 85°C (B) recorded at an incident angle of 80 degrees. ……..22

Figure 2. Solution single-pass ATR FTIR spectra of single stranded DNA (dashed spectrum) and double-stranded DNA (solid spectrum) corresponding to the same DNA strands used for the probe and target single stranded DNA on the gold surfaces. The concentration of the DNA solutions was approximately 200mM. The inset shows the larger spectral range from 970 - 1760 cm^{-1}. ……...23

Figure 3. Solution single-pass ATR FTIR spectra of single stranded DNA recorded as a function of hydration and concentration in aqueous solution. The spectra correspond to least concentrated ~20 mM (- - -), more concentrated (-- -- --), and most concentrated ~200 mM (solid spectrum) of the single stranded DNA used as the probe strand on the gold surfaces. The most concentrated sample is nearly in a gel state. ……..24

Figure 4. Dmol3 calculated frequency spectra of A. adenine (-- --), thymine (-- · --), and the adenine-thymine base pair (solid spectrum), B. guanine (-- --), cytosine (-- · --), and the guanine-cytosine base pair (solid spectrum), C. probe ssDNA before (dashed spectrum) and after hybridization (dsDNA) (solid spectrum) using the weighted average of the calculated spectra of either the individual bases or base pairs, respectively. All spectra have a Gaussian width of 10 cm^{-1}. ……....25

CHAPTER 3

Figure 1. The PM-IRRAS (A) and IRRAS (B) spectra of a monolayer of PBA on a gold surface in the low and high wavenumber regions, respectively. The PM-IRRAS and IRRAS

spectra were recorded at an incident angle of 80°. The IRRAS spectra were obtained with p-polarized IR radiation. Single-pass ATR-FTIR spectra of an initially 3 mmol/L PBA solution in ethanol allowed to concentrate on the ATR element are shown in the low (C) and high (D) wavenumber regions. DFT calculated low (E) and high (F) wavenumber regions of the infrared spectrum of PBA in the gas phase with a Gaussian width of 10 cm^{-1}. ……53

Figure 2. A. Single-pass ATR-FTIR spectra of ^{11}B (dashed) and ^{10}B (solid) boric acid solids. B. DFT calculated infrared spectra of ^{11}B (dashed) and ^{10}B (solid) boric acid in the gas phase with a Gaussian width of 30 cm^{-1}. (Inset: eigenvector projections of boric acid corresponding to the two modes of boric acid in the 1250 cm^{-1} to 1650 cm^{-1} region) ……..54

Figure 3. PM-IRRAS (A) and IRRAS (B) spectra of a monolayer of PBA exposed (solid spectrum) or unexposed (dashed spectrum) to a 3 mmol/L ethanolic solution of glucose for 30 minutes in the low (A) and high (B) wavenumber region on a gold slide recorded at an incident angle of 80 degrees. The corresponding difference spectra for the low (C) and high (D) wavenumber regions are shown for glucose bound to a PBA-SAM on gold minus a PBA-SAM on gold. (The difference of the Gaussian fits in the O-H stretching region is shown in D). Single-pass ATR-FTIR spectra solutions of PBA (solid), glucose (short dashed) and an 1:1 molar ratio of PBA and glucose (long dashed) are shown in the low (E) and high (F) wavenumber region. DFT calculated infrared spectra of PBA (solid), glucose (short dashed) and glucose bound to PBA (long dashed) with a Gaussian width of 10 cm^{-1} in the low (G) and high (H) wavenumber regions. DFT difference infrared spectra (I and J) calculated by the subtraction of the sum of the individual calculated IR spectra of glucose and PBA from the calculated IR spectra of glucose bound to PBA. ……55

Figure 4. VR-SFG spectra of a PBA-SAM (dashed) on a gold surface exposed to a 3 mmol/L solution of glucose in ethanol for 30 min. (solid) recorded with ppp polarization. ……..57

Figure 5. PM-IRRAS spectra of a monolayer of PBA exposed (solid) or not exposed (dashed) to a 3 mmol/L ethanolic solution of mannose (A) or lactose (B) for 30 min. in the 950 cm^{-1} to 1800 cm^{-1} region on a gold slide recorded at an incident

angle of 80° and the corresponding difference spectra for mannose (C) or lactose (D) bound to a PBA-SAM on gold minus a PBA-SAM on gold. ……..58

CHAPTER 4

Figure 1. A. Variable angle reflectance FTIR spectra obtained from a ratio of ITO electrode to gold. Spectra shown are for angles of incidence of 50 (-- --), 60 (- -- -) and 70 (solid line) degrees for p-polarized IR light. B. Variable angle reflectance FTIR spectra obtained from a ratio of ITO electrode to gold. Spectra shown are for angles of incidence of 50 (-- --), 60 (- -- -) and 70 (solid line) degrees for s-polarized IR light. ……...74

Figure 2. A. Variable angle reflectance FTIR spectra obtained from a ratio of SFO electrode to gold. Spectra shown are for angles of incidence of 50 (-- --), 60 (- -- -) and 70 (solid line) degrees with p-polarized IR light. B. Variable angle reflectance FTIR spectra obtained from a ratio of SFO electrode to gold. Spectra shown are for angles of incidence of 50 (-- --), 60 (- -- -) and 70 (solid line) degrees with s-polarized IR light. ……75

Figure 3. A. Variable angle reflectance FTIR spectra obtained from a ratio of glass slide (back of ITO electrode) to gold. Spectra shown are for angles of incidence of 50 (-- --), 60 (- -- -) and 70 (solid line) degrees with p-polarized IR light. B. Variable angle reflectance FTIR spectra obtained from a ratio of glass slide (back of ITO electrode) to gold. Spectra shown are for angles of incidence of 50 (-- --), 60 (- -- -) and 70 (solid line) degrees with s-polarized IR light. ……76

Figure 4. Reflectance FTIR spectra at an incident angle of 70 degrees and p-polarized radiation at three different ITO electrodes with varying resistances: 12 (solid), 9.0 (- -- -), and 6.8 (-- --) Ω. ……..77

Figure 5. Plot of the absorbance of the 1248 cm^{-1} glass mode versus resistance for the three different ITO electrodes. ……..78

Figure 6. XPS spectra of A. In $3d_{5/2,3/2}$, B. Sn $3d_{5/2,3/2}$, and C. O 1s of Bare ITO (solid). ……79

Figure 7. Plots of the calculated power reflectivity for s-(top three

curves) and p-(bottom three curves) polarized light for incident angles of 70 (solid), 60 (- - -), and 50 (- -- -) degrees as calculated from the Fresnel equations of reflection. ……80

Figure 8. Calculated power reflectivity for p-polarized radiation and an incident angle of 70 degrees for ITO with resistances of 6.8 (top), 9.0 (middle), and 12 Ω (bottom). Using a thickness of 1500Å and a value of $2x10^{-14}$s for the electronic scattering time. ……81

Figure 9. The observed reflectance (A) and the calculated power reflectivity (B) for an incident angle of 70 degrees and p-polarized radiation. The plots refer from top to bottom for A and B to 2000, 2500, 3000, and 3500 cm^{-1}, respectively. ……....82

CHAPTER 5

Figure 1. Variable angle reflectance FTIR spectra obtained from a ratio of an ITO electrode to gold. Spectra shown are for angles of incidence of 50 (— —), 60 (- - -) and 70 (solid line) degrees for p-polarized (A) and s-polarized (B) IR light. ……108

Figure 2. A. Baseline corrected variable angle reflectance FTIR spectra obtained from a ratio of 1-hexadecanethiol on ITO to bare ITO. Spectra shown are for angles of incidence of 40 (— - —), 50 (— —), 60 (- - -), and 70 (solid line) degrees for p-polarized IR light and 70 degrees for s-polarized light (— - - —). (Inset: model of 1-hexadecantheiol) B. Baseline corrected reflectance FTIR spectra (incidence angle of 70 degrees with p polarized radiation) obtained from a ratio of 1-hexadecanethiol on ITO to bare ITO (solid), ratio of 1-hexadecanethiol on SFO to bare SFO (- - -), and the subtraction of the spectrum of 1-hexadecanethiol on ITO from the spectrum of 1-hexadecanethiol on SFO (— —). The bare (reference) substrate was cleaned via 20 minutes of UV/O_3, while the monolayer deposition occurred for 16 hours. ……..109

Figure 3. Baseline corrected reflectance FTIR spectra obtained from a ratio of 12-phosphonododecanoic acid (deposited from 50/50 (v/v) DMSO/18 MΩ·cm H_2O (solid line), and DMSO (dashed line)) on ITO to bare ITO. Spectra shown are for

an incident angle of 70 degrees and p-polarized IR light. The spectra were obtained from a ratio of 12-phosphonododecanoic acid on ITO to bare ITO. The bare (reference) ITO substrate was cleaned via 20 minutes of UV/O_3, while the monolayer deposition occurred for 16 hours. (Inset: model of 12-phosphonododecanoic acid) ……...111

Figure 4. XPS spectra of A. Indium $3d_{5/2,3/2}$, B. Tin $3d_{5/2,3/2}$, and C. Carbon 1s of Bare ITO (solid), 12-phosphonododecanoic acid on ITO (- - -), and 1-hexadecanethiol on ITO (— —). ……....112

Figure 5. Oxygen 1s XPS spectra of A. Bare ITO (solid), B. 12-phosphonododecanoic acid on ITO, and C. 1-hexadecanethiol on ITO. The raw data (markers) and the individual and total 90/10 Gaussian/Lorenztian fits (solid) are shown. ……...113

Figure 6. Sulfur $2p_{3/2,1/2}$ XPS spectra corresponding to A. an adlayer of 1-hexadecanethiol on ITO and B. a partial adlayer of dodecanethiol on ITO. The raw data (markers) and the individual and total 90/10 Gaussian/Lorenztian fits (solid) are shown. ……114

Figure 7. Phosphorous $2p_{3/2,1/2}$ (133.2, 134.3 eV) XPS spectra of 12-phosphonododecanoic acid on ITO. The raw data (markers) and the individual and total 90/10 Gaussian/Lorenztian fits (solid) are shown. ……115

Figure 8. DFT calculated frequency spectra of the carboxylic acid (solid) and carboxylate (dashed) forms of 12-phosphonododecanoic acid. The spectra have a Gaussian width of 7 cm^{-1}. (Insets: models corresponding to the two spectra) ……116

Figure 9. DFT calculated frequency spectra for polymethylene (12 methylene groups per box) using periodic boundary conditions (PBC) for different box dimensions. The box dimensions are defined by sides a, b, and c. The molecular axis of the molecule is parallel to the a direction. The box angles are 60 degrees while the lengths for a, b, and c are 15, 10, and 10 Å (solid curve) and 15, 10, and 6 Å (dashed curve) respectively. The length of the box along the a direction makes the distance between carbon atoms in adjacent boxes to be the same between carbon atoms along the alkane chain in the same box. The spectra have a Gaussian width of 7 cm^{-1}. ……...117

Figure 10. Potential energy surfaces (PES) of A. the binding of S (of 1-hexadecanethiol) to In (solid) or Sn (dashed) in the gas phase B. varying the width of the box (subunit) using periodic boundary conditions for 1-hexadecanethiol (solid) and 12-phosphonododecanoic acid (dashed) with box angles of 60 degrees. The length along the molecular axis of the molecules was 30 Å and one length perpendicular to the molecular axis was 10 Å, while the finally length (perpendicular to the molecular axis) was varied from 4.5 – 10 Å to obtain the PES C. varying the width of the box using periodic boundary conditions for 1-hexadecanethiol (solid), dodecanethiol (- - -), and octanethiol (— —) using the same protocol for 1-hexadecanethiol in B. The potential energies were referenced to 10 Å for A, B, and C. ……..118

CHAPTER 6

Figure 1. A. Experimental variable angle reflectance FTIR spectra of a thin film of ITO (13.8 ohms/square) on a glass substrate relative to a gold surface in the near-IR region for incident angles ranging from 40 to 80 degrees with p-polarized radiation (air/ITO sampling geometry). B. Plot of the measured reflectance at 9164 cm^{-1} of ITO (13.8 Ω/□) as a function of incident angle for p-polarized radiation. ……140

Figure 2. Experimental (A) and calculated (B, C) reflectance spectra for incident angles of 40 (short dashed), 60 (long dashed), and 80 (solid) degrees for ITO on a glass substrate with a sheet resistance of 13.8 Ω/□ recorded or calculated with p-polarized radiation in the near-IR region. The calculated reflectance spectra of ITO used either the two-phase (air/ITO) (B) or three-phase (air/ITO/glass) (C) Fresnel equations of reflection. ……141

Figure 3. Experimental (solid) reflectance FTIR and calculated (dashed) power reflectivity spectra of three ITO electrodes with sheet resistances of 7.6, 9.7, and 13.8 Ω/□ for p-polarized radiation in the near-IR region using either the two-phase (air/ITO) (A) or the three-phase (air/ITO/glass) (B) Fresnel equations of reflection. ……143

Figure 4. Plot of the plasma frequency (ω_p) dependence on the inverse square root of the sheet resistance (R) (A) and electronic scattering time (τ) (B) of ITO. ……144

Figure 5. Experimental reflectance FTIR spectra of a thin film of ITO (13.8 Ω/□) on a glass substrate recorded in an air/glass/ITO sampling geometry for incident angles of 40 to 80 degrees to the surface normal for p-polarized radiation in the near-IR region. ……145

Figure 6. Experimental reflectance FTIR spectra of bare ITO (solid), an adlayer of 12-phosphonododecanoic acid on ITO (short dashed), and an adlayer of 1-hexadecanethiol on ITO (long dashed). The spectra were recorded at an incident angle of 60 degrees with p-polarized radiation. The sampling geometry was either air/adlayer/ITO/glass (A) or air/glass/ITO/adlayer (B). ……146

Figure 7. Experimental reflectance FTIR spectra for incident angles of 40 to 80 degrees for SFO on a glass substrate with a sheet resistance of 55.6 Ω/□ recorded with p-polarized radiation in the near-IR region with either the air/SFO (A) or air/glass/SFO (B) sampling geometry. ……148

CHAPTER 7

Figure 1. The bixbyite crystal structure of indium oxide ($In_{32}O_{48}$) showing one unit cell where the indium and oxygen atoms are represented by the black and hollow spheres, respectively. ……...171

Figure 2. Transmission FTIR spectrum of an ITO thin film on a glass substrate at normal incidence recorded with p-polarized radiation. ……...172

Figure 3. DFT calculated dependence of the optical band gap (A), Fermi energy (B) and charge carrier concentration (C) on the tin content in the ITO lattice. ……173

Figure 4. DFT calculated dependence of the Fermi energy (A) and charge carrier concentration (B) for $In_{28}Sn_4O_{48}$ on the cubic lattice parameter. (C) DFT calculated dependence of the single point energy of $In_{32}O_{48}$ (hollow squares)

and $In_{28}Sn_4O_{48}$ (black squares) and the corresponding five term polynomial fit for $In_{32}O_{48}$ (dashed curve) and $In_{28}Sn_4O_{48}$ (solid curve) on the cubic lattice parameter. ……..174

Figure 5. DFT calculated dependence of the Fermi energy (A) and charge carrier concentration (B) on the distance between two tin atoms in the $In_{30}Sn_2O_{48}$ lattice. ……..176

Figure 6. DFT calculated plasma frequency of ITO at various levels of tin doping (A) and as a function of the cubic lattice parameter for $In_{28}Sn_4O_{48}$ using the charge carrier concentration determined at point Γ and the effective free electron mass from the Δ (Γ → X) direction in the band structure. ……..177

Figure 7. DFT calculated orbital of $In_{28}Sn_4O_{48}$ for the conduction band at point Γ in the Brillouin zone showing the Sn 5s and O 2s, 2p orbitals in an antibonding configuration. (indium: purple spheres, oxygen: red spheres). …….178

CHAPTER 8

Figure 1. XPS spectra of In $3d_{5/2,3/2}$ (A) and Sn $3d_{5/2,3/2}$ (B) for bare ITO (solid), ITO modified with a monolayer of 12-phosphonododecanoic acid (short dash) and ITO modified with ssDNA coupled through a monolayer of 12-phosphonododecanoic acid (long dash). C. XPS N 1s spectra of ITO modified with a monolayer of 12-phosphonododecanoic acid (long dash) and ITO modified with ssDNA coupled through a monolayer of 12-phosphonododecanoic acid (short dash) fitted to a Gaussian line shape (solid). …….199

Figure 2. A. Reflectance FTIR spectra of ITO modified with a monolayer of 12-phosphonododecanoic acid (solid) coupled to ssDNA (short dashed) recorded at an incident angle of 80 degrees with p-polarized radiation. B. Density functional theory (DFT) calculated IR spectra of 12-phosphonododecanoic acid (solid), 12-phosphonododecanamide (short dashed) and ssDNA (long dashed) calculated from a weighted average of the calculated IR spectra of the individual nucleosides fit to a Gaussian width of 10 cm^{-1}. ……...201

Figure 3. Chronocoulometry of a ssDNA modified ITO surface with (long dash) or without (short dash) $[Ru(NH_3)_6]^{3+}$ in the electrochemical cell. ……..202

Figure 4. XPS Au $4f_{7/2,5/2}$ spectra (A) and stripping voltammograms (in a 0.5 M KCl solution) (B) of ITO modified with ssDNA (long dash XPS spectrum (A)) exposed to the complementary (solid) or non-complementary (short dash) ssDNA labeled with 10 nm gold nanoparticles (1 nM). C. The AFM image ($1\mu m^2$ with a height scale of 50 nm) of ITO modified with ssDNA exposed to the complementary ssDNA labeled with 10 nm gold nanoparticles (1 nM). ……203

Figure 5. Anodic current versus time for an ITO electrode modified with ssDNA and hybridized with the complimentary ssDNA gold-nanoparticle conjugate (1 nM). The measurement was done in 0.1 M potassium phosphate buffer with 0.05 M EDTA. At 30 s the sample was illuminated with 532 nm laser light with a power density of approximately 100 W/cm^2. After 90 s the laser light was switched off. The potential was held at 0.7 V versus a Ag(s)/AgCl reference electrode that was not fixed isothermally. ……205

Figure 6. A. Electrochemical response for 100 mM $FeCl_2$ (scan rate 100 mV/s) as a function of the amount of target ssDNA / gold nanoparticle conjugate in the hybridization solution. The four target concentrations were 1 nM, 500 pM, 100 pM and 10 pM of the gold nanoparticles (modified with the target ssDNA). The hybridization was allowed to proceed for 1 hour at 45°C and the solution was then gradually cooled to room temperature overnight. B. Electrochemical response as a function of the amount of the gold nanoparticle / target ssDNA in the hybridization solution at 887 mV (squares) for the oxidation current and 109 mV (triangles) for the reduction current fit globally to a straight line (solid). ……206

Figure 7. Electrochemical response for 100 mM $FeCl_2$ (scan rate 100 mV/s) as a function of the amount of target ssDNA in the hybridization solution with improved hybridization conditions. The three target amounts were 100 pM, 10 pM and 1 pM of the gold nanoparticles (10 nm diameter) modified with the target single stranded DNA. The hybridization was

allowed to proceed at 37°C for nineteen hours in a shaking incubator. ……..207

CHAPTER 9

Figure1. Variable angle reflectance FTIR spectra of a 110 nm iridium oxide thin film on a glass substrate. The spectra were recorded at with incident angles ranging from 40 – 80 degrees in 10 degree increments with p-polarized radiation. ……...227

Figure 2. Experimental (solid) and calculated (dashed) reflectance IR spectra of an iridium oxide thin film for an incident angle of 60 degrees with p-polarized radiation. ……228

Figure 3. DFT calculated distribution of electrons in the vicinity of the Fermi energy for iridium oxide (markers) fit to the Fermi-Dirac distribution (solid). The two vertical lines denote the optical band gap. ……..229

Figure 4. DFT calculated dependence of the optical band gap, Fermi energy, charge carrier concentration and plasma frequency of iridium oxide on temperature. ……...230

Figure 5. DFT calculated dependence of the optical band gap, Fermi energy, charge carrier concentration, plasma frequency and binding energy of iridium oxide on the compression or expansion of the unit cell of iridium oxide. ……..231

CHAPTER 10

Figure 1. Potential surface at zero field (—) and in an applied electric field (···). The electric field perturbation is linear (– – –). The potential energy surface in an applied field is the linear combination of the PES at zero field and the linear perturbation. The position of the zero field potential and the electric field shifted potential surfaces are shown as Q_0 and Q_F, respectively. The energy offset $(\partial\mu/\partial Q)(Q_0 - Q_F)F$ is shown for the perturbed surface. ……256

Figure 2. Potential energy surface formed by displacing along the CO stretching normal mode in carbon monoxide and

the first five vibrational energy levels calculated by the Numerov-Cooley method. ……257

Figure 3. Plot of the experimental versus the DFT calculated vibrational Stark tuning rates for nitriles and carbonyls fit to a line with a slope of 1.1. ……258

Figure 4. Plot of the experimental versus the DFT calculated transition polarizability for nitriles using optimized molecular geometries in the presence of an applied electric field. The plot for the molecular geometries obtained in the absence of an applied electric field is nearly identical. ……259

CHAPTER 11

Figure 1. A. Representative QCM-D measured change in frequency of the 35 MHz seventh harmonic of the fundamental frequency and dissipation change upon binding of citrate (10 mM in water) and the subsequent binding of BSA (100 μM in 10 mM citrate in water) to a gold coated quartz crystal as a function of time at 25.7±0.1°C. The data is divided by seven to normalize for the harmonic used. B. The change in frequency and the corresponding change in surface coverage of BSA as a function of concentration onto a gold surface fit to a Langmuir adsorption isotherm (Eqn. 2). ……271

Figure 2. The change in the frequency of the 35 MHz seventh harmonic of the fundamental frequency of a gold coated quartz crystal as a function of BSA concentration coated with (solid squares) or without (open squares) citrate fit to a Langmuir adsorption isotherm (solid) (Eqn. 2) measured at 25.7±0.1°C. ……..272

Figure 3. Zeta potential of 10 nm gold nanoparticles recorded as a function of stabilizing agent (citrate or BSA) and pH. ……..273

CHAPTER 12

Figure 1. Structure of the wild type three-helix bundle protein villin headpiece subdomain (HP36) (Protein Data Bank Structure 1VII) illustrating the phenylalanine residues

(F47, F51, F58) present in the hydrophobic core. ……305

Figure 2. A. Equilibrium FTIR absorbance spectra of HP36 as a function of temperature in the range of 3 – 93°C in ~ 5°C increments in the 1550 – 1750 cm^{-1} region. B. Difference FTIR spectra of HP36 formed by subtracting the absorbance spectrum at 3°C from the spectra at the higher temperatures. ……..306

Figure 3. The first (solid), second (short dashed) and third (long dashed) spectral components (A) and the corresponding temperature dependence (B) of the first (squares), second (triangles) and third (bowties) spectral components as determined from the SVD analysis of the equilibrium FTIR temperature dependent data for HP36. The temperature dependence (B) of the third spectral component was fit (solid curve) to Eqn. 5. ……..307

Figure 4. A. Representative Gaussian global fit of the temperature dependent equilibrium difference FTIR spectra of HP36 for the difference spectrum obtained by subtracting the FTIR absorbance spectrum measured at 4ºC from the spectrum recorded at 64ºC. The raw data (long dash) was fit to six Guassian bands. The individual bands (short dash) and the total Gaussian fit (solid) are shown. B. The temperature dependence of the areas of the 1614 (hollow squares), 1629 (black squares), 1645 (black triangles), 1663 (hollow triangles) and 1680 (bowties) cm^{-1} Gaussian bands as a function of temperature. The areas of the 1614, 1629, 1645, and 1680 cm^{-1} Gaussian bands were globally fit (solid) to Eqn. 5. ……308

Figure 5. Equilibrium FTIR absorbance spectra of HP36F4751L as a function of temperature in the range of 5 – 83°C in ~ 5°C increments in the 1550 – 1750 cm^{-1} region (A) and the corresponding difference FTIR spectra formed by subtracting the absorbance spectrum at 5°C from the spectra at the higher temperatures (B). ……309

Figure 6. The first (solid) and second (dashed) spectral components (A) and the corresponding temperature dependence (B) of the first (squares) and second (triangles) spectral components as determined from the SVD analysis of the equilibrium FTIR temperature dependent data for HP36F4751L. The temperature dependence (B) of the second spectral component was fit (solid curve) to Eqn. 5. ……...310

Figure 7. Representative kinetic traces of the relaxation kinetics of HP36 (A) and HP36F4751L (B) at 1632 cm^{-1} and 1650 cm^{-1} (dashed curves) fit to a bi-exponential function (solid curves). The temperature after the T-jump (T_f) is noted on the graph with temperature jumps ranging from 5 – 15°C. ……..311

Figure 8. Plot of the natural log of the measured relaxation (square, slow phase), folding (k_f, triangles) and unfolding (k_u, bowties) rates as a function of the inverse of temperature for HP36 using a two-state model of folding. The dependence of the folding and unfolding rates on temperature was fit to Eqn. 8 (solid). The relaxation rates were measured at 1632 cm^{-1} and 1650 cm^{-1}. ……...312

CHAPTER 13

Figure 1. Schematic of the time-resolved step-scan FTIR spectrometer with 5 microscecond time resolution synchronized in time with a Nd:YAG laser. ……323

Figure 2. A. Baseline corrected static absorbance spectrum of 20 mM HH MbCO in 50 mM potassium phosphate buffer pH 7 in 75/25 percent glycerol / water (v/v). B. Time-resolved step-scan FTIR difference spectra of HH MbCO illustrating the bimolecular recombination of CO to myoglobin in response to a laser flash at 532 nm that photolyzed the iron – CO bond with 5 microsecond time resolution. ……324

Figure 3. Singular value decomposition (SVD) of the time-resolved step-scan FTIR data showing the first (dashed) and second (solid) spectral components (A) with the corresponding time dependence (B) of the spectral components. ……....325

APPENDIX 1

Figure 1. Eigenvector projection for the 1572 cm^{-1} vibrational mode of adenine comprised predominately of a NH_2 bend. ……328

Figure 2. Eigenvector projection for the 1584 cm^{-1} vibrational mode of adenine comprised of a NH_2 bend and a C=N stretch. ……329

Figure 3. Eigenvector projection for the 1629 cm^{-1} vibrational mode of adenine comprised predominately of a NH_2 bend. ……330

Figure 4. Eigenvector projection for the 1649 cm^{-1} vibrational mode of thymine comprised predominately of a C-C stretch. ……..331

Figure 5. Eigenvector projection for the 1705 cm^{-1} vibrational mode of thymine comprised predominately of a carbonyl stretch. …...332

Figure 6. Eigenvector projection for the 1756 cm^{-1} vibrational mode of thymine comprised predominately of a carbonyl stretch. …...333

Figure 7. Eigenvector projection for the 1605 cm^{-1} vibrational mode of the adenine-thymine (AT) base pair comprised predominately of a NH_2 bend. ……..334

Figure 8. Eigenvector projection for the 1642 cm^{-1} vibrational mode of the adenine-thymine (AT) base pair comprised predominately of ring deformation. ……335

Figure 9. Eigenvector projection for the 1655 cm^{-1} vibrational mode of the adenine-thymine (AT) base pair comprised of a NH_2 bend and a C=N stretch. ……336

Figure 10. Eigenvector projection for the 1676 cm^{-1} vibrational mode of the adenine-thymine (AT) base pair comprised of a carbonyl stretch and a N-H bend. ……337

Figure 11. Eigenvector projection for the 1754 cm^{-1} vibrational mode of the adenine-thymine (AT) base pair comprised predominately of a carbonyl stretch. ……338

Figure 12. Eigenvector projection for the 1557 cm^{-1} vibrational mode of guanine comprised predominately of a C=N stretch. …….339

Figure 13. Eigenvector projection for the 1582 cm^{-1} vibrational mode of guanine comprised predominately of a NH_2 bend (and ring deformation). ……340

Figure 14. Eigenvector projection for the 1632 cm^{-1} vibrational mode of guanine comprised predominately of a NH_2 bend. ……341

Figure 15. Eigenvector projection for the 1742 cm^{-1} vibrational mode of guanine comprised predominately of a carbonyl stretch. …...342

Figure 16. Eigenvector projection for the 1524 cm^{-1} vibrational mode of cytosine comprised predominately of a C=N stretch (and ring deformation). ……343

Figure 17. Eigenvector projection for the 1599 cm^{-1} vibrational mode of cytosine comprised predominately of a NH_2 bend. ……344

Figure 18. Eigenvector projection for the 1653 cm^{-1} vibrational mode of cytosine comprised a NH_2 bend and C=N stretch (and ring deformation). ……345

Figure 19. Eigenvector projection for the 1733 cm^{-1} vibrational mode of cytosine comprised predominately of a carbonyl stretch. …..346

Figure 20. Eigenvector projection for the 1565 cm^{-1} vibrational mode of the guanine-cytosine (GC) base pair comprised of both a carbonyl stretch and a NH_2 bend. ……..347

Figure 21. Eigenvector projection for the 1628 cm^{-1} vibrational mode of the guanine-cytosine (GC) base pair comprised of a carbonyl stretch, a NH_2 (and N-H) bend, and a C=N stretch (and ring deformation). ……348

Figure 22. Eigenvector projection for the 1634 cm^{-1} vibrational mode of the guanine-cytosine (GC) base pair comprised of a carbonyl stretch and a NH_2 (and N-H) bend (and ring deformation). ……349

Figure 23. Eigenvector projection for the 1676 cm^{-1} vibrational mode of the guanine-cytosine (GC) base pair comprised of a carbonyl stretch and a NH_2 bend. ……350

Figure 24. Eigenvector projection for the 1684 cm^{-1} vibrational mode of the guanine-cytosine (GC) base pair comprised of a carbonyl stretch and a N-H bend. ……..351

Figure 25. Eigenvector projection for the 1717 cm^{-1} vibrational mode of the guanine-cytosine (GC) base pair comprised of a carbonyl stretch and a N-H bend. ……..352

APPENDIX 2

Figure 1. Single-pass ATR-FTIR spectra of a glucose (solid), mannose (long dashed) and lactose (short dashed). …….354

Figure 2. DFT optimized structure of a monolayer of PBA on a gold (111) surface. The PBA molecules were arranged in a $\sqrt{3}x\sqrt{3}R\ 30°$ lattice pattern on the surface, typical for alkane thiols on a gold (111) surface. ……...355

Figures 3. DFT eigenvector projections of PBA with (B) and without (A) glucose bound with the corresponding calculated normal mode wavenumbers. These structures show the conversion of the boronic acid moiety of PBA to a boronate ester upon glucose binding. ……356

APPENDIX 3

Figure 1. Experimental reflectance FTIR spectra for incident angles of 40 (short dashed), 60 (long dashed) and 80 (solid) degrees for ITO on a quartz substrate with a sheet resistance of 16.4 Ω/□ recorded with p-polarized radiation in the near-IR region (air/ITO sampling geometry). …….361

APPENDIX 4

Figure 1. Potential energy surfaces and Numerov-Cooley vibrational wavefunctions. ……380

Figure 2. Plot of the experimental versus the DFT calculated difference polarizability for nitriles using optimized molecular geometries in the absence (A) or presence of an applied electric field. ……...387

Figure 3. Optimized CO and CN containing molecules in zero applied electric field. ……388

APPENDIX 5

Figure 1. Plot of the natural log of the measured relaxation (square, slow phase), folding (k_f, triangles) and unfolding (k_u, bowties) rates as a function of the inverse of temperature for HP36F4751L using a two-state model of folding. The

relaxation rates were measured at 1632 cm^{-1} and 1650 cm^{-1}. ……..394

LIST OF SCHEMES

Page

CHAPTER 3

Scheme 1. Synthesis of N-(3-dihydroxyborylphenyl)-11-mercaptoundecanamide), PBA. ……..…51

CHAPTER 8

Scheme 1. Modification of ITO with single stranded DNA through the formation of an amide bond between the carboxylic acid functional group of a monolayer of 12-phosphonododecanoic acid with the primary amine of 5’ modified $H_2N(CH_2)_3$ ssDNA. ……..……198

Chapter 1

Introduction

Two areas of active research in science are in genomic arrays and protein folding. Genomic arrays are an important area of research for applications in detection of messenger RNA levels in cells and genomic analysis. [1-14] Protein folding studies investigating the mechanism and kinetics of folding are critical to understand how genomic information that codes for the amino acid sequences of proteins determines the three dimension fold of a protein. [15-27] This folding information is also needed to help understand the diseases related to protein misfolding such as Alzheimer's disease and prion diseases such as sheep scrapie, mad cow disease and Creutzfeldt-Jakob disease. [28,29] These two areas impact science at a fundamental level of studying both DNA and proteins by either determining better means of DNA detection on surfaces or by understanding the folding and unfolding of proteins in solution.

The methodology used to address these key areas of science will be to combine both experimental techniques and theoretical calculations. Theoretical calculations will be used to help analyze and understand the experimental results. For instance, an integral experimental spectroscopic technique used in this research is infrared (IR) spectroscopy. Infrared spectroscopy probes molecular vibrations and can probe structure by monitoring certain vibrational modes since IR spectroscopy is sensitive to hydrogen bonding and the dielectric environment of the vibrational mode of interest. Infrared spectroscopy can be used to

monitor the formation of adlayers on metal and metal oxide surfaces. Density functional theory (DFT) calculations can then be used in certain circumstances to calculate the infrared spectrum of a given molecule.

In the following studies, a variety of systems were investigated focusing on the modification and characterization of metal and metal oxide surfaces with DNA and studying protein folding. Infrared spectroscopy and density functional theory were used to detect and analyze DNA hybridization on ssDNA modified gold surfaces and sugar binding to a phenylboronic acid terminated monolayer on a gold surface. To develop possibly better means of detection of DNA hybridization on surfaces, indium tin oxide (ITO) surfaces were studied. The optical and electronic properties of this metal oxide were first characterized experimentally aided by DFT calculations of this metal oxide. The formation of self-assembled monolayers with various functional groups was then studied resulting in the modification of ITO thin films with ssDNA. These ssDNA modified thin films were then hybridized with gold nanoparticle labeled target ssDNA to detect surface DNA hybridization. The properties of other metal oxides such as fluorine doped tin oxide and iridium oxide thin films were also studied. The binding of citrate and bovine serum albumin (BSA) to gold surfaces and gold nanoparticles was studied by quartz crystal microbalance and zeta potential measurements to gain further understanding of gold nanoparticles.

The thermodynamics and kinetics of the folding and unfolding of the three alpha helix bundle protein villin headpiece subdomain was studied by equilibrium temperature dependent infrared spectroscopy and temperature jump IR spectroscopy. The folding and unfolding of the wild type protein was compared to a double mutant with a destabilized

hydrophobic core, while density functional theory was used to investigate the vibrational Stark effect for several model systems. Finally, a step scan time resolved FTIR spectrometer was implemented for future studies of protein folding and dynamics with five microsecond time resolution.

References

(1) Taton, T. A.; Mirkin, C. A.; Letsinger, R. L. *Science* **2000**, *289*, 1757-1760.

(2) Herne, T. M.; Tarlov, M. J. *Journal of the Chemical Society* **1997**, *119*, 8916-8920.

(3) Fodor, S. P. A.; Read, J. L.; Pirrung, M. C.; Stryer, L.; Lu, A. T.; Solas, D. *Science* **1991**, *251*, 767-773.

(4) Lockhart, D. J.; Winzeler, E. A. *Nature* **2000**, *405*, 827-836.

(5) Bulyk, M. L.; Gentalen, E.; Lockhart, D. J.; Church, G. M. *Nature Biotechnology* **1999**, *17*, 573-577.

(6) Chee, M.; Yang, R.; Hubbell, E.; Berno, A.; Huang, X. C.; Stern, D.; Winkler, J.; Lockhart, D. J.; Morris, M. S.; Fodor, S. P. A. *Science* **1996**, *274*, 610-614.

(7) He, L.; Musick, M. D.; Nicewarner, S. R.; Salinas, F. G.; Benkovic, S. J.; Natan, M. J.; Keating, C. D. *Journal of the Chemical Society* **2000**, *122*, 9071-9077.

(8) Brockman, J. M.; Frutos, A. G.; Corn, R. M. *Journal of the American Chemical Society* **1999**, *121*, 8044-8051.

(9) Esch, M. B.; Locascio, L. E.; Tarlov, M. J.; Durst, R. A. *Analytical Chemistry* **2001**, *73*, 2952-2958.

(10) Steel, A. B.; Herne, T. M.; Tarlov, M. J. *Analytical Chemistry* **1998**, *70*, 4670-4677.

(11) Steel, A. B.; Herne, T. M.; Tarlov, M. J. *Bioconjugate Chem.* **1999**, *10*, 419-423.

(12) Cao, Y. W.; Jin, R.; Mirkin, C. A. *Journal of the American Chemical Society* **2001**, *123*, 7961-7962.

(13) Demers, L. M.; Mirkin, C. A.; Mucic, R. C.; Reynolds, R. A.; Letsinger, R. L.; Elghanian, R.; Viswanadham, G. *Analytical Chemistry* **2000**, *72*, 5535-5541.

(14) Sauthier, M.; Carroll, R.; Gorman, C.; Franzen, S. *Langmuir* **2002**, *18*, 1825-1830.

(15) Wang, M. H.; Tang, Y. F.; Sato, S. S.; Vugmeyster, L.; McKnight, C. J.; Raleigh, D. P. *Journal of the American Chemical Society* **2003**, *125*, 6032-6033.

(16) Myers, J. K.; Oas, T. G. *Nature Structural Biology* **2001**, *8*, 552-558.

(17) Werner, J. H.; Dyer, R. B.; Fesinmeyer, R. M.; Andersen, N. H. *Journal of Physical Chemistry B* **2002**, *106*, 487-494.

(18) Maness, S. J.; Franzen, S.; Gibbs, A. C.; Causgrove, T. P.; Dyer, R. B. *Biophysical Journal* **2003**, *84*, 3874-3882.

(19) Williams, S.; Causgrove, T. P.; Gilmanshin, R.; Fang, K. S.; Callender, R. H.; Woodruff, W. H.; Dyer, R. B. *Biochemistry* **1996**, *35*, 691-697.

(20) Leeson, D. T.; Gai, F.; Rodriguez, H. M.; Gregoret, L. M.; Dyer, R. B. *Proceedings of the National Academy of Sciences of the United States of America* **2000**, *97*, 2527-2532.

(21) Dyer, R. B.; Gai, F.; Woodruff, W. H. *Accounts of Chemical Research* **1998**, *31*, 709-716.

(22) Callender, R. H.; Dyer, R. B.; Gilmanshin, R.; Woodruff, W. H. *Annual Review of Physical Chemistry* **1998**, *49*, 173-202.

(23) Lednev, I. K.; Karnoup, A. S.; Sparrow, M. C.; Asher, S. A. *Journal of the American Chemical Society* **2001**, *123*, 2388-2392.

(24) Kubelka, J.; Eaton, W. A.; Hofrichter, J. *Journal of Molecular Biology* **2003**, *329*, 625-630.

(25) Thompson, P. A.; Munoz, V.; Jas, G. S.; Henry, E. R.; Eaton, W. A.; Hofrichter, J. *Journal of Physical Chemistry B* **2000**, *104*, 378-389.

(26) Thompson, P. A.; Eaton, W. A.; Hofrichter, J. *Biochemistry* **1997**, *36*, 9200-9210.

(27) Munoz, V.; Thompson, P. A.; Hofrichter, J.; Eaton, W. A. *Nature* **1997**, *390*, 196-199.

(28) Taylor, J. P.; Hardy, J.; Fischbeck, K. H. *Science* **2002**, *296*, 1991-1995.

(29) Caughey, B.; Lansbury, P. T. *Annual Review of Neuroscience* **2003**, *26*, 267-298.

Chapter 2

Detection of DNA Hybridization on Gold Surfaces by Polarization Modulation Infrared Reflection Absorption Spectroscopy

Abstract

Polarization modulation infrared reflection absorption spectroscopy (PM-IRRAS) was used to detect DNA hybridization on gold surfaces. Mixed monolayers of 6-mercapto-1-hexanol (MCH) and single stranded DNA (ssDNA) with a C6-SH 5' modifier was first formed on the gold surface by co-deposition. Then hybridization with the complementary ssDNA strand was performed to obtain double stranded DNA (dsDNA). The PM-IRRAS spectra obtained contained absorptive features indicative of DNA arising from the phosphodiester backbone and the purine and pyrimidine rings. An infrared signature of dsDNA was observed at 1655 cm^{-1} that was absent in the ssDNA spectra. This band permitted the distinction between ssDNA and dsDNA to be made thus allowing for the detection of DNA hybridization on gold surfaces by PM-IRRAS.

Introduction

The detection of DNA hybridization on surfaces is an area of intense current investigation. A number of methods have recently been employed for analysis of surface hybridization including fluorescence,[1-4] chronocoulometry,[5-7] surface plasmon resonance[8,9] and colloidal labeling of nanoparticles.[10-12] The hybridization of DNA on gold surfaces is of particular interest because of the wide use of self-assembled monolayers on gold. However, despite the well-developed application of grazing angle Fourier transform infrared spectroscopy[13,14] there has been no direct detection of DNA hybridization on self-assembled monolayers of DNA. There have been numerous experimental studies on the DNA bases by infrared spectroscopy[15-25] and non-resonant[16,21,25-31] and resonant Raman

spectroscopy.[32-36] These studies include using vibrational spectroscopy to probe B, A, and Z DNA forms[37-42] and to study drug and protein binding to DNA.[43-46] The vibrational spectra and energetics of the individual nucleic acids and the AT and GC base pairs have also been studied by semiempirical and DFT calculations.[47-49]

Self-assembled monolayers (SAMs) of DNA are prepared as mixed monolayers from a co-deposition solution of 6-mercapto-1-hexanol and single stranded DNA (ssDNA) followed by surface hybridization with the complementary ssDNA.[50] Here we report the first direct detection of DNA hybridization on a gold surface using polarization modulation infrared reflection absorption spectroscopy (PM-IRRAS). . The advantages of PM-IRRAS are threefold. First, labeling of the DNA with fluorescent tags or radioisotopes is not required. This technique is also non-intrusive allowing quick determination of the presence of single stranded DNA (ssDNA) or double stranded DNA (dsDNA) on the surface without contaminating the sample with an electrochemical agent. Thirdly, this technique can distinguish between the A, B, and Z forms of dsDNA on the surface. Single-pass attenuated total reflection (ATR)-FTIR solution spectra were taken of the ssDNA and dsDNA samples to verify the modes obtained with PM-IRRAS. ATR-FTIR spectra were also taken at various levels of hydration to determine the degree of hydration of the DNA strands on the surface. These comparisons provide an experimental link between bulk samples and analytical applications for detecting 10 picomoles (based on the surface coverage of DNA and the sampling area of PM-IRRAS) of DNA or less on a surface.[10] The experiments performed here establish the application of grazing angle FTIR spectroscopy to the observation DNA hybridization and detection of DNA-drug interactions using surface-attached DNA. Density

Functional Theory (DFT) calculations of the individual DNA bases and base pairs were performed to yield calculated frequency spectra of ssDNA and dsDNA that were in excellent agreement with experimentally observed bands.

Methods and Materials

DNA Monolayer Formation. The mixed self-assembled monolayers (SAM) were prepared on clean polycrystalline gold deposited on a glass slide containing a chromium oxide passivation layer obtained from Evaporated Films, Inc., cleaned with piranha solution (70% conc. H_2SO_4: 30%H_2O_2 (30%)) (CAUTION, piranha solution reacts violently with organic chemicals) and rinsed with millipore 18 MΩ·cm deionized water (BARNSTEAD E-PURE). The single-stranded DNA (ssDNA) (Applied Biosystems) probe strand was modified at the 5' end with a C6-S-disulfide modifier (Applied Biosystems). The ssDNA was deprotected to form the C6-SH linker as described elsewhere.[10] A co-deposition solution of 6-mercapto-1-hexanol (MCH) (Sigma-Aldrich) and ssDNA (probe strand) was used to form the mixed SAM on the gold surface with a 0.10 mole fraction of ssDNA in a 1μM MCH solution in 1 M potassium phosphate buffer (pH 7.0) for 16 hours at room temperature. The gold slides were then rinsed with 18 MΩ·cm deionized water and placed in a 1X SSC (saline sodium citrate) (Fisher Scientific) at 65°C for one hour and then cooled to room temperature over four additional hours with or without target ssDNA (exact complement to the probe ssDNA on the gold surface) for hybridization (2.5 nmol of target ssDNA). The surfaces were then rinsed in 18 MΩ·cm deionized water and dried with nitrogen gas. Both ssDNA strands were comprised of 30 bases and the probe strand had a sequence of 5'-

GGAGACTGTTATCCGCTCACAATTCCACAC-3' and the target ssDNA was the exact complement of the probe ssDNA strand. The solution hybridization mixture, containing the two complementary ssDNA strands (in 1X SSC), was heated to 85°C for five minutes and then cooled to room temperature for 30 minutes to obtain dsDNA for solution FTIR measurements. The excess salt from the dsDNA solution was removed using Centricon YM-3 centrifugal filter units (Millipore) and 18 MΩ·cm deionized water as the wash solvent.

Polarization Modulation Infrared Reflection Absorption Spectroscopy (PM-IRRAS). The PM-IRRAS spectra were recorded on a Bio-Rad FTS 7000 spectrometer equipped with a step scan interferometer, liquid nitrogen cooled narrow band MCT detector, globar source, and a UDR-8 filter. The IR radiation was typically phase modulated at frequencies of 400 or 800Hz at an amplitude of 1.0 or 2.0 λ HeNe while stepping at 0.5 - 2.5 Hz. A gold grid polarizer was used to obtain either s- or p-polarized radiaton, which was then modulated by a Hinds ZnSe PEM operating at 37 KHz and amplitude of 0.5 λ (strain axis 45 degrees to the polarizer) before reflecting off the sample at an incident angle of 80 degrees from the surface normal. The spectra were recorded at room temperature at a resolution of 8 cm^{-1} and were the result of 4 scans with a spectral range of 900 – 1800 cm^{-1}. The digital signal processing (DSP) algorithm incorporated into the Bio-Rad spectrometer software was used to obtain the spectra. This instrument allowed the gold slide containing the monolayer to also be the reference to obtain the absorption spectra. The solution single-pass ATR FTIR spectra of the DNA (~20 – 200mM) were taken using an IR microscope (model number UMA-500) attached to a Bio-Rad FTS 6000 FTIR spectrometer equipped with a Cassegranian objective containing a germanium crystal for single-pass attenuated total

reflection (ATR). The spectrometer was equipped with a liquid nitrogen cooled MCT/A detector and the spectra were recorded at a resolution of 2 cm^{-1} with a spectral range of 650 - 4000 cm^{-1}. The absorption spectra were the result of the average of multiplies of 64 scans and were recorded at room temperature.

Density Functional Theory (DFT) Calculations. The geometry optimization and vibrational frequency calculations of the individual DNA bases and complementary base pairs were done using the MSI (Molecular Simulations, Inc) quantum chemistry software program DMol3 at the North Carolina Supercomputer Center (NCSC) on the IBM RS/6000 SP. DMol3 is an ab initio (first principles) software package that utilizes density functional theory.[51] These calculations were done in the gas phase using the DNP basis set, the GGA functional, and the method of finite differences for calculating the vibrational frequencies. The MSI software Insight II was used to build the models and to visualize the eigenvector projections of the vibrational modes of the models.

Results and Discussion

Figure 1A and 1B show the PM-IRRAS spectra corresponding to the mixed monolayer of MCH and ssDNA before and after hybridization with the complementary ssDNA with a hybridization temperature of 65°C and 85°C respectively recorded at an incident angle of 80 degrees. The hybridization temperature was varied to obtain efficient hybridization while minimizing ssDNA strand loss from the gold surface. The ssDNA and dsDNA spectra contain absorptive features indicative of DNA for both temperatures. For instance, the modes centered at 1082 and 1238 cm^{-1} correspond to the symmetric and

asymmetric PO_2^- group of the DNA phosphodiester backbone.[52,53] The mode centered at 1188 cm^{-1} is a well-known deoxyribose structural marker mode. [54] The combination of the asymmetric PO_2^- group mode at 1238 cm^{-1} and the deoxyribose mode at 1188 cm^{-1} is indicative of A-form DNA structure consistent with the low humidity environment in the current PM-IRRAS configuration.[54,55] The modes at 1464 and 1514 cm^{-1} result from the purine and pyrimidine (DNA bases) ring modes,[52,53] while the region from 1600 – 1750 cm^{-1} is due to carbonyl (C=O), C=N stretching and exocyclic -NH_2 bending vibrations in the DNA bases.[52,56] However, the intensities of these bands are not the same at 65°C and 85°C due to the quantity and orientation of the DNA on the surface. The intensity for the ssDNA and dsDNA spectra for 85°C is lower than the corresponding spectra with a hybridization temperature of 65°C. This observation suggests that strand loss is occurring at the higher temperature due to thiolate desorption.

The major distinction between the PM-IRRAS spectra for ssDNA and dsDNA in Figures 1A and 1B is the presence of a band at 1655 cm^{-1} in the dsDNA spectra, which is absent in the ssDNA spectra. This distinction is observed at both hybridization temperatures. The intensity change in this region represents changes in hydrogen bonding between complementary bases that occur upon formation of a double helix and the quantity of DNA on the surface.[52] The infrared signature at 1655 cm^{-1} of dsDNA thus permits the detection of DNA hybridization on gold surfaces by PM-IRRAS.

Figure 2 shows the single-pass ATR FTIR spectra of ssDNA and dsDNA strands in aqueous solution to verify the absorptive features observed in the PM-IRRAS spectra of

ssDNA and dsDNA are due to these DNA species. These spectra contain similar features as seen in the PM-IRRAS spectra corresponding to these species on a gold surface. However the absorptive features present in Figure 2 for ssDNA and dsDNA are not identical due to the hydrogen bonding between complementary bases in the dsDNA.[52] The features can be assigned, as done above, to arising from the phosphodiester backbone and the purine and pyrimidine rings of the DNA bases. However, ssDNA has two modes in the high frequency region at 1594 and 1681 cm^{-1} that are replaced with a single mode at 1658 cm^{-1} in dsDNA. Therefore ssDNA and dsDNA can be distinguished in both solution and on the gold surface using infrared spectroscopy. The sample conditions under single-pass ATR-FTIR resemble those of a hydrated DNA fiber. [54]

Figure 3 shows the single-pass ATR FTIR spectra of ssDNA in aqueous solution as a function of hydration to estimate the amount of hydration in the DNA monolayers on the gold surfaces. Initially, the bending vibration mode of water at 1638 cm^{-1} masks the carbonyl and amino hydrogen bonding region of the spectra and the other modes in the spectra cannot be discerned due to a low concentration of DNA.[17] However, as the water begins to evaporate the concentration of the DNA in the IR radiation path begins to increase and the masking bending mode of water begins to decrease. Finally, only water of hydration is present in the sample permitting observations of the absorptive features of the DNA. Based on the absence of the water bending mode in the PM-IRRAS spectra, it can concluded that only the water of hydration is present on the gold surface of the DNA monolayers.

Figure 4 shows the density functional theory (DFT) calculated frequency spectra of the individual DNA bases, DNA base pairs, and their weighted average to obtain calculated

frequency spectra corresponding to the ssDNA and dsDNA used in the DNA monolayers on gold. Figure 4A specifically shows the DFT calculated vibrational spectrum of adenine, thymine, and the adenine-thymine (AT) base pair in the 1550 – 1800 cm^{-1} region. The adenine calculated spectrum has three modes at 1572, 1584, and 1629 cm^{-1} due mostly from NH_2 bending (and some ring deformation). The thymine calculated spectrum has a mode at 1649 cm^{-1} due to C-C stretching and two modes at 1705 and 1756 cm^{-1} resulting from carbonyl stretching. The calculated spectrum of the AT base pair resulted in four modes at 1605, 1655, 1676, and 1754 cm^{-1}. The modes at 1605 and 1655 cm^{-1} result from NH_2 bending, the mode at 1642 cm^{-1} is a ring deformation mode, the mode at 1676 cm^{-1} results from N-H bending, while the mode at 1754 cm^{-1} results from a carbonyl stretching motion. These spectra illustrate a blue shift of the NH_2 bending modes upon base pair formation due to hydrogen bonding which involves this group. The NH_2 bending motion of adenine becomes more constrained in the base pair and hence the frequency of the NH_2 bend increases. The carbonyl stretching frequency of the carbonyl group of thymine involved in hydrogen bonding in the AT base pair decreases in frequency upon base pair formation. This red shift is the result of a weakening of the C=O force constant due to hydrogen bonding. The other carbonyl stretching frequency of thymine decreases minimally since this carbonyl group is not involved in hydrogen bonding with adenine in the AT base pair. These shifts are in qualitative agreement with previous semiempirical calculations.[47]

Figure 4B shows the DFT calculated frequency spectra of guanine, cytosine, and the guanine-cytosine (GC) base pair in the region of 1550 – 1800 cm^{-1}. The calculated spectrum of guanine shows two modes at 1582 and 1632 cm-1 primarily due to NH_2 bending and one

carbonyl stretching mode at 1742 cm^{-1}. The cytosine calculated frequency spectrum shows two modes at 1524 and 1653 cm^{-1} resulting from ring deformation (and C=N stretching), a mode at 1599 cm^{-1} due to NH_2 bending, and a carbonyl stretching mode at 1733 cm^{-1}. The GC base pair calculated frequency spectrum shows six modes at 1565 (NH_2 and N-H bending, carbonyl stretching), 1628 and 1634 (primarily NH_2 and N-H bending, small component of carbonyl stretching and ring deformation), 1676 (NH_2 bending, carbonyl stretching), and 1684 and 1717 cm^{-1} (NH_2 and N-H bending, carbonyl stretching). Similar to the calculated spectrum of the AT base pair relative to the spectra of the individual bases, the GC calculated spectrum shows a blue shift in the NH_2 (and N-H) bending frequency and a red shift in the carbonyl stretching frequency for those groups involved in hydrogen bonding in the GC base pair relative to the individual bases.

Figure 4C shows the DFT calculated frequency spectra corresponding to the probe ssDNA strand and the dsDNA (after hybridization with target ssDNA) strand used in the monolayers on gold in the 1550 – 1800 cm^{-1} region. These spectra were obtained by weighting the individual (for ssDNA) or the base pairs (for dsDNA) spectra in the appropriate amount corresponding to the sequence of the probe and target ssDNA strands used. These show the NH_2 and N-H bending modes and the carbonyl stretching frequencies as discussed above for the individual bases and base pairs. The main difference between these two spectra is the existence of an infrared signature mode at 1676 cm^{-1} in the dsDNA spectrum that is absent in the calculated ssDNA spectrum. This result is consistent with the observed differences in the surface and bulk FTIR spectra of the corresponding ssDNA and

dsDNA strands. The models and the eigenvector projections of these modes are in the Supplementary Materials (Appendix 1).

Conclusion

Polarization modulation infrared reflection absorption spectroscopy (PM-IRRAS) was successfully used to detect DNA hybridization on a gold surface. The most pronounced spectral changes between ssDNA and dsDNA are in the nucleobase hydrogen bonding region from 1550 cm^{-1} to 1720 cm^{-1}. Surface hybridization was detected by an increase in absorption intensity at 1655 cm^{-1} in dsDNA. Comparison of the single-pass ATR-FTIR spectra of ssDNA solutions with the PM-IRRAS method showed that a minimal amount of water was present in the DNA monolayers on gold due to the absence of the water bending mode, $\nu_{H\text{-}O\text{-}H}$, at 1638 cm^{-1} in the PM-IRRAS spectra. This observation is significant because, if present, $\nu_{H\text{-}O\text{-}H}$ masks the region of the DNA spectrum that contains the most information. The spectral features of surface attached DNA are similar to those of fiber DNA at low humidity. [54] However, ssDNA does not form fibers and thus the conversion of ssDNA to dsDNA cannot be detected by FTIR spectroscopy so that the observed spectral changes associated with hybridization reported here are unique. The PM-IRRAS spectra were in excellent agreement with DFT calculated spectra of dsDNA and ssDNA. The calculated frequency spectra of the DNA bases and base pairs show that the difference between ssDNA and dsDNA results from the blue shift of the NH_2 and N-H bending modes and a red shift in the carbonyl stretching frequency due to hydrogen bonding between the complementary bases. These changes permit detection of DNA hybridization on samples for

which the surface coverage is 4 x 10^{12} molecules/cm^2.[10] The measurements shown in Figure 1 demonstrate the feasibility of detecting DNA hybridization on samples with this surface coverage. The fact that A-form structure is observed in the spectra presented here indicates that the current configuration can be used directly to observe binding events to surface-immobilized RNA. The PM-IRRAS method can be used in theory in high humidity conditions favoring B-form DNA. Thus, in addition to the detection of DNA hybridization, PM-IRRAS has the potential for use in the study of protein and drug binding to RNA and DNA.

Acknowledgements

This work was done in collaboration with Selina J. Anthireya (NCSU), Simon E. Lappi (NCSU), David L. Drapcho (Digilabs) and Stefan Franzen (NCSU) and was the subject of a publication, Brewer, S. H.; Anthireya, S. J.; Lappi, S. E.; Drapcho, D. L.; Franzen, S. *Langmuir* **2002**, 18(11), 4460-4464. Scott Brewer was supported by NIH Biotechnology Training Grant T32-GM08776. Support and computational facilities were provided by the North Carolina Supercomputing Center.

References

(1) Fodor, S. P. A.; Read, J. L.; Pirrung, M. C.; Stryer, L.; Lu, A. T.; Solas, D. *Science* **1991**, *251*, 767-773.

(2) Lockhart, D. J.; Winzeler, E. A. *Nature* **2000**, *405*, 827-836.

(3) Bulyk, M. L.; Gentalen, E.; Lockhart, D. J.; Church, G. M. *Nature Biotechnology* **1999**, *17*, 573-577.

(4) Chee, M.; Yang, R.; Hubbell, E.; Berno, A.; Huang, X. C.; Stern, D.; Winkler, J.; Lockhart, D. J.; Morris, M. S.; Fodor, S. P. A. *Science* **1996**, *274*, 610-614.

(5) Esch, M. B.; Locascio, L. E.; Tarlov, M. J.; Durst, R. A. *Anal. Chem.* **2001**, *73*, 2952-2958.

(6) Steel, A. B.; Herne, T. M.; Tarlov, M. J. *Anal. Chem.* **1998**, *70*, 4670-4677.

(7) Steel, A. B.; Herne, T. M.; Tarlov, M. J. *Bioconjugate Chemistry* **1999**, *10*, 419-423.

(8) He, L.; Musick, M. D.; Nicewarner, S. R.; Salinas, F. G.; Benkovic, S. J.; Natan, M. J.; Keating, C. D. *J. Am. Chem. Soc.* **2000**, *122*, 9071-9077.

(9) Brockman, J. M.; Frutos, A. G.; Corn, R. M. *J. Am. Chem. Soc.* **1999**, *121*, 8044-8051.

(10) Sauthier, M.; Carroll, R.; Gorman, C.; Franzen, S. *Langmuir* **2001**, *in press*.

(11) Cao, Y. W.; Jin, R.; Mirkin, C. A. *J. Am. Chem. Soc.* **2001**, *123*, 7961-7962.

(12) Demers, L. M.; Mirkin, C. A.; Mucic, R. C.; Reynolds, R. A.; Letsinger, R. L.; Elghanian, R.; Viswanadham, G. *Anal. Chem.* **2000**, *72*, 5535-5541.

(13) Allara, D.; Nuzzo, R. *Langmuir* **1985**, *1*, 52-66.

(14) Allara, D.; Nuzzo, R. *Langmuir* **1985**, *1*, 45-52.

(15) Chin, S.; Scott, I.; Szczepaniak, K.; Person, W. B. *J. Am. Chem. Soc.* **1984**, *106*, 3415-3422.

(16) Delabar, J. M.; Majoube, M. *Spectrochim. Acta* **1978**, *34A*, 129-140.

(17) Falk, M.; Hartman, K. A.; Lord, R. C. *J. Am. Chem. Soc.* **1963**, *85*, 387-391.

(18) Graindourze, M.; Smets, J.; Zeegers-Huyskens, T. H.; Maes, G. *J. Mol. Struct.* **1990**, *222*, 345-364.

(19) Hirakawa, A. Y.; Okada, H.; Sasagawa, S.; Tsuboi, M. *Spectrochim. Acta* **1985**, *41A*, 209-216.

(20) Kyogoku, A. Y.; Higuchi, S.; Tsuboi, M. *Spectrochim. Acta* **1967**, *23A*, 969-.

(21) Lewis, T. P.; Miles, H. T.; Becker, E. D. *J. Phys. Chem.* **1984**, *88*, 3253-3260.

(22)Thijs, R.; Zeeger-Huyskens, T. *Spec. Acta* **1984**, *40A*, 307-313.

(23)Thomas Jr., G. J. *Biopolymers* **1969**, *7*, 325-334.

(24)Tsuboi, M.; Kyogoku, Y.; Shimanouchi, T. *Biochim. Biophys. Acta* **1962**, *55*, 1-12.

(25)Tsuboi, M.; Takahashi, S.; Harada, I. *Infrared and Raman spectra of nucleic acids - Vibrations in the base residues*; Tsuboi, M.; Takahashi, S.; Harada, I., Ed.; Academic Press: Lodon, 1973; Vol. 2, pp 92-143.

(26) Lane, M. J.; Thomas Jr., G. J. *Biochemistry* **1979**, *18*, 3839-3846.

(27) Lord, R. C.; Thomas Jr., G. J. *Spectrochim. Acta* **1967**, *23A*, 2551-2591.

(28) Lord, R. C.; Thomas Jr., G. J. *Biochim. Biophys. Acta* **1967**, *142*, 1-11.

(29) Nishimura, Y.; Tsuboi, M.; Nakano, T.; Higuchi, S.; Sato, T.; Shida, T.; Uesugi, S.; Ohtsuka, E.; Ikehara, M. *Nucl. Acids Res.* **1983**, *11*, 1579-1588.

(30) Nishimura, Y.; Tsuboi, M.; Sato, T. *Nucl. Acids Res.* **1984**, *12*, 6901-6908.

(31) Peticolas, W. A.; Kubasek, W. L.; Thomas, G. A.; Tsuboi, M. *Nucleic Acids*; Peticolas, W. A.; Kubasek, W. L.; Thomas, G. A.; Tsuboi, M., Ed.; John Wiley and Sons: New York, 1987; Vol. 1, pp 82-133.

(32) Ziegler, L. D.; Hudson, B.; Strommen, D. P.; Peticolas, W. L. *Biopolymers* **1984**, *23*, 2067-2081.

(33) Tsuboi, M.; Nishimura, Y.; Hirakawa, A. Y.; Peticolas, W. L. *Resonance Raman spectroscopy and normal modes of the nucleic acid bases*; Tsuboi, M.; Nishimura, Y.; Hirakawa, A. Y.; Peticolas, W. L., Ed.; John Wiley and Sons: New York, 1988; Vol. 2, pp 109-179.

(34) Toyama, A.; Takino, Y.; Takeuchi, H.; Harada, I. *J. Am. Chem. Soc.* **1993**, *115*, 11092-11098.

(35) Toyama, A.; Kurashiki, E.; Watanabe, Y.; Takeuchi, H.; Harada, I. *J. Am. Chem. Soc.* **1991**, *113*, 3615-3616.

(36) Fodor, S. P. A.; Rava, R. P.; Hays, T. R.; Spiro, T. G. *J. Am. Chem. Soc.* **1985**, *107*, 1520-1529.

(37) Pohl, F. M.; Ranade, A.; Stockburger, M. *Biochim. Biophys. Acta* **1973**, *335*, 85-92.

(38) Erfurth, S. C.; Kiser, E. J.; Peticolas, W. L. *Proc. Natl. Acad. Sci.* **1972**, *69*, 938-941.

(39) Erfurth, S. C.; Bond, P. J.; Peticolas, W. L. *Biopolymers* **1975**, *14*, 1245-1257.

(40) Benevides, J. M.; Thomas Jr., G. J. *Nucl. Acids Res.* **1983**, *11*, 5747-5761.

(41) LaFleur, L.; Rice, J.; Thomas Jr., G. J. *Biopolymers* **1972**, *11*, 2423-2437.

(42) Thamann, T. J.; Lord, R. C.; Wang, A. H. J.; Rich, A. *Nucl. Acids Res.* **1981**, *9*, 5443-5457.

(43) Lu, D. S.; Nonaka, Y.; Tsuboi, M.; Nakamoto, K. *J. Raman Spec.* **1990**, *21*, 321-326.

(44) Takeuchi, H.; Sasamori, J. *Biopolymers* **1995**, *35*, 359-367.

(45) Hud, N. V.; Milanovich, F. P.; Balhorn, R. *Biochemistry* **1994**, *33*, 7528-7535.

(46) Grygon, C. A.; Spiro, T. G. *Biochemistry* **1989**, *28*, 4397-4402.

(47) Hrouda, V.; Florian, J.; Hobza, P. *J. Phys. Chem.* **1993**, *97*, 1542-1557.

(48) Florian, J.; Leszczynski, J.; Johnson, B. G. *J. Mol. Struc.* **1995**, *349*, 421-426.

(49) Guerra, C.; Bickelhaupt, F.; Snijders, J.; Baerends, E. *J. Am. Chem. Soc.* **2000**, *122*, 4117-4128.

(50) Herne, T. M.; Tarlov, M. J. *J. Am. Chem. Soc.* **1997**, *119*, 8916-8920.

(51) Delley, B. *J. Phys. Chem.* **1990**, *92*, 508-517.

(52) Tsuboi, M. *Prog. Theor. Phys. Supp.* **1961**, *17*, 99-107.

(53) Falk, M.; Hartman, K. A.; Lord, R. C. *J. Am. Chem. Soc.* **1963**, *85*, 391-394.

(54) Taillandier, E.; Liquier, J. *Methods Enz.* **1992**, *211*, 307-335.

(55) Taillandier, E.; Liquier, J.; Ghomi, M. *J. Mol. Struct.* **1989**, *214*, 185-211.

(56) Liquier, J.; Coffinier, P.; Firon, M.; Taillandier, E. *J. Biomol. Struct. Dyn.* **1991**, *9*, 437-445.

Figures

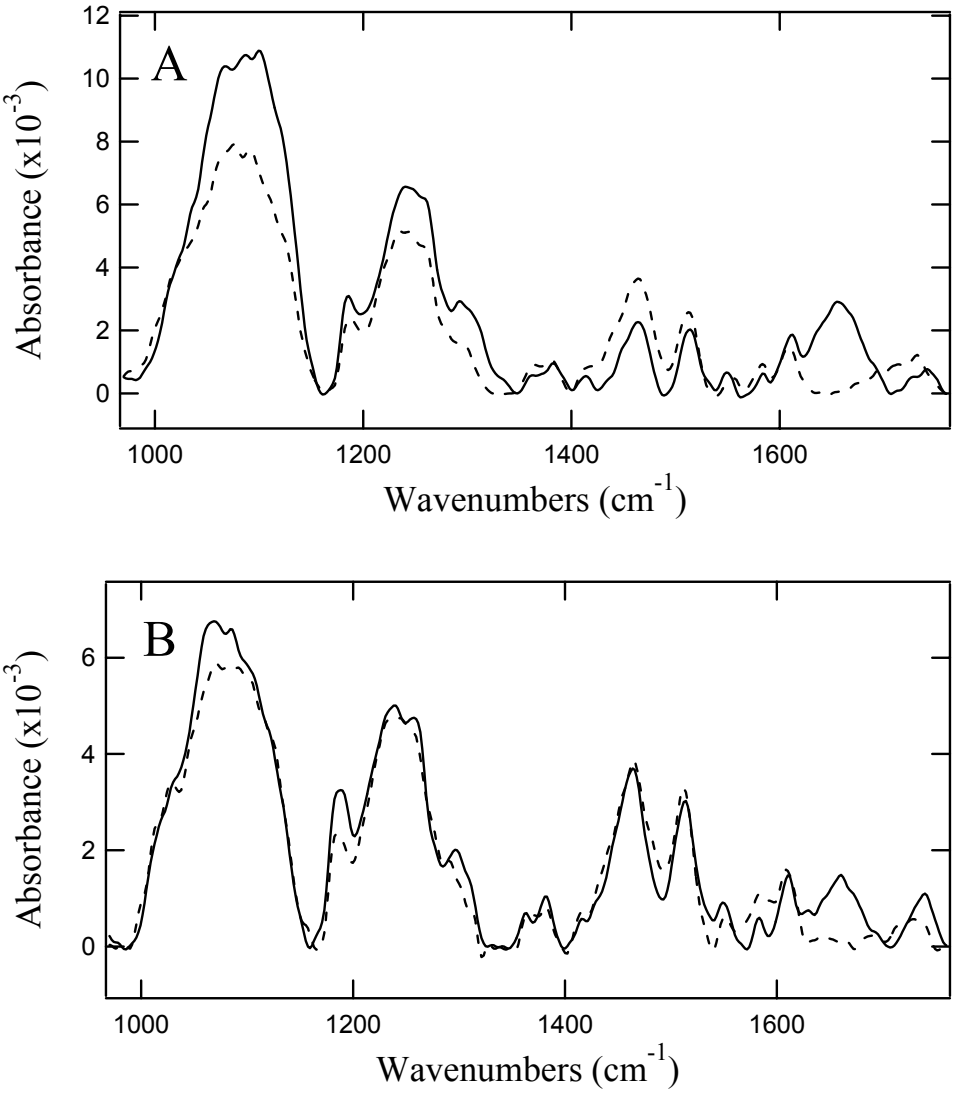

Figure 1. PM-IRRAS spectra of a mixed monolayer of 6-mercapto-1-hexanol and single stranded DNA before (dashed spectrum) and after hybridization (solid spectrum) with the complementary single stranded DNA strand to obtain double stranded DNA with a hybridization temperature of 65°C (A) or 85°C (B) recorded at an incident angle of 80 degrees.

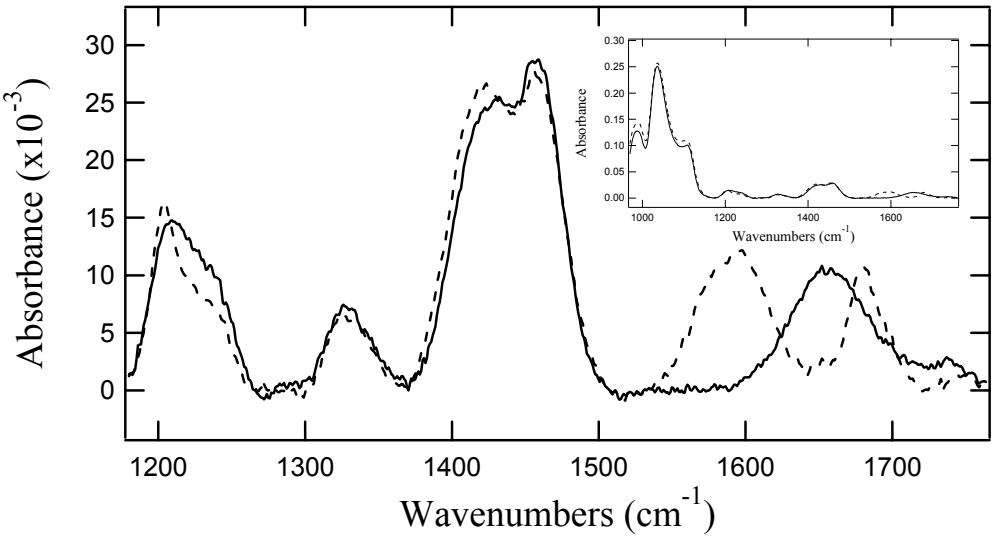

Figure 2. Solution single-pass ATR FTIR spectra of single stranded DNA (dashed spectrum) and double-stranded DNA (solid spectrum) corresponding to the same DNA strands used for the probe and target single stranded DNA on the gold surfaces. The concentration of the DNA solutions was approximately 200mM. The inset shows the larger spectral range from 970 - 1760 cm^{-1}.

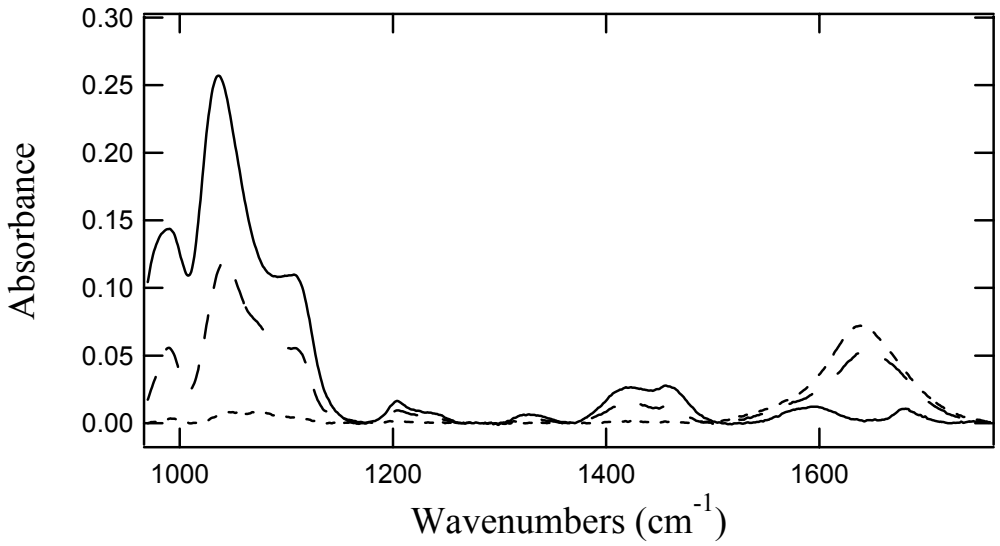

Figure 3. Solution single-pass ATR FTIR spectra of single stranded DNA recorded as a function of hydration and concentration in aqueous solution. The spectra correspond to least concentrated ~20 mM (- - -), more concentrated (-- -- --), and most concentrated ~200 mM (solid spectrum) of the single stranded DNA used as the probe strand on the gold surfaces. The most concentrated sample is nearly in a gel state.

Figure 4. Dmol3 calculated frequency spectra of A. adenine (-- --), thymine (-- · --), and the adenine-thymine base pair (solid spectrum), B. guanine (-- --), cytosine (-- · --), and the guanine-cytosine base pair (solid spectrum), C. probe ssDNA before (dashed spectrum) and after hybridization (dsDNA) (solid spectrum) using the weighted average of the calculated spectra of either the individual bases or base pairs, respectively. All spectra have a Gaussian width of 10 cm^{-1}.

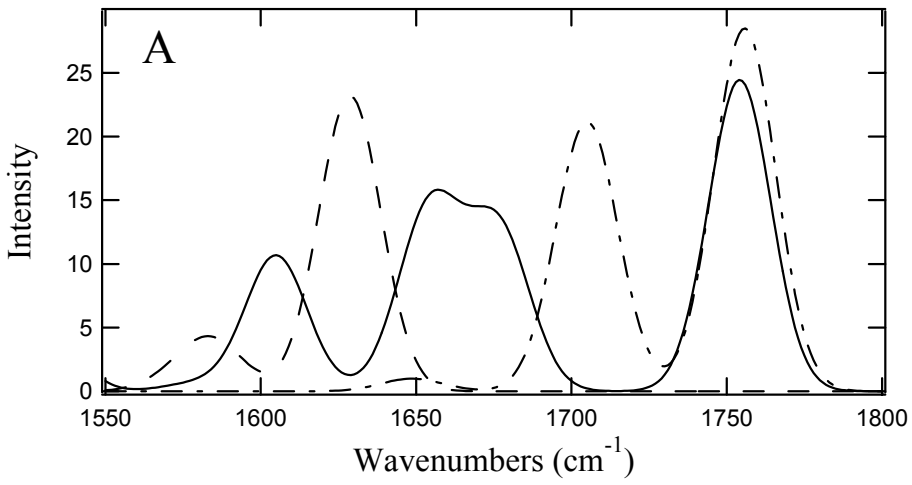
A
Intensity
0
5
10
15
20
25
1550
1600
1650
1700
1750
1800
Wavenumbers (cm-1)

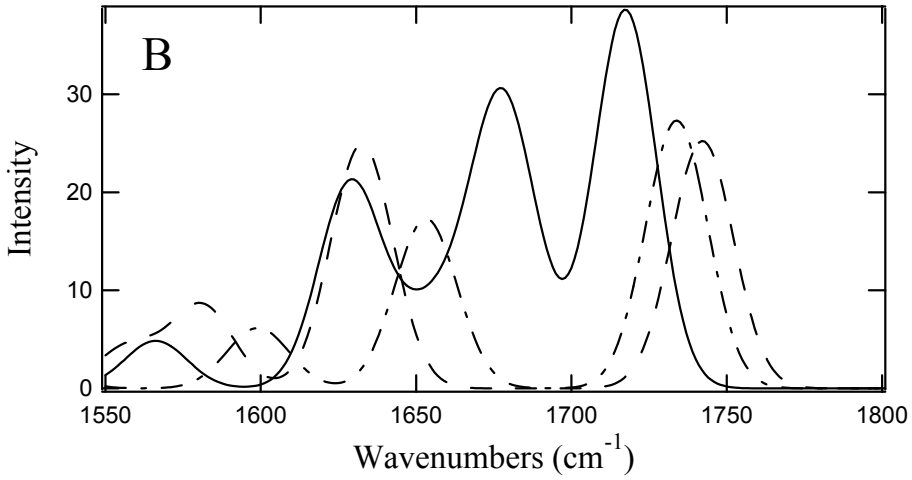
B
Intensity
0
10
20
30
1550
1600
1650
1700
1750
1800
Wavenumbers (cm-1)

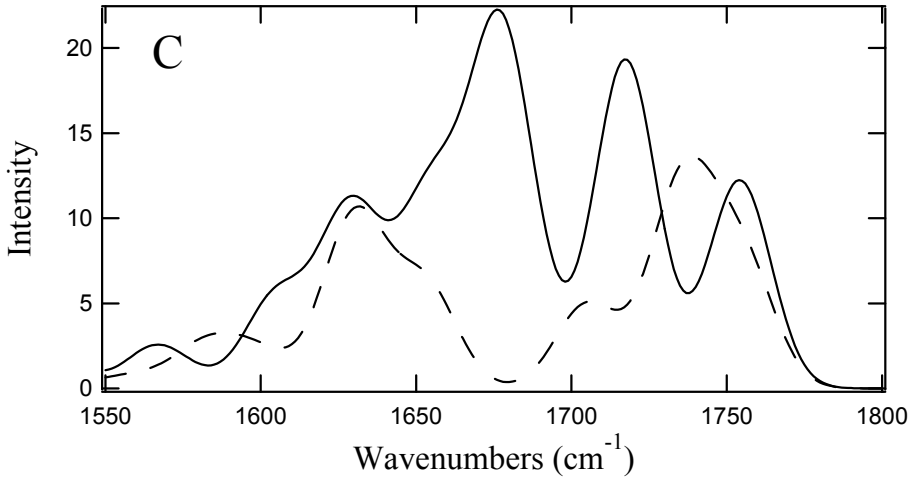
C
Intensity
0
5
10
15
20
1550
1600
1650
1700
1750
1800
Wavenumbers (cm-1)

Chapter 3

Infrared Detection of a Phenylboronic Acid Terminated Alkane Thiol Monolayer on a Gold Surface

Abstract

Polarization modulation infrared reflectance absorption spectroscopy (PM-IRRAS) and infrared reflectance absorption spectroscopy (IRRAS) have been used to characterize the formation of a self-assembled monolayer of N-(3-dihydroxyborylphenyl)-11-mercaptoundecanamide) (abbreviated PBA) on a gold surface and the subsequent binding of various sugars to the PBA adlayer through the phenylboronic acid moiety to form a phenylboronate ester. Vibrationally resonant sum frequency generation (VR-SFG) spectroscopy confirmed the ordering of the substituted phenyl groups of the PBA adlayer on the gold surface. Solution FTIR spectra and density functional theory was used to confirm the identity of the observed vibrational modes on the gold surface of PBA with and without bound sugar. The detection of the binding of glucose on the gold surface was confirmed in part by the presence of a C-O stretching mode of glucose and the O-H stretching mode of glucose that is shifted in position relative to the O-H stretching mode of boronic acid. An infrared (IR) marker mode was also observed at 1734 cm^{-1} upon the binding of glucose. Additionally, changes in the peak profile of the B-O stretching band were observed upon binding confirming formation of a phenylboronate ester on the gold surface. The binding of mannose and lactose were also detected primarily through the IR marker mode at ~1736 cm^{-1} to 1742 cm^{-1} depending on the identity of the bound sugar.

Introduction

Surface-based assays have become highly prevalent in the development of high-throughput, sensitive biosensors.[1-3] This type of technology typically involves the attachment

of a probe molecule to a surface that subsequently binds the target molecule from solution. For instance, the probe molecule can be a strand of ssDNA while the target is the complementary ssDNA. [4-6] A variety of surfaces such as glass, [2,7] gold [3-5,8-12] and indium tin oxide [13-15] have been used to detect biologically relevant molecules such as DNA and peptides. These surface-based assays have utilized a number of techniques including electrochemistry, [13,16] fluorescence, [17-20] surface plasmon resonance (SPR), [3,8,10,21,22] and infrared spectroscopy.[6,11] However, fewer surface-based assays have been developed for the detection of carbohydrates or sugars. In solution, the well-known carbohydrate-phenylboronic acid interaction has been utilized for the detection of the presence of carbohydrates and sugars predominately by fluorescence. [23-28] However, fluorescence is not the preferred detection technique on a metallic surface because the metal surface quenches the fluorescence;[29] therefore, other techniques must be employed. Recently, a phenylboronic acid terminated alkane thiol monolayer on a gold surface was probed using SPR to detect the binding of various carbohydrates.[21,22] SPR is used to detect binding by measuring the optical effect of a change in the index of refraction of the surface adlayer. SPR does not provide specific information on the orientation or surface order of bonding. Therefore, in these recent studies, reflectance infrared (IR) spectroscopy was used to confirm the presence of the dithiobis(4-butyrylamino-m-phenylboronic acid) monolayer on the surface.[21,22] However, no attempt was made to directly detect binding of a carbohydrate to the surface by reflectance IR spectroscopy. [21,22] We have recently demonstrated the detection of surface binding of DNA and proteins using reflectance IR both with and without polarization-modulation. [6,30]

Therefore it is of interest to study the infrared spectroscopic signatures of surface bound sugars as a prelude to studies of binding of lectins on surfaces.

In this study, polarization modulation infrared reflectance absorption spectroscopy (PM-IRRAS) and infrared reflectance absorption spectroscopy (IRRAS) were used for the fundamental characterization of a N-(3-dihydroxyborylphenyl)-11-mercaptoundecanamide) self-assembled monolayer (abbreviated PBA-SAM) on gold and for the characterization and detection of phenylboronate ester formation with various sugars. Infrared reflection spectroscopy is a rapid, non-intrusive method that can be used for the detection of sugars in biologically relevant concentrations. The (PM)-IRRAS technique does not require a fluorescent marker and provides information on the interaction between the phenylboronic acid moiety and the sugars. The binding of glucose, mannose and lactose was detected and characterized in this study. The sugars studied here represent mono- and disaccharides consisting of six member rings. The detection of sugar binding is through several modes including an IR marker mode at 1737 cm^{-1} for sugars bound to the phenylboronic acid moiety of PBA as well as changes in the frequency of B-O stretching modes that occur upon boronate ester formation. In principle, this information can be used to determine both bond strength and orientation of molecules on the surface. Vibrationally resonant sum frequency generation (VR-SFG) spectroscopy confirmed the formation of a well-ordered PBA-SAM on the gold surface.

Density functional theory was utilized to verify and assign the observed vibrational modes of PBA-SAMs on the gold surfaces. The present study demonstrates the feasibility of

vibrational spectroscopic studies of sugar binding to surface groups that can have wide application in studies of cell and viral surfaces, binding by lectins and cell targeting agents.

Materials and Methods

Chemicals and Substrates. 3-Aminophenylboronic acid hemisulfate was purchased from Acros Organics.[36] Glucose, mannose, lactose (all sugars were D chirality) and other chemicals and reagents used in the synthesis of N-(3-dihydroxyborylphenyl)-11-mercaptoundecanamide) were purchased from Sigma-Aldrich.[36] Absolute ethyl alcohol (200 proof) (AAPER Alcohol)[36] was used for the preparation of the monolayer deposition and sugar solutions. Boric acid (^{11}B and ^{10}B isotopes) was received from Eagle Picher.[36] Evaporated gold substrates (on glass with a Ti adhesion layer) were purchased from Evaporated Metal Films, Inc.[36]

Synthesis of N-(3-dihydroxyborylphenyl)-11-mercaptoundecanamide). The synthesis of N-(3-dihydroxyborylphenyl)-11-mercaptoundecanamide) is shown in Scheme 1 and will be abbreviated PBA. 11-mercaptoundecanoic acid (5 g, 22.9 mmol) was added to a suspension of methanol (5 ml), sodium bicarbonate (5.77 g, 68.7 mmol) and molecular iodine (2.91 g, 11.4 mmol) to yield disulfide **1** which precipitated from solution and was used without further purification. This molecule (4 g, 9.2 mmol) was converted to the bis-acid disulfide **2** by refluxing for 30 min. in thionyl chloride (21.89 g, 184.0 mmol). The excess thionyl chloride was removed by distillation. Subsequently a substitution reaction was performed to give the bis-amide disulfide **3** where the brownish oil of **2** (4 g, 8.48 mmol) was added to a mixture containing 3-aminophenylboronic acid hemisulfate (3.16 g, 17 mmol) and

N,N-diisopropylethylamine (7 mL). Reduction of **3** (1 g, 1.6 mmol) with tributylphosphine (1.58 mL) yielded the final product **4**. The identity and purity of the final product was confirmed by: proton(^{1}H) nuclear magnetic resonance (NMR) [(199.967 MHz, CD_3OD) δ 1.33 (s, 12H), 1.67 (m, 4H), 2.36 (t, 2H, J=7.3 Hz), 2.66 (t, 2H, J = 7.2 Hz), 7.30 (m, 1H), 7.48 (m, 1H), 7.61 (m, 1H), 7.78 (m, 1H)], fourier-transform infrared spectroscopy (FTIR) and elemental analysis.

Monolayer Formation on Gold Surfaces. The gold substrates used to prepare the monolayers were first cleaned in a piranha solution (3:1 ratio of H_2SO_4 and H_2O_2) (CAUTION, piranha solution reacts violently with organic chemicals), rinsed with 18 MΩ·cm deionized water (BARNSTEAD E-PURE)[36] and dried with N_2 gas. The gold surfaces were then placed in a 100 mmol/L ethanolic solution of PBA overnight at room temperature. The surfaces were then rinsed with absolute ethanol and dried with N_2 gas. Some of the PBA-SAMs on gold were then exposed to a 3 mmol/L ethanolic solution of glucose, mannose or lactose for 30 min. at room temperature, rinsed with absolute ethanol and dried with N_2 gas.

Polarization Modulation Infrared Reflection Absorption Spectroscopy (PM-IRRAS). The PM-IRRAS spectra were recorded on a Digilab FTS 6000 spectrometer[36] equipped with a step scan interferometer, liquid nitrogen cooled narrow band MCT detector, globar source and a UDR-4 filter. The IR radiation was typically phase modulated at frequencies of 400 Hz or 800 Hz at an amplitude of 1.0 λ_{HeNe} or 2.0 λ_{HeNe} while stepping at 0.5 Hz to 2.5 Hz. A gold grid polarizer was used to obtain either s- or p-polarized radiation, which was then modulated by a Hinds ZnSe photoelastic modulator (PEM) operating at 37

KHz and amplitude of 0.5 λ_{HeNe} (strain axis 45° to the polarizer) before reflecting off the sample at an incident angle of 80 degrees from the surface normal. The spectra were recorded at room temperature at a resolution of 4 cm^{-1} and were the results of 1 scan with a spectral range of 900 cm^{-1} – 4000 cm^{-1}. The digital signal processing (DSP) algorithm incorporated into the Digilab spectrometer software was used to obtain the spectra, which eliminates the need for a separate reference gold slide.

Infrared Reflection Absorption Spectroscopy (IRRAS). The reflectance FTIR spectra were recorded using a Spectra-Tech[36] grazing angle reflectance attachment in a Nicolet Magna-IR 860 FTIR[36] spectrometer. The angle of incidence used was 80° with respect to the surface normal. An infrared polarizer was used to obtain p-polarized light. The spectra of the monolayers deposited on the gold surfaces were obtained by taking a ratio of the single beam spectra of the deposited material on a gold surface to one of a freshly UV/ozoned bare gold surface. The rotational lines from gaseous water were subtracted from these spectra. The FTIR spectrometer was equipped with a liquid nitrogen cooled MCT/A detector and the spectra were recorded at a resolution of 2 cm^{-1} with a spectral range of 900 cm^{-1} to 4000 cm^{-1}. All IR spectra were the result of 256 scans and were recorded at room temperature. High quality spectra in the 900 cm^{-1} to 1800 cm^{-1} region of the monolayers on the gold surfaces were obtained by PM-IRRAS. However, due to the Bessel function nodes inherent in the PM-IRRAS spectra in the OH stretching region, IRRAS spectra were used in the 1800 cm^{-1} to 4000 cm^{-1} region.

Single-Pass Attenuated Total Reflection Fourier Transform Infrared (ATR-FTIR) Spectroscopy. The solution single-pass ATR FTIR spectra of phenylboronic acid,

glucose and glucose bound to PBA (3 mmol/L in ethanol) were taken using a PIKE Technologies[36] single-pass ATR attachment attached to a Digilab FTS 3000 spectrometer[36] equipped with a germanium crystal for single-pass attenuated total reflection (ATR). The spectrometer was equipped with a liquid nitrogen cooled MCT/A detector and the spectra were recorded at a resolution of 4 cm^{-1} with a spectral range of 650 cm^{-1} to 4000 cm^{-1}. The solutions were allowed to concentrate on the ATR element to increase the absorptive features of the molecule of interest. The absorption spectra were the result of 64 scans and were recorded at room temperature.

Vibrationally Resonant Sum Frequency Generation (VR-SFG) Spectroscopy. The experimental approach used in the broadband SFG measurements has been described in detail elsewhere.[31,32] Broadband (> 250 cm^{-1} FWHM) IR pulses, derived from a 50 fs, 1 kHz, amplified Ti-sapphire laser system, were temporally and spatially overlapped with narrow-bandwidth (4 cm^{-1}) 810 nm (VIS) pulses at the sample. The reflected sum-frequency light was collected, dispersed in a 0.33 m spectrograph, and detected with a scientific grade CCD array detector. This allowed the simultaneous acquisition of a > 250 cm^{-1} wide SFG spectrum. In this work, the energy, beam diameter, and angle of incidence with respect to the surface normal of the coincident IR and VIS pulses were typically: 3 μJ, 150 μm, 67° and 2 μJ, 250 μm, 45° respectively. Pairs of half-wave plates and polarizers in the optical pathway were used to control and detect the polarization of the IR, VIS, and SFG beams. All SFG spectra reported were taken with a ppp polarization combination, in which the IR, VIS, and detected SFG beams were polarized in the plane of incidence. The displayed spectra were normalized by the response of a freshly UV/ozoned bare Au film, which corrects for the

intensity envelope of the broad-bandwidth IR pulse. All spectra are presented with the x-axis as the IR wavenumber, to allow easy comparison with linear vibrational spectroscopies.

Density Functional Theory (DFT) Calculations. The geometry optimization and vibrational frequency calculations of the various models were done using density functional theory (DFT) as implemented in the quantum chemistry software program DMol3 (Accelrys, Inc.).[33,36] The calculations were performed at the North Carolina Supercomputer Center (NCSC) on the IBM RS/6000 SP.[36] These calculations were done in the gas phase using the DNP (double numerical plus polarization) basis set, the GGA (generalized gradient approximation) functional [34] and the method of finite differences for calculating the vibrational frequencies. The Accelrys, Inc. software Insight II[36] was used to build the models and to visualize the eigenvector projections of the normal modes of vibration of the models.

Results and Discussion

IR spectra and DFT calculations of a phenylboronic acid undecane thiol SAM

The IR spectra of PBA-SAM on a gold surface and PBA in solution are shown in Figures 1A – 1D respectively, while the density functional theory (DFT) calculated PBA IR spectrum is shown in Figures 1E and 1F for the low and high wavenumber regions. Figure 1 illustrates the formation of a PBA-SAM on a gold surface due to the presence of the characteristic vibrational modes of PBA that are verified in the solution IR spectrum of PBA. The identity of these observed vibrational modes were confirmed through the DFT calculations of the normal modes of vibration of PBA.

Figures 1A and 1B show the polarization modulation infrared reflectance absorption spectrum (PM-IRRAS) and the infrared reflectance absorption spectrum (IRRAS) of a PBA-SAM on a gold surface in the 950 cm^{-1} to 1800 cm^{-1} and 2750 cm^{-1} to 3400 cm^{-1} region, respectively. The PM-IRRAS and IRRAS spectra were recorded at an incident angle of 80°. These spectra show several key IR vibrational modes indicative of the presence of a PBA-SAM on the gold surface. A partial list of these vibrational modes along with mode assignments is given in Table 1. [37] A comparison of these surface FTIR spectra with the solution and density functional theory (DFT) calculations was done to confirm the origin and assignment of the observed vibrational modes. The vibrational modes in Figure 1A include a mode at 1663 cm^{-1} that is predominately due to carbonyl stretching and some N-H bending, while the mode at 1580 cm^{-1} is primarily a N-H bending mode. The mode at 1430 cm^{-1} is likely due to a mixture of several motions including C-C and B-O stretching while the band centered at 1342 cm^{-1} is likely due to vibrational modes involving B-O stretching motions. The mode at 1264 cm^{-1} is likely due to imperfections in the gold surface allowing the silicon oxide modes[35] of the glass substrate to be observed or that the skin depth of the gold is greater than the thickness of the gold film at these IR wavelengths. The mode at 1111 cm^{-1} is probably due to phenyl ring deformation modes. The predominant modes at 2856 cm^{-1} and 2927 cm^{-1} are due to the symmetric and asymmetric stretching motions of the methylene groups in the alkane chain of PBA. The broad mode centered at 3263 cm^{-1} ± 0.7 cm^{-1} (determined by Gaussian band fitting) is the result of O-H stretching motions of the $B(OH)_2$ moiety of PBA (with a possible component of N-H stretching). These modes and intensities are indicative of a PBA-SAM on the gold surface.

The single-pass attenuated total reflection Fourier transform infrared (ATR-FTIR) solution spectra of PBA (starting concentration of 3 mmol/L that was allowed to concentrate on the ATR element) are shown in Figures 1C and 1D for the low and high wavenumber regions, respectively. These spectra verify that the observed vibrational modes in Figures 1A and 1B of a PBA-SAM on a gold surface are due to the PBA. The characteristic modes include the C=O stretch and N-H bending modes at 1663 cm^{-1} and 1549 cm^{-1} respectively. A mode at 1427 cm^{-1} is also present which is likely due to a combination of several vibrational motions in the molecule, while the B-O stretching modes are observed in solution by the band centered at 1342 cm^{-1}. There is a weak mode observed at 1098 cm^{-1} in the spectrum obtained in solution that appears to correspond to a much more intense mode observed in the surface spectrum. The methylene symmetric and asymmetric stretching modes are present at 2853 cm^{-1} and 2926 cm^{-1}. The BO-H stretching mode is centered at 3304 cm^{-1} (with a possible component of N-H stretching). These modes in Figures 1C and 1D clearly show that the modes observed experimentally on the surface (Figures 1A and 1B) are due to the presence of PBA on the surface.

The identities of the vibrational modes found in Figures 1A – 1D were investigated by density functional theory (DFT) calculations of PBA in the gas phase. These calculations involved the optimization of the structure of PBA and the calculation of the IR spectrum of this molecule. The eigenvalues (IR frequencies) and eigenvectors (motion of the atoms giving rise to an IR mode) allow the identification and confirmation of the atomic motions resulting in the observed IR modes of this molecule. The resulting DFT calculated IR spectrum of PBA are displayed in Figures 1E and 1F in the low (950 cm^{-1} to 1800 cm^{-1}) and

high (2800 cm^{-1} to 3800 cm^{-1}) wavenumber regions with a 10 cm^{-1} Gaussian width, while the eigenvectors for several prominent modes are shown in the Supporting Information (Appendix 2). The DFT calculated infrared spectrum closely resembles the spectrum obtained on the gold surface (Figures 1A and 1B) and in solution (Figures 1C and 1D), further verifying that these observed modes arise from vibrational modes of PBA. The DFT model shows that the mode at 1664 cm^{-1} is predominately a C=O stretching mode with some N-H bending character. These DFT model calculations do not predict any modes greater than 1664 cm^{-1}, which suggests that the low intensity mode at 1717 cm^{-1} for PBA as observed in solution is not a normal mode of vibration but a combination mode. The mode at 1534 cm^{-1} is a N-H bending mode while the mode at 1412 cm^{-1} is the result of C-C stretching in the phenyl ring, B-O stretching and several other smaller components. The DFT model calculates two intense modes at 1362 cm^{-1} and 1344 cm^{-1} that are primarily due to B-O stretching motions. The DFT model does calculate a mode at 1121 cm^{-1} due to phenyl ring deformation but with a low intensity. The model does show an intense phenyl ring-breathing mode at 984 cm^{-1}, observed experimentally as relatively weak band in the solution and surface FTIR spectra. The modes at 3017 cm^{-1} and 3076 cm^{-1} are due to symmetric and antisymmetric CH_2 stretching motions of the methylene units of the alkane chain of PBA, respectively and two modes at 3158 cm^{-1} and 3211 cm^{-1} are due to C-H stretching of the phenyl ring. The DFT model also calculates modes at 3536 cm^{-1} and 3759 cm^{-1} due to N-H and O-H stretching motions, respectively. As observed in Figures 1E and 1F, the DFT calculated IR spectra overall agreed with experiment and aided in the assignment of the experimentally observed modes of PBA.

Isotopic shift in B-O stretching vibrations observed by IR spectroscopy

In order to verify the identity of the boron-oxygen stretching motions in PBA, the two isotopes (^{11}B and ^{10}B) of boric acid were investigated. Figure 2A shows the single-pass ATR-FTIR spectra of solid boric acid ^{11}B (natural abundance) and ^{10}B, while Figure 2B shows the DFT calculated IR spectra of these two isotopes of boric acid ($B(OH)_3$) in the gas phase with a 30 cm^{-1} Gaussian width. The inset in Figure 2B shows the eigenvector projections for the two calculated normal modes of vibration for natural abundance boric acid in the 1250 cm^{-1} to 1650 cm^{-1} region. These experimental and DFT calculated IR spectra of the two isotopes of boric acid illustrate the region where B-O stretching modes occur in agreement with the assignments for the B-O stretching modes for PBA above accounting for the change in environment between PBA and boric acid. Figure 2A shows a broad transition in the 1250 cm^{-1} to 1650 cm^{-1} region with three prominent modes at approximately 1437 cm^{-1}, 1412 cm^{-1} and 1376 cm^{-1} for ^{11}B. These three peaks shift to approximately 1488 cm^{-1}, 1417 cm^{-1} and 1381 for ^{10}B (peak positions determined from the maximum intensity for each component in the broad band in this region). This shift is the expected shift to higher wavenumbers ($\tilde{\upsilon}$) for the ^{10}B boric acid spectra relative to ^{11}B due to the decrease in reduced mass of ^{10}B according to Eqn. 1:

$$\tilde{\upsilon} = \frac{1}{(2\pi)c}\sqrt{\frac{k}{\mu}} \qquad (1)$$

where k is the force constant and μ is the reduced mass. Figure 2B shows that the DFT calculated IR spectra containing two intense modes in this region at 1471 cm^{-1} and 1391 cm^{-1} for ^{11}B and at 1513 cm^{-1} and 1430 cm^{-1} for ^{10}B boric acid. The peak positions and peak shifts

upon isotopic substitution are in general agreement with the experimental FTIR spectra taking into account that the DFT IR spectra were calculated in the gas phase and therefore do not account for the packing in the solid material. The eigenvectors in the inset of Figure 2B illustrates the motions in the boric acid giving rise to these two modes which are predominately B-O stretching modes.

Spectroscopic studies of boronate ester formation

Figures 3A - 3J show the surface, solution and DFT calculated IR spectra of PBA with and without glucose bound. These spectra illustrate the detection of the formation of the boronate acid by the binding of glucose to the boronic acid moiety of a PBA-SAM on a gold surface through the observed characteristic vibrational modes of this molecule. These vibrational modes were verified by the solution IR spectroscopy and the origins of the observed modes were confirmed through DFT calculations of the boronic acid and boronate ester species.

Figure 3A shows the PM-IRRAS spectra in the 950 cm^{-1} to 1800 cm^{-1} region of a monolayer of PBA on a gold surface exposed (solid) or not exposed (dashed) to a 3 mmol/L solution of glucose in ethanol for 30 minutes, while Figure 3B shows the IRRAS spectra of the same two samples in the 2750 cm^{-1} to 3400 cm^{-1} region. The corresponding difference spectra of bound minus unbound glucose to a PBA-SAM on gold are shown in Figures 3C and 3D for the low and high wavenumber regions, respectively. The identification of the modes for the PBA-SAM on a gold surface is described above. The spectra corresponding to glucose bound to a PBA-SAM through the phenylboronic moiety shows the modes characteristic of PBA while several new vibrational modes and peak shifts occur upon sugar

binding. For instance, the C-O stretching mode from the six member glucose ring is observed at 1107 cm^{-1} after the PBA monolayer was exposed to glucose suggestive of the presence of glucose. Also, shifts and changes in peak profile occur in the B-O stretching modes around 1342 cm^{-1} suggestive of glucose binding to the phenylboronic acid moiety of PBA. As before the mode at 1264 cm^{-1} is likely due to silicon oxide stretching motions in the glass substrate[35] due to imperfections (scratches) in the gold surface or could be due to the skin depth of the gold layer being larger than the thickness of the gold film on the glass slide at these IR wavelengths. Hence the intensity differences observed for the 1264 cm^{-1} mode are primarily due to the number of imperfections (scratches or variation of gold film thickness) of the gold surface. Another significant difference in the PM-IRRAS spectrum upon glucose binding to a PBA-SAM on gold is the presence of a mode at 1734 cm^{-1}. This mode is likely a combination mode whose intensity is significantly increased upon binding of glucose relative to the other vibrational modes of this molecule compared to a PBA-SAM on a gold surface. Figure 3B shows the presence of the symmetric and asymmetric methylene stretching modes at 2857 cm^{-1} and 2927 cm^{-1} respectively before and after glucose binding and a shift in the O-H stretching region. Upon glucose binding the O-H stretching mode of boronic acid shifts ~10 cm^{-1} higher to a peak centered at 3274 cm^{-1} ± 0.7 cm^{-1} (determined by Gaussian band fitting) indicative of the O-H stretching mode of glucose and the subsequent disappearance of the O-H stretching mode of the phenylboronic acid moiety of PBA prior to binding. The nature of the binding and conformation of the assignment of these modes is made below through DFT models and solution spectra of these species. Reflectance IR

spectra therefore allows for the detection of glucose binding to a PBA-SAM on a gold surface and for structural information of the binding to be obtained.

To confirm the vibrational modes of PBA and glucose bound PBA on the gold surface are due to vibrations in these two molecules, solution ATR-FTIR spectra were recorded for both species. The single-pass ATR-FTIR spectra of solutions of PBA (solid), glucose (short dashed) and an 1:1 molar ratio of PBA and glucose (long dashed) in the low and high wavenumber regions are shown in Figures 3E and 3F. The spectra were obtained by allowing these initially 3 mmol/L solutions to concentrate onto the ATR element before acquiring the spectra. The modes from PBA have already been assigned above. The most notable modes from glucose are the broad C-O stretching band centered at 1099 cm^{-1} with several modes with a C-O stretching component in the 950 cm^{-1} to 1180 cm^{-1} region and the O-H stretching mode centered at 3352 cm^{-1}. The spectra of glucose bound to PBA shows a shift in the O-H stretching mode from 3304 cm^{-1} of the boronic acid component of PBA to 3343 cm^{-1} of the O-H stretching mode of glucose bound to PBA. The B-O stretching modes around 1342 cm^{-1} are also shifted and have a different peak profile with glucose bound to PBA (phenylboronate ester) compared to PBA without glucose bound (phenylboronic acid). These two observations are suggestive of the formation of a phenylboronate ester. The C-O stretching band of glucose is also evident in the glucose bound to PBA solution FTIR spectra. Also of note is the mode at 1430 cm^{-1} which is partially due to B-O stretching, but also has a component of C-C stretching in it, making it difficult to interpret. Although there is an intensity difference in this mode upon glucose binding, this may be due to baseline correction as there appears to be no shift in the peak position. These differences between PBA and

glucose bound to PBA are consistent with those observed on the gold surface (Figure 3A – 3D).

Figures 3G and 3H show the DFT calculated infrared spectra of PBA (solid), glucose (short dashed) and glucose bound to PBA (long dashed) displayed with a Gaussian width of 10 cm^{-1}. These calculations confirm the assignments of the observed vibrational modes of glucose bound to PBA at a gold surface and in solution. Figures 3I and 3J are the difference infrared spectrum calculated by the subtraction of the sum of the individual calculated spectra of glucose and PBA from the calculated spectrum of glucose bound to PBA. The origin of these calculated vibrational modes are illustrated by the eigenvector projections of selected normal modes of vibration of glucose bound to PBA shown in the Supporting Information (Appendix 2). The model of glucose bound to PBA shows a 2 cm^{-1} shift to higher wavenumbers for the carbonyl stretching mode to 1666 cm^{-1}, whereas the N-H bending mode is shifted to lower wavenumbers by 3 cm^{-1} to 1531 cm^{-1} relative to free PBA. Figure 3G shows that the predominately B-O stretching modes in glucose bound to PBA are at 1341 cm^{-1} and 1339 cm^{-1} compared to 1362 cm^{-1} and 1344 cm^{-1} for free PBA. This shift is due to the binding of glucose through the $B(OH)_2$ moiety of the phenylboronic acid functional group of PBA. The C-O stretching mode of glucose in Figure 3G is calculated at 1131 cm^{-1} when glucose is bound to PBA. The calculated DFT frequencies also predict a glucose ring deformation mode at 1051 cm^{-1} when bound to PBA. Figure 3J shows that relatively small changes occur in the high wavenumber region of the calculated infrared spectrum of PBA with and without glucose bound compared to the low wavenumber region shown in Figure 3I. The differences calculated with these DFT models between PBA,

glucose and glucose bound to PBA give insight into the origin of the observed normal modes of vibration. The DFT model of glucose bound to PBA does not predict a normal mode of vibration near 1734 cm^{-1}. A band (intense) at this wavenumber is clearly observed in the PM-IRRAS spectrum of glucose bound to the PBA-SAM. The lack of a calculated vibrational mode at 1734 cm^{-1} indicates that this band is a combination band (the sum of two normal modes of vibration). The DFT model shows several possible normal modes of vibration that could sum to give this combination mode. The position and peak profile of this combination mode changes depending on the sugar bound (see below), therefore one of the normal modes giving rise to this combination mode probably involves the phenylboronic acid moiety of PBA. The DFT calculation for glucose bound to PBA does predict a mode at 1341 cm^{-1} (B-O stretching) and 390 cm^{-1} (involves motions in PBA and glucose) that sum to give a calculated combination mode at 1731 cm^{-1}, which is in agreement with experimental data. These two fundamental modes are among the most intense calculated modes for glucose bound to PBA that is required for a combination band to be observed experimentally.

Figure 4 shows the VR-SFG spectra recorded with ppp polarization in the 3010 cm^{-1} to 3125 cm^{-1} region of a PBA-SAM on a gold surface exposed (solid) or not exposed (dotted) to a 3 mmol/L solution of glucose in ethanol for 30 min. This region is shown so that the order of the substituted phenyl rings of the PBA-SAM could be investigated. The spectra are offset for clarity. These spectra demonstrate that the phenyl group of the PBA-SAM is ordered to the same extent both before and after exposure to a glucose solution by the presence of the aromatic C-H stretch mode presented in Figure 4. The peak positions in these spectra are identical within the 4 cm^{-1} resolution of the VR-SFG experiments.

However, since this is a non-linear spectroscopic technique, if the substituted phenyl groups were not well ordered in the PBA-SAM, little to no intensity in the VR-SFG spectra would be observed. The ordering of the PBA SAM was also investigated using DFT models of a PBA-SAM (see Supporting Information (Appendix 2)).

Figures 5A and 5B show the PM-IRRAS spectra of a PBA-SAM exposed (solid) or not exposed (dashed) to mannose and the disaccharide lactose in the 950 cm^{-1} to1800 cm^{-1} region, respectively. The corresponding difference spectra of the sugar bound to the PBA-SAM minus the PBA-SAM is shown in Figures 5C and 5D. These two spectra show that the detection of the binding of these two sugars can be made through the presence of the IR signature mode of sugar binding to a PBA-SAM on a gold surface centered at 1736 cm^{-1} and 1742 cm^{-1} for mannose and lactose, respectively. The shift in the peak position of this mode further suggests that this combination mode is comprised of a normal mode of vibration sensitive to the phenylboronic acid moiety such as the B-O stretching motion. However, the intensity of this mode for mannose is much smaller than for glucose or lactose. Both of the sugars show a shift and a change in peak profile in the B-O stretching band around 1342 cm^{-1} of the PBA that results from binding of the sugar. The sugars are binding by formation of a phenylboronate ester as expected. There are also differences in the 1100 cm^{-1} region when a PBA-SAM was exposed to each sugar probably due to modes arising from the sugar bound to PBA.

Conclusion

A self-assembled monolayer of PBA was formed on a planar gold surface and was characterized and confirmed with PM-IRRAS, IRRAS and VR-SFG spectroscopic techniques. The observed vibrational modes showed characteristics of PBA including the B-O stretching mode, amide modes (C=O stretching and N-H bending), C-H stretching modes, and O-H stretching modes. The identities of the observed modes of PBA on a gold surface were confirmed through solution single-pass ATR-FTIR spectra and density functional theory calculations. The subsequent binding of various sugars (glucose, mannose and lactose) was detected and characterized by reflectance IR spectroscopy through several vibrational modes including the presence of an IR marker mode between 1734 cm^{-1} and 1742 cm^{-1} (depending on the identity of the sugar) upon phenylboronate ester formation of the PBA-SAM on a gold surface. A shift in the 1342 cm^{-1} boron-oxygen stretching mode was observed for phenylboronate ester formation for each sugar studied. The presence of the different sugars bound to the PBA-SAM on a gold surface was also seen in C-O stretching mode around 1100 cm^{-1} which varied in intensity and peak profile depending on the sugar bound. For instance, both glucose and mannose exhibited a broad C-O stretching mode while lactose showed several more defined vibrational modes in this region.

Acknowledgements

This work was done in collaboration with Angela M. Allen (NCSU), Simon E. Lappi (NCSU), Tyson L. Chasse (NCSU), Kimberly A. Briggman (NIST), Christopher B. Gorman (NCSU) and Stefan Franzen (NCSU) and was the subject of a publication, Brewer, S. H.;

Allen, A. M.; Lappi, S. E.; Chasse, T. L.; Briggman, K. A.; Gorman, C. B.; Franzen, S. *Langmuir* **2004**, 20(13), 5512-5520. Support and computational facilities were provided by the North Carolina Supercomputing Center. Scott Brewer was supported by NIH Biotechnology Training Grant T32-GM08776. The authors from North Carolina State University would like to thank Digilabs for the use of the PM-IRRAS attachment.

References

(1) Pease, A. C.; Solas, D.; Sullivan, E. J.; Cronin, M. T.; Holmes, C. P.; Fodor, S. P. A. *Proceedings of the National Academy of Sciences of the United States of America* **1994**, *91*, 5022-5026.

(2) Taton, T. A.; Mirkin, C. A.; Letsinger, R. L. *Science* **2000**, *289*, 1757-1760.

(3) Thiel, A. J.; Frutos, A. G.; Jordan, C. E.; Corn, R. M.; Smith, L. M. *Analytical Chemistry* **1997**, *69*, 4948-4956.

(4) Herne, T. M.; Tarlov, M. J. *Journal of the American Chemical Society* **1997**, *119*, 8916-8920.

(5) Steel, A. B.; Herne, T. M.; Tarlov, M. J. *Bioconjugate Chemistry* **1999**, *10*, 419-423.

(6) Brewer, S. H.; Anthireya, S. J.; Lappi, S. E.; Drapcho, D. L.; Franzen, S. *Langmuir* **2002**, *18*, 4460-4464.

(7) Bai, X. P.; Li, Z. M.; Jockusch, S.; Turro, N. J.; Ju, J. Y. *Proceedings of the National Academy of Sciences of the United States of America* **2003**, *100*, 409-413.

(8) Nelson, B. P.; Grimsrud, T. E.; Liles, M. R.; Goodman, R. M.; Corn, R. M. *Analytical Chemistry* **2001**, *73*, 1-7.

(9) Lee, H. J.; Goodrich, T. T.; Corn, R. M. *Analytical Chemistry* **2001**, *73*, 5525-5531.

(10) Smith, E. A.; Erickson, M. G.; Ulijasz, A. T.; Weisblum, B.; Corn, R. M. *Langmuir* **2003**, *19*, 1486-1492.

(11) Frey, B. L.; Corn, R. M. *Analytical Chemistry* **1996**, *68*, 3187-3193.

(12) Sauthier, M.; Carroll, R.; Gorman, C.; Franzen, S. *Langmuir* **2002**, *18*, 1825-1830.

(13) Armistead, P.; Thorp, H. *Analytical Chemistry* **2000**, *72*, 3764-3770.

(14) Armistead, P.; Thorp, H. *Analytical Chemistry* **2001**, *73*, 558-564.

(15) Popovich, N. D.; Yen, B. K.; Wong, S. S. *Langmuir* **2003**, *19*, 1324-1329.

(16) Steel, A. B.; Herne, T. M.; Tarlov, M. J. *Analytical Chemistry.* **1998**, *70*, 4670-4677.

(17) Fodor, S. P. A.; Read, J. L.; Pirrung, M. C.; Stryer, L.; Lu, A. T.; Solas, D. *Science* **1991**, *251*, 767-773.

(18) Lockhart, D. J.; Winzeler, E. A. *Nature* **2000**, *405*, 827-836.

(19) Bulyk, M. L.; Gentalen, E.; Lockhart, D. J.; Church, G. M. *Nature Biotechnology* **1999**, *17*, 573-577.

(20) Chee, M.; Yang, R.; Hubbell, E.; Berno, A.; Huang, X. C.; Stern, D.; Winkler, J.; Lockhart, D. J.; Morris, M. S.; Fodor, S. P. A. *Science* **1996**, *274*, 610-614.

(21) Lee, M.; Kim, T. I.; Kim, K. H.; Kim, J. H.; Choi, M. S.; Choi, H. J.; Koh, K. *Analytical Biochemistry* **2002**, *310*, 163-170.

(22) Lee, M.; Hur, Y.; Kim, T.; Kim, K.; Kim, J.; Choi, H.; Koh, K. *Microchemical Journal* **2002**, *72*, 315-321.

(23) Yoon, J.; Czarnik, A. W. *Journal of the American Chemical Society* **1992**, *114*, 5874-5875.

(24) Wang, W.; Gao, S. H.; Wang, B. H. *Organic Letters* **1999**, *1*, 1209-1212.

(25) Tong, A. J.; Yamauchi, A.; Hayashita, T.; Zhang, Z. Y.; Smith, B. D.; Teramae, N. *Analytical Chemistry* **2001**, *73*, 1530-1536.

(26) Cao, H. S.; Diaz, D. I.; DiCesare, N.; Lakowicz, J. R.; Heagy, M. D. *Organic Letters* **2002**, *4*, 1503-1505.

(27) Springsteen, G.; Wang, B. H. *Tetrahedron* **2002**, *58*, 5291-5300.

(28) DiCesare, N.; Pinto, M. R.; Schanze, K. S.; Lakowicz, J. R. *Langmuir* **2002**, *18*, 7785-7787.

(29) Demers, L. M.; Mirkin, C. A.; Mucic, R. C.; Reynolds, R. A.; Letsinger, R. L.; Elghanian, R.; Viswanadham, G. *Analytical Chemistry* **2000**, *72*, 5535-5541.

(30) *Unpublished results.*

(31) Richter, L. T.; Petralli-Mallow, T. P.; Stephenson, J. C. *Optics Letters* **1998**, *23*, 1594-1596.

(32) Yang, C. S. C.; Richter, L. J.; Stephenson, J. C.; Briggman, K. A. *Langmuir* **2002**, *18*, 7549-7556.

(33) Delley, B. *Journal of Chemical Physics* **1990**, *92*, 508-517.

(34) Perdew, J. P.; Chevary, J. A.; Vosko, S. H.; Jackson, K. A.; Pederson, M. R.; Singh, D. J.; Fiolhais, C. *Physical Review B* **1992**, *46*, 6671-6687.

(35) Brewer, S. H.; Franzen, S. *Journal of Alloys and Compounds* **2002**, *338*, 73-79.

(36) We identify certain commercial equipment, instruments, or materials in this article to adequately specify the experimental procedure. In no case does such identification imply recommendation or endorsement by the National Institute of Standards and Technology, nor

does it imply that the materials or equipment identified are necessarily the best available for the purpose.

(37) The values of the experimental vibrational wavenumbers reported here were chosen to represent the highest intensity of the peak. The spectra were not fit except where noted.

Scheme

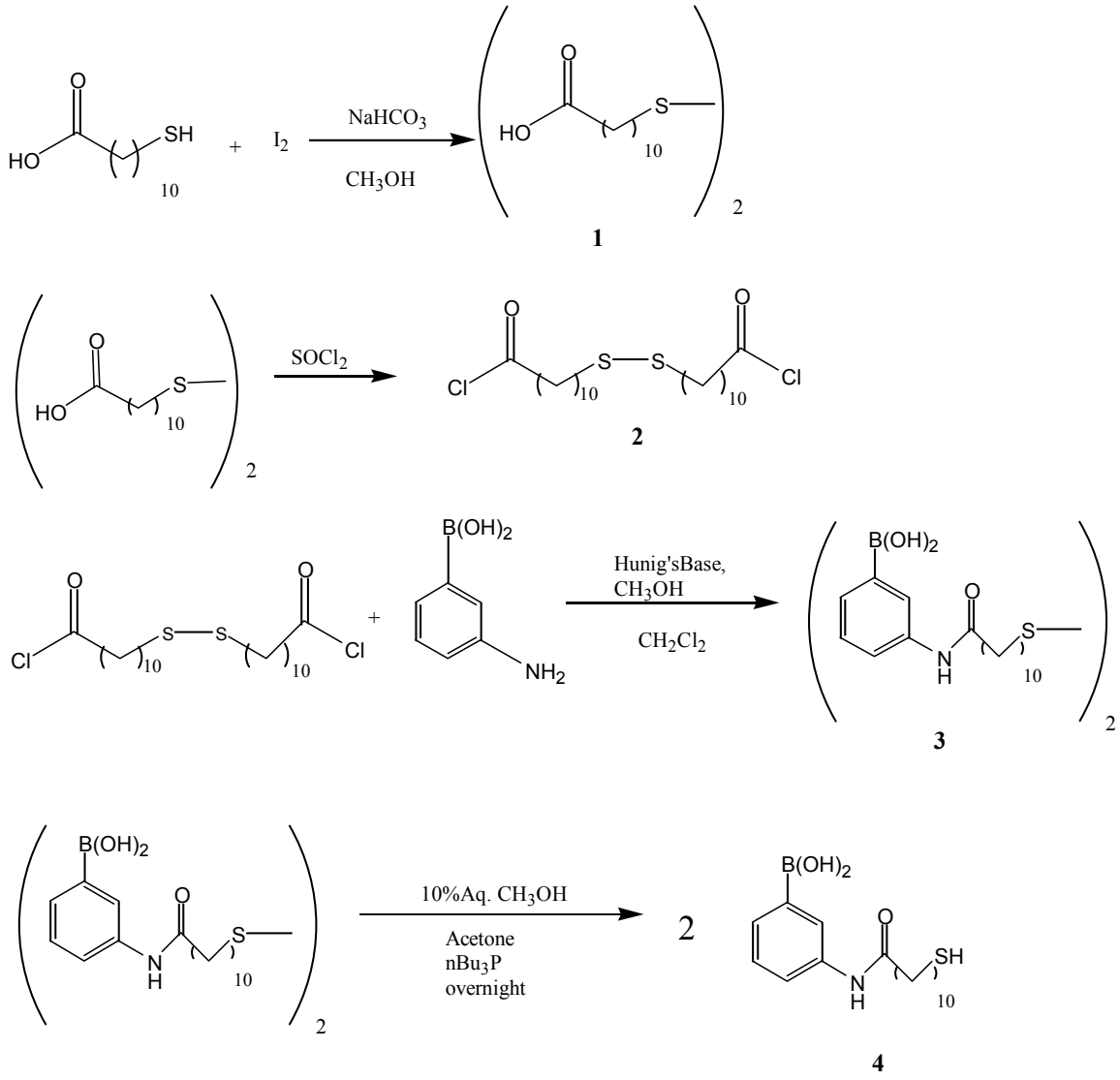

Scheme 1. Synthesis of N-(3-dihydroxyborylphenyl)-11-mercaptoundecanamide), PBA.

Table

Table 1. Partial list of vibrational modes and mode assignments corresponding to PBA on a gold surface ((PM)-IRRAS), in solution (single-pass ATR-FTIR) and calculated by DFT.

Vibrational Modes (cm^{-1})			
Experimental[37]		Calculated	
(PM)-IRRAS	Solution ATR-FTIR	DFT	Mode Assignment
1663	1663	1664	C=O stretch
1580	1549	1534	N-H bending
1430	1427	1412	C-C stretch (phenyl ring) B-O stretch
1342	1342	1362, 1344	B-O stretch
2856	2853	3017	symmetric CH_2 stretch
2927	2926	3076	asymmetric CH_2 stretch
3264	3304	3759	O-H stretch

Figures

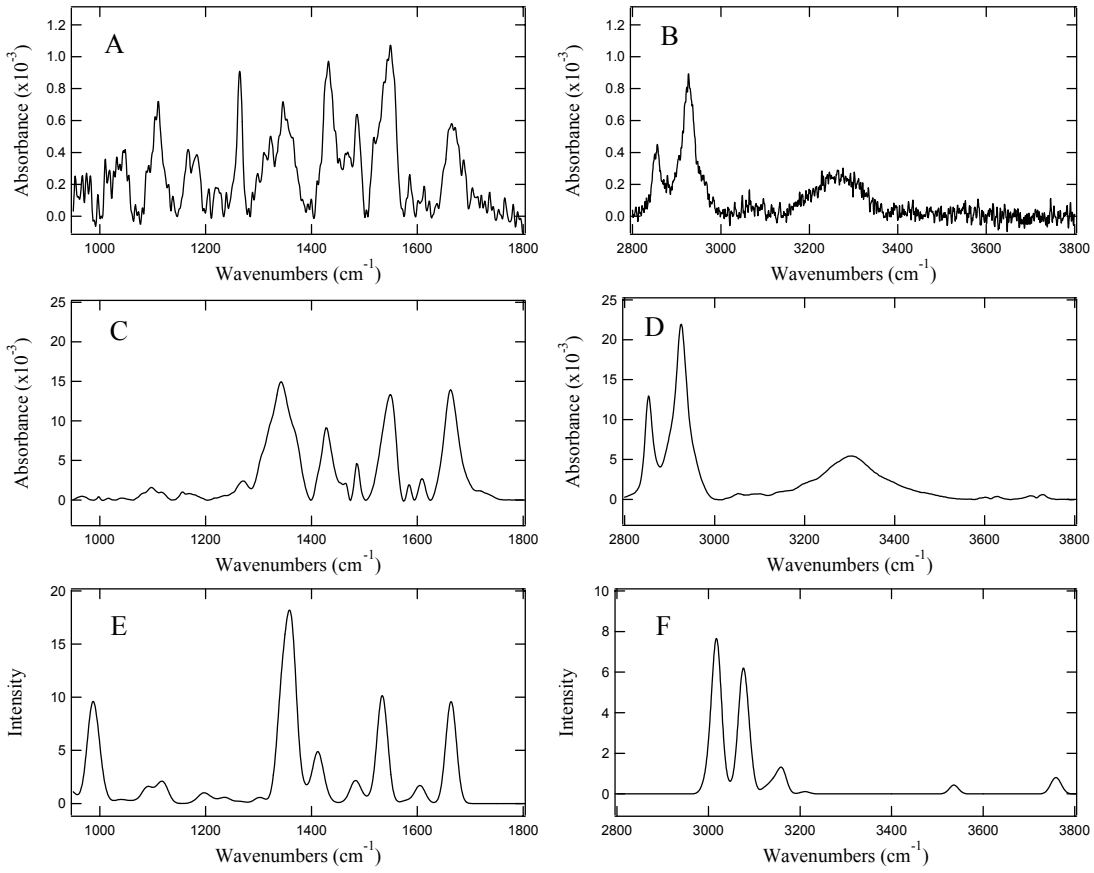

Figure 1. The PM-IRRAS (A) and IRRAS (B) spectra of a monolayer of PBA on a gold surface in the low and high wavenumber regions, respectively. The PM-IRRAS and IRRAS spectra were recorded at an incident angle of 80°. The IRRAS spectra were obtained with p-polarized IR radiation. Single-pass ATR-FTIR spectra of an initially 3 mmol/L PBA solution in ethanol allowed to concentrate on the ATR element are shown in the low (C) and high (D) wavenumber regions. DFT calculated low (E) and high (F) wavenumber regions of the infrared spectrum of PBA in the gas phase with a Gaussian width of 10 cm^{-1}.

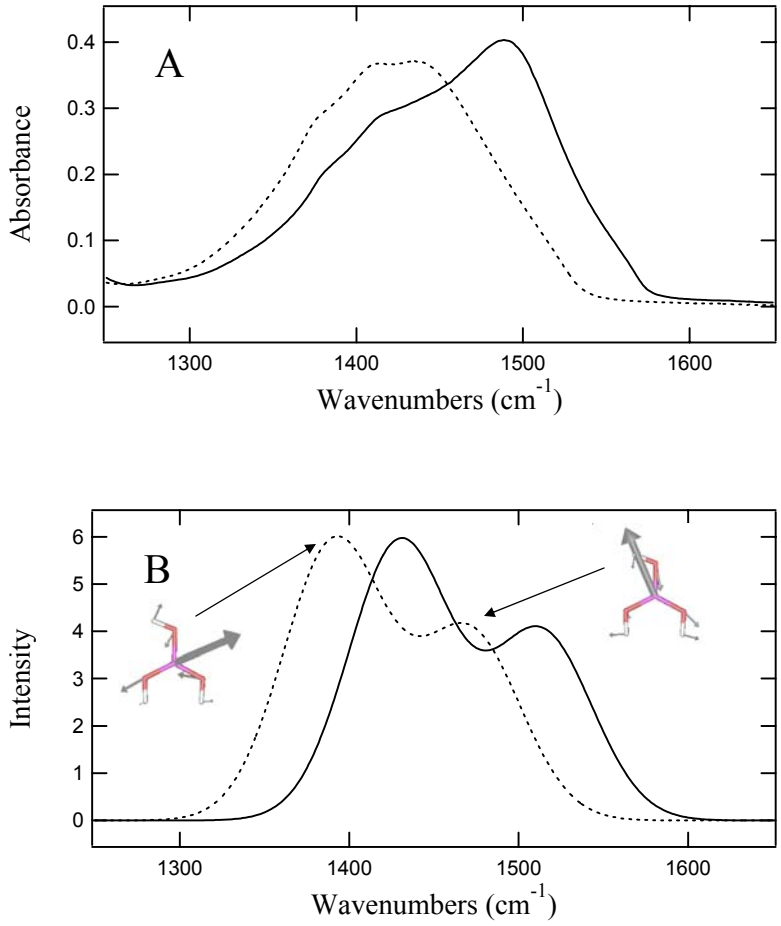

Figure 2. A. Single-pass ATR-FTIR spectra of ^{11}B (dashed) and ^{10}B (solid) boric acid solids. B. DFT calculated infrared spectra of ^{11}B (dashed) and ^{10}B (solid) boric acid in the gas phase with a Gaussian width of 30 cm^{-1}. (Inset: eigenvector projections of boric acid corresponding to the two modes of boric acid in the 1250 cm^{-1} to 1650 cm^{-1} region)

Figure 3. PM-IRRAS (A) and IRRAS (B) spectra of a monolayer of PBA exposed (solid spectrum) or unexposed (dashed spectrum) to a 3 mmol/L ethanolic solution of glucose for 30 minutes in the low (A) and high (B) wavenumber region on a gold slide recorded at an incident angle of 80 degrees. The corresponding difference spectra for the low (C) and high (D) wavenumber regions are shown for glucose bound to a PBA-SAM on gold minus a PBA-SAM on gold. (The difference of the Gaussian fits in the O-H stretching region is shown in D). Single-pass ATR-FTIR spectra solutions of PBA (solid), glucose (short dashed) and an 1:1 molar ratio of PBA and glucose (long dashed) are shown in the low (E) and high (F) wavenumber region. DFT calculated infrared spectra of PBA (solid), glucose (short dashed) and glucose bound to PBA (long dashed) with a Gaussian width of 10 cm^{-1} in the low (G) and high (H) wavenumber regions. DFT difference infrared spectra (I and J) calculated by the subtraction of the sum of the individual calculated IR spectra of glucose and PBA from the calculated IR spectra of glucose bound to PBA.

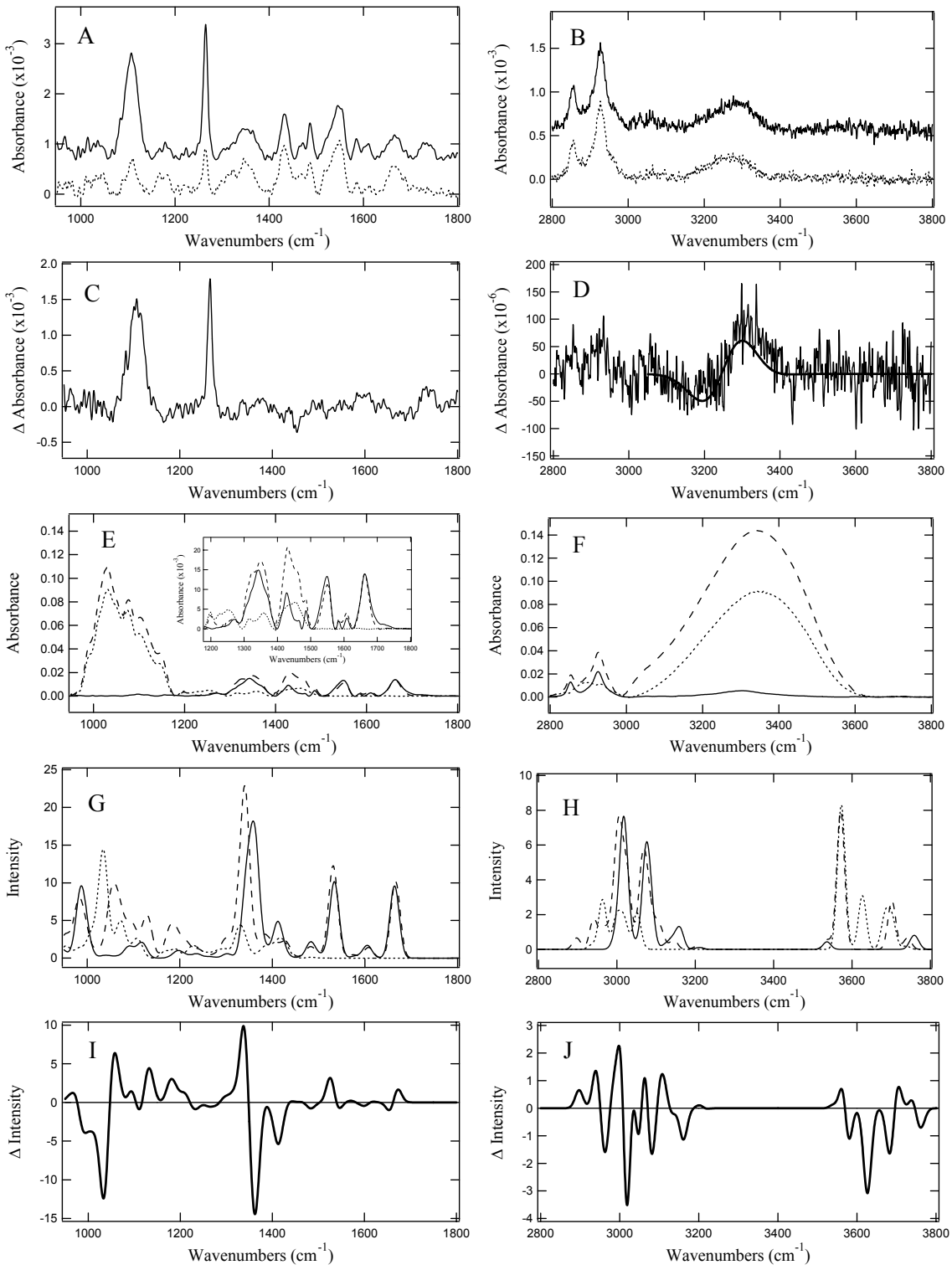
A
Absorbance (x10^{-3})
Wavenumbers (cm^{-1})
B
Absorbance (x10^{-3})
Wavenumbers (cm^{-1})
C
Δ Absorbance (x10^{-3})
Wavenumbers (cm^{-1})
D
Δ Absorbance (x10^{-6})
Wavenumbers (cm^{-1})
E
Absorbance
Absorbance (x10^{-3})
Wavenumbers (cm^{-1})
F
Absorbance
Wavenumbers (cm^{-1})
G
Intensity
Wavenumbers (cm^{-1})
H
Intensity
Wavenumbers (cm^{-1})
I
Δ Intensity
Wavenumbers (cm^{-1})
J
Δ Intensity
Wavenumbers (cm^{-1})

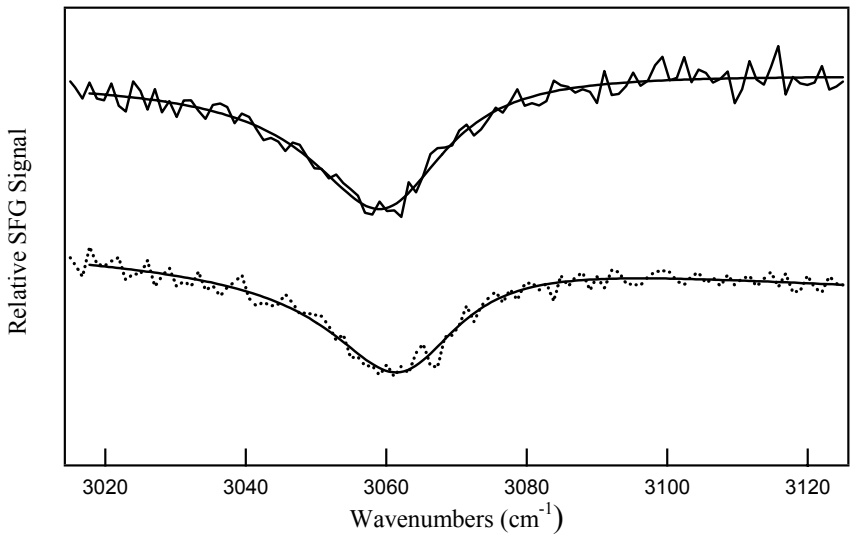

Figure 4. VR-SFG spectra of a PBA-SAM (dashed) on a gold surface exposed to a 3 mmol/L solution of glucose in ethanol for 30 min. (solid) recorded with ppp polarization.

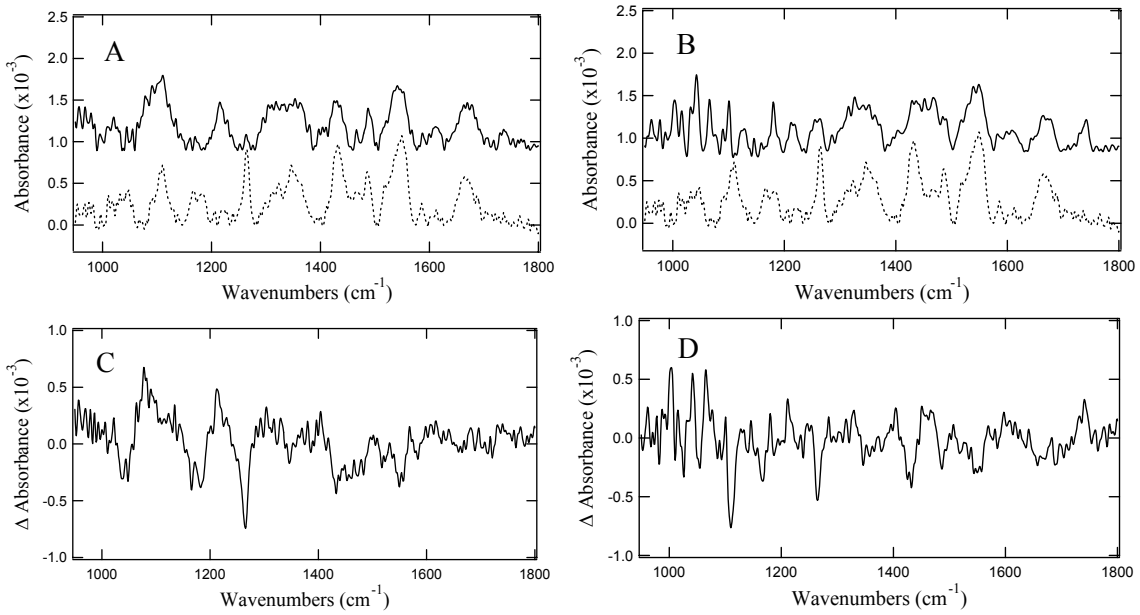

Figure 5. PM-IRRAS spectra of a monolayer of PBA exposed (solid) or not exposed (dashed) to a 3 mmol/L ethanolic solution of mannose (A) or lactose (B) for 30 min. in the 950 cm^{-1} to 1800 cm^{-1} region on a gold slide recorded at an incident angle of 80° and the corresponding difference spectra for mannose (C) or lactose (D) bound to a PBA-SAM on gold minus a PBA-SAM on gold.

Chapter 4

Optical properties of indium tin oxide and fluorine-doped tin oxide surfaces: correlation of reflectivity, skin depth, and plasmon frequency with conductivity

Abstract

Variable angle reflectance FTIR was used to investigate the reflectance of thin films of either indium tin oxide (ITO) or fluorine-doped tin oxide (SFO) on glass substrates in the mid-IR. The reflectance was observed to depend on the incident angle, wavenumber, and the polarization used. The Drude model and the Fresnel equations for reflection at a single dielectric boundary were used to interpret these results in terms of the conductivity, reflectivity, skin depth, and plasmon frequency of the metal oxides. The skin depth of thin film ITO electrodes was determined to depend on the sheet resistance linearly, while the reflectance varied according to the square root of the sheet resistance. The method shows that an optical probe can be used to determine the electrical properties of metal oxide films in a non-invasive approach.

Introduction

Indium tin oxide is widely used as an infrared reflector and as a transparent electrode material.[1-5] Because of its ready preparation as a thin film, typically with a thickness of 1500 – 2000 Å on a variety of substrates, indium tin oxide (ITO) thin films are often used as electrode materials even when its optical properties are not required. The infrared reflectivity of ITO leads to its use as a heat shielding material.[6,7] Also, its transparency in the visible spectral region leads to its use for Faraday shielding of optical displays.[8] In spite of its wide use, the preparation and characterization of ITO is still an area of active research and development. Small changes in the preparation conditions and the annealing protocol can have profound effects on the properties of an ITO film.[6,7,9-11] As a consequence, new

methods for correlating optical and electronic properties in ITO are of great interest, both from a practical point of view and for basic research into this mixed metal oxide material.

Fluorine-doped tin oxide has many of the same properties as ITO, but its conductivity is substantially lower (depending on preparation).[12-14] The comparison of ITO and fluorine-doped tin oxide (SFO) films in terms of their optical properties provides one avenue for examining the trends in optical properties as a function of the conductivity. While a traditional four-point probe measurement of the sheet resistance of the film provides a meaningful comparison of the properties of these films, the correlation of sheet resistance and optical properties, including the plasmon frequency, reflectivity, and skin depth of the conducting film provides a powerful way to examine the film in an non-intrusive fashion, and to examine the properties that are of interest in heat shielding and other applications. In this study we show that variable angle reflectance FTIR spectroscopy can be used to examine the optical properties of ITO and SFO thin films due to their high IR reflectivity. Although we do not present direct measurement of the plasmon frequency (due to limitations of our instrument) we can see the effects of the plasmon line shape, the change in reflectivity, and the change in skin depth that arises from the difference in sheet resistance of different films. In addition to comparison of ITO and SFO films, we also show that ITO films that have different preparations that alter sheet resistance also affect the optical properties in a systematic fashion.

Materials and Methods

ITO and SFO Electrodes. Indium tin oxide (ITO) electrodes were received from Delta Technologies, Limited. The ITO electrodes were composed of 90% indium oxide and 10% tin oxide, had a nominal thickness of 1,500 Å, and a sheet resistance of 6-12 Ω. The substrate for the ITO electrodes was polished float (soda-lime) glass. The fluorine-doped tin oxide (SFO) electrodes were obtained from PPG Industries, Inc. and had a sheet resistance of 49-51 Ω, while the gold electrodes were obtained from Evaporated Films, Inc. The ITO and SFO electrodes were cleaned via 20 minutes of UV/O_3 (UVO-cleaner (UVO-60), model number 42, Jelight Company, Inc) to yield a clean hydrophilic surface. The sheet resistances of these electrodes were measured with a 4-point probe consisting of a Signatone D27M probe station, a Keithley 224 programmable current source, and a Hewlett Packard 3456A digital voltmeter. The electrodes were stored in millipore 18 MΩ deionized (BARNSTEAD E-PURE) water until their use (approximately 1 hour). The clean electrodes were dried by N_2 gas.

Reflectance FTIR Spectroscopy. The variable angle reflectance FTIR spectra were recorded using a Spectra-Tech variable angle reflectance attachment (The Veemax) in a Nicolet 550 Magna-IR spectrometer. The angle of incidence ranged from 50-70 degrees. An infrared polarizer was used to obtain s- or p-polarized light. A ratio of the single beam spectra of bare ITO electrodes, SFO electrodes or glass to a single beam spectrum of a gold electrode was performed to obtain the reflectance spectra of either ITO, SFO or glass. The rotational lines from gaseous water were subtracted from these spectra. The FTIR

spectrometer was equipped with a liquid nitrogen cooled MCT/A detector and the FTIR spectra were recorded at a resolution of 4 cm^{-1} with a spectral range of 650-4000 cm^{-1}. All IR spectra were the result of the average of 256 scans and were recorded at room temperature.

X-ray Photoelectron Spectroscopy (XPS). XPS spectra were recorded on a Riber LAS 2000 Surface Analysis System equipped with a cylindrical mirror analyzer (CMA) and a MAC2 Analyzer with Mg Kα X-rays (model CX 700 (Riber source) (hν = 1253.6 eV). The resolution of the survey scans was 2.0 eV while the individual elemental scans were at a resolution of 1.0 eV. The survey scans were the result of the average of 3 scans and the individual elemental scans were the result of either 5 or 20 scans (all spectra were normalized to 5 scans). XPS spectra were smoothed using a 9 point (second order) Savitzky-Golay algorithm, baseline corrected, and the peaks were fitted using Gaussian/Lorenztian (90/10) line shapes.

Results

Figure 1A and 1B shows the variable angle reflectance FTIR spectra of an ITO electrode for angles of incidence from 50-70 degrees for p- and s-polarized light, respectively. The reflectance for both p- and s-polarized spectra decreases in the wavenumber range from 1500 to 4000 cm^{-1}. The decrease in reflectance is due to the onset of the plasmon absorption of ITO as discussed below. The reflectance for the p-polarized spectra increases while the reflectance for the s-polarized spectra decreases with decreasing angle of incidence. The longitudinal optical (LO) glass (Si-O-Si stretching) mode at 1248

cm^{-1} for 70 degrees of incidence decreases to 1236 and 1229 cm^{-1} for 60 and 50 degrees, respectively. This type of behavior can be compared with the data obtained from the glass substrate itself (see below). The s-polarized ITO reflectance spectra do not exhibit a LO mode, but do show evidence for a dispersion feature due to the transverse optical (TO) Si-O-Si stretching mode at 1064 cm^{-1}. The presence of these vibrational modes from the substrate indicates that the skin depth of the ITO conducting film is greater than the film thickness of approximately 1700 Å. The skin depth (δ) is related to the decay of the magnitude of the electric vector (E) in ITO by:

$$E = E_o \exp (- t / \delta) \qquad (1)$$

where t is the thickness of ITO and E_o is original magnitude of the electric vector. [15] The skin depth (δ) can also be related to the conductivity as described below in Equation 11.

The reflectivities for p- and s-polarized spectra of SFO surfaces are significantly lower than for ITO. Moreover, the skin depth for SFO is significantly larger than for ITO. Figure 2A and 2B shows the variable angle reflectance FTIR spectra for angles of incidence from 50-70 degrees for a SFO electrode for p- and s-polarized light, respectively. As observed for ITO, the reflectance of the p- and s-spectra both decrease from 2500 to 4000 cm^{-1} (except for the 70 degree p-polarized spectrum), and the lower reflectivity and curve shapes of SFO relative to ITO are indicative of a plasmon band that is significantly lower in wavenumber for SFO than ITO. The plasmon band wavenumber and conductivity both depend on charge carrier density, n. The lower wavenumber plasmon band in SFO is consistent with the lower charge carrier density in SFO than in ITO. Also, as observed for ITO, p- and s-polarized spectra show an increase and decrease in reflectance, respectively for

decreasing angle of incidence. As observed for ITO, the TO/LO mode of the glass substrate is observed in the p-polarized spectra. Consistent with the data in ITO and spectra of glass substrate, the LO mode decreases from a maximum wavenumber of 1236 cm^{-1} for 70 degrees to 1225 and 1213 cm^{-1} for 60 and 50 degrees, respectively. The dispersive feature associated with the TO mode at 1064 cm^{-1} is observed as well. This feature is also significantly larger in SFO than in ITO.

Figure 3A and 3B shows the variable angle reflectance FTIR spectra of the uncoated glass side of the back of an ITO electrode. Figure 3A contains spectra corresponding to angles of incidence of 40-70 degrees and p-polarized IR light. The s-polarized spectra for the same angles of incidence are present in Figure 3B. The observed features for an incident angle of 70 degrees are at 1230 and 1059 cm^{-1} for p-polarized and at 1059 cm^{-1} for s-polarized spectra and several features in the higher frequency part of the spectra. Interestingly, in these spectra both the LO mode at 1230 cm^{-1} and TO mode at 1059 cm^{-1} are principally absorptive rather than dispersive. In fact, for the s-polarized spectra it is the LO mode that appears dispersive as opposed to the spectra of the glass substrate for the ITO and SFO thin films shown in Figures 1 and 2.

Figure 4 shows the reflectance FTIR spectra of three ITO electrodes with various sheet resistances corresponding to an incident angle of 70 degrees and p-polarized IR radiation. This figure shows that the reflectivity of ITO for this set of experimental parameters decreases as the sheet resistance is increased. Also, the skin depth is affected as the resistances of the ITO substrates are varied. Figure 5 illustrates this result by showing the

absorbance of the glass substrates (LO mode at 1248 cm^{-1} of silicon dioxide) under the ITO thin film that is determined by the skin depth of ITO.

Figure 6A, 6B, and 6C show the XPS spectra of In $3d_{5/2,3/2}$, Sn $3d_{5/2,3/2}$, and O 1s peaks of bare ITO. The position of the In $3d_{5/2,3/2}$ (445.1, 452.7 eV) and Sn $3d_{5/2,3/2}$ (487.2, 495.7 eV) of bare ITO corresponds to the oxidation states, In^{3+} and Sn^{4+} in ITO, respectively.[16] The XPS spectra of O 1s is comprised of two components of the occurring at 530.7 and 531.7 eV that correspond to indium oxide and tin oxide species with a ratio of 1:7, respectively.[16]

Discussion

Glass Substrate Mode Analysis. The modes present in the lower frequency region of both of the electrode variable angle reflectance FTIR spectra are due to the glass substrate under the metal oxide layer. Previous work has used the Si-O-Si moiety of glass to interpret its IR spectrum. The region between 900-1300 cm^{-1} has been described as arising from the asymmetrical stretching motions of the bridging oxygen atoms,[17,18] specifically, the in phase and out of phase asymmetric motion of the oxygen atoms AS1 and AS2, respectively. These asymmetrical modes are comprised of longitudinal (LO) and transverse (TO) modes. The transverse optical modes can be observed in normal transmittance IR spectroscopy and in s- and p-polarized IR spectra at oblique angles of incidence. However, the LO modes can only be detected at oblique angles of incidence with p-polarized light.[19,20] The LO modes involve transition dipole moments perpendicular to the surface, while TO modes involve transition dipole moments parallel to the surface.[21] Therefore, the 1064 and 1248 cm^{-1}

modes in the variable angle reflectance FTIR spectra of the uncoated side of an ITO glass slide for p-polarized and 70 degrees of incidence arise from the TO and LO modes of AS1, respectively. As the incidence angle increases in the p-polarized spectra, the intensity of the LO modes increases while the TO mode is present throughout the incident angle range. In the s-polarized spectra, primarily only the TO mode is observed in all of incident angles shown. The reflectance of the glass in the region shown generally increases as the incident angle increases, except near the higher energy end of the frequency window. The other features of this spectrum at higher frequencies are probably due to the ITO coating on the reverse side of the glass slide since these features are absent for a microscope glass slide without an ITO coating on the reverse side (data not shown).

Fresnel Equations of Reflection at a Single Dielectric Interface. The magnitude of light reflected by these metal oxide electrodes relative to the magnitude of the incident light is calculated from the Fresnel equations for s- and p-polarizations of incident light. The ratios of the amplitudes of the reflected light and incident light for each polarization for a single dielectric interface are shown in equations 2 - 4:

$$r_s = \frac{\cos\theta - N\cos\varphi}{\cos\theta + N\cos\varphi} \qquad (2)$$

$$r_p = \frac{-N\cos\theta + \cos\varphi}{N\cos\theta + \cos\varphi} \qquad (3)$$

where

$$\cos \varphi = \left(1 - \frac{\sin^2\theta}{N^2}\right)^{\frac{1}{2}} \qquad (4)$$

In these equations, r is the amplitude of the reflected light (relative to incident light amplitude), s and p represent s- and p-polarizations respectively, N is the complex refractive index of the material, θ is the angle of incidence relative to the surface normal, and ϕ is the complex angle between the refracted light to the surface normal.[22] Also, the power reflectivity for each polarization of light are shown in equation 5 and 6:

$$R_s = \left| r_s \right|^2 \qquad (5)$$

$$R_p = \left| r_p \right|^2 \qquad (6)$$

where R_s and R_p are the power reflectivity for s- and p-polarization, respectively.[22]

In order to use the Fresnel equations in the thin film geometry considered here, the complex refractive index (N) of the material must be known which can be estimated from the Drude free-electron model. The Drude model defines the dielectric function (ε (ω)) as:

$$\varepsilon(\omega)^{\frac{1}{2}} = N(\omega) = n(\omega) + ik(\omega) \qquad (7)$$

where N is the complex refractive index, n is the real, in-phase, dispersive component and k is the imaginary, out-of-phase, absorptive component of the refractive index.[22] The dielectric function can also be written as:

$$\varepsilon(\omega) = \varepsilon_\infty - \omega_p^2 \frac{1}{\omega^2 + \frac{i\omega}{\tau}} \qquad (8)$$

where ε_∞ is the high-frequency dielectric constant, ω_p is the plasmon frequency, ω is the frequency, and τ is the electronic scattering time.[22] The plasmon frequency is defined by:

$$\omega_p^2 = \frac{ne^2}{m\varepsilon_o} \qquad (9)$$

where n is the free charge carrier concentration, e is the charge of an electron, ε_o is the dielectric constant in vacuum, and m is the free electron mass.[22] The electronic scattering time is calculated from the Hall mobility by:

$$\mu = \frac{e\tau}{m} \qquad (10)$$

where μ is the Hall mobility.[22]

Figure 7 shows the calculated power reflectivity of ITO using literature values for the Hall mobility (35 $cm^2V^{-1}s^{-1}$), free carrier concentration ($6x10^{20}cm^{-3}$), and the bare electron mass.[10] The figure shows that for s-polarized radiation in the mid-IR region that the power reflectivity decreases as the incident angle decreases while the reverse trend is seen for p-polarized radiation. Also, the power reflectivity for s-polarized radiation is greater for each incident angle shown than the corresponding incident angle for p-polarized radiation. These calculated results are in agreement with the observations made on ITO thin films above.

The measured sheet resistances of these ITO electrodes are directly related to the classical skin depth as defined in the Drude free electron model for metals. The skin depth (δ) is defined by:

$$\delta = \frac{c}{(2\,\pi\,\sigma\,\mu\,\omega)^{\frac{1}{2}}} \qquad (11)$$

where c is the speed of light and σ is the conductivity.[15] The conductivity (σ) is defined as:[15]

$$\sigma = \frac{n e^2 \tau}{m} \frac{1}{1 - i \omega \tau} \qquad (12)$$

Substituting into the previous equation, the skin depth becomes:

$$\delta = \frac{c}{\sigma} \left(\frac{n e}{2 \pi \omega} \right)^{\frac{1}{2}} \qquad (13)$$

provided $\omega\tau << 1$ and the skin depth δ includes only of the real part of the conductivity σ. The resistance, R and the dc resistivity, ρ_{dc} are related to one another by

$$\rho_{dc} = R t = \frac{1}{\varepsilon_o \omega_p^2 \tau} \qquad (14)$$

where t is the thickness.[12] Hence the plasmon band is related to the resistance by:

$$\omega_p = \left(\frac{1}{R t \varepsilon_o \tau} \right)^{\frac{1}{2}} \qquad (15)$$

This relation is shown in Figure 8 where the resistance is used to calculate the plasmon frequency (at a constant value for the electronic scattering time), which was used in the Drude model to calculate the optical properties needed for the Fresnel equations of reflection. Figure 8 shows the calculated reflectance using Equations 2 – 6 for each of the resistances at an incident angle of 70 degrees and p-polarized radiation. Figure 8 also shows that as the ITO resistance increases, the calculated reflectance in agreement with experimental observations. Also, Figure 9A and 9B shows that the experimentally observed reflectance and the calculated power reflectivity of ITO vary linearly with the square root of the resistance for p-polarized radiation and an incident angle of 70 degrees. Therefore, the sheet resistance and the skin depth are related by:

$$\delta = R\, t\, c\, (\frac{n\, e}{2\, \pi\, \omega})^{\frac{1}{2}} \qquad (16)$$

The experimental measurement in Figure 5 would suggest that the skin depth is directly proportional to resistance in the ITO samples with slightly different preparation. However, when ITO is compared to SFO, both n and τ differ so that SFO does not follow the linear correlation shown in Figure 5 and Equation 16. SFO has a higher sheet resistance (≈ 50 Ω) and corresponding greater skin depth and lower reflectivity as expected based on the above equations. Quantitative comparison of these equations for two different materials such as ITO and SFO would require independent measurement of the plasmon frequency. Such measurements are possible in a grazing angle configuration and the plasmon frequencies are expected to occur in the range 5,000 – 10,000 cm^{-1} for ITO based on both calculated values of n and τ and experimental data.[7] The plasmon frequency for SFO is expected to be lower than that for ITO.

Conclusion

The reflectance of ITO and SFO was observed to be a function of incident angle, wavenumber, and polarization for a given electrode and the reflectance of ITO was always higher than SFO in the mid-IR region. Additionally, the skin depth was shown theoretically and experimentally to vary linearly with the sheet resistance of ITO while the experimental reflectance and calculated power reflectivity of ITO varied linearly with the square root of the sheet resistance. Variable angle reflectance FTIR spectroscopy is an excellent probe of the conducting properties based on the correlation with the reflectance and skin depth of ITO thin films. Based on these results, we can hypothesize that a correlation with plasmon

frequency will also exist, although it requires measurement in the near infrared for confirmation. The method described here has general validity for thin films of metal oxides and mixed metal oxides when absorptive infrared bands are present in the substrate.

Acknowledgements

This work was done in collaboration with Stefan Franzen (NCSU) and was the subject of a publication, Brewer, S. H.; Franzen, S. *Journal of Alloys and Compounds* **2002**, 338, 73-79**.**

References

(1) Tamada, M.; Koshikawa, H.; Hosoi, F.; Suwa, T. *Thin Solid Films* **1998**, *315*, 40-43.

(2) Purvis, K.; Lu, G.; Schwartz, J.; Bernasek, S. *The Journal of the American Chemical Society* **2000**, *122*, 1808-1809.

(3) VanderKam, S.; Gawalt, E.; Schwartz, J.; Bocarsly, A. *Langmuir* **1999**, *15*, 6598-6600.

(4) Oh, S.; Han, S. *Langmuir* **2000**, *16*, 6777-6779.

(5) Armistead, P.; Thorp, H. *Analytical Chemistry* **2000**, *72*, 3764-3770.

(6) Hamberg, I.; Hjortsberg, A.; Granqvist, C. *Applied Physics Letters* **1982**, *40*, 362-364.

(7) Hjortsberg, A.; Hamberg, I.; Granqvist, C. *Thin Solid Films* **1982**, *90*, 323-326.

(8) Appleyard, S.; Day, S.; Pickford, R.; Willis, M. *Journal of Material Chemistry* **2000**, *10*, 169-173.

(9) Bregman, J.; Shapira, Y.; Aharoni, H. *Journal of Applied Physics* **1990**, *67*, 3750-3753.

(10) Fan, J.; Bachner, F.; Foley, G. *Applied Physics Letters* **1977**, *31*, 773-775.

(11) Shin, J.; Shin, S.; Park, J.; Kim, H. *Journal of Applied Physics* **2001**, *89*, 5199-5203.

(12) Stjerna, B.; Olsson, E.; Granqvist, C. *Journal of Applied Physics* **1994**, *76*, 3797-3817.

(13) Ray, S.; Karanjai, M.; Dasgupta, D. *Thin Solid Films* **1997**, *307*, 221-227.

(14) Mwamburi, M.; Wackelgard, E.; Roos, A. *Thin Solid Films* **2000**, *374*, 1-9.

(15) Wooten, F. *Optical Properties of Solids*; Academic Press, Inc.: San Diego, 1972.

(16) Yan, C.; Zharnikov, M.; Golzhauser, A.; Grunze, M. *Langmuir* **2000**, *16*, 6208-6215.

(17) Gunde, M. *Physica B* **2000**, *292*, 286-295.

(18) Wang, J.; Zou, B.; El-Sayed, M. *Journal of Molecular Structure* **1999**, *508*, 87-96.

(19) Berreman, D. *Physical review* **1963**, *130*, 2193-2198.

(20) Yamamoto, K.; Ishida, H. *Applied Spectroscopy* **1994**, *48*, 775-787.

(21) Parikh, A.; Allara, D. *Journal of Chemical Physics* **1992**, *96*, 927-944.

(22) Fowles, G. *Introduction to Modern Optics*; Second ed.; Dover Publications, Inc.: New York, 1989.

Figures

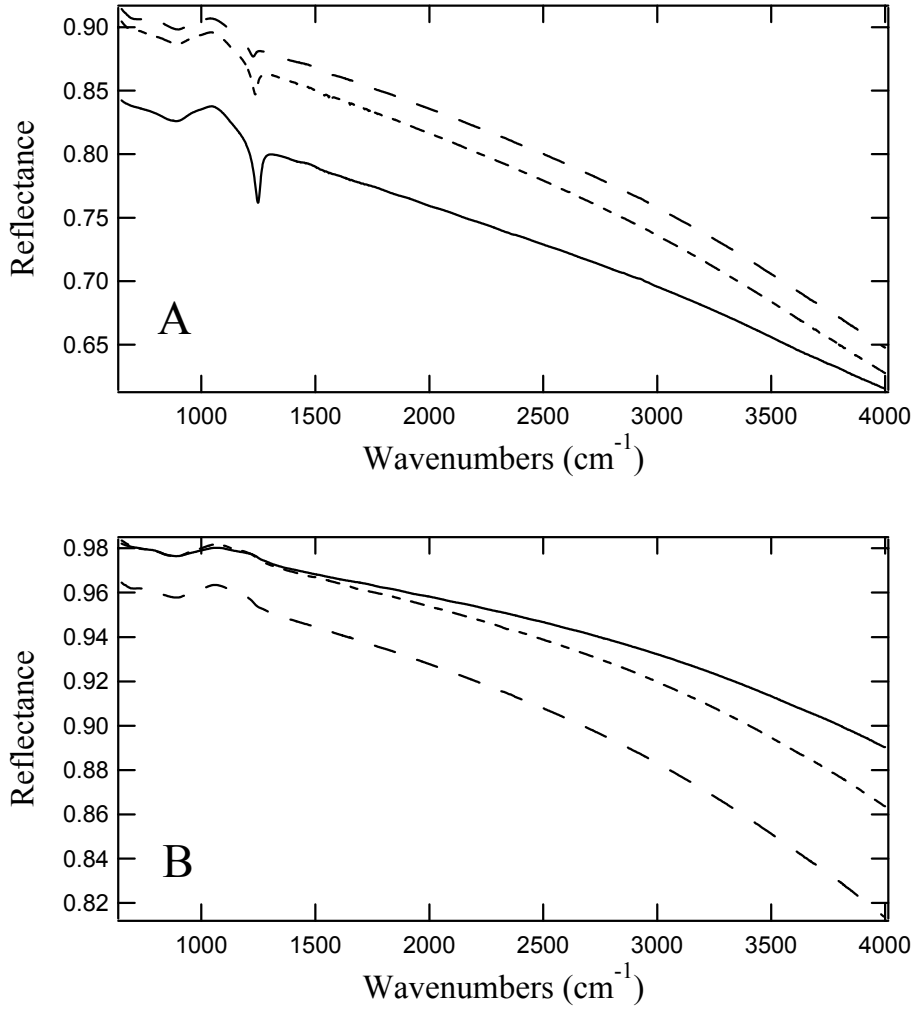

Figure 1. A. Variable angle reflectance FTIR spectra obtained from a ratio of ITO electrode to gold. Spectra shown are for angles of incidence of 50 (-- --), 60 (- -- -) and 70 (solid line) degrees for p-polarized IR light. B. Variable angle reflectance FTIR spectra obtained from a ratio of ITO electrode to gold. Spectra shown are for angles of incidence of 50 (-- --), 60 (- -- -) and 70 (solid line) degrees for s-polarized IR light.

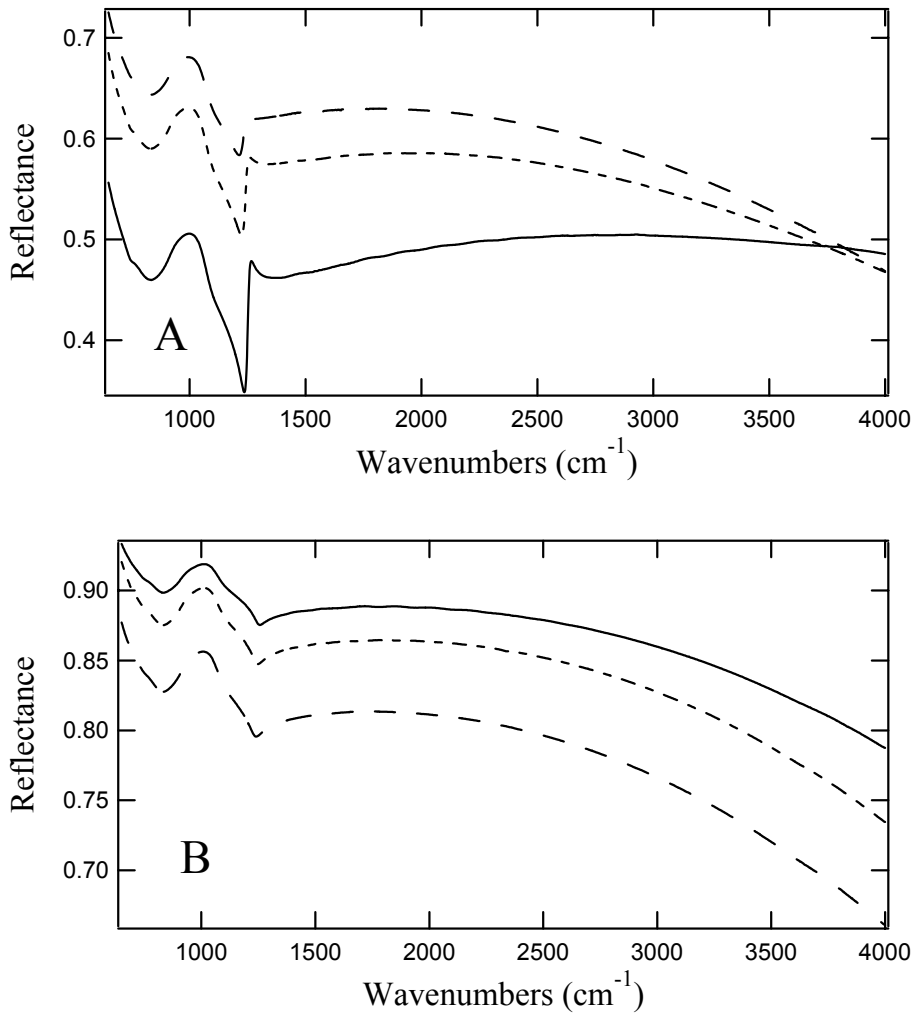

Figure 2. A. Variable angle reflectance FTIR spectra obtained from a ratio of SFO electrode to gold. Spectra shown are for angles of incidence of 50 (-- --), 60 (- -- -) and 70 (solid line) degrees with p-polarized IR light. B. Variable angle reflectance FTIR spectra obtained from a ratio of SFO electrode to gold. Spectra shown are for angles of incidence of 50 (-- --), 60 (- -- -) and 70 (solid line) degrees with s-polarized IR light.

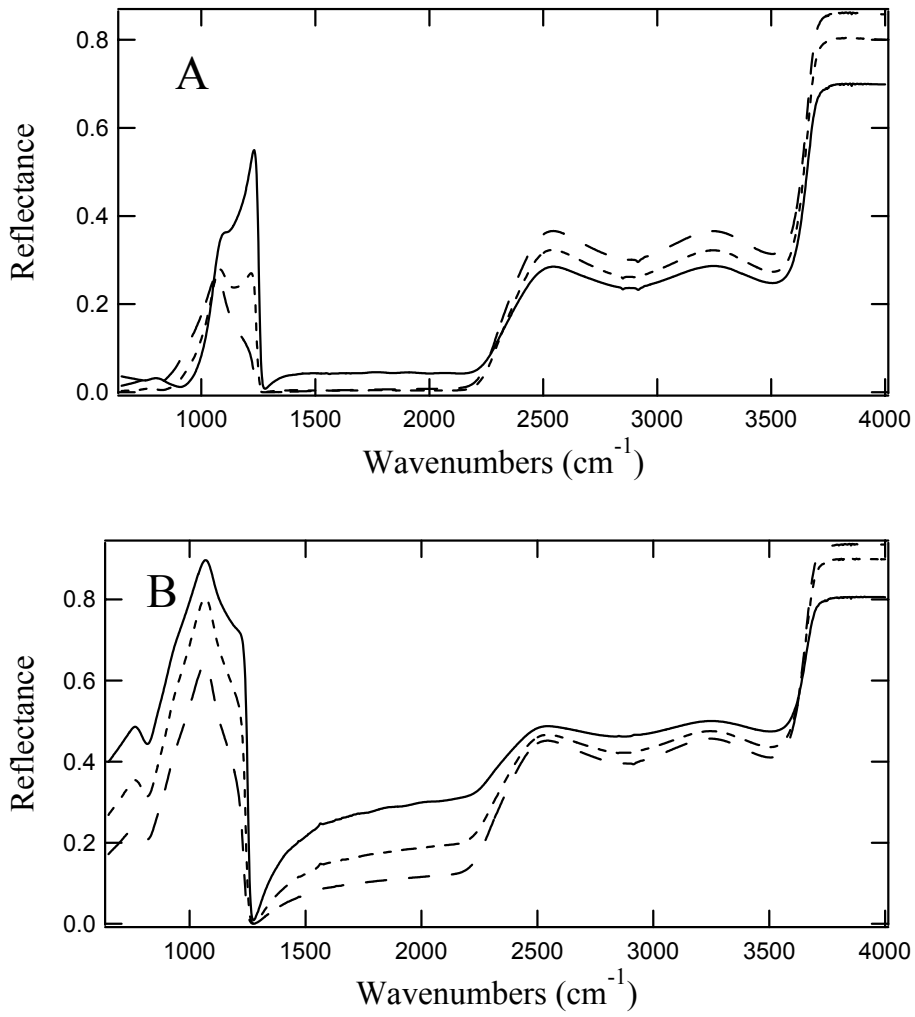

Figure 3. A. Variable angle reflectance FTIR spectra obtained from a ratio of glass slide (back of ITO electrode) to gold. Spectra shown are for angles of incidence of 50 (-- --), 60 (- -- -) and 70 (solid line) degrees with p-polarized IR light. B. Variable angle reflectance FTIR spectra obtained from a ratio of glass slide (back of ITO electrode) to gold. Spectra shown are for angles of incidence of 50 (-- --), 60 (- -- -) and 70 (solid line) degrees with s-polarized IR light.

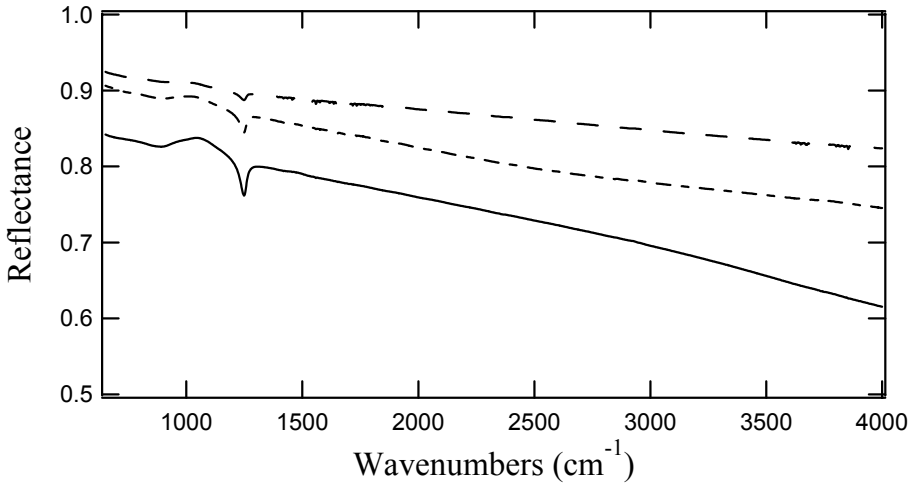

Figure 4. Reflectance FTIR spectra at an incident angle of 70 degrees and p-polarized radiation at three different ITO electrodes with varying resistances: 12 (solid), 9.0 (- -- -), and 6.8 (-- --) Ω.

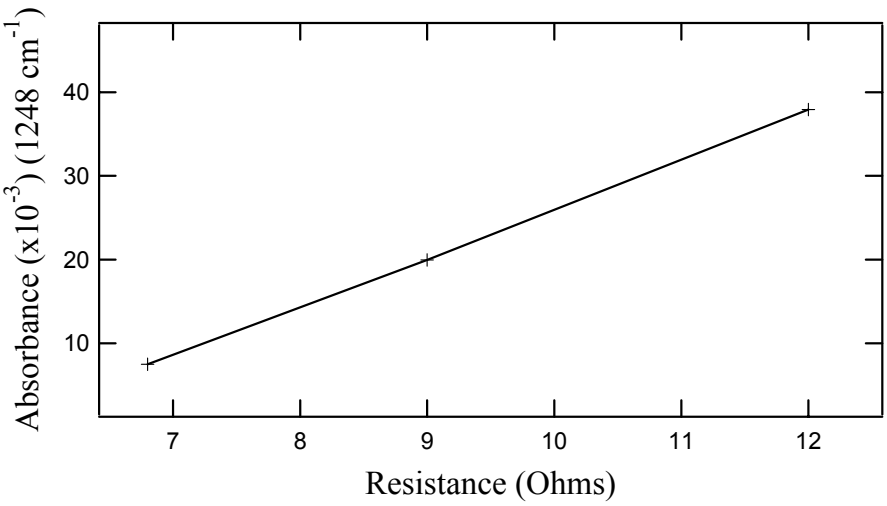

Figure 5. Plot of the absorbance of the 1248 cm^{-1} glass mode versus resistance for the three different ITO electrodes.

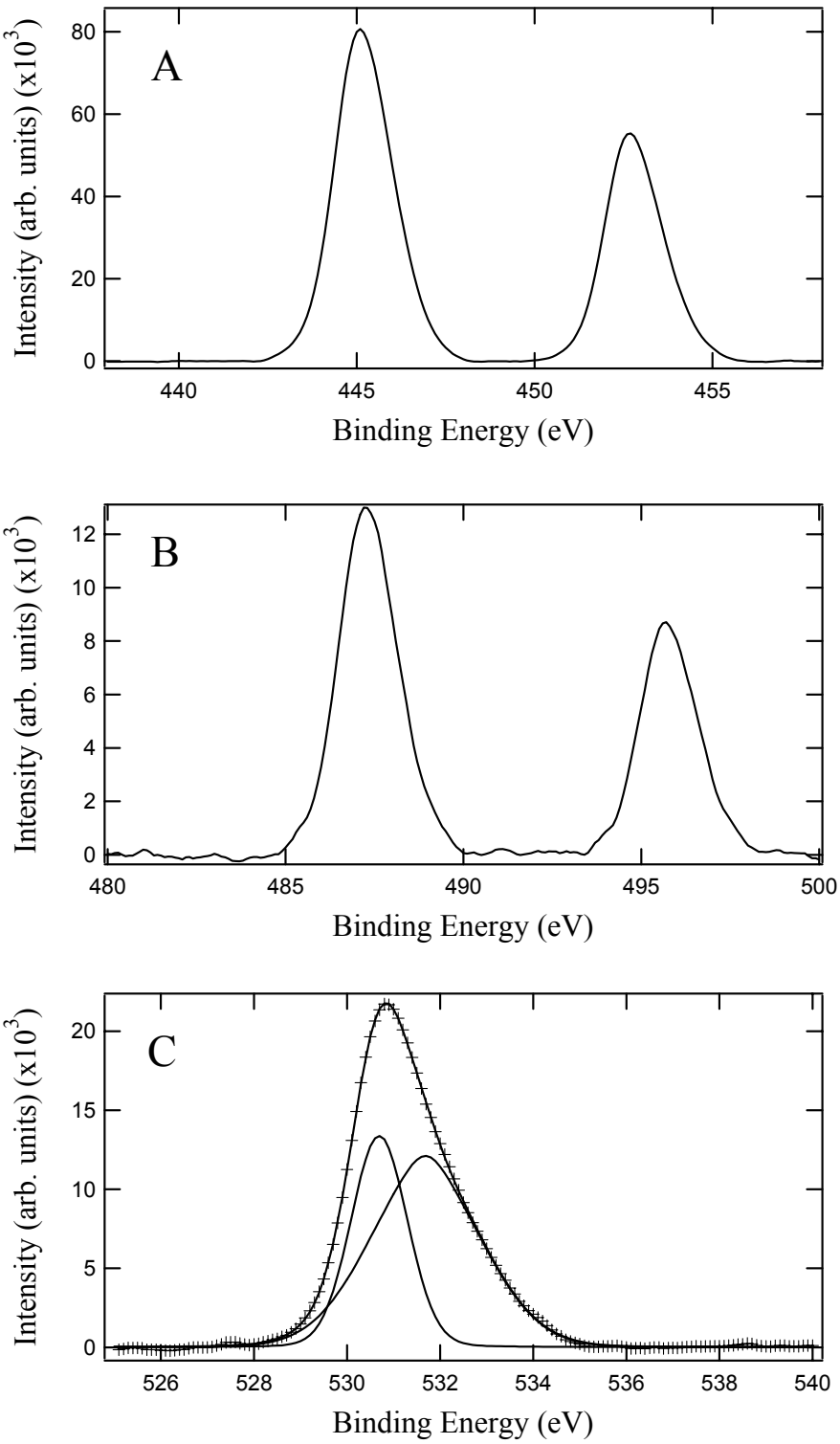

Figure 6. XPS spectra of A. In $3d_{5/2,3/2}$, B. Sn $3d_{5/2,3/2}$, and C. O 1s of Bare ITO (solid).

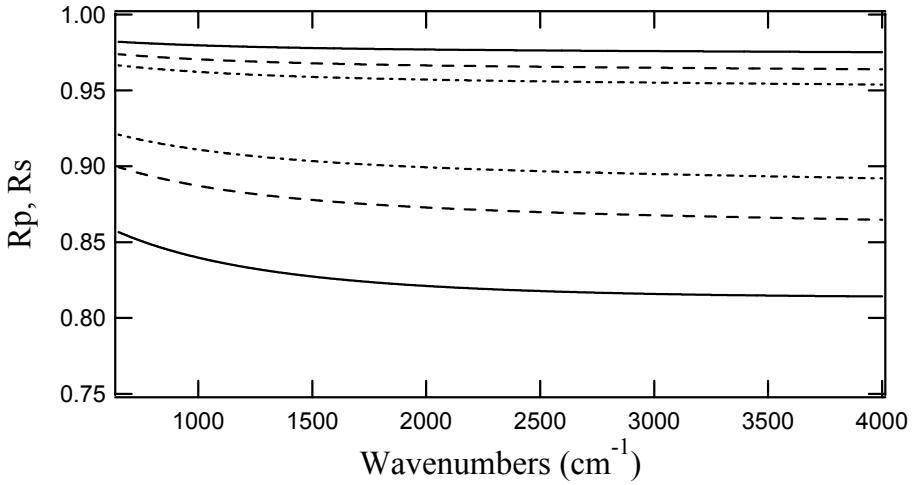

Figure 7. Plots of the calculated power reflectivity for s-(top three curves) and p-(bottom three curves) polarized light for incident angles of 70 (solid), 60 (- - -), and 50 (- -- -) degrees as calculated from the Fresnel equations of reflection.

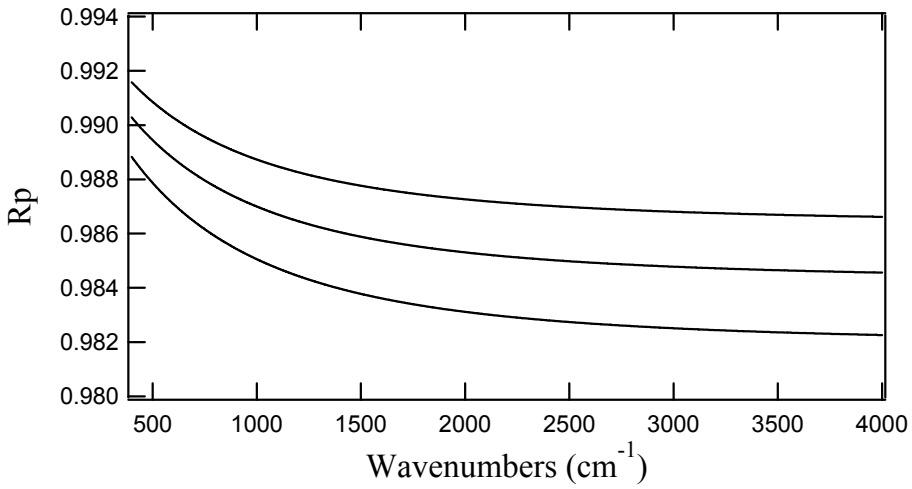

Figure 8. Calculated power reflectivity for p-polarized radiation and an incident angle of 70 degrees for ITO with resistances of 6.8 (top), 9.0 (middle), and 12 Ω (bottom). Using a thickness of 1500Å and a value of $2x10^{-14}$s for the electronic scattering time.

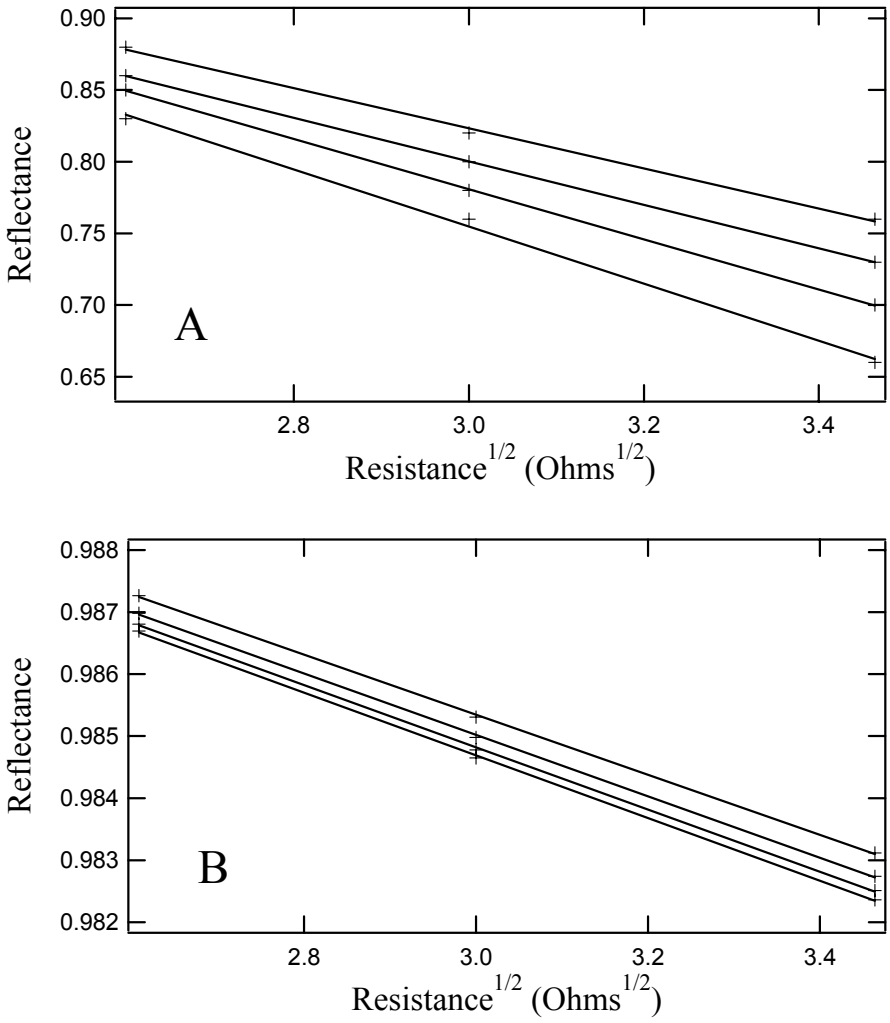

Figure 9. The observed reflectance (A) and the calculated power reflectivity (B) for an incident angle of 70 degrees and p-polarized radiation. The plots refer from top to bottom for A and B to 2000, 2500, 3000, and 3500 cm^{-1}, respectively.

Chapter 5

Formation of thiolate and phosphonate adlayers on indium tin oxide: Optical and electronic characterization

Abstract

Variable angle reflectance Fourier transform infrared (FTIR) spectroscopy and X-ray photoelectron spectroscopy (XPS) were used to investigate adlayers on indium tin oxide (ITO) and fluorine-doped tin oxide (SFO) surfaces. A close-packed, ordered adlayer was observed to form on both surfaces by 1-hexadecanethiol through thiolate–indium or thiolate-tin bonding on the two surfaces, respectively. Additionally, a close-packed, ordered adlayer of 12-phosphonododecanoic acid was observed to form on ITO through a phosphonate–indium bonding interaction. The chain length dependence on adlayer formation was studied using alkane thiols of varying chain lengths and the enthalpic factors affecting adlayer formation were modeled using density functional theory (DFT) calculations along with periodic boundary conditions (PBC).

Introduction

Thin organic films on gold have shown tremendous utility for surface attachment strategies.[1-8] Recently, there has been a great deal of interest in expanding the repertoire of substrates for thin film formation to include metal oxides and selenides.[3,9-15] These materials offer a range of new physical properties that are important for the design of new spectroscopic and electrochemical applications.[16-20] The goals of such studies include the fundamental characterization of the films themselves, but may also be key to development of new evanescent wave spectroscopies.[13] The stability of self-assembled monolayers is determined both by the bonding interaction with the metal or metal chalcogenide substrate and the hydrophobic effect between aliphatic regions of adlayer molecules. The

determination of the relative strength of these competing factors on gold has been well studied, particularly in the case of the family of derivatized alkane thiols.[3,21]

Because thiols have been widely used for the creation of self-assembled monolayers, it is logical to consider their application on metal chalcogenides. However, the interaction of thiols with metal oxides is not necessarily as strong as that with gold, [15] but thiols may still form adlayers on metal oxide surfaces under certain deposition conditions. The nature of the bonding of thiols to indium tin oxide surfaces has recently been characterized as a bonding interaction between thiolate and indium.[22] A recent study has also indicated that thiols can form adlayers on zinc selenide.[13] Previous work has showed the formation of adlayers of phosphonic and carboxylic acids on ITO.[15] However here we compare the relative affinities of these two functional groups for ITO. In this study we compare thiols (or thiolates) with phosphonates and sulfonates on indium tin oxide (ITO) and fluorine-doped tin oxide (SFO) surfaces. While thiols and phosphonates form stable surface layers for alkane chain lengths of greater than 16 and 12 respectively, sulfonates do not form stable adlayers. Phosphonic acid functional groups were found to preferentially interact with the ITO surface relative to carboxylic acid functional groups. We show that variable angle reflectance Fourier transfer infrared (FTIR) spectroscopy and X-ray photoelectron spectroscopy (XPS) is a powerful tool for examination of the organization of surface layers including their order and relative surface coverage. A novel application of density functional theory (DFT) is presented using periodic boundary conditions to address the relative strength of chemical bonding between metal atoms and thiolate or phosphonate layers compared to non-bonding interactions between aliphatic chains. Although solvent is not explicitily included, these studies indicate

the relative importance of hydrophobic interactions in stabilizing films. Both DFT calculations and experimental observations such as the presence of phosphonate layers and absence of sulfonate layers indicate that there is indeed a strong ionic bonding interaction between the adlayer molecules and metal atoms in the metal oxide substrate.

Methods and Materials

Chemicals and Subtrates. 1-Hexadecanethiol, dodecanethiol, octanethiol, and dimethyl sulfoxide (DMSO) were used as received from Sigma-Aldrich. Sodium dodecyl sulfate (SDS) was used as received from Bio-Rad Laboratories. 12-Phosphonododecanoic acid was obtained from Xanthon, Inc. Millipore 18 MΩ·cm deionized water (BARNSTEAD E-PURE) was used for aqueous solutions. Indium Tin Oxide (ITO) electrodes were received from Delta Technologies, Limited and were comprised of 90% indium oxide and 10% tin oxide. The ITO electrodes had a nominal thickness of 1,500 Å and a sheet resistance of 8-12 Ω. The substrate for the ITO electrodes was polished float (soda-lime) glass. The fluorine-doped tin oxide (SFO) electrodes were obtained from PPG Industries, Inc. and had a sheet resistance of 49-51 Ω while the gold electrodes were obtained from Evaporated Films, Inc.

Deposition on ITO and SFO Electrodes. The ITO and SFO electrodes were cleaned via 20 minutes of UV/O_3 (UVO-cleaner (UVO-60), model number 42, Jelight Company, Inc) to yield a clean hydrophilic surface.[22] The sheet resistances of these electrodes were measured with a four-point probe consisting of a Signatone D27M probe station, a Keithley 224 programmable current source, and a Hewlett Packard 3456A digital voltmeter. The clean electrodes then immersed for 16 hours in one of the deposition

solutions. The deposition solutions were 10mM 12-phosphonododecanoic acid in DMSO or 50/50 (v/v) DMSO/18 MΩ·cm H_2O, 10mM SDS in 18 MΩ·cm H_2O or 50/50 (v/v) DMSO/18 MΩ·cm H_2O, neat 1-hexadecanethiol, neat dodecanethiol, and neat ocatanethiol. Then electrodes immersed in either 12-phosphonododecanoic acid or SDS were rinsed with 18 MΩ·cm H_2O followed by drying the electrodes with N_2 gas. The electrodes immersed in 1-hexadecanethiol, dodecanethiol, or octanethiol were rinsed with ethanol and dried with N_2 gas. Then the electrodes first immersed in neat 1-hexadecanethiol (16 hours) were then immersed in 10mM 12-phosphonododecanoic acid in 50/50 (v/v) DMSO/18 MΩ·cm H_2O (16 hours), rinsed with 18 MΩ·cm H_2O, and dried with N_2 gas. Also the electrodes first immersed in 10mM 12-phosphonododecanoic acid in 50/50 (v/v) DMSO/18 MΩ·cm H_2O (16 hours) were then immersed in 1-hexadecanethiol (16 hours), rinsed with ethanol, and dried with N_2 gas.

Reflectance FTIR Spectroscopy. The variable angle reflectance FTIR spectra were recorded using a Spectra-Tech variable angle reflectance attachment (The Veemax) in a Nicolet 550 Magna-IR spectrometer. The angle of incidence ranged from 40-70 degrees. An infrared polarizer was used to obtain s- (horizontal) or p- (vertically) polarized light. A ratio of the single beam spectra of bare ITO electrodes, SFO electrodes, or glass to a single beam spectrum of a gold electrode was performed to obtain the reflection spectrum of the ITO, SFO, or glass. The spectra of the material deposited on the electrodes were obtained by taking a ratio of the single beam spectra of the deposited material on the electrode to one of the bare electrode. The rotational lines from gaseous water were subtracted from these spectra. The solid and solution FTIR spectra of the compounds were taken using an IR

microscope (model number UMA-500) attached to a Bio-Rad Digilab FTS 6000 FTIR spectrometer equipped with a Cassegranian objective containing a germanium crystal for single pass attenuated total reflection (ATR). Both FTIR spectrometers were equipped with a liquid nitrogen cooled MCT/A detector and were recorded at a resolution of 4 cm^{-1} with a spectral range of 650-4000 cm^{-1}. All IR spectra were the result of the average of 256 scans and were recorded at room temperature.

X-ray Photoelectron Spectroscopy (XPS). XPS spectra were recorded on a Riber LAS 2000 Surface Analysis System equipped with a cylindrical mirror analyzer (CMA) and a MAC2 analyzer with Mg Kα X-rays (model CX 700 (Riber source) (hν = 1253.6 eV). The elemental scans had a resolution of 1.0 eV and were the result of either 5 or 20 scans (all spectra were normalized to 5 scans). XPS spectra were smoothed using a 9 point (second order) Savitzky-Golay algorithm, baseline corrected, and the peaks were fitted using Gaussian/Lorenztian (90/10) line shapes. The phosphorus and sulfur 2p 3/2 and 1/2 angular momentum components were fit with a fixed 2:1 peak area ratio.

Density Functional Theory (DFT) Calculations. The geometry optimization, single point energy, and vibrational frequency calculations of the molecules were done using the MSI (Molecular Simulations, Inc) quantum chemistry software program DMol3 at the North Carolina Supercomputer Center (NCSC) on either the SGI Origin 2400 or the IBM RS/6000 SP. DMol3 is an ab initio (first principles) software package that utilizes density functional theory.[23] These calculations were done in the gas phase or with periodic boundary conditions using the DNP basis set, the GGA functional, and the method of finite differences for calculating the vibrational frequencies. The MSI software Insight II was used to build the

models and to visualize the eigenvector projections of the vibrational modes of the molecules. The intensities of the normal modes calculated in the gas phase were used for the corresponding normal modes in the periodic boundary condition (PBC) calculations.

Results

Reflectance FTIR Spectra of ITO.

ITO films have sufficiently high reflectivity in the infrared region to permit the acquisition of reflectance FTIR spectra of ITO and adlayers on ITO to be obtained in a grazing angle geometry. Figures 1A and 1B show the variable angle reflectance FTIR spectra of an ITO electrode for angles of incidence from 50-70 degrees for p- and s-polarized light, respectively. There are several features of these spectra that are important for consideration in optical detection of adlayer formation such as the relatively high reflectance of ITO in the mid-IR. In the methylene (CH_2) stretching region near 3000 cm^{-1}, the reflectance is > 0.7 for ITO for p-polarized light (usually employed in studies on metallic surfaces due to surface selection rules) [24] in the grazing angle geometry. The reflectance for both p- and s-polarized spectra decreases in the wavenumber range from 1500 to 4000 cm^{-1} due to the onset of the plasmon absorption of ITO as discussed elsewhere.[25] The reflectance for the p-polarized spectra increases with decreasing angle of incidence while the opposite is true for s-polarized light thus suggesting that an angle of 50–70 degrees is optimal for detection of surface adlayers. The longitudinal optical (LO) and transverse optical (TO) Si-O-Si stretching modes are observed at 1248cm^{-1} and 1064 cm^{-1} respectively for an incident angle of 70 degrees and p-polarized radiation. The correlation of the intensity of this band to

the skin depth of the ITO film is considered elsewhere.[25] In this study it is important to note that interference from these glass bands can complicate the analysis of any features from surface adlayers that may fall in the region from 900 – 1300 cm^{-1}. Fortunately, the most important features occur elsewhere and are easily distinguished from the glass bands.

Deposition of Alkane Thiols, Phosphonates, and Sulfonates.

FTIR Characterization. Figure 2A shows the variable angle reflectance FTIR spectra of a 1-hexadecanethiol adlayer on an ITO electrode. The figure shows spectra corresponding to angles of incidence of 40, 50, 60, and 70 degrees for p-polarized infrared light and the spectrum of s-polarized light at an incident angle of 70 degrees. The intensity of the bands corresponding to the symmetric and asymmetric stretches of the CH_2 groups and asymmetric CH_3 stretches decrease as the incident angle for the p- polarized spectra decreases. The observed peaks for the s-polarized spectrum at 70 degrees of incidence are significantly less intense as compared to the p-polarized spectra at the same angle of incidence. Figure 2B shows the reflectance FTIR spectra of an adlayer of 1-hexadecanethiol on either an ITO or SFO electrode corresponding to an angle of incidence of 70 degrees and p-polarized light. The figure also shows the subtraction of these two spectra illustrating that the peak widths (of the previously mentioned vibrations) are the same for the monolayer on both electrodes but the intensity of the signal is greater on SFO. Table 1 gives the values of the various vibrational frequencies on these two metal oxide surfaces and for neat 1-hexadecanethiol.

Figures 3A and 3B show the reflectance FTIR spectra of an adlayer or partial adlayer of 12-phosphonododecanoic acid on an ITO electrode deposited from either 50/50 (v/v)

DMSO/18 MΩ·cm H_2O or DMSO at an angle of incidence of 70 degrees for p-polarized light, respectively. The spectra in Figure 3A show vibrational modes corresponding to the symmetric and asymmetric stretching motions of CH_2 groups. As seen in Figure 3B the carbonyl stretch is observed only for the adlayer formed from 50/50 (v/v) DMSO/18 MΩ·cm H_2O deposition solution. Table 2 gives the values of the vibrational frequencies of the adlayer or partial adlayer structures of 12-phosphonododecanoic acid on ITO and the corresponding solid and solution values of these modes.

The variable angle reflectance FTIR spectra of a partial adlayer of 12-phosphonododecanoic acid on a SFO electrode deposited from either DMSO or 50/50 (v/v) DMSO/18 MΩ·cm H_2O show low intensity modes (below approximately $400x10^{-6}$ absorbance units) for 70 degrees incident angle and p-polarized infrared light (data not shown) in the methylene (CH_2) symmetric and asymmetric stretching region. These modes have a lower intensity and different peak profile as compared to the corresponding modes of an adlayer of 12-phosphonododecanoic acid on ITO. The values of the various vibrational frequencies of the partial adlayer structures of 12-phosphonododecanoic acid on SFO are listed in Table 2.

The variable angle reflectance FTIR spectra of an ITO surface following application of sodium dodecyl sulfate (SDS) from 50/50 (v/v) DMSO/18 MΩ·cm H_2O show low intensity peaks (below $3x10^{-4}$ absorbance units) at 2848 and 2918 cm^{-1}, which correspond to the symmetric and asymmetric CH_2 stretching modes observed at 2849 and 2916 cm^{-1}, respectively in solid SDS. No observable modes in this region are observed for the deposition of SDS on ITO from 18 MΩ·cm H_2O leading to the conclusion that no adlayer is

formed under these conditions. The variable angle FTIR spectra for SDS deposited on SFO electrodes from either 18 MΩ·cm H_2O or 50/50 (v/v) DMSO/18 MΩ·cm H_2O also do not show any detectable peaks corresponding to SDS on the surface further substantiating the conclusion that no adlayer is formed by SDS (data not shown).

XPS Characterization. Figure 4A and 4B shows the XPS spectra of indium $3d_{5/2,3/2}$ and tin $3d_{5/2,3/2}$ of bare ITO and an adlayer of either 1-hexadecanethiol or 12-phosphonododecanoic acid (deposited from 50/50 (v/v) DMSO/18MΩ·cm H_2O) on ITO. The position of the indium $3d_{5/2,3/2}$ (445.1, 452.7 eV) and tin $3d_{5/2,3/2}$ (487.2, 495.7 eV) of bare ITO corresponds to the In^{3+} and Sn^{4+} oxidation states in ITO, respectively.[22] These spectra show a significant attenuation of these signals in the spectra corresponding to either a monolayer of 1-hexadecanethiol or 12-phosphonododecanoic acid on ITO relative to bare ITO. Figure 4C shows the carbon 1s spectra of bare ITO, 1-hexadecanethiol on ITO, and 12-phosphonododecanoic acid on ITO. The carbon 1s signal occurs at 285.2 eV (for adventitious carbon on bare ITO) and an increase in this peak is observed for either 1-hexadecanethiol or 12-phosphonododecanoic acid on ITO. An additional peak at 289.7 eV, corresponding to the carbon 1s peak of a carbon of a carbonyl group, is observed for 12-phosphonododecanoic acid on ITO.[22] These results and a summary of the peaks for dodecanethiol, octanethiol, and sodium dodecyl sulfate are in Table 3.

Figure 5 shows the XPS spectra of O 1s of bare ITO, an adlayer of 1-hexadecanethiol on ITO, and an adlayer of 12-phosphonododecanoic acid on ITO. The two components of the O 1s spectra for bare ITO occur at 530.7 and 531.7 eV that correspond to indium oxide and tin oxide species, respectively.[22] The ratio between In-O and Sn-O is 1.7 for bare ITO

and shifts to 1.6 and 1.3 for 1-hexadecanethiol and 12-phosphonododecanoic acid on ITO, respectively. Also the peak positions for both of the monolayer structures on ITO are 530.8 and 532.2 eV. The O 1s spectra of the other samples did not show any difference in the peak position or peak area ratio relative to bare ITO.

Figure 6 shows the sulfur $2p_{3/2,1/2}$ XPS spectra of A. an adlayer of 1-hexadecanethiol on ITO and B. a partial adlayer of dodecanethiol on ITO. These peaks occur at 162.8 and 164.2 eV for 1-hexadecanethiol on ITO and at 162.9 and 164.3 eV for dodecanethiol on ITO. There were no observable peaks for octanethiol on ITO (data not shown). The overall peak intensities for dodecanethiol and octanethiol on ITO are 90 and 0% of the intensity of sulfur $2p_{3/2,1/2}$ relative to 1-hexadecanethiol on ITO, respectively. The peak positions for 1-hexadecanethiol and dodecanethiol are characteristic of a thiolate species of the alkane thiols.[2,22]

Figure 7 shows the phosphorous $2p_{3/2,1/2}$ signals at 133.2 and 134.3 eV, respectively from an adlayer of 12-phosphonododecanoic acid (deposited from 50/50 (v/v) DMSO/18MΩ·cm H_2O) on ITO. These peak positions correspond to a fully deprotonated phosphonate group (PO_3^{2-}).[26-28] The corresponding phosphorous $2p_{3/2,1/2}$ peak intensities are 30% lower for the partial adlayer formed from DMSO (data not shown).

Modeling of 12-Phosphonododecanoic Acid Monolayer.

Figure 8 shows the DFT calculated (using DMol3) frequency spectra of two possible forms of the carboxylic acid functional group of 12-phosophonododecanoic acid. Figure 8 shows the calculated frequency spectra for the acid (COOH) form of this molecule with a carbonyl stretch at 1772 cm^{-1} while the highest stretching frequency of the carboxylate

(COO-) group is at 1523 cm^{-1}. The frequency decrease in the carboxylate species is the result of a decrease in bond order between the carbon and oxygen atoms.

Modeling of Frequency Shifts Upon Adlayer Formation.

The experimental observation of a lowering of the vibration frequency of methylene CH_2 stretches upon adlayer formation as compared to solution values was successfully modeled theoretically using periodic boundary conditions (PBC). The model was polymethylene with 12 methylene groups in each subunit. The model is similar to an infinite chain of methylene groups because the distance between carbon atoms in adjacent subunits (boxes) is the same as the distance between carbon atoms in the same subunit. The box length perpendicular to the molecular axis of the molecule was varied to simulate the effect of close packing in adlayers. Figure 9 shows the calculated frequency spectra for two different box dimensions. The mode type and the corresponding frequencies are listed in Table 4. As seen in Figure 4, as the box dimension becomes smaller the symmetric and asymmetric methylene CH_2 stretches decrease compared to the corresponding frequencies with a larger box dimension. This effect is similar to the experimental result that occurs upon adlayer formation due to the molecules coming into closer contact as compared to in solution. Similar trends were found using PBC with both 12-phosphonododecanoic acid and 1-hexadecanethiol.

Enthalpic Considerations in Monolayer Formation.

The enthalpic contribution to monolayer formation was modeled using density functional calculations with PBC. The energetics of headgroups of adlayer molecules interacting with atoms of the surface can be quantified by calculating potential energy

surfaces (PES) corresponding to these interactions in the gas phase. PBC models can be used to model the dispersion forces between adjacent alkane chains. PBC calculations use arrays, with subunits of defined dimensions, each containing one molecule. Therefore by changing the dimensions of the subunits the energetics between adjacent molecules (subunits) can be studied. Potential energy surfaces for the binding of sulfur (of 1-hexadecanethiol) to either indium or tin (with hydroxyl groups completing the coordination shell of the metal) are shown in Figure 10A. These curves show a binding energy of –118 and –155 kJ/mol for the S-Sn (2.55 Å) and S-In (2.45 Å) bonds, respectively. Similar PES of the binding of the deprotonated phosphonate (PO_3^{2-}) form of 12-phosphonododecanoic acid to either tin or indium (with hydroxyl groups completing the coordination shell of the metal) showed binding energies of –98 (2.97 Å) and –116 (2.82 Å) kJ/mol, respectively (data not shown). Figure 10B shows the PES of varying the box width (perpendicular to molecular axis of the molecule) of 1-hexadecanethiol and 12-phosphonododecanoic acid to illustrate the enthalpic contribution to monolayer formation from interaction between neighboring molecules. These potential energy surfaces show an enthalpy of interaction of –34 and –22 kJ/mol for 1-hexadecanethiol and 12-phosphonododecanoic acid, respectively. Similar calculations for dodecanethiol and octanethiol showed an enthalpy of interaction of –19 and –3 kJ/mol, respectively as shown in Figure 10C. The absolute value of this enthalpy of interaction is likely greater for 1-hexadecanethiol primarily due to larger number of methylene groups that can interact with neighboring alkane chains, as shown with the alkane thiols of varied alkane chain length, and due to the bulky functional groups of 12-phosphonododecanoic acid limiting the distance between neighboring alkane chains. The expected correlation that the

enthalpy of interaction of adjacent alkane chains decreases as the alkane chain length decreases was shown with alkane thiols of varied chain length.

Sequential Electrode Immersions.

The stability of the adlayer structures of 1-hexadecanethiol and 12-phosphononododecanoic acid on ITO were investigated through exchange reactions. The ITO electrodes that were first immersed in 10mM 12-phosphonododecanoic acid in 50/50 (v/v) DMSO/18 MΩ·cm H_2O (16 hours) were then immersed in 1-hexadecanethiol (16 hours) and vice versa. The resulting reflectance FTIR spectra showed that neither of the adlayers were displaced by the other molecule (data not shown). Earlier work showed that phosphonic acids have a higher affinity than thiols to form adlayers on ITO[15] which is similar to the present results were an adlayer of 1-hexadecanethiol on ITO was formed only when deposited from the corresponding neat thiol, while 12-phosphonododecanoic acid formed an adlayer on ITO from a much more dilute deposition solution (10mM) of the phosphonic acid.

Discussion

FTIR reflectance measurements have shown that indium tin oxide (and SFO) electrodes are highly reflective in the mid-IR region (650-4000 cm^{-1}) and that the reflectance is a function of incident angle, polarization, and wavenumber.[25] This high reflectivity allows reflectance FTIR spectroscopy to probe structures on the surfaces of these two electrodes. The combination of reflectance FTIR spectroscopy and X-ray photoelectron

spectroscopy provide evidence that chemisorbed adlayers of alkyl thiolates and phosphonates form on ITO and SFO films.

Reflectance FTIR and XPS show that a close-packed, stable monolayer structure of 1-hexadecanethiol is formed on ITO and SFO electrodes through a thiolate interaction with the metal atoms of the surface. Our XPS results agree with those of a previous report[22] and the optical spectroscopy lends further support to the hypothesis that the thiolate film is well-ordered. Variable angle reflectance FTIR spectroscopy demonstrates an ordered monolayer structure on both ITO and SFO electrodes by the decrease of the frequency of the CH_2 methylene stretches relative to neat 1-hexadecanethiol and by their signal intensities. This frequency decrease is the result of packing interactions between neighboring molecules, as the close-packed monolayer is formed, which was successfully modeled using periodic boundary conditions. The position of the sulfur $2p_{3/2,1/2}$ signal, the attenuation of indium $3d_{5/2,3/2}$ and tin $3d_{5/2,3/2}$, and the increase in carbon 1s XPS signals relative to bare ITO demonstrates the presence of a monolayer of 1-hexadecanethiol on ITO with a thiolate-metal interaction[2,22]; however, the preferential affinity of the thiolate-metal interaction for either indium or tin cannot be deduced from the experimental data.[22]

The formation of a monolayer of 1-hexadecanethiol on either ITO or SFO is enthalpically driven by the thiolate–metal (In or Sn) interaction and the interaction between neighboring alkane chains. The DFT PES calculations show that the S-In is more energetically stable than the S-Sn interaction. Although the majority of the enthalpic driving force is from the thiolate-metal interaction, there is some enthalpic gain from the packing interactions. The enthalpy of interaction of alkane chains was found to decrease as the chain

length decreased similar to previous experimental work[21]; however, the absolute value of the calculated enthalpy of interaction will depend on the periodic boundary conditions used. This enthalpic difference contributes to the formation of complete adlayers as the chain length was increased. As observed previously on Au surfaces[3,21] the chain length dependence of film stability is demonstrated experimentally here by the formation of a partial monolayer of dodecanethiol and the lack of any monolayer structure of octanethiol. Evidence for the relative coverage as a function of alkane chain length is found in the relative attenuation of the indium $3d_{5/2,3/2}$ and tin $3d_{5/2,3/2}$ XPS signals and the small or absent sulfur $2p_{3/2,1/2}$ signal for dodecanethiol or octanethiol, respectively. However, given that the In-S bond is stronger than the dispersion forces between adjacent alkane chains, entropic effects (not modeled here) must contribute significantly to the energitics of adlayer formation. The competing entropic factors for the alkane thiols are sequestering in solvent analogous to micelle formation versus formation of an adlayer due to the hydrophobic effect.

12-Phosphonododecanoic acid also formed a close-packed, stable monolayer structure on ITO as shown by reflectance FTIR and XPS through the interaction between fully deprotonated phosphonate groups (PO_3^{2-}) and metal atoms of the surface when deposited from 50/50 (v/v) DMSO/18 MΩ·cm H_2O. The position of the XPS phosphorous $2p_{3/2,1/2}$ peak shows that the phosphonate group is in the PO_3^{2-} form in this monolayer structure and that only a partial monolayer is formed from DMSO by the relatively smaller attenuation of the indium $3d_{5/2,3/2}$ and tin $3d_{5/2,3/2}$ XPS signals and a decrease in the carbon 1s and phosphorous $2p_{3/2,1/2}$ signals.[26-28] Therefore demonstrating that monolayer formation of 12-phosphonododecanoic acid is highly dependent upon the deposition parameters.

Reflectance FTIR spectroscopy demonstrated a close-packed, ordered monolayer structure of 12-phosphonododecanoic acid when deposited from 50/50 (v/v) DMSO/18 MΩ·cm H_2O from the signal intensities and from the frequencies of the carbonyl and methylene CH_2 stretches being intermediate between the solid and solution values of these frequencies. The decrease in frequencies of these vibrations as compared to solution values is again the result of packing interactions between neighboring chains in the monolayer. However the increase in the methylene CH_2 symmetric stretch relative to the solution values demonstrates that a disordered structure was formed when 12-phosphonododecanoic acid was deposited from DMSO on ITO.

The enthalpic driving forces for the formation of a monolayer of 12-phosphonododecanoic acid on ITO are the interaction between the phosphonate group and the metal atoms of the surface and the packing interactions. DFT calculations showed that the phosphonate-indium interaction is thermodynamically more stable than the corresponding phosphonate-tin interaction. Also, the binding energy for phosphonate is smaller than the corresponding thiolate (of 1-hexadecanethiol) interaction with either metal atom. Therefore along with the smaller packing stabilization energy than 1-hexadecanethiol, the monolayer of 12-phosphonododecanoic acid forms a theoretically enthalpically less stable monolayer than 1-hexadecanethiol. However neither molecule could replace an existing monolayer structure of the other molecule on ITO. Moreover, the carboxylic acid of 12-phosphonododecanoic is protonated in the monolayer structure formed from 50/50 (v/v) DMSO/18 MΩ·cm H_2O based on DFT frequency calculations of the carbonyl or carboxylate forms and literature values of carboxylate stretching frequencies of carboxylate groups interacting with oxidized aluminum

surfaces.[12] For example, n-alkanoic acids interacting with oxidized aluminum surfaces in the carboxylate form experimentally showed a frequency at 1608 cm^{-1} on metal oxide surfaces involving carbon and oxygen.[12] The lack of a carbonyl frequency in the DMSO deposited material suggests that the transition dipole moment of the carbonyl group is parallel to the surface.

Many of the conditions used did not lead to formation of ordered monolayers on the two metal oxides studied. Based on the reflectance FTIR and XPS data signal intensities, no monolayers were formed by sodium dodecyl sulfate on ITO or SFO electrodes or by 12-phosphonododecanoic acid on SFO by any of the deposition solvent systems used. All of these samples showed no or low intensity signals in the reflectance FTIR spectra and little if any attenuation of indium $3d_{5/2,3/2}$ and tin $3d_{5/2,3/2}$ or an increase in carbon 1s XPS signals (or presence of other elements of the monolayer material).

Conclusion

Variable angle reflectance FTIR spectroscopy was shown to be effective in characterizing adlayers on both ITO and SFO electrodes due to their high reflectivity in the mid-IR. Reflectance FTIR and XPS showed that an adlayer of 1-hexadecanethiol formed on both ITO and SFO through a thiolate–metal interaction while an adlayer of 12-phosphonododecanoic acid was observed on ITO through a phosphonate–indium interaction. The enthalpic factors contributing to adlayer formation were found to be packing interactions between neighboring alkane chains and the interaction of thiolate or phosphonate groups with the metal atoms of the surface. The importance of these packing interactions was shown by a

decrease in the both the DFT calculated enthalpy of interaction of neighboring alkane chains and the relative surface coverage on ITO of alkane thiols as the alkane chain length decreased.

Acknowledgements

This work was done in collaboration with Derek A. Brown (NCSU) and Stefan Franzen (NCSU) and was the subject of a publication, Brewer, S. H.; Brown, D. A.; Franzen, S. *Langmuir* **2002**, 18(18), 6857-6865. Scott Brewer was supported by NIH Biotechnology Training Grant T32-GM08776. Support and computational facilities were provided by the North Carolina Supercomputing Center.

References

(1) Terril, R.; Tanzer, T.; Bohn, P. *Langmuir* **1998**, *14*, 845-854.

(2) Bain, C.; Biebuyck, H.; Whitesides, G. *Langmuir* **1989**, *5*, 723-727.

(3) Ulman, A. *Chemical Reviews* **1996**, *96*, 1533-1554.

(4) Karyakin, A.; Presnova, G.; Rubtsova, M.; Egorov, A. *Analytical Chemistry* **2000**, *72*, 3805-3811.

(5) Kitano, H.; Taira, Y.; Yamamoto, H. *Analytical Chemistry* **2000**, *72*, 2976-2980.

(6) Kittredge, K.; Fox, M.; Whitesell, J. *Journal of Physical Chemistry B* **2001**, *ASAP article*.

(7) Ringsdorf, H. *Macromolecules* **1997**, *30*, 5913-5919.

(8) Nakashima, N. *Langmuir* **1999**, *15*, 3823-3830.

(9) Tamada, M.; Koshikawa, H.; Hosoi, F.; Suwa, T. *Thin Solid Films* **1998**, *315*, 40-43.

(10) Folkers, J.; Gorman, C.; Laibinis, P.; Buchholz, S.; Whitesides, G. *Langmuir* **1995**, *11*, 813-824.

(11) Allara, D.; Nuzzo, R. *Langmuir* **1985**, *1*, 45-52.

(12) Allara, D.; Nuzzo, R. *Langmuir* **1985**, *1*, 52-66.

(13) Noble-Luginbuhl, A.; Nuzzo, R. *Langmuir* **2001**, *17*, 3937-3944.

(14) Purvis, K.; Lu, G.; Schwartz, J.; Bernasek, S. *The Journal of the American Chemical Society* **2000**, *122*, 1808-1809.

(15) Gardner, T.; Frisbie, C.; Wrighton, M. *The Journal of the American Chemical Society* **1995**, *117*, 6927-6933.

(16) VanderKam, S.; Gawalt, E.; Schwartz, J.; Bocarsly, A. *Langmuir* **1999**, *15*, 6598-6600.

(17) Armistead, P.; Thorp, H. *Analytical Chemistry* **2000**, *72*, 3764-3770.

(18) Zotti, G.; Schiavon, G.; Zecchin, S.; Berlin, A.; Pagani, G. *Langmuir* **1998**, *14*, 1728-1733.

(19) Li, L.; Wang, R.; Fitzsimmons, M.; Li, D. *Journal of Physical Chemistry B* **2000**, *104*, 11195-11201.

(20) Oh, S.; Yun, Y.; Kim, D.; Han, S. *Langmuir* **1999**, *15*, 4690-4692.

(21) Lavrich, D.; Wetterer, S.; Bernasek, S.; Scoles, G. *Journal of Physical Chemistry B* **1998**, *102*, 3456-3465.

(22) Yan, C.; Zharnikov, M.; Golzhauser, A.; Grunze, M. *Langmuir* **2000**, *16*, 6208-6215.

(23) Delley, B. *Journal of Chemical Physics* **1990**, *92*, 508-517.

(24) Parikh, A.; Allara, D. *Journal of Chemical Physics* **1992**, *96*, 927-944.

(25) Brewer, S.; Franzen, S. *Jounal of Alloys and Compounds* **2002,** *338*, 73-79.

(26) Kohli, P.; Blanchard, G. *Langmuir* **2000**, *16*, 8518-8524.

(27) Petruska, M.; Fanucci, G.; Talham, D. *Chemistry of Materials* **1998**, *10*, 177-189.

(28) Seip, C.; Talham, D. *Materials Research Bulletin* **1999**, *34*, 437-445.

Tables

Table 1. Normal mode frequencies of neat 1-hexadecanethiol and frequencies corresponding to a monolayer of 1-hexadecanethiol on ITO and SFO respectively at an incidence angle of 70 degrees with p-polarized light.

	Neat (liquid)	ITO	SFO
$\nu_s CH_2$ (cm^{-1})	2851	2848	2848
$\nu_a CH_2$ (cm^{-1})	2920	2918	2918
$\nu_a CH_3$ (cm^{-1})	2953	2961	2959

Table 2. Solid and solution values corresponding to normal mode frequencies of 12-phosphonododecanoic acid and the frequencies of the corresponding monolayer or partial monolayer of the same material on ITO and SFO respectively at an incidence angle of 70 degrees with p- polarized light.

	solid	solution	ITO[a]	ITO[b]	SFO[a]	SFO[b]
$\nu_s C{=}O$ (cm^{-1})	1686	1721	1716	---	---	---
$\nu_s CH_2$ (cm^{-1})	2845	2851	2848	2854	2850	2862
$\nu_a CH_2$ (cm^{-1})	2914	2928	2922	2926	2924	2926

(a: 50/50 (v/v) DMSO/18MΩ·cm H_2O, b: DMSO deposition solution)

Table 3. In $3d_{5/2,3/2}$ (445.1, 452.7 eV), Sn $3d_{5/2,3/2}$ (487.2, 495.7 eV), and C 1s (285.2 eV) XPS intensities and percentage differences from bare ITO reference.

	In $3d_{3/2}$	In $3d_{5/2}$	Sn $3d_{3/2}$	Sn $3d_{5/2}$	C 1s
Bare ITO	55300	80664	8709	12994	1860
1-Hexadecanethiol	26737	39577	4133	6287	6895
	(-52%)	(-51%)	(-53%)	(-52%)	(+271%)
Dodecanethiol	40729	58617	6393	9118	3966
	(-26%)	(-27%)	(-27%)	(-30%)	(+113%)
Octanethiol	44859	64854	7535	10736	2532
	(-19%)	(-20%)	(-13%)	(-17%)	(+36%)
12-Phosphonododecanoic acid[a]	33417	49442	5297	7930	7068
	(-40%)	(-39%)	(-39%)	(-39%)	(+280%)
12-Phosphonododecanoic acid[b]	44573	65276	6478	9969	4537
	(-19%)	(-19%)	(-26%)	(-23%)	(+144%)
Sodium Dodecyl Sulfate[c]	49141	72095	7514	11554	2572
	(-11%)	(-11%)	(-14%)	(-11%)	(+38%)

(a: 50/50 (v/v) DMSO/18MΩ·cm H_2O, b: DMSO , c: 18MΩ·cm H_2O deposition solvent system)

Table 4. Calculated frequencies for polymethylene (12 methylene groups per box) using PBC with two different box dimensions. The box angles were 60 degrees. (Length a is parallel to the molecular axis of the molecule while b and c are perpendicular to a).

	$C_{12}H_{24}$[1]	$C_{12}H_{24}$[2]	Difference
$\nu_s CH_2$ (cm^{-1})	2946	2925	21
$\nu_s CH_2$ (cm^{-1})	2965	2956	9
$\nu_a CH_2$ (cm^{-1})	2987	2976	11
$\nu_a CH_2$ (cm^{-1})	3022	3011	11

1. Box dimensions: 15, 10, and 10 Å for a, b, and c respectively
2. Box dimensions: 15, 10, and 6 Å for a, b, and c respectively

Figures

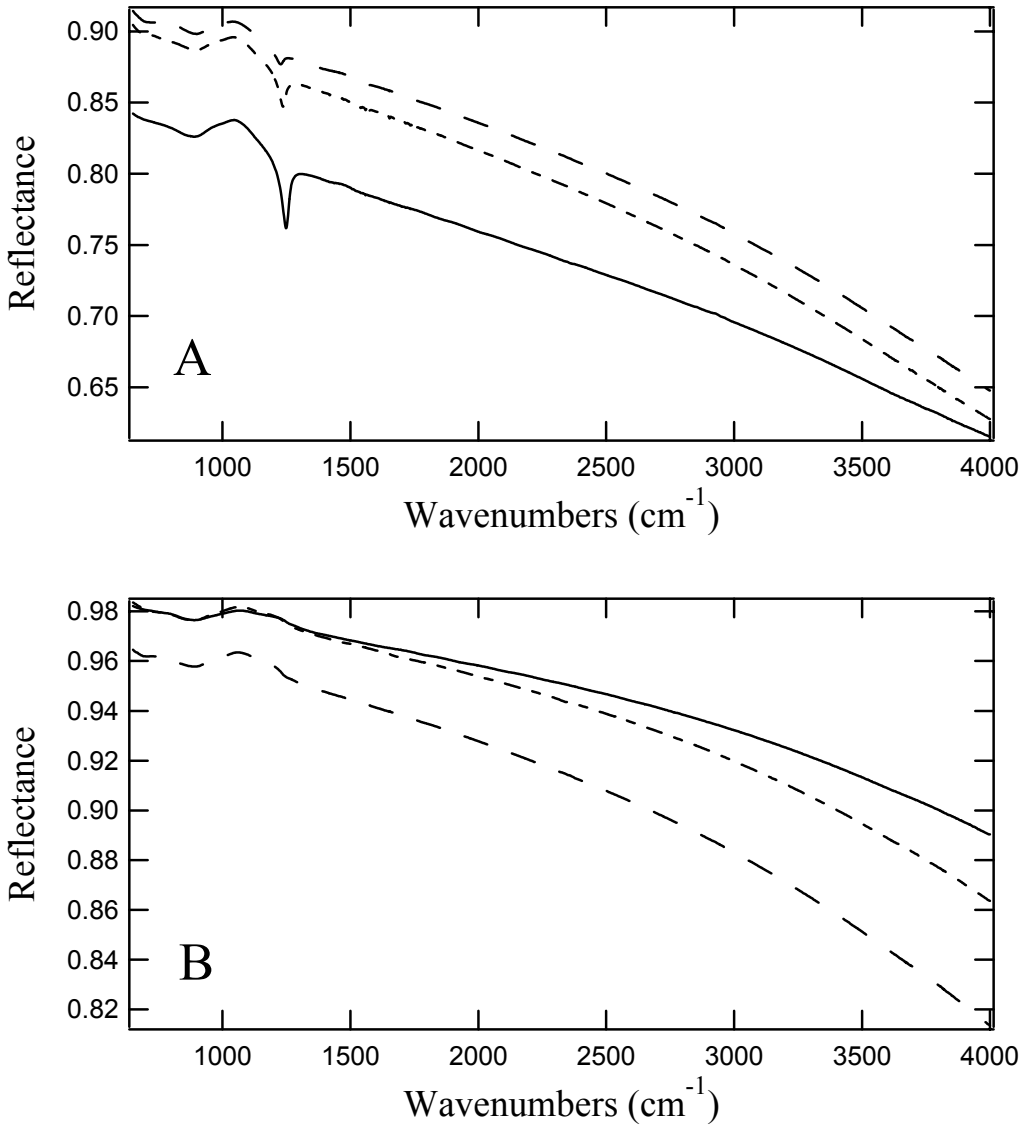

Figure 1. Variable angle reflectance FTIR spectra obtained from a ratio of an ITO electrode to gold. Spectra shown are for angles of incidence of 50 (— —), 60 (- - -) and 70 (solid line) degrees for p-polarized (A) and s-polarized (B) IR light.

Figure 2. A. Baseline corrected variable angle reflectance FTIR spectra obtained from a ratio of 1-hexadecanethiol on ITO to bare ITO. Spectra shown are for angles of incidence of 40 (— - —), 50 (— —), 60 (- - -), and 70 (solid line) degrees for p-polarized IR light and 70 degrees for s-polarized light (— - - —). (Inset: model of 1-hexadecantheiol) B. Baseline corrected reflectance FTIR spectra (incidence angle of 70 degrees with p polarized radiation) obtained from a ratio of 1-hexadecanethiol on ITO to bare ITO (solid), ratio of 1-hexadecanethiol on SFO to bare SFO (- - -), and the subtraction of the spectrum of 1-hexadecanethiol on ITO from the spectrum of 1-hexadecanethiol on SFO (— —). The bare (reference) substrate was cleaned via 20 minutes of UV/O_3, while the monolayer deposition occurred for 16 hours.

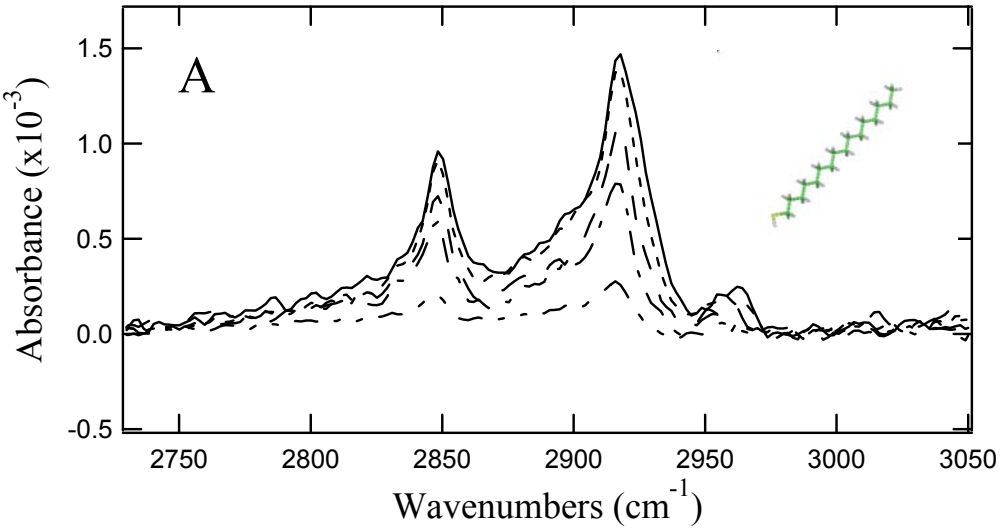
A
Absorbance (x10-3)
1.5
1.0
0.5
0.0
-0.5
2750
2800
2850
2900
2950
3000
3050
Wavenumbers (cm-1)

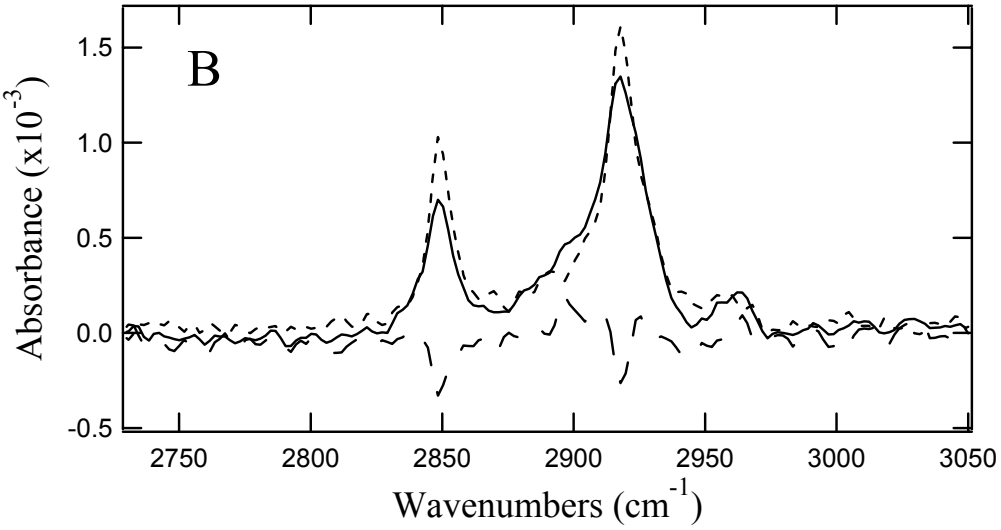
B
Absorbance (x10-3)
1.5
1.0
0.5
0.0
-0.5
2750
2800
2850
2900
2950
3000
3050
Wavenumbers (cm-1)

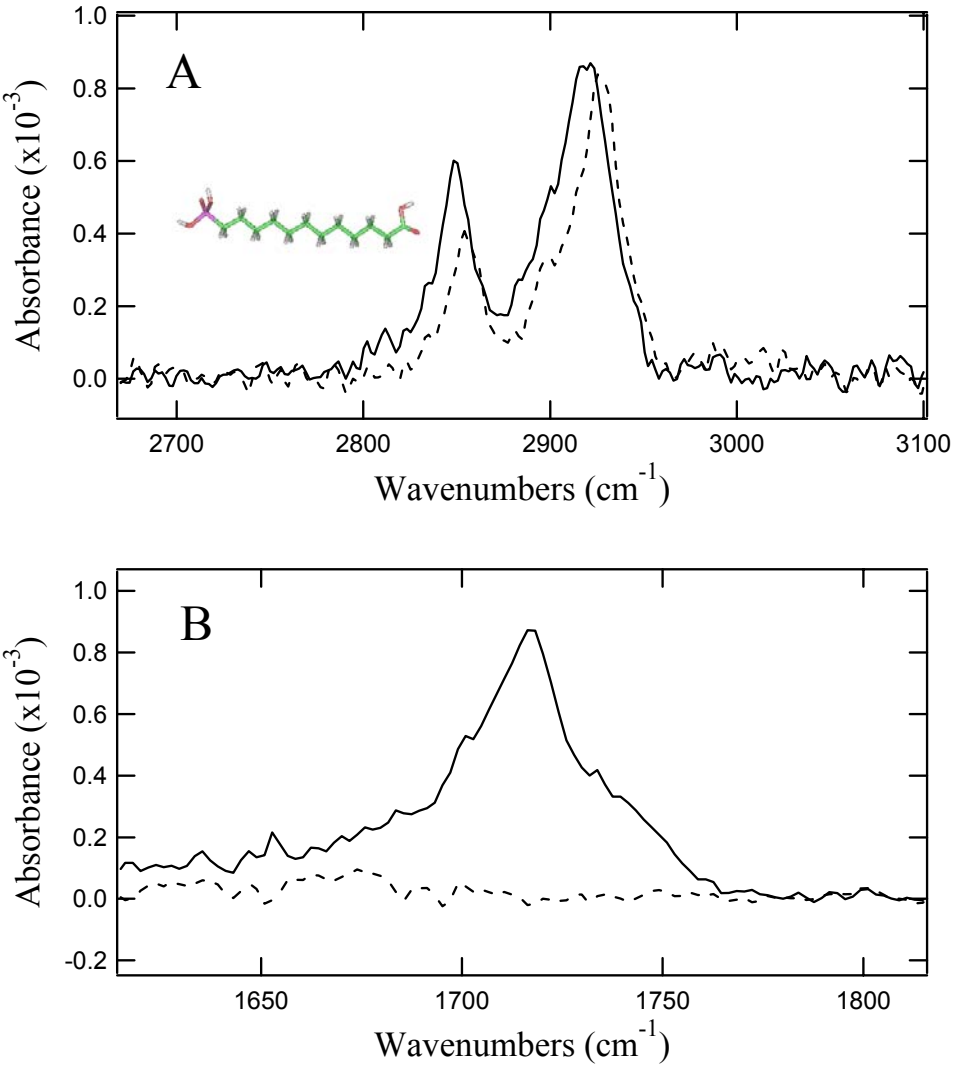

Figure 3. Baseline corrected reflectance FTIR spectra obtained from a ratio of 12-phosphonododecanoic acid (deposited from 50/50 (v/v) DMSO/18 MΩ·cm H_2O (solid line), and DMSO (dashed line)) on ITO to bare ITO. Spectra shown are for an incident angle of 70 degrees and p-polarized IR light. The spectra were obtained from a ratio of 12-phosphonododecanoic acid on ITO to bare ITO. The bare (reference) ITO substrate was cleaned via 20 minutes of UV/O_3, while the monolayer deposition occurred for 16 hours. (Inset: model of 12-phosphonododecanoic acid)

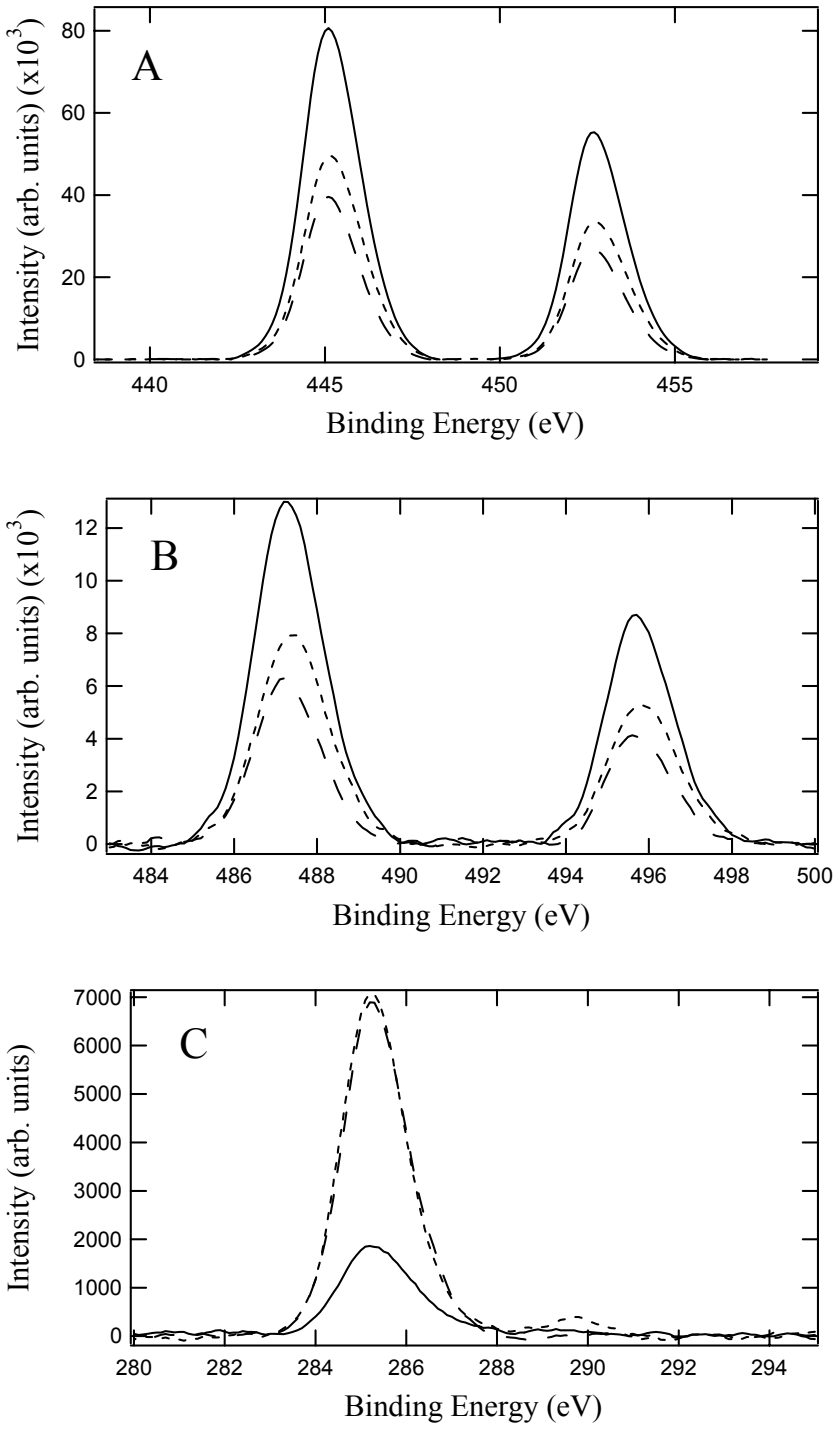

Figure 4. XPS spectra of A. Indium $3d_{5/2,3/2}$, B. Tin $3d_{5/2,3/2}$, and C. Carbon 1s of Bare ITO (solid), 12-phosphonododecanoic acid on ITO (- - -), and 1-hexadecanethiol on ITO (— —).

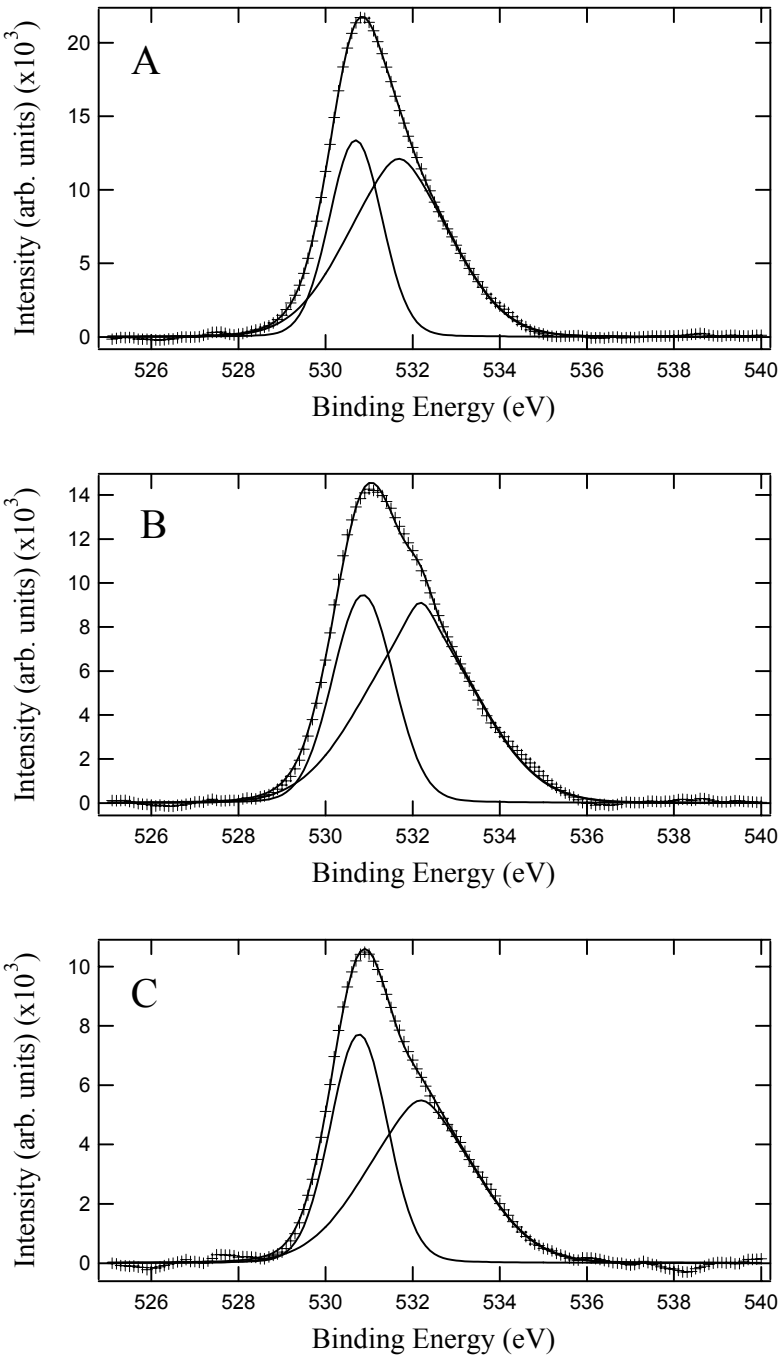

Figure 5. Oxygen 1s XPS spectra of A. Bare ITO (solid), B. 12-phosphonododecanoic acid on ITO, and C. 1-hexadecanethiol on ITO. The raw data (markers) and the individual and total 90/10 Gaussian/Lorenztian fits (solid) are shown.

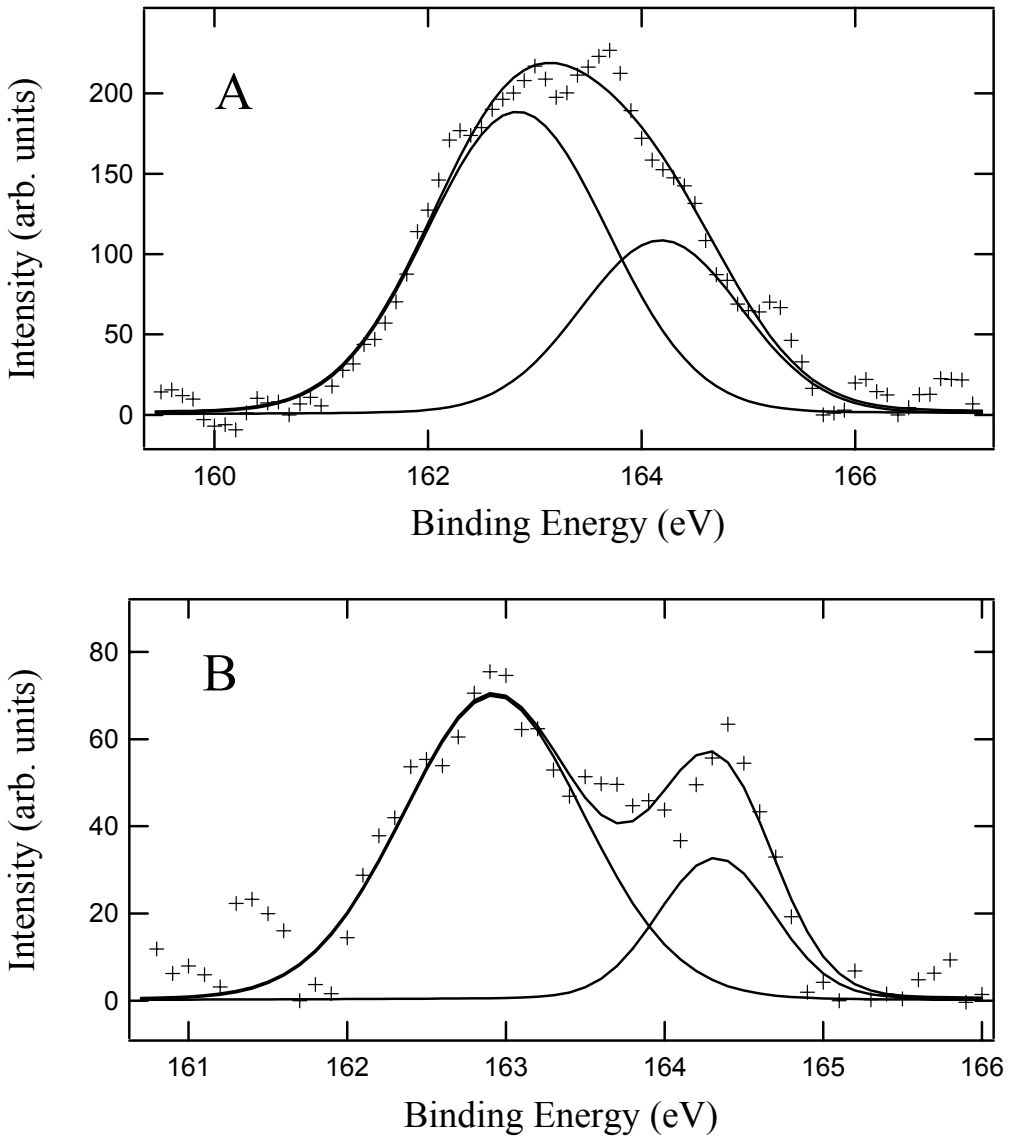

Figure 6. Sulfur $2p_{3/2,1/2}$ XPS spectra corresponding to A. an adlayer of 1-hexadecanethiol on ITO and B. a partial adlayer of dodecanethiol on ITO. The raw data (markers) and the individual and total 90/10 Gaussian/Lorenztian fits (solid) are shown.

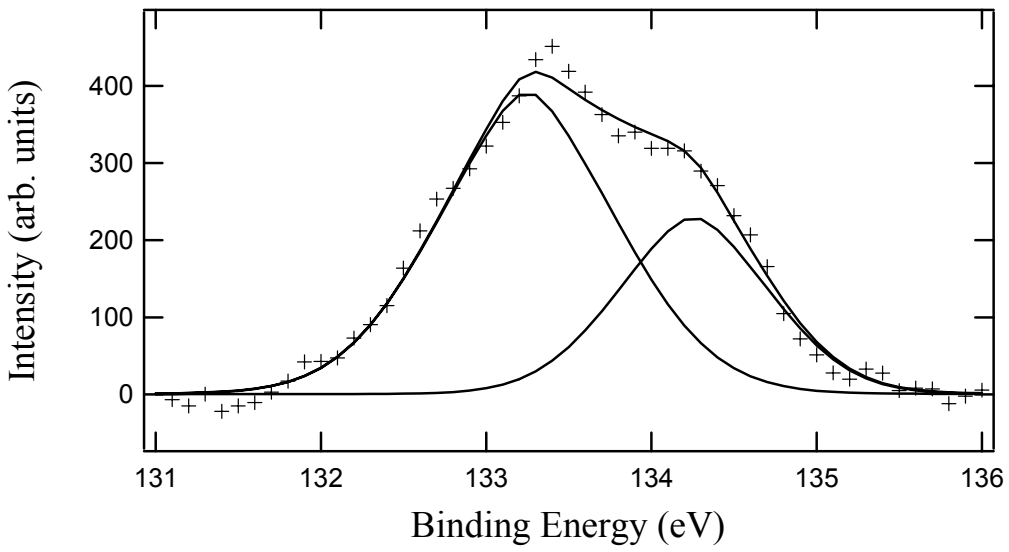

Figure 7. Phosphorous $2p_{3/2,1/2}$ (133.2, 134.3 eV) XPS spectra of 12-phosphonododecanoic acid on ITO. The raw data (markers) and the individual and total 90/10 Gaussian/Lorenztian fits (solid) are shown.

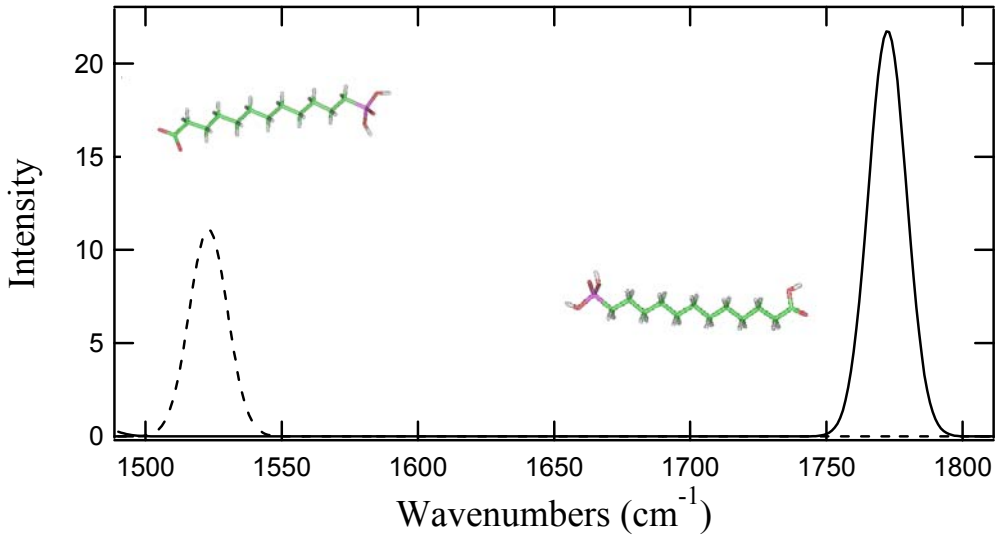

Figure 8. DFT calculated frequency spectra of the carboxylic acid (solid) and carboxylate (dashed) forms of 12-phosphonododecanoic acid. The spectra have a Gaussian width of 7 cm^{-1}. (Insets: models corresponding to the two spectra)

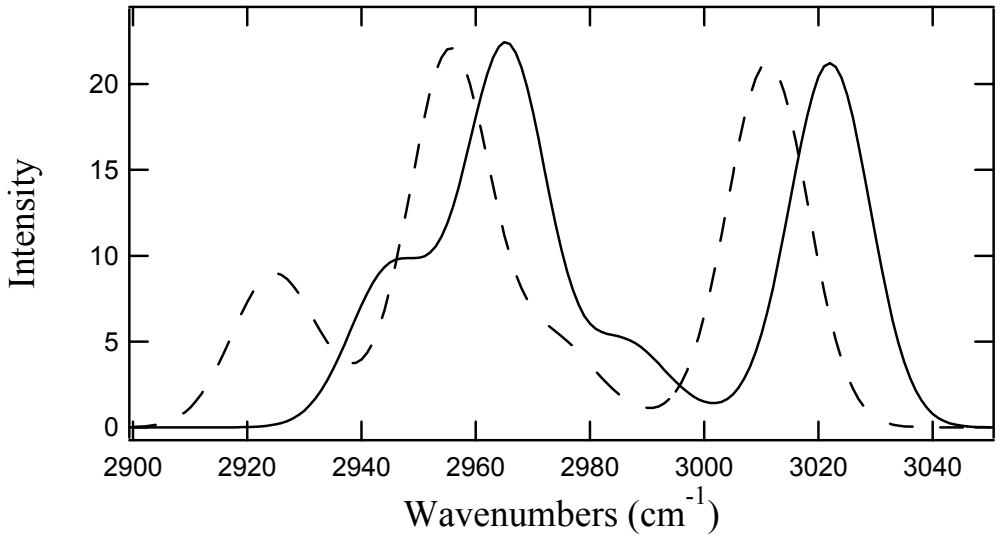

Figure 9. DFT calculated frequency spectra for polymethylene (12 methylene groups per box) using periodic boundary conditions (PBC) for different box dimensions. The box dimensions are defined by sides a, b, and c. The molecular axis of the molecule is parallel to the a direction. The box angles are 60 degrees while the lengths for a, b, and c are 15, 10, and 10 Å (solid curve) and 15, 10, and 6 Å (dashed curve) respectively. The length of the box along the a direction makes the distance between carbon atoms in adjacent boxes to be the same between carbon atoms along the alkane chain in the same box. The spectra have a Gaussian width of 7 cm^{-1}.

Figure 10. Potential energy surfaces (PES) of A. the binding of S (of 1-hexadecanethiol) to In (solid) or Sn (dashed) in the gas phase B. varying the width of the box (subunit) using periodic boundary conditions for 1-hexadecanethiol (solid) and 12-phosphonododecanoic acid (dashed) with box angles of 60 degrees. The length along the molecular axis of the molecules was 30 Å and one length perpendicular to the molecular axis was 10 Å, while the finally length (perpendicular to the molecular axis) was varied from 4.5 – 10 Å to obtain the PES C. varying the width of the box using periodic boundary conditions for 1-hexadecanethiol (solid), dodecanethiol (- - -), and octanethiol (— —) using the same protocol for 1-hexadecanethiol in B. The potential energies were referenced to 10 Å for A, B, and C.

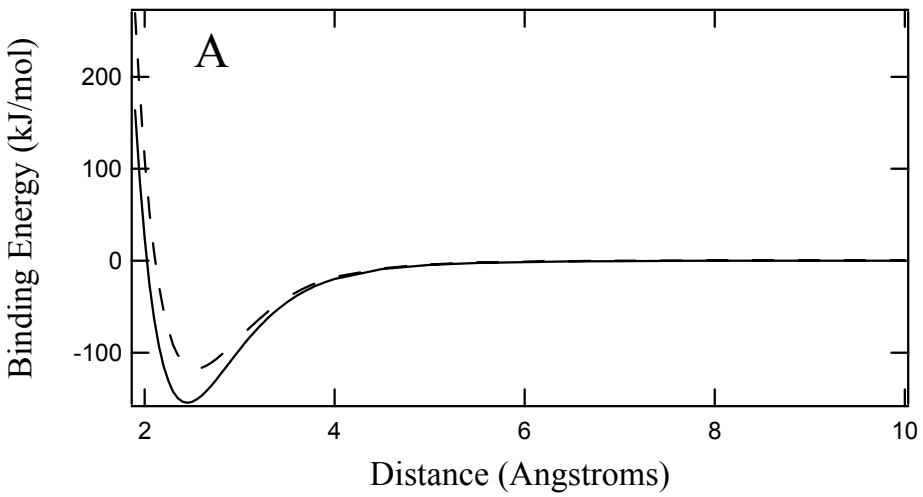
A
Binding Energy (kJ/mol)
200
100
0
-100
2
4
6
8
10
Distance (Angstroms)

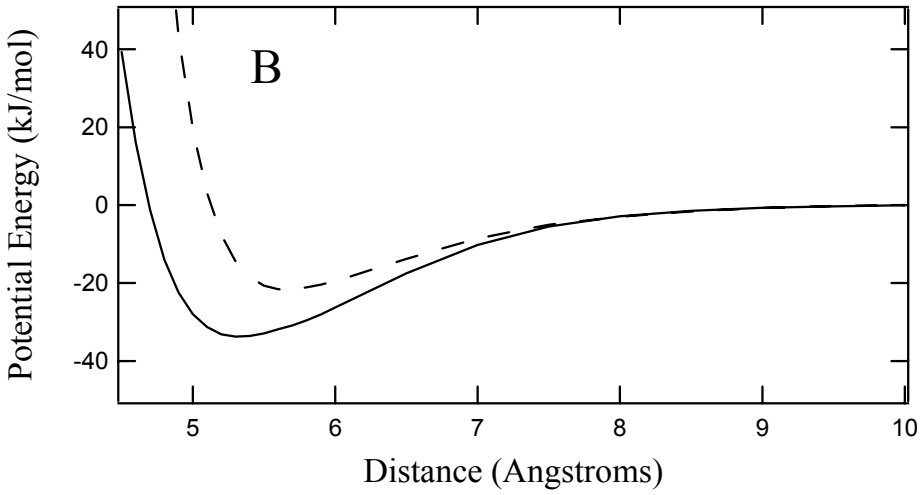
B
Potential Energy (kJ/mol)
40
20
0
-20
-40
5
6
7
8
9
10
Distance (Angstroms)

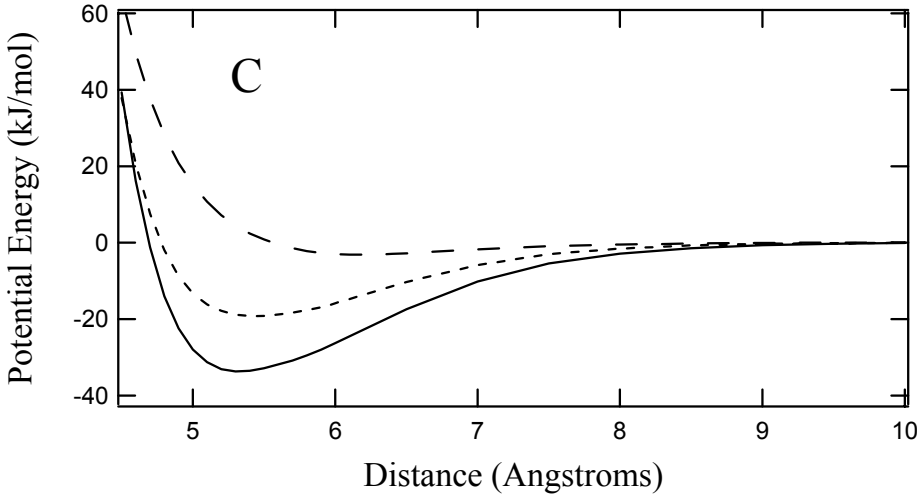
C
Potential Energy (kJ/mol)
60
40
20
0
-20
-40
5
6
7
8
9
10
Distance (Angstroms)

Chapter 6

Indium tin oxide plasma frequency dependence on sheet resistance and surface adlayers determined by reflectance FTIR spectroscopy

Abstract

Variable angle reflectance FTIR spectroscopy was used to investigate the optical properties of indium tin oxide (ITO) and fluorine-doped tin oxide (SFO) thin films in the near-IR spectral region. The reflectance data was used to determine the plasma frequency and the electronic scattering time using the Drude free-electron model the dielectric function of ITO and the two- and three-phase Fresnel equations for reflection. The reflectance, plasma frequency and electronic scattering time of ITO thin films were found to be dependent on the sheet resistance. Surface adlayers were also found to affect the reflectance and the position of the plasma frequency of the ITO thin films. The reflectance and observed plasma frequency for the SFO thin films were lower than any of the ITO films studied.

Introduction

Indium tin oxide (ITO) thin films are widely used as infrared reflectors and transparent electrodes in the visible region of the electromagnetic spectrum.[1-11] These properties allow ITO thin films to be used in a wide range of optical and electronic applications such as heat shielding materials[12,13] and electrochemical sensors.[5,6] The optical properties of ITO thin films are highly sensitive to small variations in their preparation and annealing procedures.[12-16] Therefore the preparation of these films to obtain desired optical properties is still an active area of research. Indium tin oxide thin films, similar to gold[17-24] and other metal oxides[25,26], have been used as a substrate for modification with several different materials such as silanes,[27] amines,[28] carboxylic acids,[29,30] phosphonates, [30,31] thiols, [29,31] zirconium complexes,[3] tin complexes,[2] and

DNA.[5] However, the effects of these adlayers on the properties of ITO depend on a firm understanding of the optical properties of the electrode material. Several different techniques have been used to investigate the properties of ITO such as spectroscopic ellipsometry,[32,33] X-ray photoelectron spectroscopy,[29] fixed angle reflection and transmission techniques,[7,13] diffuse reflectance FTIR spectroscopy[34] and electrochemistry.[3,5,28,35,36] However variable angle reflectance FTIR spectroscopy has not been fully utilized. This technique allows the optical parameters of films with different preparations and annealing protocols to be determined in a non-intrusive manner in two sampling geometries. The reflectance and therefore optical properties of ITO can be determined from monitoring the reflectance with the light impinging directly on the ITO surface (air/ITO/glass substrate) or with the radiation first impinging on the glass substrate and then reflecting off the backside of the ITO surface (air/glass/ITO). These two sampling geometries offer flexibility in monitoring the affects on the optical properties of ITO thin films during annealing protocols or surface modification with adlayers (surface binding events).

The optical properties of ITO are a direct consequence of the position of the plasma frequency and the magnitude of the electronic scattering time as defined in the Drude free-electron model.[37,38] The plasma frequency for ITO occurs in the near-IR region thus causing this material to be reflective in the mid-IR region and transparent in the visible region. Therefore the position of the plasma frequency is critical in determining the optical properties of the material. In this study, the reflectance properties in the near-IR region were studied for ITO electrodes with varying sheet resistances. The Drude free-electron model was used to model the dielectric function of the ITO films to obtain values for the plasma

frequency and electronic scattering times of the ITO thin films. The two- and three-phase Fresnel equations for reflection were then used to compare calculated and experimental reflectance infrared data. The reflectance of the ITO electrodes was studied with varying angles of incidence using p-polarized radiation. The effect of surface adlayers of 12-phosphonododecanoic acid and 1-hexadecanethiol on the optical properties (reflectivity and plasma frequency) of ITO thin films were also investigated. This surface adlayer effect is similar to surface plasmon resonance (SPR) that has typically been done on metal substrates;[39] however, this work proposes that SPR can also be done on metal oxide surfaces using reflectance FTIR spectroscopy in the near-IR region. Fluorine-doped tin oxide (SFO) thin films were also studied to aid in the understanding of how sheet resistance affects the optical properties of metal oxides, since this material is also a conducting metal oxide, but generally has a higher sheet resistance than ITO thin films.[40-42]

Materials and Methods

ITO and SFO Electrodes. Indium tin oxide (ITO) electrodes were obtained from Delta Technologies, Limited. The ITO electrodes were composed of 90% indium oxide and 10% tin oxide, had a nominal thickness of 1,500 Å and a sheet resistance of 7-14 Ω/□. The substrate for the ITO electrodes was polished float (soda-lime) glass. The fluorine doped tin oxide (SFO) thin films deposited on glass substrates were obtained from PPG Industries, Inc. and had a sheet resistance of ~55 Ω/□, while the gold electrodes were obtained from Evaporated Metal Films, Inc. The ITO and SFO electrodes were cleaned by 20 minutes of UV/O_3 (UVO-cleaner (UVO-60), model number 42, Jelight Company, Inc) to yield a clean

hydrophilic surface (as determined from contact angle measurements) (NRL C.A. Goniometer (Rame-Hart, Inc.), model 100-00). The sheet resistances of these electrodes were measured with a 4-point probe consisting of a Signatone D27M probe station, a Keithley 224 programmable current source and a Hewlett Packard 3456A digital voltmeter.

Reflectance FTIR Spectroscopy. The variable angle reflectance FTIR spectra were recorded using a Spectra-Tech variable angle reflectance attachment (Model 500) or the Bruker AutoSeagull variable angle reflectance attachment in a Bruker IFS v/s spectrometer. The angle of incidence ranged from 40 - 80 degrees relative to the surface normal. An infrared polarizer was used to obtain p-polarized light. A ratio of the single beam spectra of ITO or SFO electrodes to a single beam spectrum of a planar gold electrode was performed to obtain the reflectance spectra of ITO or SFO. A tungsten source, quartz beamsplitter and a liquid nitrogen cooled InSb detector was used in the spectral range 3000-13,000 cm^{-1}. All IR spectra were the result of the average of 512 scans at a resolution of 8 cm^{-1} and were recorded at room temperature under vacuum.

Theoretical Models

Drude Free-Electron Model. The Drude free-electron model describes the dielectric function ($\varepsilon(\omega)$) of a material by the plasma frequency and electronic scattering time as shown in Eqn. 1:[38]

$$\varepsilon(\omega) = \varepsilon_\infty - \omega_p^2 \frac{1}{\omega^2 + \frac{i\omega}{\tau}} \qquad (1)$$

where ε_∞ is the high-frequency dielectric constant, ω_p is the plasma frequency, ω is the frequency and τ is the electronic scattering time. The plasma frequency is defined in Eqn. 2:[38]

$$\omega_p^2 = \frac{ne^2}{m\varepsilon_o} \qquad (2)$$

where n is the free charge carrier concentration and m is the free electron mass. Eqn.3 relates the dielectric function to the complex refractive index of the material:[38]

$$\varepsilon(\omega)^{\frac{1}{2}} = N(\omega) = n(\omega) + ik(\omega) \qquad (3)$$

where N is the complex refractive index, n is the real, dispersive component and k is the imaginary, absorptive component of the refractive index. This complex refractive index along with angle of incidence is used by the Fresnel equations of reflection for a two-phase (single dielectric interface) or three-phase system to model the reflectance of the material for p-polarized radiation.

Two-Phase Fresnel Equations for Reflectance. The two-phase Fresnel equations model the reflectance for a single dielectric interface. For instance, these equations model the air/ITO interface where the refractive of index of ITO is complex (n and k components determined from the Drude free-electron model) and the refractive index of air (vacuum) is not complex (only a real component) and taken to be 1 (n=1, k=0). The ratios of the amplitudes of the reflected and incident light for p-polarized radiation for a single dielectric interface is shown in Eqns. 4-5:[37]

$$r_p = \frac{-N\cos\theta + \cos\varphi}{N\cos\theta + \cos\varphi} \qquad (4)$$

where

$$\cos \varphi = \left(1 - \frac{\sin^2 \theta}{N^2}\right)^{\frac{1}{2}} \qquad (5)$$

In these equations, r is the amplitude of the reflected light (relative to incident light amplitude), p represent p-polarization, N is the complex refractive index of the material, θ is the angle of incidence relative to the surface normal and ϕ is the complex angle between the refracted light to the surface normal. Then the power reflectivity for p-polarization is shown in Eqn. 6:[37]

$$R_p = \left| r_p \right|^2 \qquad (6)$$

where R_p is the power reflectivity for p-polarization.

Three-Phase Fresnel Equations for Reflectance. The three-phase Fresnel equations of reflectance models a system composed of two dielectric interfaces. The system used in this analysis is air/ITO/glass, where the glass is the substrate on which the ITO thin film is deposited. The refractive index of air is again taken to only having a real component (n=1, k=0) and the complex dielectric function of ITO is determined from the Drude free-electron model, while literature values for the complex refractive index in the near-IR region for silicon dioxide (glass)[43] were used. The three-phase model takes into account the decay

in the magnitude of the electric field through the ITO and the refraction of the light through this thin film before the radiation impinges on the ITO/glass interface. The general form of the ratio of the reflected and incident radiation for a three-phase model of the Fresnel equation is shown in Eqn. 7:[44]

$$r_p = \frac{r_{p12} + r_{p23}e^{2i\beta}}{1 + r_{p12}r_{p23}e^{2i\beta}} \qquad (7)$$

where r is the amplitude of reflected radiation, p refers to p-polarization and the numerical subscripts (1, 2, 3) refer to the three phases (air, ITO, glass) respectively. β is defined in Eqn. 8:[44]

$$\beta = 2\pi\left(\frac{h}{\lambda}\right)N_j \cos\Theta_j \qquad (8)$$

where h is the thickness of layer j (taken to be 170 nm for ITO), λ is the wavelength of radiation, N is the complex index of refraction (Eqn. 3) of layer j and Θ is the angle relative to the surface normal in layer j. The general form of the two-phase Fresnel equations needed to determine r_{p12} and r_{p23} is defined in Eqn. 9:[44]

$$r_{pjk} = \frac{N_j \cos\Theta_j - N_k \cos\Theta_k}{N_j \cos\Theta_j + N_k \cos\Theta_k} \qquad (9)$$

where the subscripts j and k refer to the jth and k^{th} phase of the model. Θ_k can be determined from Eqn.10:[44]

$$\cos\Theta_k = \left(1 - \frac{\sin^2\Theta_j}{N_k^2}\right)^{1/2} \qquad (10)$$

where Θ_k is the angle in phase k relative to the surface normal. The power reflectivity or calculated reflectance, R_p, for p-polarized radiation is defined in Eqn. 6.

Results and Discussion

Figure 1 shows the experimental variable angle reflectance FTIR spectra of a thin film of an indium tin oxide (ITO) on a glass substrate in the near-IR region with a sheet resistance of 13.8 Ω/□. The measured reflectance was referenced to a gold surface. The angles of incidence were varied between 40 - 80 degrees relative to the surface normal using p-polarized IR radiation. Overall the reflectance spectra of ITO shows relatively high reflectance below ~7500 cm^{-1} and then the reflectance drops substantially. This sharp change in the reflectivity of the ITO is due to the plasma frequency (as defined in the Drude free-electron model) of the material. The plasma frequency is characterized by a sharp decrease in the measured reflectance of a material. Therefore, ITO is reflective below the plasma frequency and transparent at higher wavenumbers. However, the reflectance and transmittance of the material is dependent on the angle at which the radiation impinges on the material as shown in Figure 1. The observed value of the plasma frequency shifted to lower energy as the incident angle decreased. The position of the plasma frequency did not change with varying angles of incidence for s-polarized radiation as expected by the Fresnel equations for reflection (data not shown). Figure 1B shows the angle dependence of the reflection of an ITO thin film (13.8 Ω/□) for p-polarized radiation at 9164 cm^{-1}. This plot shows a minimum in the experimental reflectance of ITO, as expected from the Fresnel equations of reflection (data not shown), at ~ 55 degrees. These same trends in ITO

reflectance and plasma frequency were found on ITO thin films deposited on fused quartz substrates (see supplementary information (Appendix 3)).

Figures 2A, 2B and 2C show a comparison of the experimental reflectance FTIR and calculated power reflectivity for p-polarized IR radiation of an ITO thin film deposited on a glass (soda-lime) substrate for incident angles of 40, 60 and 80 degrees with a sheet resistance of 13.8 Ω/□. The power reflectivity of this sample was calculated from the Fresnel equations for reflection at a single dielectric interface (two-phase model (air/ITO)) (B) or the three-phase (air/ITO/glass) (C) Fresnel equations of reflection using the Drude free-electron model to determine the dielectric function of the ITO. The calculated reflectance for both the two- and three-phase Fresnel equations for reflection accurately models the observed trends in reflectance and the position of the plasma frequency with varying angles of incidence determined experimentally.

Figure 3A and 3B shows the experimental reflectance FTIR spectra in the region of the plasma frequency for ITO thin films of three different resistances (7 – 14 Ω/□) recorded at an incident angle of 60 degrees with p-polarized radiation. Figure 3A also shows the calculated reflectance spectra obtained from the Drude free-electron model and the Fresnel equations for a single dielectric interface (two-phase, air/ITO), while the three-phase (air/ITO/glass) was used in to obtain the calculated reflectance in Figure 3B. Figure 3A and 3B illustrates that the observed plasma frequency of ITO was a function of sheet resistance. A red shift in the observed plasma frequency was observed as the sheet resistance of the metal oxide electrode decreased. The fitted parameters for the Drude free-electron model for these ITO electrodes are listed in Table 1A and 1B using a constant value of 3.8 for the high

frequency dielectric constant using the two- and three-phase Fresnel equations for reflection, respectively. The values in Table 1A and 1B show that both the plasma frequency and the electronic scattering time decreased as the sheet resistance of the ITO electrode increased. The value of the plasma frequency (ω_p) is dependent on the charge carrier density (n) and the effective electron mass (m) of the ITO thin film as defined by the Drude free-electron model defined in Equation 2. The value of the plasma frequency affects the observed sharp decrease in reflectance, while the electronic scattering time affects the curvature of the reflectance spectrum near the observed plasma frequency. The two parameters of plasma frequency, the charge carrier density and effective electron mass are coupled and cannot be individually determined in these experiments. The Drude free-electron model and the Fresnel equations of reflection accurately model the region of the reflectance spectra near the plasma frequency. However, the two-phase model calculates an overall higher absolute reflectance than experimentally observed at wavenumbers lower in energy than the plasma frequency. The three-phase Fresnel equations of reflection more accurately fit the experimental reflectance of the different ITO samples in the entire near-IR region studied. Therefore, the shifts in the observed plasma frequency and curvature of the experimental reflectance spectra of ITO thin films with varying sheet resistances were successfully calculated using these theoretical models. The two- or three-phase Fresnel equations of reflection calculated plasma frequencies that differed by ~100 - 250 cm^{-1} different while the electronic scattering times were ~ 5 – 6 ($x10^{-16}$) s higher using the three-phase model compared to the two-phase model.

The observed trends in the reflectance and plasma frequency on the sheet resistance of ITO thin films complement our earlier reflectance FTIR data in the mid-IR. [45] In this work, the following relationship between the plasma frequency (ω_p) and sheet resistance (R) was suggested (Eqn.11): [45]

$$\omega_p = \left(\frac{1}{R\, t\, \varepsilon_o\, \tau}\right)^{\frac{1}{2}} \qquad (12)$$

where t is the thickness of the ITO film. However, only trends in the mid-IR reflectance suggestive of the onset of the plasma frequency were used to support this relationship. In the current work, the relationship between the plasma frequency and the sheet resistance and the electronic scattering time are confirmed. Figures 4A and 4B show the linear dependence of the plasma frequency with the inverse square root of the sheet resistance (R) and electronic scattering time (τ), respectively using the optical parameters from fitting the experimental reflectance FTIR data with the Drude free-electron model and the three-phase Fresnel equations of reflection (Table 1B).

Figure 5 shows the experimental variable angle reflectance FTIR spectra of a thin film of ITO (13.8 Ω/□) deposited on a glass substrate with p-polarized radiation impinging on the backside of the ITO thin film (air/glass/ITO sampling geometry) in the near-IR. This sampling geometry in contrast to air/ITO/glass sampling geometry used previously illustrates that the plasma frequency of ITO can also be monitored in an alternative geometry that would be beneficial when studying surface events (binding) on the ITO thin film from solution. This figure shows the angular dependence of the reflectance of the sample and the position of the observed plasma frequency for incident angles of 40 - 80 degrees relative to

the surface normal. The plasma frequency shifts to lower energy as the incident angle decreases and the reflectance drops substantially at wavenumbers higher than the plasma frequency. However, the observed plasma frequency transition of the ITO is not as sharp in this sampling geometry (air/glass/ITO) as the air/ITO/glass geometry and the observed reflectance is lower throughout the spectral region. The reflectance reaches a maximum at ~4000 cm^{-1} where the glass substrate becomes nearly transparent to the radiation and stays transparent throughout the rest of the near-IR region of interest. Therefore, this sampling geometry (air/glass/ITO) is a second geometry that can be used in monitoring the optical properties (plasma frequency and reflectivity) of ITO.

Figure 6A and 6B illustrates the effect of a surface adlayer on the reflectivity and plasma frequency of ITO in the near-IR region at an incident angle of 60 degrees with p-polarized radiation. The experimental reflectance FTIR spectra in Figure 6A were recorded in an air/adlayer/ITO/glass sampling geometry while a air/glass/ITO/adlayer sampling geometry was used to measure the reflectance FTIR spectra in Figure 6B. An adlayer of 12-phosphonododecanoic acid or 1-hexadecanethiol on ITO[31] were used to illustrate the effect of adlayer formation on the optical properties of ITO. In both of the sampling geometries (Figure 6A and 6B), the reflectance and observed plasma frequency of ITO decreases due to the presence of either of these adlayers relative to bare ITO. Therefore, both the shift in the plasma frequency and the change in reflectivity in the near-IR of ITO due to adlayer formation can be utilized to observe binding events such as the formation of an adlayer on ITO.

Other metal oxide thin films such as fluorine-doped tin oxide (SFO) have similar optical properties as ITO in the near-IR. Figures 7A and 7B show the observed reflectance FTIR spectra of a SFO deposited on a glass substrate recorded in the same two sampling geometries utilized with the ITO thin films with p-polarized light and incident angles ranging from 40 – 80 degrees relative to the surface normal. Figure 6A and 6B were recorded in the air/SFO or air/glass/SFO sampling geometry, respectively. The overall reflectivity of this thin film and the plasma frequency was lower than the ITO thin films studied for both sampling geometries; however, the overall trends in the reflectance were similar to those observed for ITO thin films. For instance, the plasma frequency red shifts and the reflectance of SFO thin films decreases with decreasing angle near the plasma frequency, while the reflectance decreases substantially after the plasma frequency relative to the reflectance prior to the onset of the plasma frequency. This decrease in reflectance was partly due to the higher sheet resistance (55.6 Ω/□) of SFO than the ITO films studied, while the change in the observed plasma frequency is due to differences in the charge carrier density and effective electron mass of SFO compared to ITO. The plasma frequency transition in Figure 7B is not as sharp as the ITO transition in the same backside sampling geometry. However, the plasma frequency can be detected and monitored in this geometry. Similar to ITO, Figure 7A and 7B demonstrates that two sampling geometries are possible for monitoring the plasma frequency and reflectivity (optical properties) of SFO thin films.

Conclusion

The plasma frequency of indium tin oxide (ITO) thin films were observed experimentally by variable angle reflectance FTIR spectroscopy and were found to decrease as the sheet resistance of the ITO thin films increased. The electronic scattering time and reflectance of these films also decreased with increasing sheet resistance. These results confirmed previous work[45] concerning the dependence of the reflectance and plasma frequency on the sheet resistance of the ITO thin films. The Drude free-electron model and the two- or three-phase Fresnel equations of reflection were used to fit the experimental data to obtain values for the plasma frequency and electronic scattering time for the ITO thin films. These models accurately fit the area near the plasma frequency but the two-phase model overestimated the absolute reflectance of the ITO thin films at lower wavenumbers than the plasma frequency while the three-phase Fresnel equations of reflection fit the experimental data more closely throughout the entire near-IR region investigated. The calculated values of the plasma frequency and electronic scattering time differed by ~100 – 250 cm^{-1} and 5 – 6 ($x10^{-16}$) s, respectively between the two- and three-phase Fresnel equations of reflection. As expected from the Fresnel equations of reflection, the observed plasma frequency of ITO and reflectance just prior to the plasma frequency decreased with decreasing angles of incidence for p-polarized radiation. Surface adlayers of 12-phosphonododecanoic acid or 1-hexadecanethiol on the ITO thin films were shown to decrease the reflectivity and the observed plasma frequency of ITO using the air/adlayer/ITO/glass or air/glass/ITO/adlayer sampling geometries in the near-IR region.

Fluorine-doped tin oxide (SFO) thin films were found to be less reflective and had a lower observed plasma frequency than the ITO thin films studied. The optical properties of these metal oxide thin films determined from reflectance FTIR spectroscopy offer a direct probe, specifically the plasma frequency and reflectivity, to monitor surface events such as adlayer formation (binding of molecules to the surface) or chemical modification of these metal oxide films. These properties could be monitored *in situ* to yield kinetic information on the binding of molecules to surface bound material or directly to these thin film metal oxide surfaces. The multiplex advantage of FTIR spectroscopy allows the simultaneous determination of the reflectance over a broad spectral range at a fixed or variable angle of incidence instead of monitoring only the reflectance at a single wavelength, while incrementally varying the incident angle typically done with surface plasmon resonance (SPR) protocols using metal surfaces.[39] The sensitivity of ITO thin films is such that surface adlayer formation on ITO can easily be observed in the change in reflectivity and the plasma frequency of ITO, while the two different sampling geometries offer flexibility in monitoring the observed plasma frequency and reflectivity of these metal oxide thin films during surface modifications or annealing procedures.

Acknowledgements

This work was done in collaboration with Stefan Franzen (NCSU) and was the subject of a publication, Brewer, S. H.; Franzen, S. *Journal of Physical Chemistry B* **2002**, 106, 12986-12992. Scott Brewer was supported by the NIH Biotechnology Training Grant T32-GM08776.

References

(1) Tamada, M.; Koshikawa, H.; Hosoi, F.; Suwa, T. *Thin Solid Films* **1998**, *315*, 40-43.

(2) Purvis, K.; Lu, G.; Schwartz, J.; Bernasek, S. *The Journal of the American Chemical Society* **2000**, *122*, 1808-1809.

(3) VanderKam, S.; Gawalt, E.; Schwartz, J.; Bocarsly, A. *Langmuir* **1999**, *15*, 6598-6600.

(4) Oh, S.; Han, S. *Langmuir* **2000**, *16*, 6777-6779.

(5) Armistead, P.; Thorp, H. *Analytical Chemistry* **2000**, *72*, 3764-3770.

(6) Armistead, P.; Thorp, H. *Analytical Chemistry* **2001**, *73*, 558-564.

(7) Hamberg, I.; Granqvist, C. G. *Journal of Applied Physics* **1986**, *60*, R123-R159.

(8) Ambrosini, A.; Duarte, A.; Poeppelmeier, K. R.; Lane, M.; Kannewurf, C. R.; Mason, T. O. *Journal of Solid State Chemistry* **2000**, *153*, 41-47.

(9) Kim, D.; Kim, S. *Thin Solid Films* **2002**, *408*, 218-222.

(10) Losurdo, M.; Barreca, D.; Capezzuto, P.; Bruno, G.; Tondello, E. *Surface and Coatings Technology* **2002**, *151-152*, 2-8.

(11) Mryasov, O.; Freeman, A. *Physical Review B* **2001**, *64*, 233111-233113.

(12) Hamberg, I.; Hjortsberg, A.; Granqvist, C. *Applied Physics Letters* **1982**, *40*, 362-364.

(13) Hjortsberg, A.; Hamberg, I.; Granqvist, C. *Thin Solid Films* **1982**, *90*, 323-326.

(14) Bregman, J.; Shapira, Y.; Aharoni, H. *Journal of Applied Physics* **1990**, *67*, 3750-3753.

(15) Fan, J.; Bachner, F.; Foley, G. *Applied Physics Letters* **1977**, *31*, 773-775.

(16) Shin, J.; Shin, S.; Park, J.; Kim, H. *Journal of Applied Physics* **2001**, *89*, 5199-5203.

(17) Bain, C.; Biebuyck, H.; Whitesides, G. *Langmuir* **1989**, *5*, 723-727.

(18) Karyakin, A.; Presnova, G.; Rubtsova, M.; Egorov, A. *Analytical Chemistry* **2000**, *72*, 3805-3811.

(19) Kitano, H.; Taira, Y.; Yamamoto, H. *Analytical Chemistry* **2000**, *72*, 2976-2980.

(20) Kittredge, K.; Fox, M.; Whitesell, J. *The Jounal of Physical Chemistry B* **2001**, *ASAP article*.

(21) Nakashima, N. *Langmuir* **1999**, *15*, 3823-3830.

(22) Naud, C.; Calas, P.; Commeyras, A. *Langmuir* **2001**, *17*, 4851-4857.

(23) Ringsdorf, H. *Macromolecules* **1997**, *30*, 5913-5919.

(24) Terril, R.; Tanzer, T.; Bohn, P. *Langmuir* **1998**, *14*, 845-854.

(25) Allara, D.; Nuzzo, R. *Langmuir* **1985**, *1*, 52-66.

(26) Allara, D.; Nuzzo, R. *Langmuir* **1985**, *1*, 45-52.

(27) Markovich, I.; Mandler, D. *Journal of Electroanalytical Chemistry* **2001**, *500*, 453-460.

(28) Oh, S.; Yun, Y.; Kim, D.; Han, S. *Langmuir* **1999**, *15*, 4690-4692.

(29) Yan, C.; Zharnikov, M.; Golzhauser, A.; Grunze, M. *Langmuir* **2000**, *16*, 6208-6215.

(30) Gardner, T.; Frisbie, C.; Wrighton, M. *The Journal of the American Chemical Society* **1995**, *117*, 6927-6933.

(31) Brewer, S.; Brown, D.; Franzen, S. *Langmuir* **2002**, 18, 6857-6865.

(32) Synowicki, R. *Thin Solid Films* **1998**, *313*, 394-397.

(33) Gerfin, T.; Gratzel, M. *Journal of Applied Physics* **1996**, *79*, 1722-1729.

(34) Lee, D.; Vuong, K.; Sr., R. C.; Wang, X. W. *Materials Letters* **1996**, *28*, 179-182.

(35) Zotti, G.; Schiavon, G.; Zecchin, S.; Berlin, A.; Pagani, G. *Langmuir* **1998**, *14*, 1728-1733.

(36) Li, L.; Wang, R.; Fitzsimmons, M.; Li, D. *Journal of Physical Chemistry B* **2000**, *104*, 11195-11201.

(37) Fowles, G. *Introduction to Modern Optics*; Second ed.; Dover Publications, Inc.: New York, 1989.

(38) Wooten, F. *Optical Properties of Solids*; Academic Press, Inc.: San Diego, 1972.

(39) Brockman, J.; Nelson, B.; Corn, R. *Annual Review of Physical Chemistry* **2000**, *51*, 41-63.

(40) Stjerna, B.; Olsson, E.; Granqvist, C. *Journal of Applied Physics* **1994**, *76*, 3797-3817.

(41) Ray, S.; Karanjai, M.; Dasgupta, D. *Thin Solid Films* **1997**, *307*, 221-227.

(42) Mwamburi, M.; Wackelgard, E.; Roos, A. *Thin Solid Films* **2000**, *374*, 1-9.

(43) Philipp, H. *Handbook of Optical Constants of Solids*; Palik, E., Ed.; Academic Press: San Diego, 1985, pp 749-763.

(44) Hansen, W. *Journal of the Optical Society of America* **1968**, *58*, 380-390.

(45) Brewer, S. H.; Franzen, S. *Journal of Alloys and Compounds* **2002**, *338*, 73-79.

Tables

Table 1. The electronic scattering time and plasma frequency of three different ITO electrodes with different sheet resistances as determined from fitting the experimental reflectance data using the Drude free-electron model with a constant value of 3.8 for the high frequency dielectric value to determine the dielectric function of the ITO thin film and the two-phase (air/ITO) (A) or the three-phase (air/ITO/glass) (B) Fresnel equations for reflection.

A.

Sheet Resistance ($\Omega/\square$)	Electronic Scattering Time (τ) (10^{-15} s)	Plasma Frequency (ω_p) (cm^{-1})
7.6	6.0	17,200
9.7	4.8	15,800
13.8	4.0	14,650

B.

Sheet Resistance ($\Omega/\square$)	Electronic Scattering Time (τ) (10^{-15} s)	Plasma Frequency (ω_p) (cm^{-1})
7.6	7.0	17,100
9.7	5.6	15,900
13.8	4.8	14,900

Figures

A.

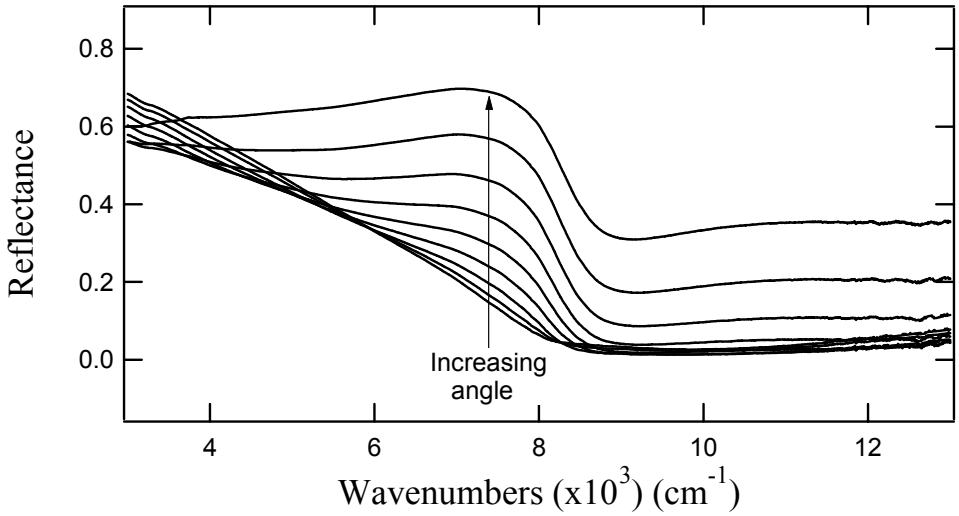

B.

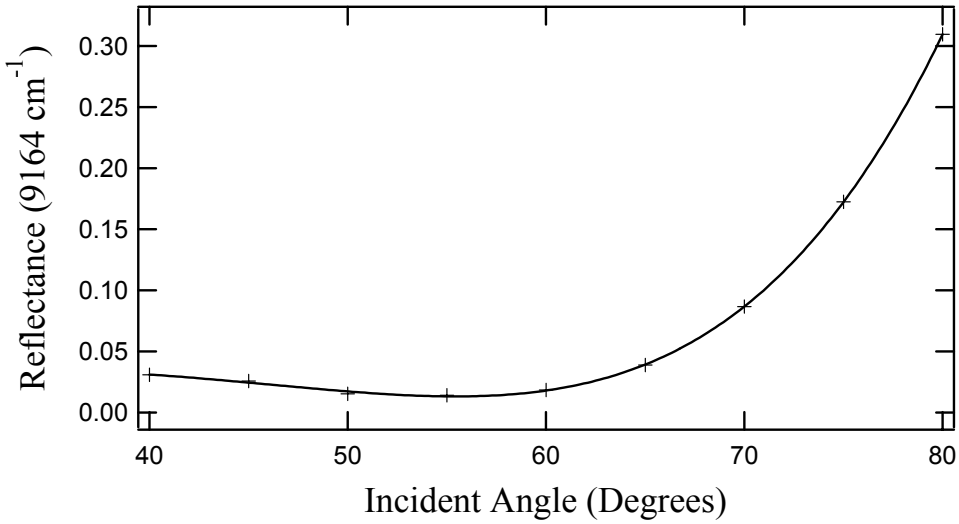

Figure 1. A. Experimental variable angle reflectance FTIR spectra of a thin film of ITO (13.8 ohms/square) on a glass substrate relative to a gold surface in the near-IR region for incident angles ranging from 40 to 80 degrees with p-polarized radiation (air/ITO sampling geometry). B. Plot of the measured reflectance at 9164 cm^{-1} of ITO (13.8 Ω/□) as a function of incident angle for p-polarized radiation.

Figure 2. Experimental (A) and calculated (B, C) reflectance spectra for incident angles of 40 (short dashed), 60 (long dashed), and 80 (solid) degrees for ITO on a glass substrate with a sheet resistance of 13.8 Ω/□ recorded or calculated with p-polarized radiation in the near-IR region. The calculated reflectance spectra of ITO used either the two-phase (air/ITO) (B) or three-phase (air/ITO/glass) (C) Fresnel equations of reflection.

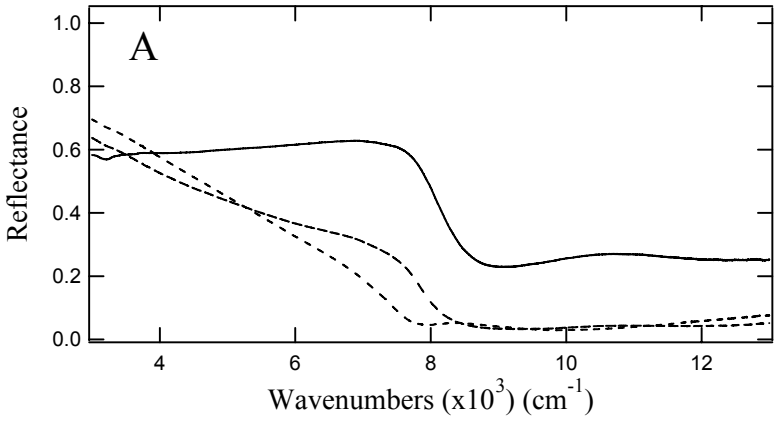
A
Reflectance
1.0
0.8
0.6
0.4
0.2
0.0
4
6
8
10
12
Wavenumbers (x10^3) (cm^-1)

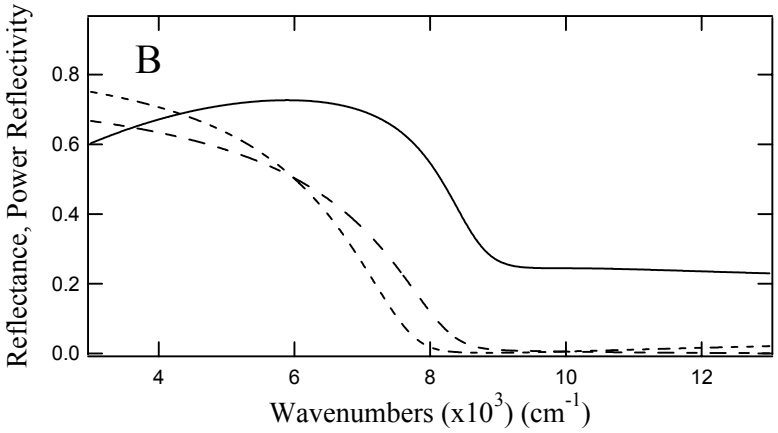
B
Reflectance, Power Reflectivity
0.8
0.6
0.4
0.2
0.0
4
6
8
10
12
Wavenumbers (x10^3) (cm^-1)

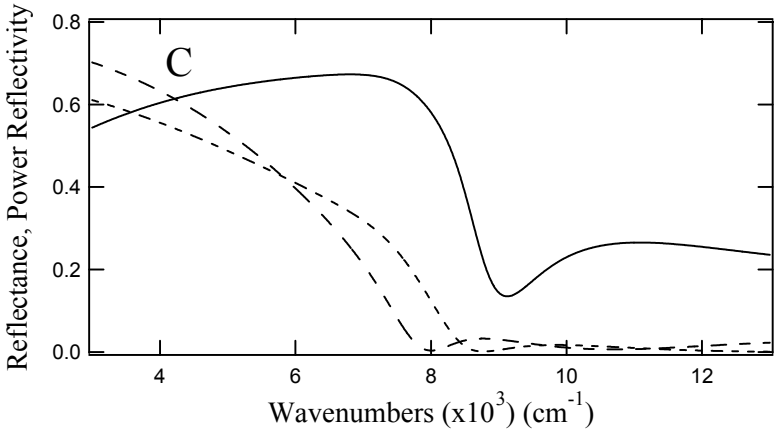
C
Reflectance, Power Reflectivity
0.8
0.6
0.4
0.2
0.0
4
6
8
10
12
Wavenumbers (x10^3) (cm^-1)

A.

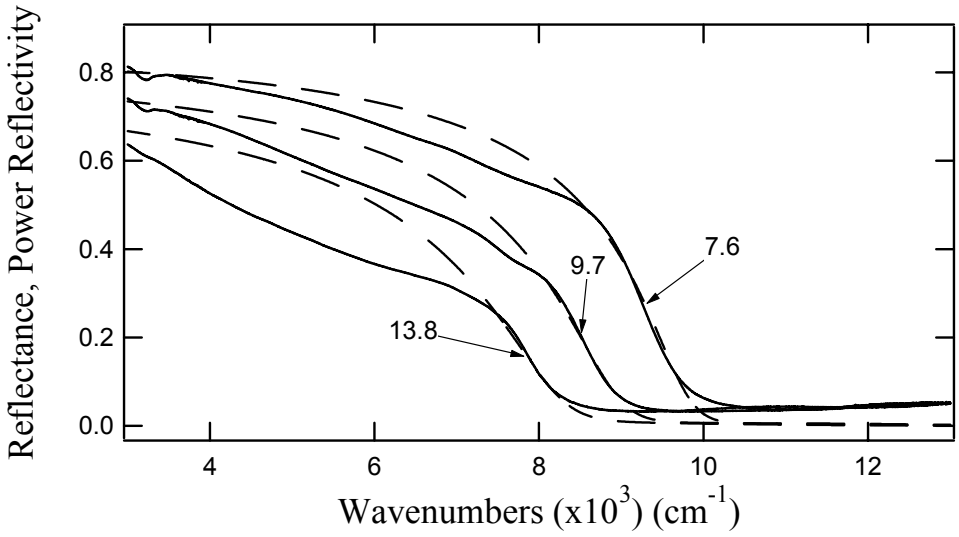

B.

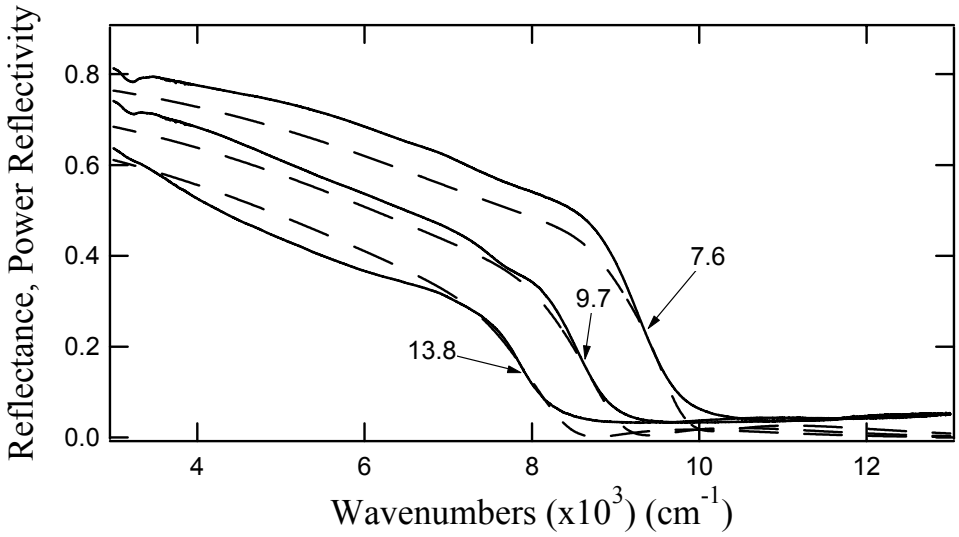

Figure 3. Experimental (solid) reflectance FTIR and calculated (dashed) power reflectivity spectra of three ITO electrodes with sheet resistances of 7.6, 9.7, and 13.8 Ω/□ for p-polarized radiation in the near-IR region using either the two-phase (air/ITO) (A) or the three-phase (air/ITO/glass) (B) Fresnel equations of reflection.

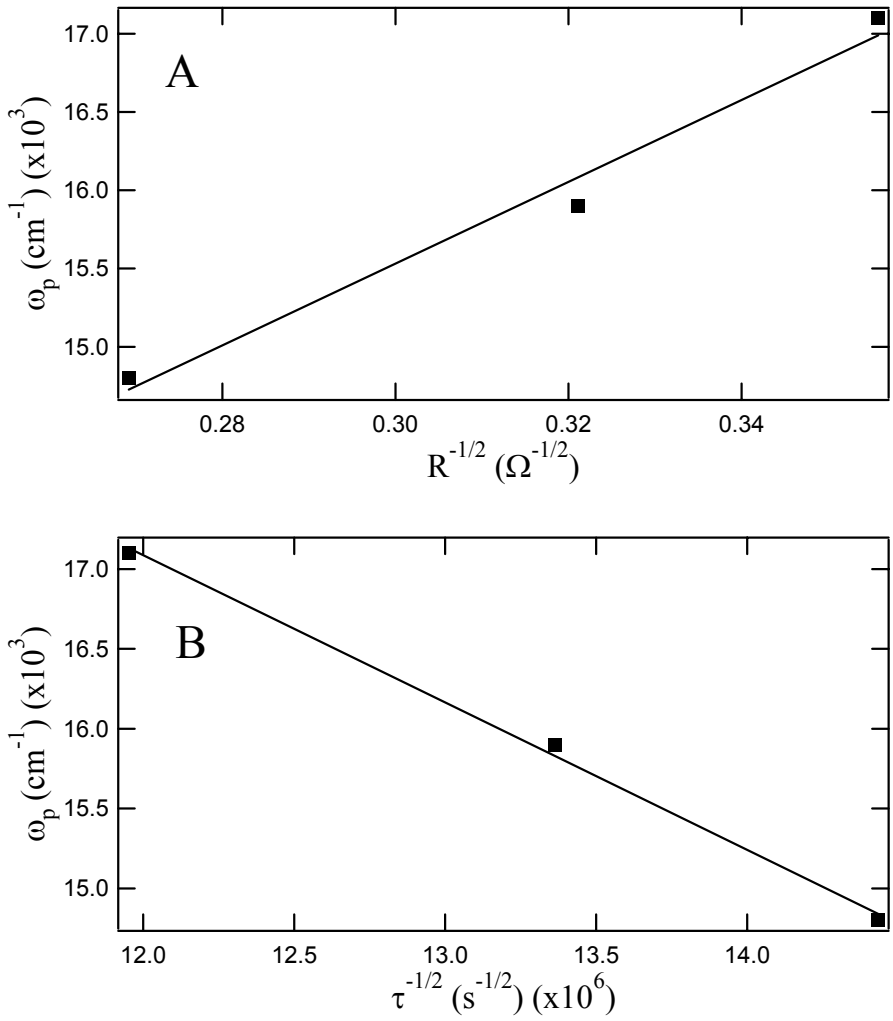

Figure 4. Plot of the plasma frequency (ω_p) dependence on the inverse square root of the sheet resistance (R) (A) and electronic scattering time (τ) (B) of ITO.

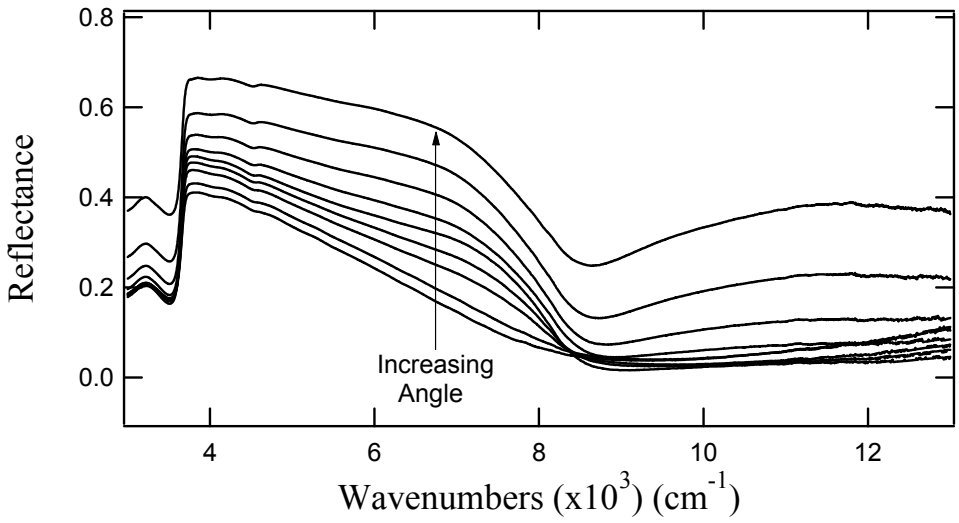

Figure 5. Experimental reflectance FTIR spectra of a thin film of ITO (13.8 Ω/□) on a glass substrate recorded in an air/glass/ITO sampling geometry for incident angles of 40 to 80 degrees to the surface normal for p-polarized radiation in the near-IR region.

Figure 6. Experimental reflectance FTIR spectra of bare ITO (solid), an adlayer of 12-phosphonododecanoic acid on ITO (short dashed), and an adlayer of 1-hexadecanethiol on ITO (long dashed). The spectra were recorded at an incident angle of 60 degrees with p-polarized radiation. The sampling geometry was either air/adlayer/ITO/glass (A) or air/glass/ITO/adlayer (B).

A.

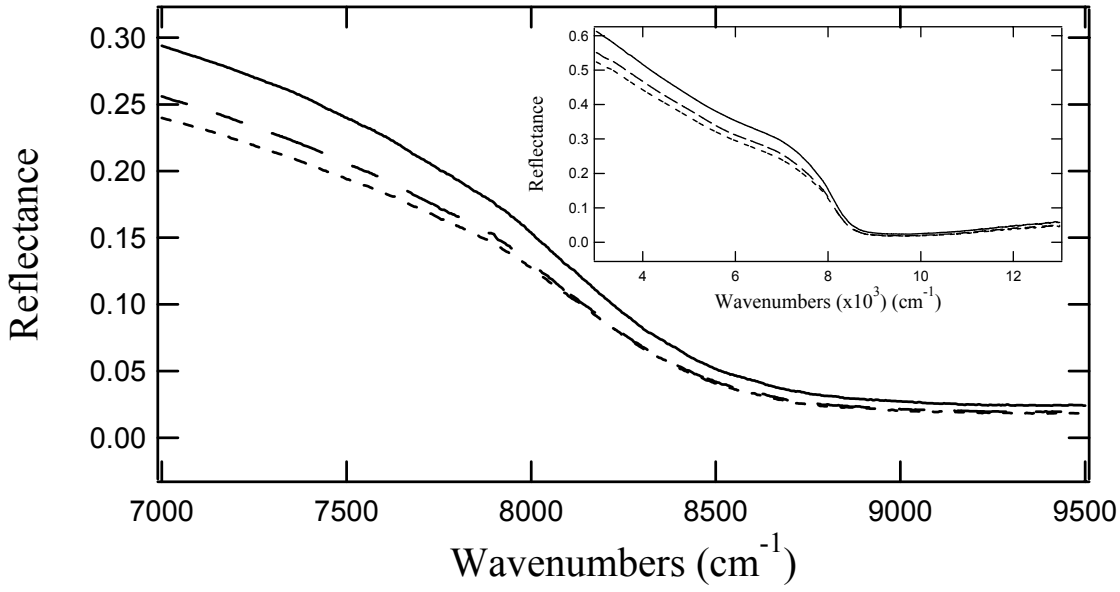
Reflectance
0.30
0.25
0.20
0.15
0.10
0.05
0.00
7000
7500
8000
8500
9000
9500
Wavenumbers (cm-1)
Reflectance
0.6
0.5
0.4
0.3
0.2
0.1
0.0
4
6
8
10
12
Wavenumbers (x103) (cm-1)

B.

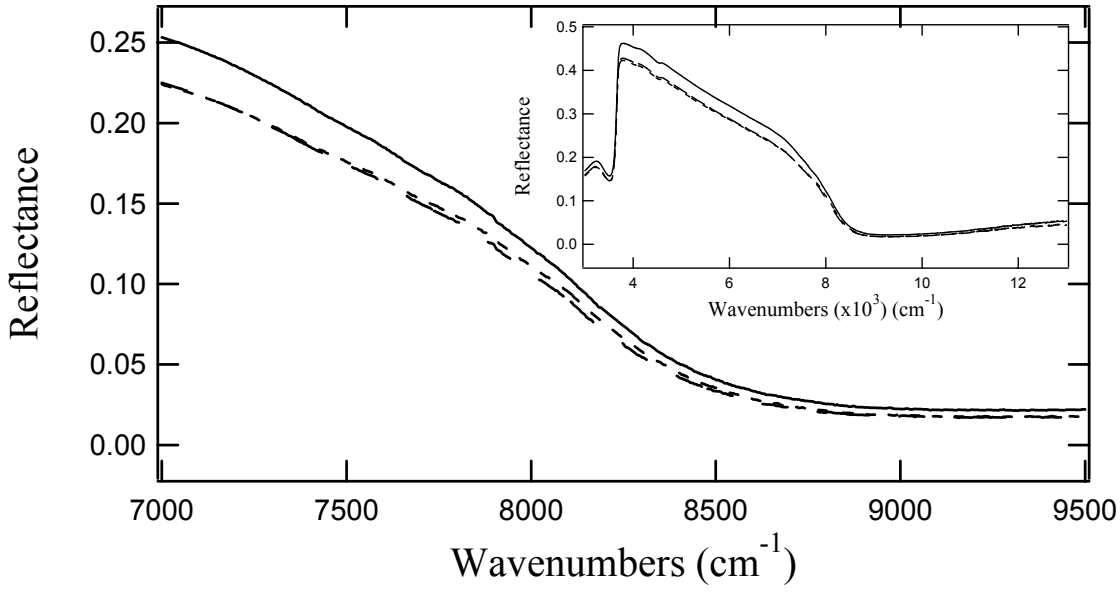
Reflectance
0.25
0.20
0.15
0.10
0.05
0.00
7000
7500
8000
8500
9000
9500
Wavenumbers (cm-1)
Reflectance
0.5
0.4
0.3
0.2
0.1
0.0
4
6
8
10
12
Wavenumbers (x103) (cm-1)

A.

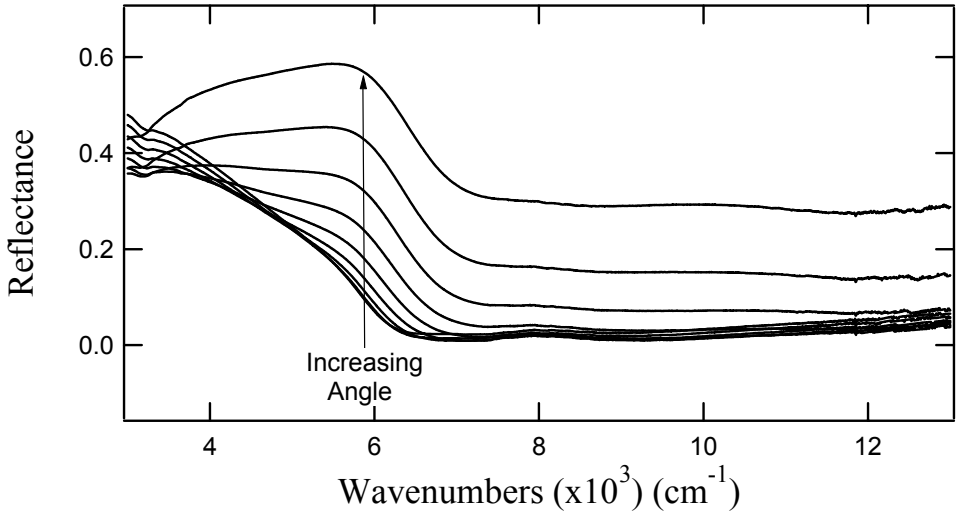

B.

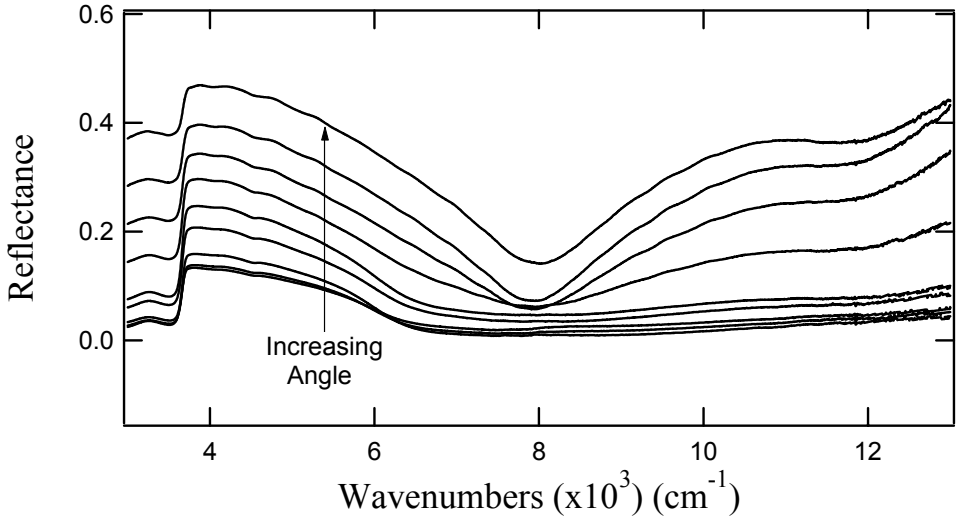

Figure 7. Experimental reflectance FTIR spectra for incident angles of 40 to 80 degrees for SFO on a glass substrate with a sheet resistance of 55.6 Ω/□ recorded with p-polarized radiation in the near-IR region with either the air/SFO (A) or air/glass/SFO (B) sampling geometry.

Chapter 7

Calculation of the Electronic and Optical Properties of Indium Tin Oxide by Density Functional Theory

Abstract

Density functional theory (DFT) was used to calculate the bulk electronic and optical properties of indium tin oxide (ITO). The ITO model was constructed replacing indium atoms with tin atoms in the cubic unit cell of indium oxide. To allow more possibilities for tin atom substitution than afforded by the forty-atom primitive cell of indium oxide all eighty atoms of the unit cell were included in the stoichiometry ($In_{32-x}Sn_xO_{48}$) using periodic boundary conditions. A number of properties of ITO were calculated including the optical band gap, charge carrier density and plasma frequency. The dependence of the electronic and optical properties of ITO on a variety of parameters such as the tin content, cubic lattice parameter and the distance between adjacent tin atoms was investigated. The electronic and optical properties agreed well with experimental data and allowed insight into the origin of the electronic and optical properties of ITO.

Introduction

Indium tin oxide (ITO) is an n-type degenerate semiconductor. [1] ITO has an optical band gap of 3.6 eV with a plasma frequency in the near-IR spectral region. [1-5] As a result of these properties, ITO is transparent in the visible and reflective in the infrared spectral regions. ITO is also conductive which makes it an ideal material for a variety of applications. [6,7] For instance, ITO thin films are used as flat panel displays, heat shields and electrodes. [1,2,8] The electronic and optical properties of ITO are strongly dependent on the preparation and annealing procedures used in the production of thin films. [2,8-11] For instance, the plasma frequency of ITO has been shown to be a function of sheet resistance. [5]

Furthermore, ITO surfaces have been used in a variety of electrochemical studies including the oxidation of DNA. [12,13] Similar to metal [14-21] and other metal oxide surfaces, [22,23] ITO has been modified with a variety of surface adlayers such as phosphonates, [24,25] silanes, [26] amines, [27] carboxylic acids, [24,28] thiols, [25,28] zirconium complexes [29] and tin [30] complexes to modify the electronic and optical properties and for electrochemical sensors. The success of these applications is dependent on an understanding of the optical and electronic properties of ITO.

Although for most commercial and research purposes ITO is prepared as a thin film, the understanding of the bulk properties of ITO is still important. [7] Information concerning bulk properties is critical to begin to understand thin films of ITO. To begin to fundamentally understand this material, a number of experimental studies using X-ray photoelectron spectroscopy, [28,31] reflectance FTIR spectroscopy, [4,5,8,32] ellipsometry [33,34] and diffuse reflectance UV/Visible [1,3] and FTIR [35] spectroscopy have been performed in addition to theoretical investigations on ITO and the electronic band structure of the parent materials indium oxide and tin oxide. [6,36-39] The electronic band structures of the parent materials are well known; [38] however, less work has been done to investigate the mixed metal oxide ITO.

In the present study density functional theory (DFT) was used to calculate the electronic and optical properties based on a model that included the entire parent cubic unit cell (80 atoms corresponding to 16 In_2O_3 formula units) of indium oxide. Previous studies have been based on calculations of the forty-atom indium oxide primitive unit cell. [6,36-38] The method used here permits all possible sites for the replacement of In by Sn atoms to be sampled. [40] The studies of the cubic lattice parameter and the distance between tin atoms that

were carried out as a function of tin doping ($In_{32-x}Sn_xO_{48}$) require population of Sn sites not available in the primitive lattice. This choice for the unit cell has the obvious disadvantage of larger size by a factor of two, which makes the DFT calculation more expensive. However, there is an additional advantage in choosing the full unit cell that a greater variety of doping levels can be probed (i.e. there are 32 possible sites instead of 16).

The motivation for the computational study is the recent determination of the plasma resonance frequency in the near-IR using grazing angle spectroscopy. [5] Moreover, the experimental correlation of optical and electronic properties [5] can be further tested by DFT calculation of the optical band gap, charge carrier density and the plasma frequency. The charge carrier density and plasma frequency were found to be in agreement with electronic and optical measurements. [5,32] The band gap is too small by a factor of roughly 50 % as observed in silicon. [41] Unlike silicon, ITO is a degenerate semiconductor whose charge carrier density depends on high doping levels of Sn atoms. These calculations showed that small differences in the tin doping level alter the charge carrier concentration strongly affect the electronic (conductivity) and optical (plasma frequency) properties of ITO. It is well-known that oxygen deficiencies also contribute to the charge carrier density, and therefore the conductivity of conducting metal oxides such as ITO. The role of oxygen deficiencies will be treated in a future study. In this study, we are primarily interested in determining the correlation between optical and electronic properties that we have observed experimentally. [5,32]

Experimental Methods

The normal incident FTIR transmission spectrum of ITO was recorded on a Digilab FTS 3000 FTIR spectrometer. The FTIR spectrometer was equipped with a tungsten source, quartz beamsplitter and a liquid nitrogen cooled InSb detector for the spectral range of 3,700 to 11,000 cm^{-1}. The IR spectrum was the result of the average of 128 scans at a resolution of 8 cm^{-1} and was recorded at room temperature. The ITO transmission spectrum was the result of the ratio of the single beam of ITO at normal incidence to the single beam of the empty sample holder. The ITO electrode (Delta Technologies, Limited) was composed of 90 % indium oxide and 10 % tin oxide, had a nominal thickness of 1,500 Å and a sheet resistance of 7.7 Ω/□. The substrate for the ITO electrodes was polished float (soda-lime) glass. The ITO electrode was cleaned by 20 minutes of UV/O_3 (UVO-cleaner (UVO-60), model number 42, Jelight Company, Inc) to yield a clean hydrophilic surface (as determined from contact angle measurements) (NRL C.A. Goniometer (Rame-Hart, Inc.), model 100-00). The sheet resistance of this IT thin film was measured with a 4-point probe consisting of a Signatone D27M probe station, a Keithley 224 programmable current source and a Hewlett Packard 3456A digital voltmeter.

Computational Methods

The density functional theory (DFT) calculations were performed using the quantum chemical software DMol3 (Accelrys, Inc.). [42] The calculations were performed on the indium oxide ($In_{32}O_{48}$) unit cell containing 16 In_2O_3 units shown in Figure 1 that has a bixbyite crystal structure in the Ia3 space group. [40] The cubic unit cell has a lattice parameter of

10.117 Å. The calculations used all 80 atoms with periodic boundary conditions to determine bulk electronic and optical properties of the materials. Various levels of tin doping were introduced into the indium oxide unit cell by replacing an In atom with a Sn atom ($In_{32-x}Sn_xO_{48}$, x = 0 to 12) to model indium tin oxide (ITO). The DNP (double numerical plus polarization function) basis set was employed with effective core potentials used for indium and tin below the 4d and 5s orbitals, respectively. The basis set used the O(1s, 2(2s), 2(2p), 2(3d), In(4d, 2(5s), 2(5p), 5d), and Sn(2(5s), 2(5p), 5d) orbitals for the three atoms with an atomic cutoff of either 3.2 Å or 5.5 Å. The Perdew and Wang GGA functional was used for all of the DFT calculations. [43] The band structure calculations at multiple k-points were performed at an electronic temperature of T=0 K (known as the FERMI option), [44] while the rest of the calculations used an approach that permits partial electron occupation which is well suited for charge carrier calculations (known as the THERMAL option). [45] The effective electronic temperature in the THERMAL calculations is 0.02 Hartrees or ~6300 K. [45] This high temperature guarantees self-consistent field (SCF) convergence with the THERMAL option. [45] However, a more realistic estimate of the electronic temperature is provided by calculation at an electronic temperature of k_BT = 0.00095 Ha or 300 K. As discussed below, the results at the higher temperature can be compared to a calculation carried out at an electronic temperature of 300 K, where SCF convergence is not as readily obtained. The calculated charge carrier concentration decreases with decreasing temperature as expected demonstrating the validity of the approach. The program InsightII (Accelrys, Inc.) was used to visualize the models and orbitals calculated by

DMol3. The DFT calculations were performed at the North Carolina Supercomputing Center (NCSC) on the IBM RS/6000 SP.

Single point energy calculations were performed at the Γ point in the Brillouin Zone for the determination of the Fermi energy and charge carrier concentration, while additional points in k-space along high-symmetry lines in the Brillouin zone were performed for the calculation of the band structure for indium oxide and indium tin oxide. The charge carrier concentration was calculated by summing the number of electrons in the conduction band of ITO divided by the volume of the unit cell calculated based on the cubic lattice constant. The minimum calculated band gap was observed at point Γ. In other words, the curvature of the energy surface was negative in the valence band and positive in the conduction band near point Γ. A primitive (P1) cell was used in the multiple k-points calculations of the electronic band structure. The curvature in the conduction band was fit to Eqn. 1: [3,46]

$$E(k) = E_o + \frac{h^2 k^2}{8\pi^2 m^*} \qquad (1)$$

where E is the energy in eV, E_o is the energy offset depending on where the zero value was chosen, k is the wave vector and m^* is the effective free electron mass. Eqn. 1 allowed the determination of m^* for indium oxide and indium tin oxide. This value was used in Eqn. 2: [46]

$$\omega_p^2 = \frac{ne^2}{m^* \varepsilon_o} \qquad (2)$$

where ω_p is the plasma frequency and n is the charge carrier concentration in the Drude free-electron model to calculate the plasma frequency of ITO directly from first principles.

Results and Discussion

Our study is directed towards calculation of the parameters that yield insight into the visible transparency, infrared reflectivity and conductivity of ITO. These parameters include the Fermi energy, the charge carrier concentration, the effective free electron mass and the plasma frequency. The calculations performed here are validated by their agreement with both previous experimental and theoretical work on this conducting metal oxide.

Figure 2 shows the experimental transmission spectrum at normal incidence of ITO in the near-IR spectral region. This figure is shown to illustrate the optical properties of ITO in the near-IR that are in agreement with previous experimental work, [5,32] to allow comparison to the theoretical calculations of the optical properties of ITO. Figure 2 shows that the transmission of an ITO thin film on a glass substrate is relatively high around 11,000 cm^{-1} but begins to decrease quickly between 10,000 to 7,000 cm^{-1} due to the onset of the plasma frequency. The transmission is high at wavenumbers above the plasma frequency and low at wavenumbers below the plasma frequency. Consequently this figure illustrates that the plasma frequency for this ITO thin film is observed experimentally in the near-IR spectral region around 8,500 cm^{-1}.

The dependence of the Fermi level and charge carrier concentration of ITO as a function of increasing tin content was investigated first and the resulting values are shown in Figure 3. Figure 3A shows the distribution of the electrons near the band gap at point Γ of the material fit to the Fermi-Dirac distribution shown in Eqn. 3: [47]

$$f(e) = \frac{1}{1 + e^{-\beta(e_f - e)}} \qquad (3)$$

where ε_f is the Fermi energy.

This optical band gap was found to range from 1.7 – 2.6 eV for $In_{32-x}Sn_xO_{48}$ with x = 0 to 12. The optical band gap increased as the percentage of tin increased. Figure 3A shows this widening of the optical band gap as the tin content increases due to the Burstein-Moss (BM) shift calculated here and observed experimentally. [48,49] This widening is the result of the conduction band becoming partially filled as the tin doping level increases. The optical band gap for a typical tin doping level of 9 %, the optical band gap was calculated to be 1.97 eV that is approximately 50 % smaller than the experimental values in the range 3.6-3.75 eV. [1,3] Figure 3B illustrates how the Fermi energy increases as the tin content is increased, with the largest increase in the first few substitutions of indium by tin. After approximately four tin atoms the Fermi energy increases more gradually. Figure 3C shows the corresponding values of the charge carrier concentration, n, for the same doping levels as given in Figure 3B. The first Sn atom can be placed at either the b or d octahedral site. Comparison calculations were carried out for each of these possible placements. The Fermi energy of $In_{31}Sn_1O_{48}$ with the indium-to-tin substitution at a b site was only 0.011 eV less than at a d site. The charge carrier concentration of $In_{31}Sn_1O_{48}$ with the indium to tin substitution at the b or d site was $3.25x10^{20}$ or $3.13x10^{20}$ electrons/cm^3, respectively. The charge carrier concentration first increases proportional to the tin content and then begins to decrease for substitution by more than 8 tin atoms. The maximum in the charge carrier concentration occurs when 8 of the 32 metal atoms are tin (25% doping level). Since the charge carrier concentration is directly related to the conductivity of the material in the Drude model, [46] these calculations suggest that the conductivity of ITO will be maximized for a tin mole

fraction of 0.25; however, these calculations do not account for the scattering events in the material that determine the electronic scattering time of the material. Typical tin doping levels for commercially available ITO thin films are approximately 10 % tin oxide,[5,32] but these films are designed to balance optical transparency with electrical conductivity. The variation of n is also directly related to the optical properties, as shown in Eqn. 2 for the plasma frequency, and will be discussed later. For example, the material is transparent above the plasma frequency and reflective below this frequency. Therefore these calculations yield insights into both the electrical conductivity and optical properties of ITO that complement the experimental results we have obtained previously. [5,32]

The effect of increasing the cubic lattice volume of ITO was investigated for one doping level of ITO ($In_{28}Sn_4O_{48}$) because experimental evidence demonstrated an increase of the lattice parameter with tin doping. [50] Figures 4 A, B and C show the dependence of the Fermi energy, the charge carrier concentration and the single point energy on the unit cell volume of ITO. These calculations involved the expansion or compression of the entire unit cell with the corresponding change in the cubic lattice parameter. The calculations yielded a decrease in the Fermi energy with increasing lattice parameter, while the charge carrier concentration increased rapidly when the lattice parameter increased. Figure 4B did not show a maximum that would be suggestive of an optimal (preferred) lattice parameter that ITO ($In_{28}Sn_4O_{48}$) would adopt. Prior to a determination of an expansion of the lattice, the optimal lattice parameters of the indium oxide structure are required. Figure 4C shows that the energy minimum for the variation of the cubic lattice parameter for $In_{32}O_{48}$ was calculated at a value 2.9 % larger than the crystal structure value of 10.117 Å for the cubic

lattice parameter (at an electronic temperature of ~6300 K). Better agreement for with the experimental value could probably be achieved with a larger basis set. The calculated energy minimum for the cubic lattice parameter for $In_{28}Sn_4O_{48}$ was found at 3.1 % larger than the crystal structure value, which is a 0.2 % increase in the cubic lattice parameter relative to $In_{32}O_{48}$. This value (0.2 %) is in close agreement with the experimental increase in the cubic lattice parameter of 0.06 % for a tin doping level of 6 % for ITO relative to indium oxide. [50]

Another key factor in determining the electronic and optical properties of ITO by regulating the charge carrier concentration is the distance between tin atoms in the ITO unit cell. This factor was examined with an indium tin oxide unit cell containing two tin atoms. The correlations of the distance between these two tin atoms ($In_{30}Sn_2O_{48}$) with the Fermi energy and the charge carrier concentration are shown in Figure 5A and 5B. Figure 5A illustrates that the Fermi energy increases with increasing distance between the two tin atoms, while Figure 5B shows that the charge carrier concentration decreases with increasing Sn-Sn distance. The calculated charge carrier concentration in Figure 5 suggests that the electrical conductivity, ignoring scattering events and the decrease of the plasma frequency of ITO, decreases with increasing distance between tin atoms in the unit cell.

As mentioned earlier, the optical properties of ITO are determined by the plasma frequency. Eqn. 2 shows that the plasma frequency depends on both the charge carrier concentration and the effective free electron mass. [5,32,46] The charge carrier concentration has been determined at point Γ as shown above; however, a more complete description of the electronic band structure is required to estimate the value of the effective free electron mass. As shown in Eqn. 1, the effective free electron mass was determined from fitting the

electronic band structure to a parabolic function. The effective free electron masses determined as a function of tin doping for three directions in the Brilluoin zone are shown in Table 1A. The calculated values are $0.31m_e$, $0.42m_e$ and $0.54m_e$, where m_e is the mass of an electron for the Δ ($\Gamma \rightarrow$ X), Σ ($\Gamma \rightarrow$ M) and Λ ($\Gamma \rightarrow$ R) directions in agreement with experimentally and theoretically determined values. [3,36] The calculated effective free electron mass decreased as the tin doping increased for all three Brillouin zone directions for ITO. Table 1B shows the values for the effective free electron mass as the cubic lattice parameter was increased. Overall the effective free electron mass did not change more than $0.02m_e$ units for the Σ ($\Gamma \rightarrow$ M) and Λ ($\Gamma \rightarrow$ R) directions as the cubic lattice parameter increased. The plasma frequency can be determined in the Drude model approximation (Eqn. 2) using the calculated effective free electron masses.

The plasma frequency was determined within the Drude model to determine the correlations between the optical properties and the amount of tin doping and lattice parameter for ITO. The values of the plasma frequency calculated for ITO with varying tin doping levels is shown in Table 2A. These values for the plasma frequency occur in the near-IR spectral region in agreement with experiment, [2,4,5] which implies that ITO is transparent in the visible region and reflective in the infrared region of the electromagnetic spectrum. This result is in agreement with typical commercially available ITO thin films. [5,25,32] These results show that the plasma frequency of ITO increases with increasing tin doping levels for all three Brillouin zone directions. The calculated values of the plasma frequencies for the Δ ($\Gamma \rightarrow$ X) direction are plotted in Figure 6A as a function of tin doping. This plot is representative of the other three directions and illustrates the increase in plasma frequency

with increasing amounts of tin, but shows that the value begins to level out at about 8 tin atoms in agreement with the charge carrier concentration dependence shown in Figure 2C. However the plasma frequency does not reach a maximum in Figure 6A as did the charge carrier concentration in Figure 2C due to the continual decrease in the effective free electron mass with increasing tin doping levels. Table 2B gives the values of the plasma frequency calculated for $In_{28}Sn_4O_{48}$ for three directions as a function of the cubic lattice parameter. These values are plotted in Figure 6B for the Δ ($\Gamma \rightarrow$ X) direction. The results given in Table 2B and Figure 6B show that the plasma frequency increases with increasing cubic lattice parameter in accordance with the charge carrier concentration dependence as shown in Figure 3B.

The electronic and optical properties of ITO for one level of tin doping ($In_{28}Sn_4O_{48}$) at room temperature (300K) was calculated for comparison with experimentally observed properties. Calculations at ~300 K have much lower tendency to converge and thus most of the calculations were carried out for an electronic temperature of ~6300 K. The results for ~300 K are tabulated in Table 3 for the Fermi energy, charge carrier concentration and plasma frequency. The charge carrier concentration of 4.55 x 10^{20} electrons/cm^3 at ambient temperature is in agreement with experimental values that are of the same order of magnitude with some dependence on preparation and annealing protocols. [3] The corresponding plasma frequency values of 11,430, 9,876 and 8,666 cm^{-1} for the Δ ($\Gamma \rightarrow$ X), Σ ($\Gamma \rightarrow$ M) and Λ ($\Gamma \rightarrow$ R) directions are also in agreement with experimental observations of the plasma frequency occurring in the near-IR and observed using reflectance FTIR spectroscopy. [2,4,5]

The DFT calculations also yielded information concerning the orbital character of the conduction bands of indium oxide, indium tin oxide and tin oxide. The calculations showed predominately In 5s / O 2s antibonding and Sn 5s / O 2s antibonding character for the conduction bands of indium oxide and tin oxide, respectively (data not shown). However, the orbitals in the conduction band of ITO were predominately Sn 5s / O 2p antibonding character with a small admixture of Sn 5s / O 2s antibonding character. This orbital character of the conduction band is illustrated for $In_{28}Sn_4O_{48}$ at point Γ in Figure 7.

Conclusion

The DFT calculations presented in this study have accurately determined the bulk electronic and optical properties of ITO, namely the optical band gap, charge carrier concentration, effective free electron mass, the plasma frequency and the conduction band orbital character. These properties were investigated as a function of the tin doping level and the cubic lattice parameter. The optical band gap was calculated to be 1.97 eV for 9 % tin doping, which differs from experiment by 50 % as observed in silicon. The plasma frequency was calculated to be in the near-IR at ~10,000 cm^{-1} in agreement with experimental measurements on ITO thin films. The calculated charge carrier concentration and effective free electron mass were approximately 10^{20} - 10^{21} electrons/cm^3 and 0.6 - 0.1m_e for the various ITO models, respectively. The charge carrier concentration increased with increasing tin content until a maximum at the 25% doping level, and the optimal (lowest energy) cubic lattice parameter was determined to be an increase of 0.2% for $In_{28}Sn_4O_{48}$ relative to $In_{32}O_{48}$. The electrical conductivity, ignoring scattering events and the plasma frequency was also found to increase with increasing tin content. The conduction band

orbitals resulting in electrical conductivity for ITO were predominately the Sn 5s / O 2p/2s orbitals further illustrating the important role of tin in the electronic and optical bulk properties of ITO.

These calculations illustrate the importance of the preparation and annealing protocols for ITO due to the effect these procedures have on the charge carrier concentration that directly affects the electronic and optical properties of ITO. These two classes of properties are related by the charge carrier concentration since both the electrical conductivity and the plasma frequency are dependent upon this parameter. Therefore, there is a balance between making an ITO thin film of high conductivity (high charge carrier concentration) while maintaining transparency in the visible region by having a plasma frequency in the near-IR (lower charge carrier concentration). Consequently, control of the charge carrier concentration (tin doping) is essential in forming ITO thin films with desirable electronic and optical properties. This investigation provides a foundation for studying the effects of surface adlayers on the electronic and optical properties of ITO thin films because it provides a quantitative relationship between the macroscopic thermodynamic state of the bulk material and its charge carrier concentration.

Acknowledgements

This work was done in collaboration with Stefan Franzen (NCSU) and is the subject of a publication, Brewer, S. H.; Franzen, S. *Chemical Physics* **2004**, 300, 285-293. Support and computational facilities were provided by the North Carolina Supercomputing Center.

We thank Dr. H. F. Franzen of Iowa State University and Dr. J. Folmer of North Carolina State University for helpful comments.

References

(1) Ambrosini, A.; Duarte, A.; Poeppelmeier, K. R.; Lane, M.; Kannewurf, C. R.; Mason, T. O. *Journal of Solid State Chemistry* **2000**, *153*, 41-47.

(2) Hamberg, I.; Hjortsberg, A.; Granqvist, C. *Applied Physics Letters* **1982**, *40*, 362-364.

(3) Hamberg, I.; Granqvist, C. G.; Berggren, K. F.; Sernelius, B. E.; Engstrom, L. *Physical Review B* **1984**, *30*, 3240-3249.

(4) Hamberg, I.; Granqvist, C. G. *Journal of Applied Physics* **1986**, *60*, R123-R159.

(5) Brewer, S. H.; Franzen, S. *Journal of Physical Chemistry B* **2002**, *106*, 12986-12992.

(6) Mryasov, O. N.; Freeman, A. J. *Physical Review B* **2001**, *6423*, art. no.-233111.

(7) Freeman, A. J.; Poeppelmeier, K. R.; Mason, T. O.; Chang, R. P. H.; Marks, T. J. *MRS Bulletin* **2000**, *25*, 45-51.

(8) Hjortsberg, A.; Hamberg, I.; Granqvist, C. *Thin Solid Films* **1982**, *90*, 323-326.

(9) Bregman, J.; Shapira, Y.; Aharoni, H. *Journal of Applied Physics* **1990**, *67*, 3750-3753.

(10) Fan, J.; Bachner, F.; Foley, G. *Applied Physics Letters* **1977**, *31*, 773-775.

(11) Shin, J.; Shin, S.; Park, J.; Kim, H. *Journal of Applied Physics* **2001**, *89*, 5199-5203.

(12) Armistead, P.; Thorp, H. *Analytical Chemistry* **2000**, *72*, 3764-3770.

(13) Armistead, P.; Thorp, H. *Analytical Chemistry* **2001**, *73*, 558-564.

(14) Bain, C.; Biebuyck, H.; Whitesides, G. *Langmuir* **1989**, *5*, 723-727.

(15) Karyakin, A.; Presnova, G.; Rubtsova, M.; Egorov, A. *Analytical Chemistry* **2000**, *72*, 3805-3811.

(16) Kitano, H.; Taira, Y.; Yamamoto, H. *Analytical Chemistry* **2000**, *72*, 2976-2980.

(17) Kittredge, K.; Fox, M.; Whitesell, J. *The Jounal of Physical Chemistry B* **2001**, *ASAP article*.

(18) Nakashima, N. *Langmuir* **1999**, *15*, 3823-3830.

(19) Naud, C.; Calas, P.; Commeyras, A. *Langmuir* **2001**, *17*, 4851-4857.

(20) Ringsdorf, H. *Macromolecules* **1997**, *30*, 5913-5919.

(21) Terril, R.; Tanzer, T.; Bohn, P. *Langmuir* **1998**, *14*, 845-854.

(22) Allara, D.; Nuzzo, R. *Langmuir* **1985**, *1*, 52-66.

(23) Allara, D.; Nuzzo, R. *Langmuir* **1985**, *1*, 45-52.

(24) Gardner, T.; Frisbie, C.; Wrighton, M. *The Journal of the American Chemical Society* **1995**, *117*, 6927-6933.

(25) Brewer, S. H.; Brown, D. A.; Franzen, S. *Langmuir* **2002**, *18*, 6857-6865.

(26) Markovich, I.; Mandler, D. *Journal of Electroanalytical Chemistry* **2001**, *500*, 453-460.

(27) Oh, S.; Yun, Y.; Kim, D.; Han, S. *Langmuir* **1999**, *15*, 4690-4692.

(28) Yan, C.; Zharnikov, M.; Golzhauser, A.; Grunze, M. *Langmuir* **2000**, *16*, 6208-6215.

(29) VanderKam, S.; Gawalt, E.; Schwartz, J.; Bocarsly, A. *Langmuir* **1999**, *15*, 6598-6600.

(30) Purvis, K.; Lu, G.; Schwartz, J.; Bernasek, S. *The Journal of the American Chemical Society* **2000**, *122*, 1808-1809.

(31) Yu, H. Y.; Feng, X. D.; Grozea, D.; Lu, Z. H.; Sodhi, R. N. S.; Hor, A. M.; Aziz, H. *Applied Physics Letters* **2001**, *78*, 2595-2597.

(32) Brewer, S. H.; Franzen, S. *Journal of Alloys and Compounds* **2002**, *338*, 73-79.

(33) Gerfin, T.; Gratzel, M. *Journal of Applied Physics* **1996**, *79*, 1722-1729.

(34) Synowicki, R. *Thin Solid Films* **1998**, *313*, 394-397.

(35) Lee, D.; Vuong, K.; Sr., R. C.; Wang, X. W. *Materials Letters* **1996**, *28*, 179-182.

(36) Odaka, H.; Shigesato, Y.; Murakami, T.; Iwata, S. *Japanese Journal of Applied Physics Part 1-Regular Papers Short Notes & Review Papers* **2001**, *40*, 3231-3235.

(37) Odaka, H.; Iwata, S.; Taga, N.; Ohnishi, S.; Kaneta, Y.; Shigesato, Y. *Japanese Journal of Applied Physics Part 1-Regular Papers Short Notes & Review Papers* **1997**, *36*, 5551-5554.

(38) Mi, Y. M.; Odaka, H.; Iwata, S. *Japanese Journal of Applied Physics Part 1-Regular Papers Short Notes & Review Papers* **1999**, *38*, 3453-3458.

(39) Maki-Jaskari, M. A.; Rantala, T. T. *Physical Review B* **2001**, *6407*, art. no.-075407.

(40) Marezio, M. *Acta Crystallographica* **1966**, *20*, 723-728.

(41) Godby, R. W.; Schlüter, M.; Sham, L. J. *Phys. Rev. Lett.* **1986**, *56*, 2415-2418.

(42) Delley, B. *Journal of Chemical Physics* **1990**, *92*, 508-517.

(43) Perdew, J. P.; Chevary, J. A.; Vosko, S. H.; Jackson, K. A.; Pederson, M. R.; Singh, D. J.; Fiolhais, C. *Physical Review B* **1992**, *46*, 6671-6687.

(44) Kohn, W.; Sham, L. *Phys. Rev. A* **1965**, *137*, 1697-1699.

(45) Mermin, D. *Phys. Rev. A* **1965**, *137*, 1441-1443.

(46) Wooten, F. *Optical Properties of Solids*; Academic Press, Inc.: San Diego, 1972.

(47) McQuarrie, D. A. *Statistical Mechanics*; Harper Collins Publishers Inc.: New York, 1976.

(48) Burstein, E. *Physical Review* **1954**, *93*, 632-633.

(49) Moss, T. S. *Proceedings of the Physical Society of London Section B* **1954**, *67*, 775-782.

(50) Nadaud, N.; Lequeux, N.; Nanot, M.; Jove, J.; Roisnel, T. *Journal of Solid State Chemistry* **1998**, *135*, 140-148.

(51) Slater, J. C. *Symmetry and Energy Bands in Crystals*; Dover Publications: New York, **1972.**

Tables

Table 1A. Calculated effective free electron mass (fraction of the free electron mass, m_e) for indium oxide and indium tin oxide.

	(0,0,0) → (½,0,0) Δ (Γ → X)	(0,0,0) → (½,½,0) Σ (Γ → M)	(0,0,0) → (½,½,½) Λ (Γ → R)
$In_{32}O_{48}$	$0.30m_e$	$0.36m_e$	$0.41m_e$
$In_{30}Sn_2O_{48}$	$0.32m_e$	$0.47m_e$	$0.64m_e$
$In_{28}Sn_4O_{48}$	$0.31m_e$	$0.42m_e$	$0.54m_e$
$In_{26}Sn_6O_{48}$	$0.28m_e$	$0.33m_e$	$0.49m_e$
$In_{24}Sn_8O_{48}$	$0.14m_e$	$0.33m_e$	$0.45m_e$
$In_{22}Sn_{10}O_{48}$	$0.13m_e$	$0.32m_e$	$0.39m_e$

Table 1B. Calculated effective free electron mass (fraction of the free electron mass, m_e) for $In_{28}Sn_4O_{48}$ as a function of the cubic lattice parameter.

Percent Cubic Lattice Parameter Increase for $In_{28}Sn_4O_{48}$	(0,0,0) → (½,0,0) Δ (Γ → X)	(0,0,0) → (½,½,0) Σ (Γ → M)	(0,0,0) → (½,½,½) Λ (Γ → R)
0	$0.31m_e$	$0.42m_e$	$0.54m_e$
2	$0.30m_e$	$0.42m_e$	$0.54m_e$
4	$0.30m_e$	$0.42m_e$	$0.56m_e$
6	$0.30m_e$	$0.43m_e$	$0.57m_e$
8	$0.31m_e$	$0.44m_e$	$0.58m_e$

* Both the fractional coordinates (that are related to the lattice wave vectors (k_x,k_y,k_z) by $(f(2\pi/a),f(2\pi/a),f(2\pi/a))$ where f is the fractional coordinate and k_x, k_y, and k_z are the three components of the lattice wave vector (k) that are related by $k^2 = k_x^2 + k_y^2 + k_z^2$ where a is the cubic lattice parameter) and the notation of Boucksert, Smoluchowski and Wigner are presented. [51]

Table 2A. Calculated plasma frequencies (cm^{-1}) for indium oxide and indium tin oxide.

	(0,0,0) → (½,0,0) Δ (Γ → X) (cm^{-1})	(0,0,0) → (½,½,0) Σ (Γ → M) (cm^{-1})	(0,0,0) → (½,½,½) Λ (Γ → R) (cm^{-1})
$In_{32}O_{48}$	4,163	3,820	3,562
$In_{30}Sn_2O_{48}$	12,994	10,662	9,173
$In_{28}Sn_4O_{48}$	24,545	21,209	18,610
$In_{26}Sn_6O_{48}$	35,456	32,788	26,927
$In_{24}Sn_8O_{48}$	56,255	36,113	31,013
$In_{22}Sn_{10}O_{48}$	56,332	35,476	32,155

Table 2B. Calculated plasma frequencies (cm^{-1}) for $In_{28}Sn_4O_{48}$ as a function of the cubic lattice parameter.

Percent Cubic Lattice Parameter Increase for $In_{28}Sn_4O_{48}$	(0,0,0) → (½,0,0) Δ (Γ → X) (cm^{-1})	(0,0,0) → (½,½,0) Σ (Γ → M) (cm^{-1})	(0,0,0) → (½,½,½) Λ (Γ → R) (cm^{-1})
0	24,545	21,209	18,610
2	24,786	21,203	18,512
4	25,142	21,359	18,581
6	25,941	21,885	18,977
8	27,085	22,695	19,620

* Both the fractional coordinates (that are related to the lattice wave vectors (k_x,k_y,k_z) by (f(2π/a),f(2π/a),f(2π/a)) where f is the fractional coordinate and k_x, k_y, and k_z are the three components of the lattice wave vector (k) that are related by $k^2 = k_x^2 + k_y^2 + k_z^2$ where a is the cubic lattice parameter) and the notation of Boucksert, Smoluchowski and Wigner are presented. [51]

Table 3. Properties of $In_{28}Sn_4O_{48}$ calculated at room temperature (300K).

Fermi Energy (eV)		-3.387	
Charge Carrier Concentration (electrons/cm^3)		$4.55x10^{20}$	
	(0,0,0) → (½,0,0) Δ (Γ → X)	(0,0,0) → (½,½,0) Σ (Γ → M)	(0,0,0) → (½,½,½) Λ (Γ → R)
Plasma Frequency (cm^{-1})	11,430	9,876	8,666

* Both the fractional coordinates (that are related to the lattice wave vectors (k_x,k_y,k_z) by (f(2π/a),f(2π/a),f(2π/a)) where f is the fractional coordinate and k_x, k_y, and k_z are the three components of the lattice wave vector (k) that are related by $k^2 = k_x^2 + k_y^2 + k_z^2$ where a is the cubic lattice parameter) and the notation of Boucksert, Smoluchowski and Wigner are presented[51].

Figures

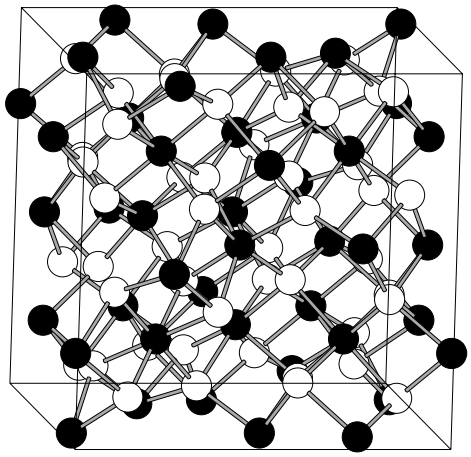

Figure 1. The bixbyite crystal structure of indium oxide ($In_{32}O_{48}$) showing one unit cell where the indium and oxygen atoms are represented by the black and hollow spheres, respectively.

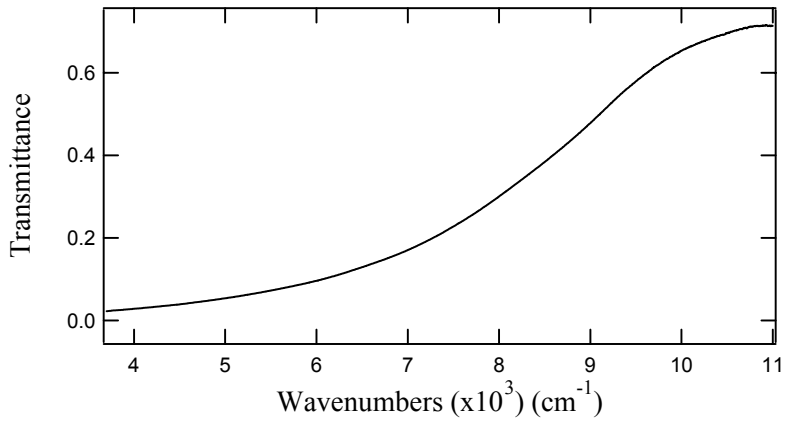

Figure 2. Transmission FTIR spectrum of an ITO thin film on a glass substrate at normal incidence recorded with p-polarized radiation.

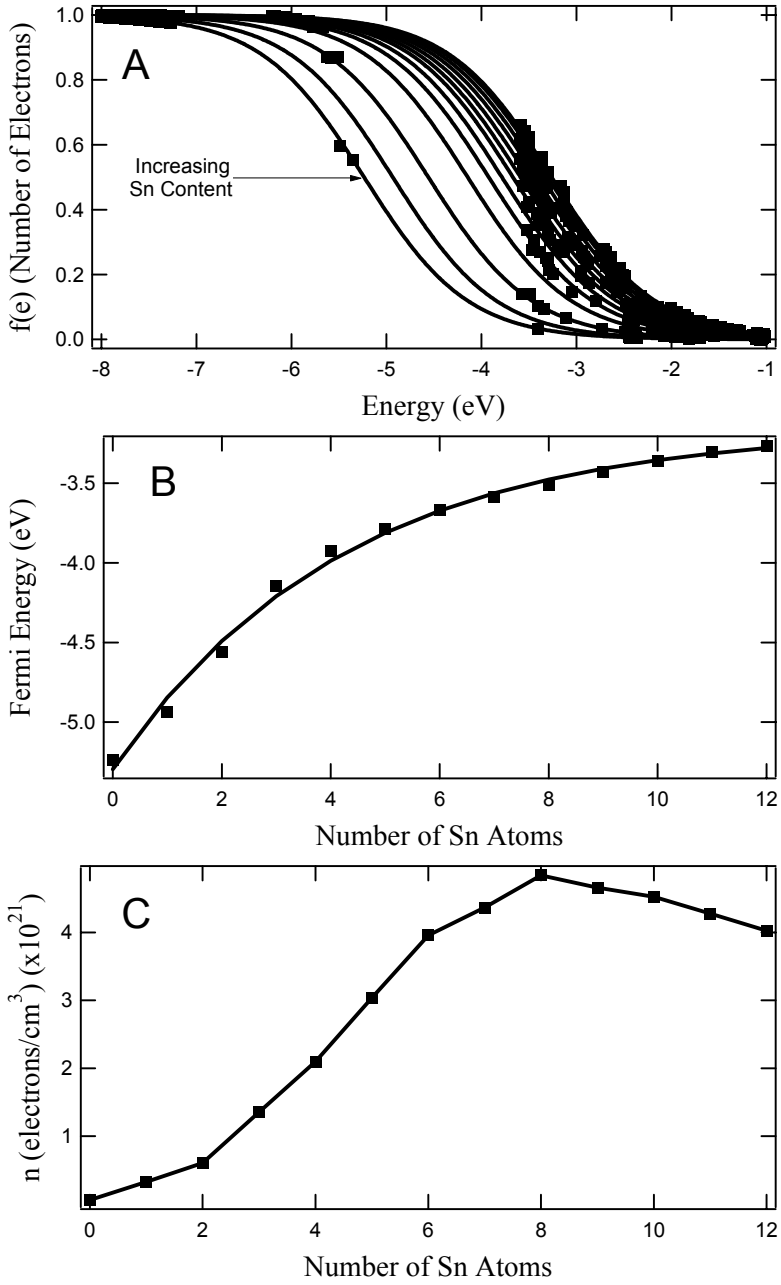

Figure 3. DFT calculated dependence of the optical band gap (A), Fermi energy (B) and charge carrier concentration (C) on the tin content in the ITO lattice.

Figure 4. DFT calculated dependence of the Fermi energy (A) and charge carrier concentration (B) for $In_{28}Sn_4O_{48}$ on the cubic lattice parameter. (C) DFT calculated dependence of the single point energy of $In_{32}O_{48}$ (hollow squares) and $In_{28}Sn_4O_{48}$ (black squares) and the corresponding five term polynomial fit for $In_{32}O_{48}$ (dashed curve) and $In_{28}Sn_4O_{48}$ (solid curve) on the cubic lattice parameter.

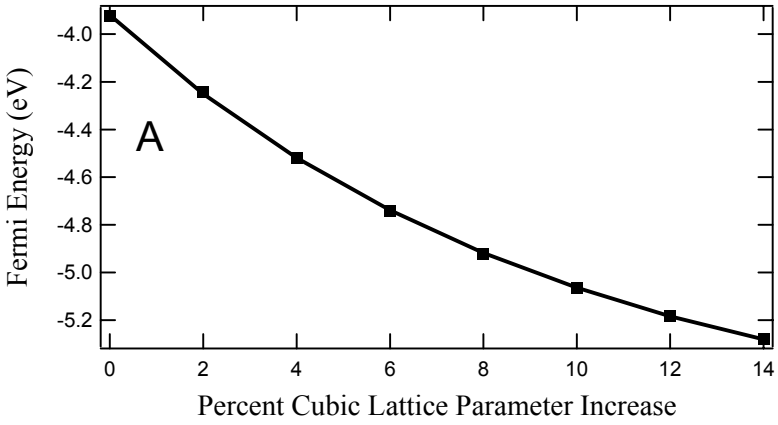
A
Fermi Energy (eV)
-4.0
-4.2
-4.4
-4.6
-4.8
-5.0
-5.2
0
2
4
6
8
10
12
14
Percent Cubic Lattice Parameter Increase

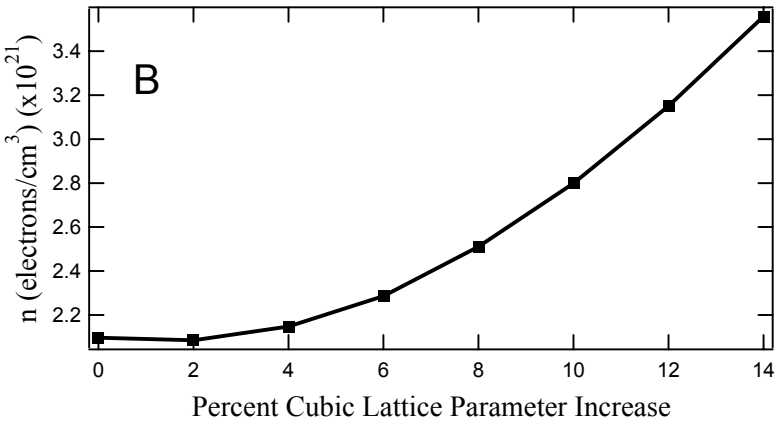
B
n (electrons/cm^3) (x10^{21})
3.4
3.2
3.0
2.8
2.6
2.4
2.2
0
2
4
6
8
10
12
14
Percent Cubic Lattice Parameter Increase

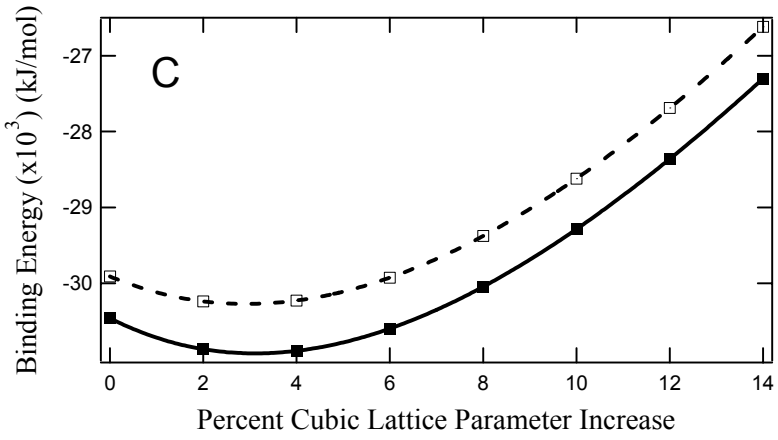
C
Binding Energy (x10^3) (kJ/mol)
-27
-28
-29
-30
0
2
4
6
8
10
12
14
Percent Cubic Lattice Parameter Increase

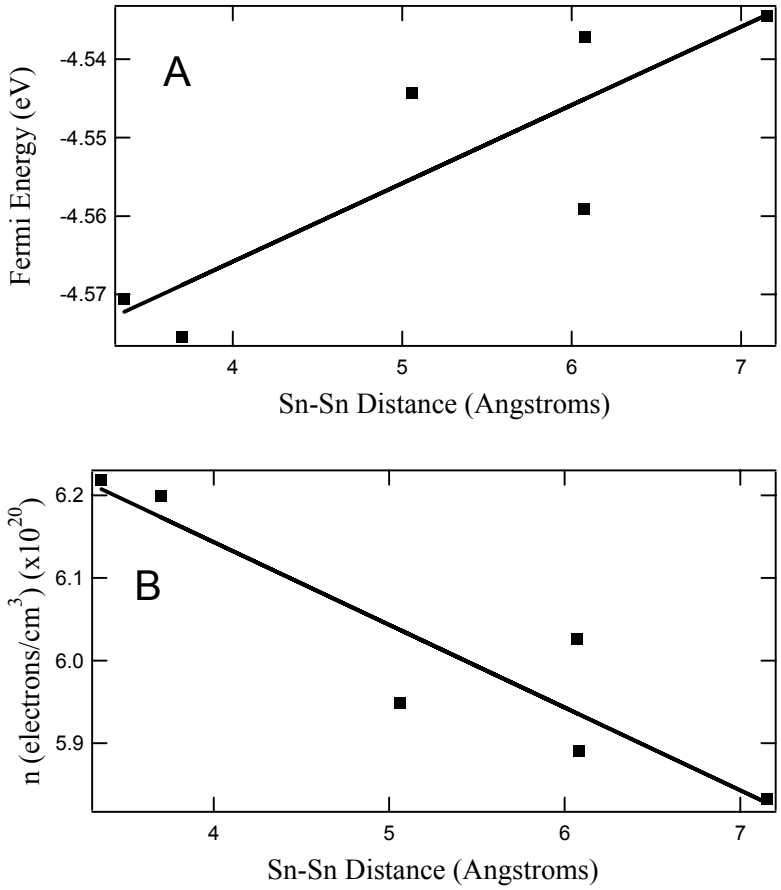

Figure 5. DFT calculated dependence of the Fermi energy (A) and charge carrier concentration (B) on the distance between two tin atoms in the $In_{30}Sn_2O_{48}$ lattice.

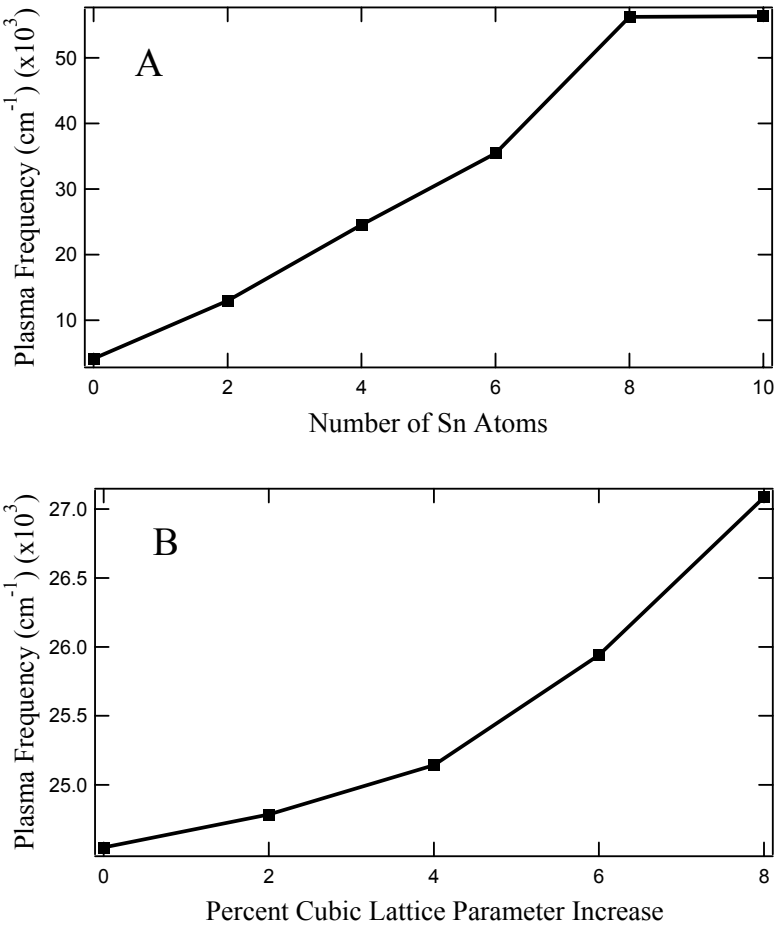

Figure 6. DFT calculated plasma frequency of ITO at various levels of tin doping (A) and as a function of the cubic lattice parameter for $In_{28}Sn_4O_{48}$ using the charge carrier concentration determined at point Γ and the effective free electron mass from the Δ (Γ → X) direction in the band structure.

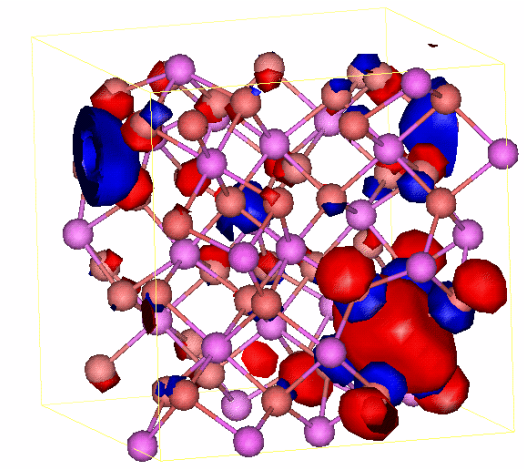

Figure 7. DFT calculated orbital of $In_{28}Sn_4O_{48}$ for the conduction band at point Γ in the Brillouin zone showing the Sn 5s and O 2s, 2p orbitals in an antibonding configuration. (indium: purple spheres, oxygen: red spheres).

Chapter 8

Detection of DNA Hybridization on Indium Tin Oxide Surfaces

Abstract

Indium tin oxide (ITO) surfaces were modified with ssDNA by coupling oligonucleotides to a monolayer of 12-phosphonododecanoic acid (12-PDA) on the ITO surface. This coupling involved the formation of an amide bond between the carboxylic acid moiety of 12-PDA to the amine group of a 5'-$H_2N(CH_2)_3$ labeled single strand of DNA. This modification was characterized by X-ray photoelectron and reflectance FTIR spectroscopy while the ssDNA surface coverage was determined to be $2.2(\pm 0.3)x10^{13}$ molecules/cm^2 by chronocoulometry. The detection of selective surface DNA hybridization was achieved by labeling the target ssDNA with gold nanoparticles. The presence of gold nanoparticles was probed using X-ray photoelectron spectroscopy, stripping voltammetry, atomic force microscopy, thermography, photoelectrochemistry (chronoamperometry) and cyclic voltammetry (CV). CV successfully detected DNA hybridization for nanoparticle concentrations as low as 10 pM when using the gold nanoparticles bound to an ITO electrode as catalysts for the electrochemical oxidation of $FeCl_2$.

Introduction

The detection of surface DNA hybridization continues to be an important area of research for applications in detection of messenger RNA levels in cells and genomic analysis. Various surface attachment and detection strategies have been investigated to determine the optimal system for detecting surface DNA hybridization. Gold[1] and glass[2] substrates have been utilized in several of these systems due to the ability to form self-assembled monolayers on these surfaces with thiol or silane containing molecules,[3] respectively. These systems

have shown the detection of selective DNA hybridization through a variety of detection techniques including fluorescence,[4-7] surface plasmon resonance (SPR),[8,9] electrochemistry,[10-12] FTIR spectroscopy,[13] X-ray photoelectron spectroscopy (XPS)[1] and through the labeling with nanoparticles.[14-16]

In this study, indium tin oxide (ITO) thin films were investigated to develop a surface DNA modification procedure to be used for the subsequent detection of DNA hybridization. The electronic and optical properties of ITO have spurred interest in the formation of adlayers on ITO[17-23] and technologies have been developed for the detection of DNA or PNA on ITO.[24-26] ITO offers unique properties that allow for various detection strategies. For instance, ITO thin films are transparent in the visible region and reflective in the infrared region.[27-32] ITO electrodes also have the desired ability to sustain relatively high potentials needed for many applications including direct or mediated oxidation of guanosine nucleotides [24] or metal stripping voltammetry using nanoparticle labels to name two. The detection strategies employed in this study involve the detection of gold nanoparticle labeled target single stranded DNA (ssDNA).[33] The modification of the ITO thin films was confirmed by XPS, reflectance FTIR spectroscopy and chronocoulometry. The gold nanoparticle / target ssDNA conjugates were detected on the ITO surface by XPS, stripping voltammetry, atomic force microscopy (AFM), thermography, photoelectrochemistry (chronoamperometry) and cyclic voltammetry (CV).

Materials and Methods

ssDNA Modification of ITO. Scheme 1 outlines the strategy employed in the modification of indium tin oxide (ITO) (Delta Technologies, Ltd.) surfaces with ssDNA. The ITO thin films were comprised of 90% indium oxide and 10% tin oxide, had a nominal thickness of 1,500 Å and a sheet resistance of 8-12 Ω. Initially a monolayer of 12-phosphonododecanoic acid (12-PDA) (Xanthon, Inc.) (10mM in 50/50 DMSO/18 MΩ cm H_2O for 16 hours) was formed on the ITO surface (cleaned 20 minutes with UV/O_3 (UVO-cleaner (UVO-60), model number 42, Jelight Company, Inc)). The carboxylic acid functional group of 12-PDA was activated by 1-ethyl-3-(3-dimethylaminopropyl)carbodiimide hydrochloride (EDC) (Sigma-Aldrich) and reacted with the primary amine of a 5' modified H_2N-$(CH_2)_3$ ssDNA (5'H_2N-$(CH_2)_3$ modified 5'-GTGAGCGGATAATCCTGGTT-3') (Applied Biosystems, Inc.) to form an amide bond between the 12-PDA and the 5' modified H_2N-$(CH_2)_3$ ssDNA. The coupling conditions were 1 μM 5' modified H_2N-$(CH_2)_3$ ssDNA and 200 mM EDC for 4 hours in a 0.1 M MES (2-(N-morpholino)ethane sulfonic acid) buffer at pH 5 with 0.25 M NaCl. The surface was then rinsed with 18 MΩ cm H_2O (BARNSTEAD E-PURE) and dried with N_2 gas.

Preparation of the Gold Nanoparticle / Oligonucleotide Conjugates. The gold nanoparticle conjugates were synthesized by the attachment of 5' thiol modified ssDNA. The complementary ssDNA target strand used in the hybridization experiments was 5'-$HS(CH_2)_6$ modified 5'-AACCAGGATTATCCGCTCAC-3' while the non-complementary ssDNA target strand was 5'-$HS(CH_2)_6$ modified 5'-GTGAGCGGATAATCCTGGTT-3'. Gold nanoparticles (10 nm diameter) coated with bis(*p*-sulfonatophenyl)phenylphosphine

dihydrate dipotassium salt (BSPP) were synthesized by a literature procedure.[34] Briefly, 10 nm citrate coated Au colloids (Ted Pellar) were stirred with an excess of BSPP at room temperature overnight. To slightly aggregate the nanoparticles 50 mg of NaCl was added progressively until the color of the colloidal suspension changed from burgundy to a slightly purplish color. The sample was centrifuged to pellet the particles and the supernatant was removed. Afterwards the pellet was re-suspended in a 250 mg/L solution of BSPP. Methanol was added drop wise until the color of the particles turned from a burgundy red to a purplish color again. The colloidal solution was centrifuged and the supernatant was discarded. The gold nanoparticles were finally re-dissolved in the BSPP solution and stored at 4 ^{o}C.

For the preparation of the gold nanoparticle / ssDNA conjugates, a 1:100 ratio of gold nanoparticles to ssDNA was stirred at room temperature overnight. In order to remove non-reacted ssDNA, the solution was centrifuged at 14,000 rpm for 30 min and the precipitate was re-suspended into 1xSSC (saline sodium citrate) buffer. This procedure was performed twice and resulted in approximately 5 – 6 ssDNA strands per gold nanoparticle determined by fluorescence (data not shown). The final concentration conjugate solution had a final concentration of 3.7 nM gold nanoparticles as determined from the absorbance of the plasmon band of the gold nanoparticles using an extinction coefficient of 8.9×10^{7} $M^{-1}cm^{-1}$.

DNA Hybridization Conditions. The DNA hybridization was carried out either at 37 ^{o}C overnight in a shaking incubator or by keeping the hybridization solution for 1 hour at 45 °C and then allowing the solution to gradually cool to room temperature overnight. The concentrations of the gold nanoparticle / ssDNA conjugate solutions used in this study were in the range of 1 nM to 1 pM of the gold nanoparticle.

X-ray Photoelectron Spectroscopy (XPS). XPS spectra were recorded on a Riber LAS 2000 Surface Analysis System equipped with a cylindrical mirror analyzer (CMA) and a MAC2 analyzer with Mg Kα X-rays (model CX 700 (Riber source) (hν = 1253.6 eV). The elemental scans had a resolution of 1.0 eV and were the result of 5 scans. XPS spectra were smoothed using a 9 point (second order) Savitzky-Golay algorithm, baseline corrected and the peaks were fitted using Gaussian line shapes.

Infrared Reflection Absorption Spectroscopy (IRRAS). The reflectance FTIR spectra were recorded using a Spectra-Tech grazing angle reflectance attachment in a Nicolet Magna-IR 860 FTIR spectrometer. The angle of incidence used was 80 degrees. An infrared polarizer was used to obtain p- (vertically) polarized light. The spectra of the monolayers deposited on the ITO surfaces were obtained by taking a ratio of the single beam spectra of the deposited material on an ITO surface to one of a clean ITO surface. The rotational lines from gaseous water were subtracted from these spectra. The FTIR spectrometer was equipped with a liquid nitrogen cooled MCT/A detector and the spectra were recorded at a resolution of 2 cm^{-1} with a spectral range of 900 - 4000 cm^{-1}. All IR spectra were the result of 256 scans and were recorded at room temperature.

Density Functional Theory (DFT) Calculations. The geometry optimization and vibrational frequency calculations of the various nucleosides were done using density functional theory (DFT) as implemented in the quantum chemistry software program DMol3 (Accelrys, Inc.).[35] The calculations were performed at the North Carolina Supercomputer Center (NCSC) on a IBM RS/6000 SP. These calculations were done in the gas phase using the DND basis set, the GGA (generalized gradient approximation) functional[36] and the

method of finite differences for calculating the vibrational frequencies. The Accelrys, Inc. software Insight II was used to build the models and to visualize the eigenvector projections of the normal modes of vibration of the models. The calculated vibrational spectrum of ssDNA was calculated from a weighted average of the calculated IR spectra of the individual nucleosides according to Eqn. 1:

$$IR_{ssDNA} = \frac{f_A(IR_A) + f_T(IR_T) + f_G(IR_G) + f_C(IR_C)}{n} \qquad (1)$$

where IR corresponds to the calculated IR spectrum, f is the fraction of a particular base in the ssDNA sequence, n refers to the number of bases in the ssDNA sequence while A, T, G and C correspond to the four DNA bases.

Electrochemical Measurements. The electrochemical measurements were performed on an EG & G Princeton Applied Research instrument (Potentiostat Model 273A). The electrochemical setup consisted of a three-electrode cell consisting of $Ag_{(s)}$/AgCl as the reference electrode and a Pt wire as the counter electrode. The area of the working electrode was 0.28 cm^2.

Chronocoulometry was done in 10 mM Tris buffer (pH 7.1) in the presence and absence of 50 μM $[Ru(NH_3)_6]^{3+}$ after purging it thoroughly with argon gas for 10 min. The surface density of probe ssDNA can be calculated from the chronocoulometric measurements using the assumption that one $[Ru(NH_3)_6]^{3+}$ molecule binds to the anionic phosphodiester backbone of DNA for every three bases [11] The integrated Cottrell equation, which expresses charge Q as a function of time, can be used to calculate the surface excess term as shown in Eqn. 2:

$$Q = \frac{2nFAD_0^{1/2}C_0^*}{\pi^{1/2}}t^{1/2} + Q_{\mathrm{dl}} + nFA\Gamma_0 \qquad (2)$$

where n is the number of electrons per molecule for reduction, F is the Faraday constant (C/equiv), A the electrode area (cm^2), D_0 the diffusion coefficient (cm^2/s), C_0^* bulk concentration (mol/cm^2), Q_{dl} the capacitive charge (C) and $nFA\Gamma_0$ the charge from the reduction of Γ_0 (mol/cm^2) of adsorbed $[Ru(NH_3)_6]^{3+}$. The surface excess term Γ_0 denotes the amount of redox marker confined at the surface of the electrode. The difference between the chronocoulometric intercepts at time zero from the experiments performed under identical conditions with and without the redox marker yields the surface term. The surface density on the electrode surface can be calculated from this term using the relation in Eqn. 3:

$$\Gamma_{\mathrm{DNA}} = \Gamma_0 (z/m)(N_A) \qquad (3)$$

where Γ_{DNA} is the surface coverage of DNA, m is the number of bases in the probe ssDNA, z is the charge of the redox molecule and N_A is Avogadro's number.

The photoelectrochemical measurements were performed in a custom electrochemical cell allowing for the direct illumination of the electrode surface. The electrolyte was 0.1 M potassium phosphate buffer (pH 7) with 0.05 M EDTA. The change in electrode potential was monitored with chronoamperometry. Therefore the potential was stepped to 0.7 V versus $Ag_{(s)}$/AgCl while the current was monitored as a function of time. Electrochemical oxidation (stripping) of the gold nanoparticles on the ITO surface was performed in 0.5 M KCl at a scan rate of 100 mV/s. The cyclic voltammograms (CV) of the oxidation of $FeCl_2$ (100 mM), catalyzed by the gold nanoparticles were performed at a scan rate of 100 mV/s.

Thermographic Measurements. The modified ITO surfaces were illuminated with 532 nm light from a frequency doubled quasi-CW Nd:YAG laser (Coherent Antares 76-Nd:YAG laser) and the change in surface temperature was monitored by infrared (IR) thermography (Inframetrics 740). The laser beam was focused to approximately 1 mm diameter and the light intensity was adjusted to 1 W.

Atomic Force Microscopy (AFM). The ITO surface modified with ssDNA and hybridized with 10 nm gold nanoparticle labeled complimentary target ssDNA was imaged by Digital Instruments Nanoscope IIIa Scanning Probe Microscope in tapping mode. The AFM images were $1\mu m^2$ with a height scale of 50 nm.

Results and Discussion

Characterization of ssDNA Modified ITO Surfaces

Figure panels 1A and 1B show the XPS spectra of In $3d_{5/2,3/2}$ (444.4, 452.0 eV) and Sn $3d_{5/2,3/2}$ (486.5, 494.9 eV), respectively, for bare ITO (solid), ITO modified with a monolayer of 12-phosphonododecanoic acid (short dash) and ITO modified with ssDNA coupled through a monolayer of 12-PDA (long dash). These spectra show that the intensity for both metals decreased as the monolayer of 12-PDA was formed on the ITO surface relative to bare ITO. The intensities of indium and tin decreased further as ssDNA was chemically bound to the monolayer of 12-PDA using EDC-coupling. The decrease in XPS intensities with each step in the modification of the surface is consistent with surface modification first with 12-PDA and then with ssDNA. To confirm the presence of ssDNA on the surface, Figure 1C shows the XPS N 1s (400.1 eV) spectra of ITO modified with a

monolayer of 12-PDA (long dash) and ITO modified with ssDNA coupled through a monolayer of 12-PDA (short dash) fitted to a Gaussian line shape (solid). Nitrogen is not present in the 12-PDA modified surface but is present in the ssDNA modified surface indicative of successful chemical attachment of ssDNA to the ITO substrate.

Figure 2A shows the reflectance FTIR spectra of ITO modified with a monolayer of 12-PDA (solid) coupled to ssDNA (short dashed). The FTIR spectra of the 12-PDA monolayer contains a vibrational mode at 1717 cm^{-1} corresponding to the carbonyl stretch of the carboxylic acid functional group of 12-PDA.[19] However, when the surface is subsequently modified with ssDNA the maximum intensity shifts to 1706 cm^{-1}. This band is broader due to the presence of DNA and contains multiple vibrational modes in the 1500 – 1800 cm^{-1} region due to NH_2 bending and carbonyl stretching modes from the nucleobases in the DNA (with a possible contribution from the N-H bending of the amide bond to 12-PDA).[13] Density functional theory (DFT) calculations were used to model the vibrational spectra. Figure 1B shows the DFT calculated IR spectra of 12-phosphonododecanoic acid (solid), 12-phosphonododecanamide (short dashed) and ssDNA (long dashed) calculated from a weighted average of the calculated IR spectra of the individual nucleosides fit to a Gaussian width of (10 cm^{-1}). DFT methods calculated the carbonyl stretching frequency of 12-PDA to be 1727 cm^{-1} with a decrease in energy to 1723 cm^{-1} as an amide bond was formed with NH_3 as a model system. This shift to lower energy is in qualitative agreement with the experimental results and supports the assignment of the carbonyl stretching vibration and is downshift due to hydrogen bonding. The DFT calculated spectra of the nucleosides (a model for ssDNA) show several modes throughout this region (1500 – 1800 cm^{-1}) that are

due primarily to NH_2 bending and carbonyl stretching motions of the nucleobases, in agreement with experiment.

The chronocoulometric (CC) response of the indium tin oxide (ITO) substrate modified with probe ssDNA on the surface is shown in Figure 3 showing the ITO sample modified with ssDNA in Tris buffer (dotted line) and in the presence of $[Ru(NH_3)_6]^{3+}$ (dashed line) extrapolated (solid line) to time zero. $[Ru(NH_3)_6]^{3+}$ binds to the anionic phosphate backbone of ssDNA on the surface in a ratio of 1:3 and therefore the surface coverage of DNA can be determined as described previously. [11] The surface coverage of ssDNA on the ITO surface was found to be $2.2(\pm0.3)x10^{13}$ molecules/cm^2 as calculated from chronocoulometry. This value is approximately an order of magnitude higher than self-assembled monolayers of thiol modified ssDNA and 6-mercapto-1-hexanol on gold surfaces reported under similar conditions.[11] Assuming a diameter of 1 nm for ssDNA, an atomically flat surface and hexagonal close packing the maximum surface coverage would be $7.4x10^{13}$ molecules/cm^2.

Detection of Hybridization by Au-Nanoparticle DNA Conjugates on ITO Surfaces

After the characterization of the ssDNA modified ITO surfaces, the detection of DNA hybridization to this surface was detected through the use of 10 nm gold colloid labeled target ssDNA. The gold nanoparticle label on the target ssDNA allowed for detection of successful surface DNA hybridization by detecting the presence of the gold nanoparticles on the modified ITO surface. The gold nanoparticles were detected by XPS, stripping voltammetry, thermography, photoelectrochemistry (chronoamperometry) and cyclic voltammetry (CV).

Figure 4A shows the XPS Au $4f_{7/2,5/2}$ (83.3, 87.0 eV) spectra while Figure 4B shows the stripping voltammograms in a 0.5 M KCl solution of ITO modified with ssDNA coupled through a monolayer of 12-PDA (long dash) exposed to the complementary (solid) or non-complementary (short dash) ssDNA labeled with a 10 nm gold nanoparticle (1nM). The presence of gold nanoparticles on these ssDNA modified surfaces reveals DNA hybridization between the probe ssDNA on the surface and the target ssDNA labeled with the gold colloid. This hybridization occurred at a concentration of 1 nM of the gold nanoparticle / ssDNA conjugate and the solution was heated to 45 °C for one hour and then allowed to cool overnight. The XPS spectrum for the complementary ssDNA shows the presence of gold on the surface and the stripping voltammogram shows an oxidative (864 mV) and reductive (465 mV) peak of gold on the surface. Therefore both of these techniques show that DNA hybridization occurred on the surface. These experimental measurements also show selective DNA hybridization because the signals detected for the complementary ssDNA are significantly larger than the corresponding signall from the non-complementary ssDNA. The XPS spectra suggest that the non-specific binding to the surface (as determined from a comparison of the gold detected between the surfaces exposed to either the non-complementary or complementary target ssDNA) is ~ 32 % however the XPS spectra were not normalized to an internal reference and possible orientation affects were not taken into account that could result in some error in this value. Therefore stripping voltammetry was used to quantitate non-specific absorption of gold colloid labeled non-complementary ssDNA to the ssDNA modified ITO surfaces. The stripping voltammograms showed in Figure 4B illustrate that non-specific binding of the non-complementary ssDNA to the ssDNA modified

ITO surface based on the integrated area of the reductive peak of the gold was ~ 13 %. This value represents the amount of non-specific adsorption of the gold nanoparticle / ssDNA conjugate to the ITO surface more accuarately than the XPS results. The corresponding AFM image ($1\mu m^2$ image with a 50 nm height scale) captured in tapping mode for the hybridization of the complementary ssDNA / gold nanoparticle conjugate to the ssDNA modified ITO surface is shown in Figure 4C. This image allows the number of gold nanoparticles to be counted in this area. Based on the surface coverage of probe ssDNA on the ITO surface and the surface coverage of the gold nanoparticle / target ssDNA conjugates (assuming that each nanoparticle represents one surface DNA hybridization event), a surface DNA hybridization efficiency of 0.4±0.1 % can be estimated for this system.

The presence of gold nanoparticles attached to the DNA modified ITO surface through DNA hybridization was also detected by thermography, photoelectrochemistry and cyclic voltammetry (CV). The thermographic and photoelectrical experiments are based on laser induced temperature jumps where the plasmon band of the gold nanoparticles bound to the DNA modified ITO surface through DNA hybridization is excited by 532 nm laser radiation. The temperature increase was either monitored on a dry surface using a thermographic camera or in solution using a home-built electrochemical cell that allowed the sample to be irradiated while monitoring the resulting current from the temperature increase.[33] The presence of the gold nanoparticles was also confirmed by stripping voltammetry where the oxidation and reduction of the gold nanoparticles is detected (data not shown). For these experiments, the hybridization was carried out for 19 hours at 37 °C in a shaking incubator.

After irradiating the hybridized sample for 30 seconds with 532 nm radiation (100 W/cm^2), the gold nanoparticles attached to the ITO substrate through DNA hybridization (1 nM gold nanoparticle / ssDNA conjugate) yielded a temperature increase of 3.9 °C over background (ssDNA modified ITO). The change in current due to this temperature increase was monitored with chronoamperometry where the potential was stepped to 0.7 V versus $Ag_{(s)}$/AgCl and the current was monitored over time (Figure 5A). When the sample was irradiated with 532 nm light, the current deceased rapidly at first and then slowly leveled off over a period of approximately 90 seconds. At this point the laser was switched off and it was observed that the current returned to its initial value. The fast components of the temperature change in this experiment are typical for laser induced temperature jump experiments.[37-40]

DNA hybridization on ITO surfaces was also detected by the oxidation of a specific redox species catalyzed by gold nanoparticles. The identity of the redox species is crucial because the electron transfer kinetics of this species must be slow on bare ITO but fast in the presence of gold nanoparticles. The change in electron transfer rate can easily be detected using cyclic voltammetry. The best redox species for this type of electrochemical detection strategy was determined to be $FeCl_2$.

The presence of $FeCl_2$ in solution generated oxidation currents much larger than that recorded by electrochemical stripping and thus allowed for a lower limit of detection of gold nanoparticles bound to the ITO electrode through DNA hybridization. The results of this technique are shown in Figure 6A where a range of concentrations of target gold nanoparticle / ssDNA conjugates was used to hybridize to ssDNA modified ITO surfaces. The

concentrations of the gold nanoparticle / ssDNA conjugate solutions used in these experiments were 1 nM, 500 pM, 100 pM and 10 pM. Each of these solutions were hybridized to the ssDNA modified ITO surfaces by maintaining the solution at 45 °C for one hour and then allowing it to cool to room temperature overnight. The presence of the gold nanoparticle-ssDNA conjugates were then detected electrochemically. The currents measured at the maximum of the oxidation (887 mV) and reductive peak (109 mV) recorded by CV were found to increase linearly with the target concentration in solution (Figure 6B). The minimum amount of labeled target detected corresponded to 100 pM of gold nanoparticles modified with the target ssDNA.

In order to decrease the limit of detection, the hybridization conditions were varied to increase the hybridization efficiency. For this system, the hybridization efficiency was found to increase when hybridization was performed at 37 °C for 19 hours in a shaking incubator. Figure 7 shows the electrochemical results for the detection of gold nanoparticles attached to the ITO surface through DNA hybridization using $FeCl_2$ as the redox species in solution. Three gold nanoparticle / ssDNA target concentrations were used: 100, 10 and 1 pM. Figure 7 shows that it was possible to detect gold nanoparticles modified with ssDNA targets bound to the ITO substrate for concentrations as low as 10 pM.

Conclusion

Indium tin oxide (ITO) thin films were successfully modified with single stranded DNA. This modification was achieved by coupling the amine group of 5'-$H_2N(CH_2)_3$ labeled ssDNA probes to the carboxylic acid moiety of a monolayer of 12-

phosphonodododecanoic acid on the ITO surface by EDC coupling to create an amide linkage. The resulting surface was characterized by X-ray photoelectron and reflectance FTIR spectroscopy to confirm the presence of the DNA on the surface. The surface coverage of the DNA on the ITO surface was found to be $2.2(\pm 0.3)x10^{13}$ molecules/cm^2 by chronocoulometry. Surface DNA hybridization to ssDNA modified ITO surfaces was detected by labeling ssDNA targets with 10 nm gold nanoparticles. Therefore the detection of gold nanoparticles on the ITO surface confirmed selective DNA hybridization. The gold nanoparticles were detected by XPS, stripping voltammetry, AFM, thermography and photoelectrochemistry (chronoamperometry) for a 1 nM gold nanoparticle / target ssDNA concentration in the hybridization solution. However target concentrations as low as 10 pM gold nanoparticles modified with target ssDNA were detected through the electrochemical oxidation of $FeCl_2$ catalyzed by the gold nanoparticles bound to the ITO surface via DNA hybridization.

Acknowledgments

This work was done in collaboration with Marc Sauthier (NCSU), Stephan Kraemer (NCSU), Ryan R. Fuierer (NCSU), Selina Moses (NCSU), Lisa B. Lowe (NCSU), Chiamaka Agbasi (NCSU), Daniel L. Feldheim (NCSU) and Stefan Franzen (NCSU). Scott Brewer was supported by NIH Biotechnology Training Grant T32-GM08776. Marc Sauthier, Selina Moses and Lisa Lowe were supported by Applied Biosystems, Inc. Support and computational facilities were provided by the North Carolina State University High

Performance Computing Resource. We would like to thank Dr. Kimberly Briggman at NIST for her help in the acquisition of the reflectance FTIR spectra.

References

(1) Herne, T. M.; Tarlov, M. J. *J. Am. Chem. Soc.* **1997**, *119*, 8916-8920.

(2) Taton, T. A.; Mirkin, C. A.; Letsinger, R. L. *Science* **2000**, *289*, 1757-1760.

(3) Ulman, A. *Chemical Reviews* **1996**, *96*, 1533-1554.

(4) Fodor, S. P. A.; Read, J. L.; Pirrung, M. C.; Stryer, L.; Lu, A. T.; Solas, D. *Science* **1991**, *251*, 767-773.

(5) Lockhart, D. J.; Winzeler, E. A. *Nature* **2000**, *405*, 827-836.

(6) Bulyk, M. L.; Gentalen, E.; Lockhart, D. J.; Church, G. M. *Nat. Biotechnol.* **1999**, *17*, 573-577.

(7) Chee, M.; Yang, R.; Hubbell, E.; Berno, A.; Huang, X. C.; Stern, D.; Winkler, J.; Lockhart, D. J.; Morris, M. S.; Fodor, S. P. A. *Science* **1996**, *274*, 610-614.

(8) He, L.; Musick, M. D.; Nicewarner, S. R.; Salinas, F. G.; Benkovic, S. J.; Natan, M. J.; Keating, C. D. *J. Am. Chem. Soc.* **2000**, *122*, 9071-9077.

(9) Brockman, J. M.; Frutos, A. G.; Corn, R. M. *J. Am. Chem. Soc.* **1999**, *121*, 8044-8051.

(10) Esch, M. B.; Locascio, L. E.; Tarlov, M. J.; Durst, R. A. *Anal. Chem.* **2001**, *73*, 2952-2958.

(11) Steel, A. B.; Herne, T. M.; Tarlov, M. J. *Anal. Chem.* **1998**, *70*, 4670-4677.

(12) Steel, A. B.; Herne, T. M.; Tarlov, M. J. *Bioconjugate Chem.* **1999**, *10*, 419-423.

(13) Brewer, S. H.; Anthireya, S. J.; Lappi, S. E.; Drapcho, D. L.; Franzen, S. *Langmuir* **2002**, *18*, 4460-4464.

(14) Cao, Y. W.; Jin, R.; Mirkin, C. A. *J. Am. Chem. Soc.* **2001**, *123*, 7961-7962.

(15) Demers, L. M.; Mirkin, C. A.; Mucic, R. C.; Reynolds, R. A.; Letsinger, R. L.; Elghanian, R.; Viswanadham, G. *Anal. Chem.* **2000**, *72*, 5535-5541.

(16) Sauthier, M.; Carroll, R.; Gorman, C.; Franzen, S. *Langmuir* **2002**, *18*, 1825-1830.

(17) Gardner, T.; Frisbie, C.; Wrighton, M. *J. Am. Chem. Soc.* **1995**, *117*, 6927-6933.

(18) Yan, C.; Zharnikov, M.; Golzhauser, A.; Grunze, M. *Langmuir* **2000**, *16*, 6208-6215.

(19) Brewer, S. H.; Brown, D. A.; Franzen, S. *Langmuir* **2002**, *18*, 6857-6865.

(20) Markovich, I.; Mandler, D. *Journal of Electroanalytical Chemistry* **2001**, *500*, 453-460.

(21) Oh, S.; Yun, Y.; Kim, D.; Han, S. *Langmuir* **1999**, *15*, 4690-4692.

(22) VanderKam, S.; Gawalt, E.; Schwartz, J.; Bocarsly, A. *Langmuir* **1999**, *15*, 6598-6600.

(23) Purvis, K.; Lu, G.; Schwartz, J.; Bernasek, S. *The Journal of the American Chemical Society* **2000**, *122*, 1808-1809.

(24) Popovich, N. D.; Yen, B. K.; Wong, S. *Langmuir* **2003**, *19*, 1324-1329.

(25) Armistead, P.; Thorp, H. *Analytical Chemistry* **2000**, *72*, 3764-3770.

(26) Armistead, P.; Thorp, H. *Analytical Chemistry* **2001**, *73*, 558-564.

(27) Ambrosini, A.; Duarte, A.; Poeppelmeier, K. R.; Lane, M.; Kannewurf, C. R.; Mason, T. O. *J. Solid State Chem.* **2000**, *153*, 41-47.

(28) Hamberg, I.; Hjortsberg, A.; Granqvist, C. *Applied Physics Letters* **1982**, *40*, 362-364.

(29) Hamberg, I.; Granqvist, C. G.; Berggren, K. F.; Sernelius, B. E.; Engstrom, L. *Physical Review B* **1984**, *30*, 3240-3249.

(30) Hamberg, I.; Granqvist, C. G. *J. Appl. Phys.* **1986**, *60*, R123-R159.

(31) Brewer, S. H.; Franzen, S. *J. Alloy. Compd.* **2002**, *338*, 73-79.

(32) Brewer, S. H.; Franzen, S. *Journal of Physical Chemistry B* **2002**, *106*, 12986-12992.

(33) Lowe, L. B.; Brewer, S. H.; Kramer, S.; Fuierer, R. R.; Qian, G. G.; Agbasi-Porter, C. O.; Moses, S.; Franzen, S.; Feldheim, D. L. **2003**, *125*, 14258-14259.

(34) Loweth, C. J.; Caldwell, W. B.; Peng, X. G.; Alivisatos, A. P.; Schultz, P. G. **1999**, *38*, 1808-1812.

(35) Delley, B. *J. Phys. Chem.* **1990**, *92*, 508-517.

(36) Perdew, J. P.; Chevary, J. A.; Vosko, S. H.; Jackson, K. A.; Pederson, M. R.; Singh, D. J.; Fiolhais, C. *Phys. Rev. B* **1992**, *46*, 6671-6687.

(37) Smalley, J. F.; Krishnan, C. V.; Goldman, M.; Feldberg, S. W.; Ruzic, I. **1988**, *248*, 255-282.

(38) Smalley, J. F.; Geng, L.; Feldberg, S. W.; Rogers, L. C.; Leddy, J. **1993**, *356*, 181-200.

(39) Smalley, J. F.; Chalfant, K.; Feldberg, S. W.; Nahir, T. M.; Bowden, E. F. **1999**, *103*, 1676-1685.

(40) Smalley, J. F.; Geng, L.; Chen, A.; Feldberg, S. W.; Lewis, N. S.; Cali, G. **2003**, *549*, 13-24.

Scheme

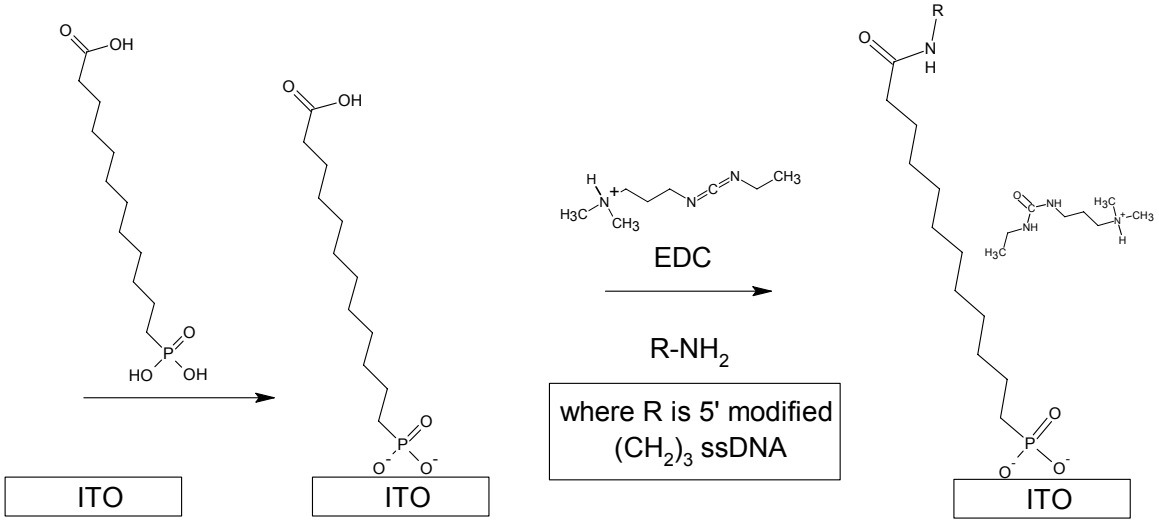

Scheme 1. Modification of ITO with single stranded DNA through the formation of an amide bond between the carboxylic acid functional group of a monolayer of 12-phosphonododecanoic acid with the primary amine of 5' modified $H_2N(CH_2)_3$ ssDNA.

Figures

Figure 1. XPS spectra of In $3d_{5/2,3/2}$ (A) and Sn $3d_{5/2,3/2}$ (B) for bare ITO (solid), ITO modified with a monolayer of 12-phosphonododecanoic acid (short dash) and ITO modified with ssDNA coupled through a monolayer of 12-phosphonododecanoic acid (long dash). C. XPS N 1s spectra of ITO modified with a monolayer of 12-phosphonododecanoic acid (long dash) and ITO modified with ssDNA coupled through a monolayer of 12-phosphonododecanoic acid (short dash) fitted to a Gaussian line shape (solid).

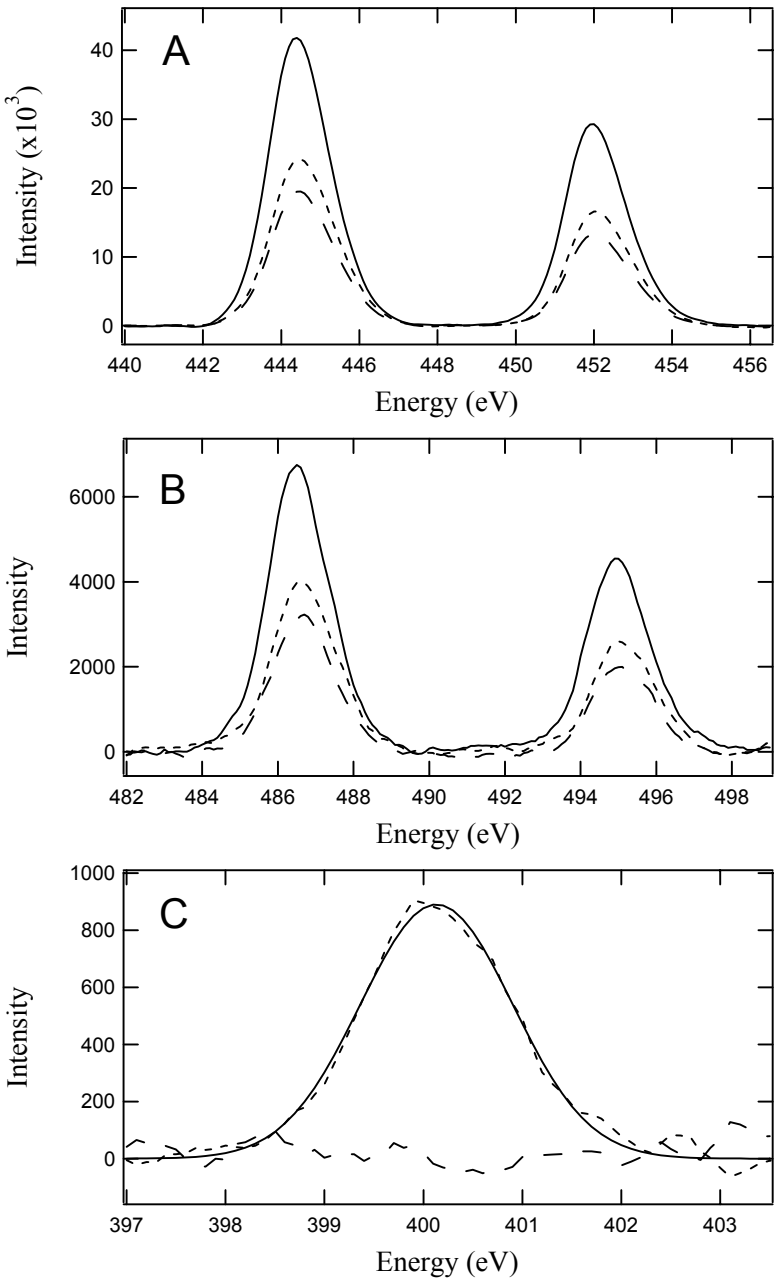
A
Intensity (x10^3)
40
30
20
10
0
440
442
444
446
448
450
452
454
456
Energy (eV)
B
Intensity
6000
4000
2000
0
482
484
486
488
490
492
494
496
498
Energy (eV)
C
Intensity
1000
800
600
400
200
0
397
398
399
400
401
402
403
Energy (eV)

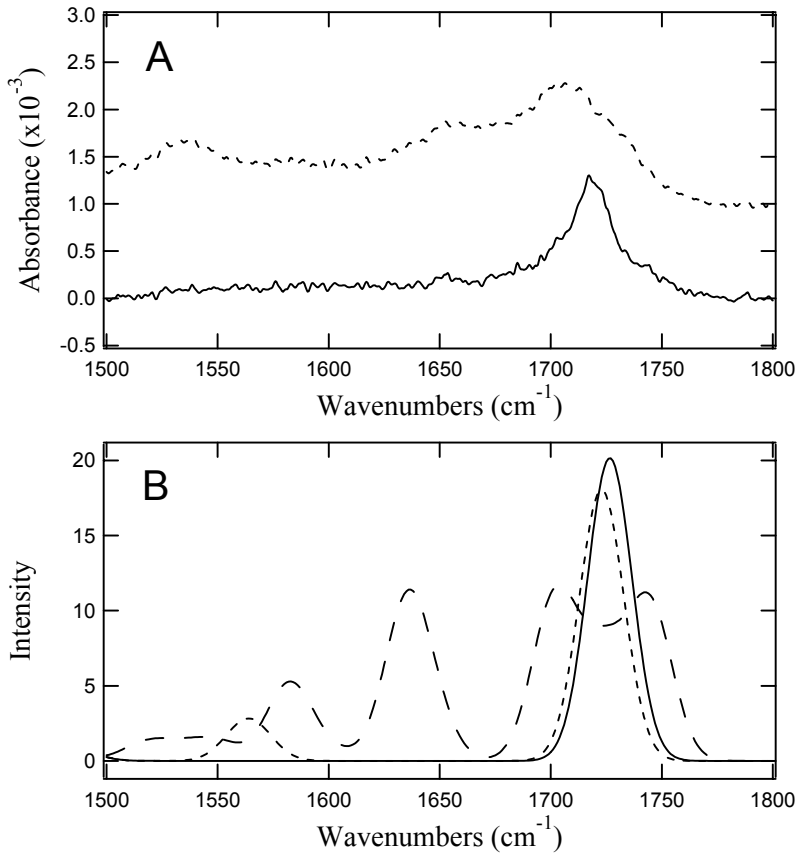

Figure 2. A. Reflectance FTIR spectra of ITO modified with a monolayer of 12-phosphonododecanoic acid (solid) coupled to ssDNA (short dashed) recorded at an incident angle of 80 degrees with p-polarized radiation. B. Density functional theory (DFT) calculated IR spectra of 12-phosphonododecanoic acid (solid), 12-phosphonododecanamide (short dashed) and ssDNA (long dashed) calculated from a weighted average of the calculated IR spectra of the individual nucleosides fit to a Gaussian width of 10 cm^{-1}.

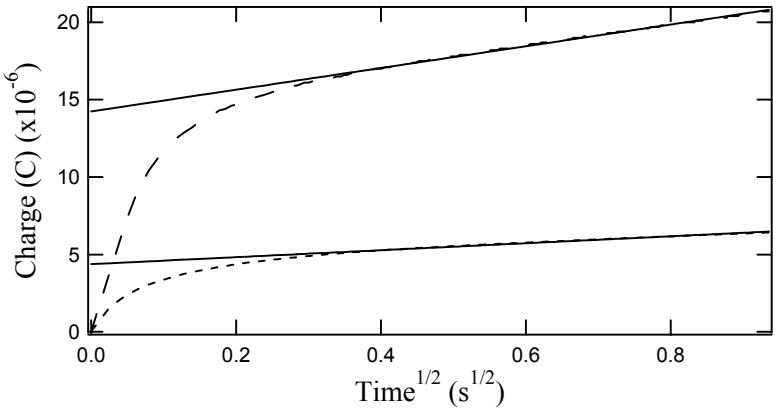

Figure 3. Chronocoulometry of a ssDNA modified ITO surface with (long dash) or without (short dash) $[Ru(NH_3)_6]^{3+}$ in the electrochemical cell.

Figure 4. XPS Au $4f_{7/2,5/2}$ spectra (A) and stripping voltammograms (in a 0.5 M KCl solution) (B) of ITO modified with ssDNA (long dash XPS spectrum (A)) exposed to the complementary (solid) or non-complementary (short dash) ssDNA labeled with 10 nm gold nanoparticles (1 nM). C. The AFM image ($1\mu m^2$ with a height scale of 50 nm) of ITO modified with ssDNA exposed to the complementary ssDNA labeled with 10 nm gold nanoparticles (1 nM).

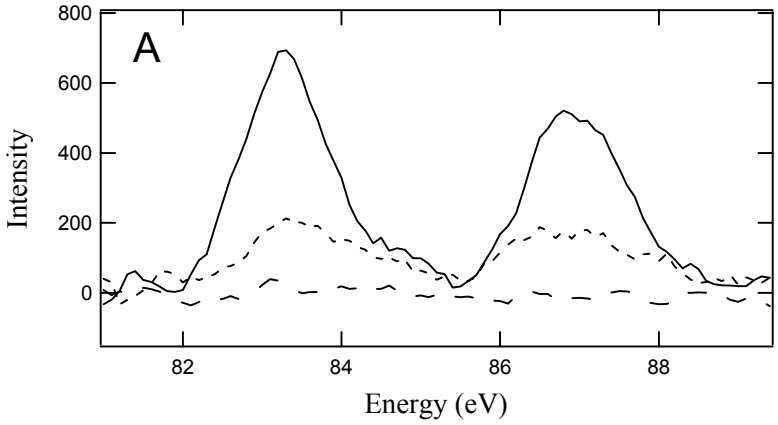
A
800
600
400
200
0
Intensity
82
84
86
88
Energy (eV)

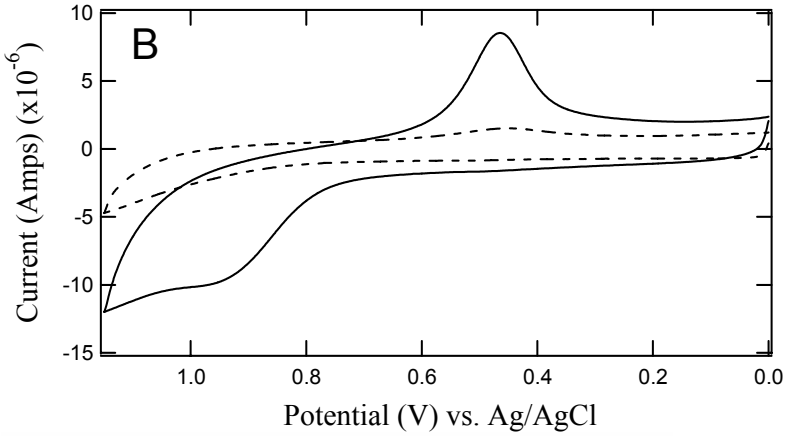
B
10
5
0
-5
-10
-15
Current (Amps) (x10-6)
1.0
0.8
0.6
0.4
0.2
0.0
Potential (V) vs. Ag/AgCl

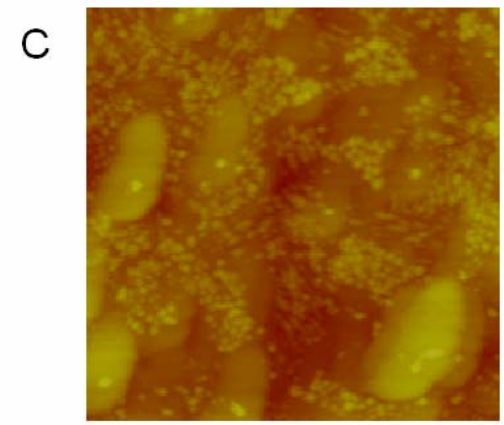
C

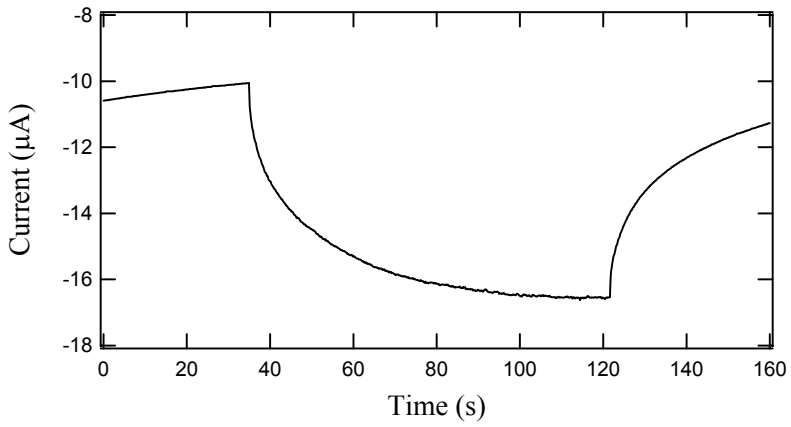

Figure 5. Anodic current versus time for an ITO electrode modified with ssDNA and hybridized with the complimentary ssDNA gold-nanoparticle conjugate (1 nM). The measurement was done in 0.1 M potassium phosphate buffer with 0.05 M EDTA. At 30 s the sample was illuminated with 532 nm laser light with a power density of approximately 100 W/cm^2. After 90 s the laser light was switched off. The potential was held at 0.7 V versus a Ag(s)/AgCl reference electrode that was not fixed isothermally.

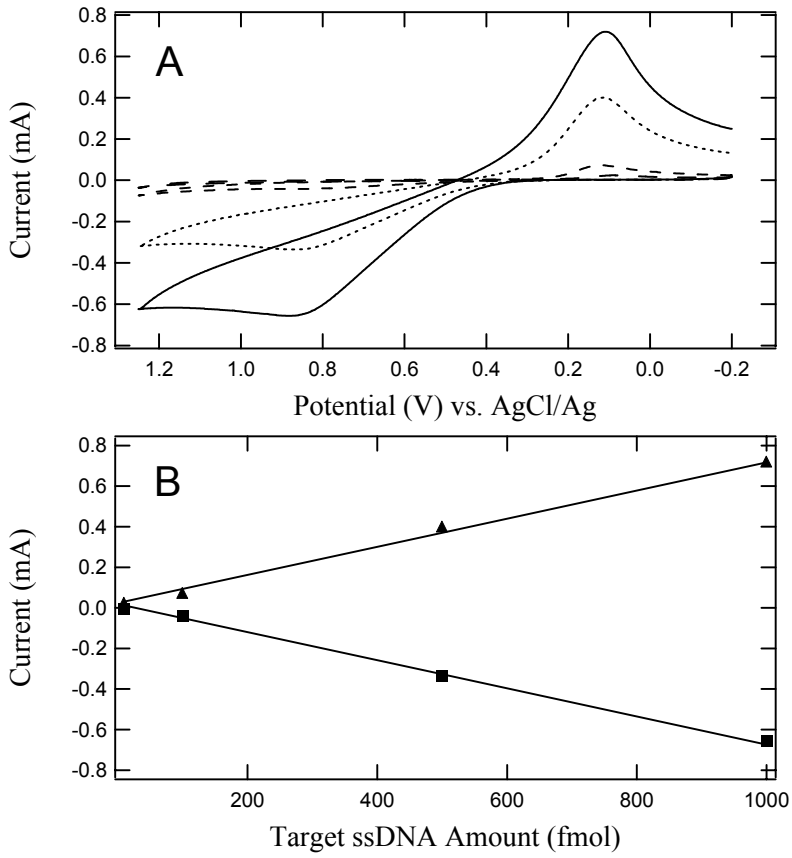

Figure 6. A. Electrochemical response for 100 mM $FeCl_2$ (scan rate 100 mV/s) as a function of the amount of target ssDNA / gold nanoparticle conjugate in the hybridization solution. The four target concentrations were 1 nM, 500 pM, 100 pM and 10 pM of the gold nanoparticles (modified with the target ssDNA). The hybridization was allowed to proceed for 1 hour at 45°C and the solution was then gradually cooled to room temperature overnight. B. Electrochemical response as a function of the amount of the gold nanoparticle / target ssDNA in the hybridization solution at 887 mV (squares) for the oxidation current and 109 mV (triangles) for the reduction current fit globally to a straight line (solid).

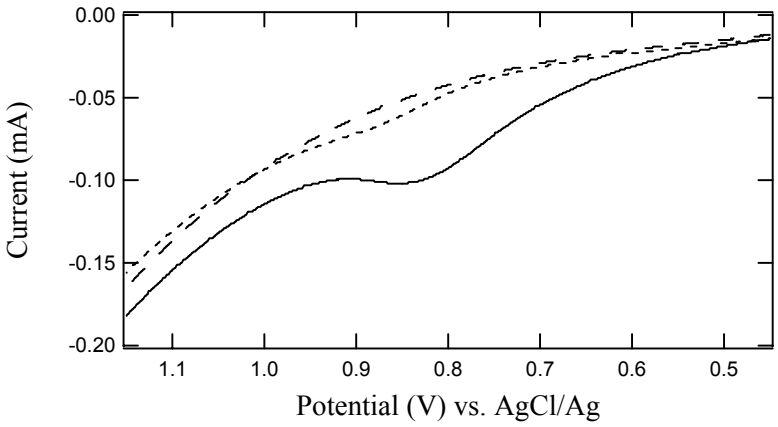

Figure 7. Electrochemical response for 100 mM $FeCl_2$ (scan rate 100 mV/s) as a function of the amount of target ssDNA in the hybridization solution with improved hybridization conditions. The three target amounts were 100 pM, 10 pM and 1 pM of the gold nanoparticles (10 nm diameter) modified with the target single stranded DNA. The hybridization was allowed to proceed at 37°C for nineteen hours in a shaking incubator.

Chapter 9

Investigation of the Electrical and Optical Properties of Iridium Oxide by Reflectance FTIR Spectroscopy and Density Functional Theory Calculations

Abstract

Variable angle reflectance FTIR spectroscopy was used to investigate the optical properties of iridium oxide thin films deposited on glass substrates in the near-IR spectral region. The reflectance was studied as a function of incident angle and wavenumber for p-polarized radiation. The Drude free-electron model along with the Fresnel equations of reflection were utilized to fit the experimental reflectance FTIR data to determine the plasma frequency and electronic scattering time of this conducting metal oxide thin film. These experimental studies were complemented by density functional theory (DFT) calculations of the electronic and optical properties of iridium oxide. The calculations used the crystal structure of iridium oxide with periodic boundary conditions. These theoretical studies yielded the optical band gap, Fermi energy, charge carrier concentration, effective electron mass, plasma frequency and the conduction band orbital character of iridium oxide. The computed dependence of the optical band gap, Fermi energy, charge carrier concentration and the plasma frequency on compression or expansion of the iridium oxide unit cell was investigated.

Introduction

Iridium oxide (IrO_2) is a conducting metal oxide whose conduction band is comprised of d electrons from iridium.[1,2] Iridium oxide thin films can be deposited on solid substrates such as glass in a variety of techniques such as reactive sputtering, electrodepostion, spray pyrolysis technique, sol-gel and thermal or anodic oxidation.[3-8] These thin films have been used for a variety of applications that utilize the electrical and optical properties of iridium

oxide. For instance, iridium oxide thin films have been used for electrochromic devices, electrocatalysis, optical information storage and pH sensing.[3,4,6-10] Iridium oxide differs from other conducting metal oxides such as indium tin oxide (ITO) whose conduction band is comprised of s and p electron character[11] in that the conduction band in iridium oxide is mainly of d character. However, iridium oxide thin films exhibit a plasma frequency in the near-IR spectral region similar to indium tin oxide (ITO) and fluorine doped tin oxide (SFO) thin films despite difference in the conduction band orbital character.[1,2,12] The position of the plasma frequency is critical to the properties of iridium oxide, since this value is dependent on the charge carrier concentration of the material that is related to the electrical conductivity.[13] However, the electrical and optical properties of metal oxide thin films such as ITO[14-18] and iridium oxide[3,4] are strongly dependent on the deposition and annealing procedures used. The optical and electronic properties of a variety of metal oxides such as indium oxide, tin oxide, indium tin oxide and zinc oxide have been studied using a variety of theoretical methods.[19-23] However, the correlation of optical and electronic properties of iridium oxide thin films has been less studied.[1,2]

In this study, optical measurements of iridium oxide thin films deposited on glass substrates were complemented with density functional theory (DFT) calculations of the optical and electrical properties of iridium oxide. The position of the plasma frequency of iridium oxide thin films on glass substrates was determined by reflectance FTIR spectroscopy. The reflectance of these films was investigated as a function of the incident angle of the IR radiation and wavenumber with p-polarized radiation. The Drude free-electron model was used to model the frequency dependent dielectric function of iridium

oxide, while the Fresnel equations were used to fit the experimental reflectance data to obtain values of the plasma frequency and electronic scattering time of iridium oxide thin films on glass substrates. The optical band gap, Fermi energy, charge carrier concentration, effective electron mass and the plasma frequency were calculated using DFT for iridium oxide. The optical and electronic parameters (except the effective electron mass) were investigated as a function of the compression or expansion of the iridium oxide unit cell. The conduction band orbital character was also calculated for iridium oxide. These calculations were based on the crystal structure of bulk iridium oxide and oxygen deficient iridium oxide. The DFT calculations are relevant to the properties of thin films of metal oxides demonstrated by previous theoretical work.[11,19,21,22]

Materials and Methods

Iridium Oxide Thin Films. Iridium oxide (IrO_2) thin films were formed on glass substrates cleaned in methanol in an ultrasonic bath. The IrO_2 films were deposited using DC magnetron reactive sputtering with an Ir target. The Ar:O_2 gas mixture was 7:3 with a total pressure of 30 mTorr with a DC power of 150 W. The deposition rate was ~1 nm/s with the film thickness determined by Alphastep profilometry. The IrO_2 thin films were 110 nm thick on the glass substrates and were annealed in a standard furnace with fast-fire technique at 700 °C in an air atmosphere for 10 minutes. After annealing XRD analysis showed that IrO_2 was predominant although some Ir was still present (data not shown).

Reflectance FTIR Spectroscopy. The variable angle reflectance FTIR spectra were recorded using a Spectra-Tech variable angle reflectance attachment (Model 500) in a Bruker

IFS v/s spectrometer with p-polarized IR radiation. The angle of incidence ranged from 40 - 80 degrees relative to the surface normal. A ratio of the single beam spectra of IrO_2 thin films on a glass substrate to a single beam spectrum of a gold surface was performed to obtain the reflectance spectra of IrO_2. A tungsten source, quartz beamsplitter and a liquid nitrogen cooled InSb detector was used in the spectral range 3,000-12,500 cm^{-1}. All IR spectra were the result of the average of 256 scans at a resolution of 8 cm^{-1} and were recorded at room temperature under vacuum.

Computational Methods.

Drude Free-Electron Model. The Drude free-electron model describes the dielectric function ($\varepsilon(\omega)$) of a material by the plasma frequency and electronic scattering time as shown in Eqn. 1:[13]

$$\varepsilon(\omega) = \varepsilon_\infty - \omega_p^2 \frac{1}{\omega^2 + \frac{i\omega}{\tau}} \qquad (1)$$

where ε_∞ is the high-frequency dielectric constant, ω_p is the plasma frequency, ω is the frequency and τ is the electronic scattering time. The plasma frequency is defined in Eqn. 2:[13]

$$\omega_p^2 = \frac{ne^2}{m\varepsilon_o} \qquad (2)$$

where n is the free charge carrier concentration and m is the free electron mass. Eqn.3 relates the complex refractive index of the material to the dielectric function:[13]

$$\varepsilon(\omega)^{\frac{1}{2}} = N(\omega) = n(\omega) + ik(\omega) \qquad (3)$$

where N is the complex refractive index, n is the real, dispersive component and k is the imaginary, absorptive component of the refractive index.

Two-Phase Fresnel Equations for Reflectance. The complex refractive index can then be used in the two-phase Fresnel equations to model the reflectance for a single dielectric interface for a given angle of incidence and polarization of light. Eqn. 4-6 shows the calculated reflectance using the two-phase Fresnel equations for the air (n=1, k=0) / IrO_2 interface for p-polarized radiation:[24]

$$r_p = \frac{-N\cos\theta + \cos\varphi}{N\cos\theta + \cos\varphi} \qquad (4)$$

where

$$\cos\varphi = \left(1 - \frac{\sin^2\theta}{N^2}\right)^{\frac{1}{2}} \qquad (5)$$

In these equations, r is the amplitude of the reflected light (relative to incident light amplitude), p represent p-polarization, N is the complex refractive index of the material, θ is the angle of incidence relative to the surface normal and ϕ is the complex angle between the refracted light to the surface normal. Then the power reflectivity for p-polarization is shown in Eqn. 6:[24]

$$R_p = \left| r_p \right|^2 \qquad (6)$$

where R_p is the power reflectivity for p-polarization which can be used to fit experimental reflectance data.

Density Functional Theory Calculations. The density functional theory (DFT) calculations were performed using the quantum chemical software DMol3 (Accelrys, Inc.).[25] The calculations were performed on the iridium oxide unit cell containing 2 IrO_2 units that

has a rutile-type structure.[26] The unit cell has lattice parameters of 4.5051, 4.5051 and 3.1586 Å. The calculations used periodic boundary conditions to determine bulk electronic and optical properties of the material. The DNP (double numerical plus polarization function) basis set was employed with effective core potentials used for iridium below the 5s orbital. The basis set used the O(1s, 2(2s), 2(2p), 2(3d)) and Ir(5s, 5p, 2(5d), 2(6s), 6p) orbitals for the two atoms with an atomic cutoff of 3.2 or 5.5 Å. The Perdew and Wang GGA functional was used for all of the DFT calculations.[27] The band structure calculations at multiple k-points were performed with the canonical ensemble approach at T = 0 K (known as the FERMI option),[28] while the rest of the calculations used the grand canonical ensemble approach that permits partial electron occupation which is well suited for charge carrier calculations (known as the THERMAL option).[29] The effective electronic temperature in the THERMAL calculations is 0.02 Hartrees or ~ 6,300 K.[29] This high temperature guarantees self-consistent field (SCF) convergence with the THERMAL option.[29] The temperature dependence of the optical band gap, Fermi energy, charge carrier concentration and plasma frequency was investigated. The program InsightII (Accelrys, Inc.) was used to visualize the models and orbitals calculated by DMol3. The DFT calculations were performed at the North Carolina Supercomputing Center (NCSC) on the IBM RS/6000 SP.

Single point energy calculations were performed at the Γ point in the Brillouin zone for the determination of the Fermi energy and charge carrier concentration, while additional points in k-space along high-symmetry lines in the Brillouin zone were performed for the calculation of the band structure for iridium oxide. The charge carrier concentration was

calculated by summing the number of electrons in the conduction band of iridium oxide divided by the volume of the unit cell calculated based on the lattice constants. A primitive (P1) cell was used in the multiple k-points calculations of the electronic band structure. The curvature in the conduction band was fit to Eqn. 7:[13,30]

$$E(k) = E_o + \frac{h^2 k^2}{8\pi^2 m^*} \qquad (7)$$

where E is the energy in eV, E_o is the energy offset depending on where the zero value was chosen, k is the reciprocal wave vector and m^* is the effective free electron mass. Eqn. 7 allowed the determination of m^* for iridium oxide to be made. This value was used in Eqn. 2 above[13] to calculate ω_p, the plasma frequency directly from first principles.

Results and Discussion

The present study combines the use of reflectance FTIR spectroscopy and density functional theory (DFT) calculations to yield insight into the electrical and optical properties of iridium oxide thin films. Through the Drude free-electron model and the Fresnel equations of reflection, the reflectance IR data can be analyzed in terms of the plasma frequency and electronic scattering time of the IrO_2 thin films on glass substrates. The dependence of the thin film reflectance of p-polarized radiation on incident angle and wavenumber serves to determine the frequency dependent dielectric constant experimentally. The DFT calculations of the optical band gap, Fermi energy, charge carrier concentration, plasma frequency and the conduction band orbital character of bulk IrO_2 complement these experimental results.

Reflectance FTIR Spectroscopy of Iridium Oxide Thin Films

Figure 1 shows the variable angle FTIR reflectance spectra of a 110 nm iridium oxide thin film on a glass substrate with p-polarized IR radiation. These spectra were recorded with an incident angle of 40 - 80 degrees from the surface normal in 10 degree increments. These spectra show a significant decrease in the observed reflectance around 6,500 cm^{-1} due to the plasma frequency of IrO_2. At wavenumbers below the plasma frequency the reflectance is high and the reflectance decreases above the plasma frequency. However there is an increase in the reflectance at approximately 10,500 cm^{-1} that has been attributed to d-d intraband transition in iridium oxide.[1,2] Above and below the plasma frequency the reflectance increases with increasing angle. The reflectance minima of this metal oxide thin film at 7,945 cm^{-1} is at an incident angle of 70 degrees. This minimum in the angular dependence of the reflectance spectra is expected and has been seen with metal oxide thin films such as indium tin oxide (ITO) thin films on glass substrates.[12] This minimum of the reflectance of iridium oxide thin films has not been previously reported

Figure 2 shows the experimental (solid) and calculated (dashed) reflectance IR spectra of an iridium oxide thin film (110 nm) on a glass substrate recorded at an incident angle of 60 degrees with p-polarized radiation. The calculated reflectance spectrum used the Drude free-electron model to determine the dielectric function of iridium oxide in the near-IR spectral region while the Fresnel equations of reflectance at a single dielectric interface were used to calculate the reflectance. The fit to the experimental spectrum yielded values of 20,200 cm^{-1} for the plasma frequency and 2.8×10^{-15} seconds for the electronic scattering time using a value of 6.4 for the high frequency dielectric constant.[31] The Drude model yields a

good fit to the experimental reflectance spectrum in the region below the plasma frequency; however the fit deviates from the experimental spectrum at higher energies than the plasma frequency. This fit is expected since the Drude model accurately models the region in the spectra due to free carriers (plasma frequency) but does not model the d-d intraband transitions above the plasma frequency.

DFT Calculated Optical and Electronic Properties of Iridium Oxide

The approach taken to calculate the electronic and optical properties of iridium oxide thin films is to use a thermal population of electrons in the conduction band as a model for the charge carrier density. SCF convergence in the DFT calculations requires electronic temperatures above ~ 2,500 K. Thus the values obtained here are not for direct comparison to room temperature, but rather the results will be used to understand trends in the optical properties. The DFT calculations suggest that oxygen deficiency might play a role in the conductivity of iridium oxide thin films. To qualitatively model oxygen deficiency, three different stoichiometries of iridium to oxygen were compared in order to obtain an indication of the relative enhancement in conductivity and plasma frequency in oxygen depleted thin films.

Figure 3 shows the density functional theory (DFT) calculated electron distribution near the Fermi energy using periodic boundary conditions and the experimental crystal structure of iridium oxide at point Γ. The distribution of the electrons near the band gap at point Γ was fit to the Fermi-Dirac distribution (solid curve) shown in Eqn. 8:[32]

$$f(e) = \frac{1}{1 + e^{-\beta(e_f - e)}} \qquad (8)$$

where ε_f is the Fermi energy. The vertical lines illustrate the calculated optical band gap of iridium oxide to be 3.12 eV. The Fermi energy for this metal oxide was calculated to be –5.3 eV. Based upon the orbital occupancy, the Fermi energy and the volume of the unit cell of iridium oxide the charge carrier concentration was determined to be 4.2×10^{21} cm^{-3}. The charge carrier concentration is related to the conductivity of this material as shown in Eqn. 9:[13]

$$\sigma = \frac{ne^2\tau}{m^*}\frac{1}{1-i\omega\tau} \qquad (9)$$

where σ is the conductivity and τ is the electronic scattering time. The exact conductivity cannot be calculated because these DFT calculations do not allow for the determination of the electronic scattering time. To correlate the calculated charge carrier concentration with the plasma frequency of iridium oxide, the conduction band of IrO_2 in the Δ ($\Gamma \rightarrow$ X) direction that is equivalent to the (0,0,0) $\rightarrow$ (½,0,0) wave vector in the Brilluoin zone was fit to Eqn. 7 to determine the effective electron mass of this material in this direction. The effective mass (m^*) in the Δ ($\Gamma \rightarrow$ X) direction was determined to be 0.67 m_e where m_e is the mass of an electron in agreement with the experimental and theoretical effective masses of other metal oxides.[11,21,22] Based upon this value for the charge carrier concentration and effective mass, the calculated plasma frequency is 23,762 cm^{-1} at ~ 6,300 K. To determine the relevance of this calculated plasma frequency at elevated temperature to ambient temperatures the temperature dependence on the optical band gap, Fermi energy, charge carrier concentration and plasma frequency were calculated as shown below (Figures 4 and 5).

The DFT calculations showed that the conduction band of IrO_2 had a primarily d-electron character in agreement with previous theoretical studies.[1,2] The orbital character of the conduction band of IrO_2 is d-band and that of ITO is sp-band.[12] The observed plasma frequencies for both metal oxides were observed in the near-IR spectral region despite the differences in their orbital character. The major difference in the measured reflectance IR spectra between iridium oxide and indium tin oxide thin films was the increase in reflectance above the plasma frequency for iridium oxide thin films due to d-d intraband transitions.

The optical band gap, Fermi energy, charge carrier concentration and plasma frequency were calculated as a function of electronic temperature as shown in Figures 4A - 4D for iridium oxide. This temperature dependence was calculated to determine how calculations at elevated electronic temperatures relate to ambient temperature where the experimental reflectance data were measured. The electronic temperature range was used ~ 2,500 to 9,500 K. Calculations at lower electronic temperatures could not be performed due to SCF convergence problems. Figure 4A shows the Fermi-Dirac fits to the electron occupation in the vicinity of the Fermi energy as a function of temperature. Through this temperature range, the calculated optical band gap changed from 2.99 eV to 3.26 eV at ~ 2,500 and 9,500 K, respectively. Figure 4B shows that the Fermi energy increased as the temperature increased. The Fermi energy increased gradually up to ~ 5,000 K, while above this temperature the change in the Fermi energy as a function of temperature increased more rapidly. Figure 4C illustrates the dependence in the calculated charge carrier concentration of iridium oxide on the temperature. The charge carrier concentration increased as the temperature increased as expected with a range of 6.2×10^{19} to 1.2×10^{22} cm^{-3}. This figure

shows that electrical conductivity of iridium oxide is hence dependent upon the temperature and increases as the temperature rises since the charge carrier concentration and electrical conductivity are related. The plasma frequency varies as a function of the square root of the charge carrier concentration since the effective mass of iridium oxide was calculated at the limit of T = 0 K because calculations at different points in k-space can only be carried out using the FERMI option. This plasma frequency dependence on the temperature is shown in Figure 4D. As with the charge carrier concentration, the plasma frequency increases with increasing temperature. The values of the plasma frequency varied from 2,882 to 39,720 cm^{-1} in this temperature range.

The calculated trend in the charge carrier concentration and plasma frequency for iridium oxide shows that at room temperature the calculated plasma frequency of iridium oxide would be considerably lower than the experimental value. This difference suggests that the conduction mechanism of iridium oxide is not accurately modeled in these calculations using the iridium oxide unit cell. However, the higher conductivity in these films is possibly due to a non-stoichiometric ratio of iridium and oxygen in the iridium oxide thin films. Therefore oxygen atoms were removed systematically from the iridium oxide unit cell to create oxygen deficient iridium oxide models to determine the effect on the calculated charge carrier concentration and plasma frequency. The resulting values are shown in Table 1 at ~ 6,300 K. The oxygen deficient iridium oxide results show that the charge carrier concentration and plasma frequency of iridium oxide increase significantly as oxygen is removed from the unit cell giving better agreement to experimental measurements of the plasma frequency of iridium oxide thin films. However since the exact composition of the

iridium oxide thin films is not known, the electronic temperature dependence of these oxygen deficient iridium oxide models were not calculated.

Figures 5A - 5E illustrate the dependence of the optical and electronic properties of iridium oxide as a function of the expansion or compression of the unit cell of iridium oxide to show that the theoretical energy minimized structure and the experimental determined crystal structure parameters are nearly identical. For instance, Figure 5A shows the electron occupation as a function of orbital energy in the region near the Fermi energy. This figure along with Figure 5B shows that the Fermi energy of this system decreases when the unit cell is compressed, while the Fermi energy increases with the expansion of the unit cell. Figures 5C and 5D show that the charge carrier concentration and plasma frequency of iridium oxide increases or decreases due to the expansion or compression of the iridium oxide unit cell, respectively. However Figure 5E shows that the energy minimum for these structures occurs at a compression of the unit cell by 0.3 %. Therefore, the experimentally determined lattice parameters and structure are nearly the same as the calculated energy minimized structure of iridium oxide. These studies validate the use of the experimentally determined crystal structure parameters for the calculations of the optical and electronic properties of iridium oxide.

Conclusion

Reflectance FTIR spectroscopy was complemented by density functional theory calculations to investigate the optical and electronic properties of iridium oxide. Reflectance FTIR spectroscopy showed that iridium oxide thin films deposited on a glass slide had a

sharp decrease in intensity ~ 6,500 cm^{-1} indicative of the plasma frequency. These spectra showed an angular minimum in the reflectance at 70 degrees for p-polarized radiation at 7,945 cm^{-1}. The Drude free-electron model and the Fresnel equations for reflection were used to fit the experimental reflectance spectra and values of 20,200 cm^{-1} and $2.8x10^{-15}$ seconds were obtained for the plasma frequency and electronic scattering time using a value of 6.4 for the high frequency dielectric constant, respectively. The DFT models calculated the charge carrier concentration and plasma frequency of iridium oxide to be $4.2x10^{21}$ cm^{-3} and 23,762 cm^{-1} at ~ 6,300K, respectively. However, the calculated plasma frequencies extrapolated near room temperature were significantly lower than experimental values. Removal of oxygen atoms from the iridium oxide unit cell increased the calculated charge carrier concentration and plasma frequency suggesting that a non-stoichiometric ratio of iridium and oxygen in iridium oxide thin films could contribute to the experimentally observed conductivity of these thin films. The optimal unit cell of iridium oxide was determined to be at a compression of 0.3 % compared to the experimental determined values. The optical band gap was calculated to be 3.12 eV, and the effective electron mass was found to be 0.67 m_e for the Δ ($\Gamma \rightarrow X$) direction. The conduction band of iridium oxide consisted of d-electrons from iridium giving rise to the conductivity of this metal oxide. This orbital character differed from other conducting metal oxide thin films such as indium tin oxide (ITO) that had s and p orbital character in the conduction band that have similar optical properties in the infrared. Both iridium oxide and ITO thin films have plasma frequencies in the near-IR, but the presence of d-d intraband transitions in iridium oxide affected the optical properties of IrO_2 at energies just above the plasma frequency.

Acknowledgements

This work was done in collaboration with Dwi Wicaksana (NCSU), Jon-Paul Maria (NCSU), Angus I. Kingon (NCSU) and Stefan Franzen (NCSU). Support and computational facilities were provided by the North Carolina Supercomputing Center.

References

(1) Goel, A. K.; Skorinko, G.; Pollak, F. H. *Physical Review B* **1981**, *24*, 7342-7350.

(2) Mattheiss, L. F. *Physical Review B* **1976**, *13*, 2433-2450.

(3) Kawar, R. K.; Chigare, P. S.; Patil, P. S. *Applied Surface Science* **2003**, *206*, 90-101.

(4) Hackwood, S.; Dayem, A. H.; Beni, G. *Physical Review B* **1982**, *26*, 471-478.

(5) Mo, Y. B.; Stefan, I. C.; Cai, W. B.; Dong, J.; Carey, P.; Scherson, D. A. *Journal of Physical Chemistry B* **2002**, *106*, 3681-3686.

(6) Bezbaruah, A. N.; Zhang, T. C. *Analytical Chemistry* **2002**, *74*, 5726-5733.

(7) Marzouk, S. A. M. *Analytical Chemistry* **2003**, *75*, 1258-1266.

(8) Nishio, K.; Watanabe, Y.; Tsuchiya, T. *Thin Solid Films* **1999**, *350*, 96-100.

(9) Dautremont-Smith, W. C.; Beni, G.; Schiavone, L. M.; Shay, J. L. *Applied Physics Letters* **1979**, *35*, 565-567.

(10) Wipf, D. O.; Ge, F. Y.; Spaine, T. W.; Bauer, J. E. *Analytical Chemistry* **2000**, *72*, 4921-4927.

(11) Brewer, S. H.; Franzen, S. *Chemical Physics* **2004**, *300*, 285-293.

(12) Brewer, S. H.; Franzen, S. *Journal of Physical Chemistry B* **2002**, *106*, 12986-12992.

(13) Wooten, F. *Optical Properties of Solids*; Academic Press, Inc.: San Diego, 1972.

(14) Hamberg, I.; Hjortsberg, A.; Granqvist, C. *Applied Physics Letters* **1982**, *40*, 362-364.

(15) Hjortsberg, A.; Hamberg, I.; Granqvist, C. *Thin Solid Films* **1982**, *90*, 323-326.

(16) Shin, J.; Shin, S.; Park, J.; Kim, H. *Journal of Applied Physics* **2001**, *89*, 5199-5203.

(17) Fan, J.; Bachner, F.; Foley, G. *Applied Physics Letters* **1977**, *31*, 773-775.

(18) Bregman, J.; Shapira, Y.; Aharoni, H. *Journal of Applied Physics* **1990**, *67*, 3750-3753.

(19) Mryasov, O. N.; Freeman, A. J. *Physical Review B* **2001**, *64*, art. no.-233111.

(20) Odaka, H.; Iwata, S.; Taga, N.; Ohnishi, S.; Kaneta, Y.; Shigesato, Y. *Japanese Journal of Applied Physics Part 1-Regular Papers Short Notes & Review Papers* **1997**, *36*, 5551-5554.

(21) Odaka, H.; Shigesato, Y.; Murakami, T.; Iwata, S. *Japanese Journal of Applied Physics Part 1-Regular Papers Short Notes & Review Papers* **2001**, *40*, 3231-3235.

(22) Mi, Y. M.; Odaka, H.; Iwata, S. *Japanese Journal of Applied Physics Part 1-Regular Papers Short Notes & Review Papers* **1999**, *38*, 3453-3458.

(23) Maki-Jaskari, M. A.; Rantala, T. T. *Physical Review B* **2001**, *64*, art. no.-075407.

(24) Fowles, G. *Introduction to Modern Optics*; Second ed.; Dover Publications, Inc.: New York, 1989.

(25) Delley, B. *Journal of Chemical Physics* **1990**, *92*, 508-517.

(26) Bolzan, A. A.; Fong, C.; Kennedy, B. J.; Howard, C. J. *Acta Crystallographica Section B-Structural Science* **1997**, *53*, 373-380.

(27) Perdew, J. P.; Chevary, J. A.; Vosko, S. H.; Jackson, K. A.; Pederson, M. R.; Singh, D. J.; Fiolhais, C. *Physical Review B* **1992**, *46*, 6671-6687.

(28) Kohn, W.; Sham, L. *Physical Review A* **1965**, *137*, 1697-1699.

(29) Mermin, D. *Physical Review A* **1965**, *137*, 1441-1443.

(30) Hamberg, I.; Granqvist, C. G.; Berggren, K. F.; Sernelius, B. E.; Engstrom, L. *Physical Review B* **1984**, *30*, 3240-3249.

(31) Lide, D. R., Ed. *CRC Handbook of Chemistry and Physics*; 75 ed.; CRC Press: Ann Arbor, 1994.

(32) McQuarrie, D. A. *Statistical Mechanics*; Harper Collins Publishers Inc.: New York, 1976.

Table

Table 1. DFT calculated values of the charge carrier concentration and plasma frequency of oxygen deficient iridium oxide models.

Model	Charge Carrier Concentration (cm^{-3})	Plasma Frequency (cm^{-1})
Ir_2O_4	$4.24x10^{21}$	23,762
Ir_2O_3	$4.99x10^{21}$	25,773
Ir_2O_2	$1.32x10^{22}$	41,956

Figures

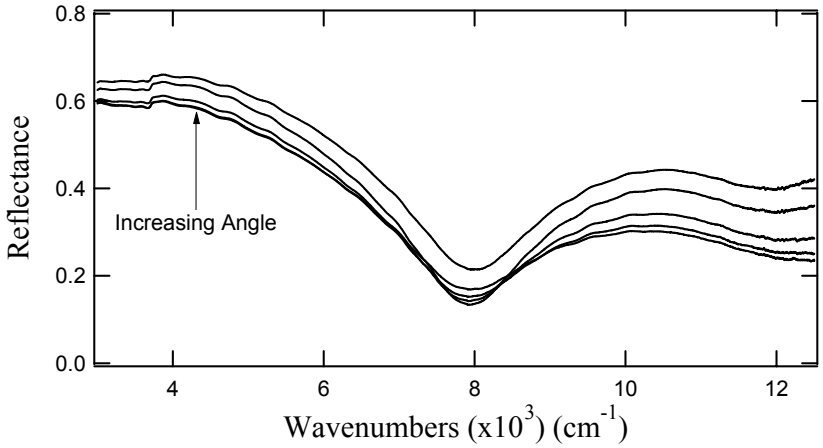

Figure1. Variable angle reflectance FTIR spectra of a 110 nm iridium oxide thin film on a glass substrate. The spectra were recorded at with incident angles ranging from 40 – 80 degrees in 10 degree increments with p-polarized radiation.

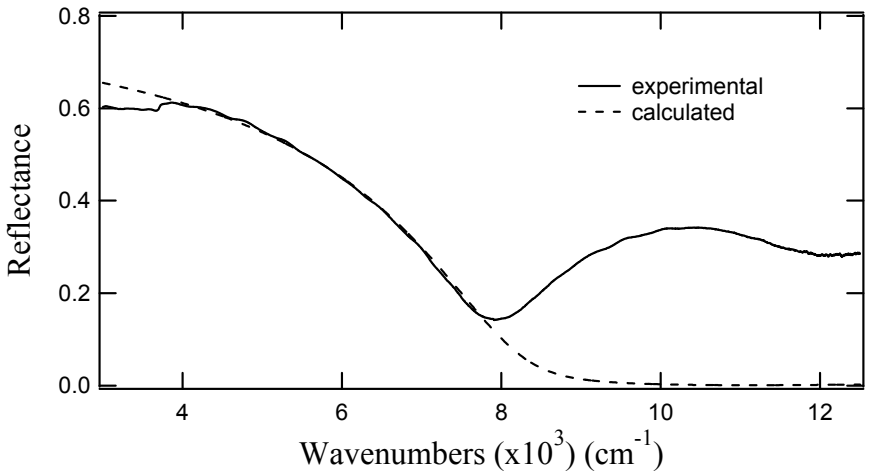

Figure 2. Experimental (solid) and calculated (dashed) reflectance IR spectra of an iridium oxide thin film for an incident angle of 60 degrees with p-polarized radiation.

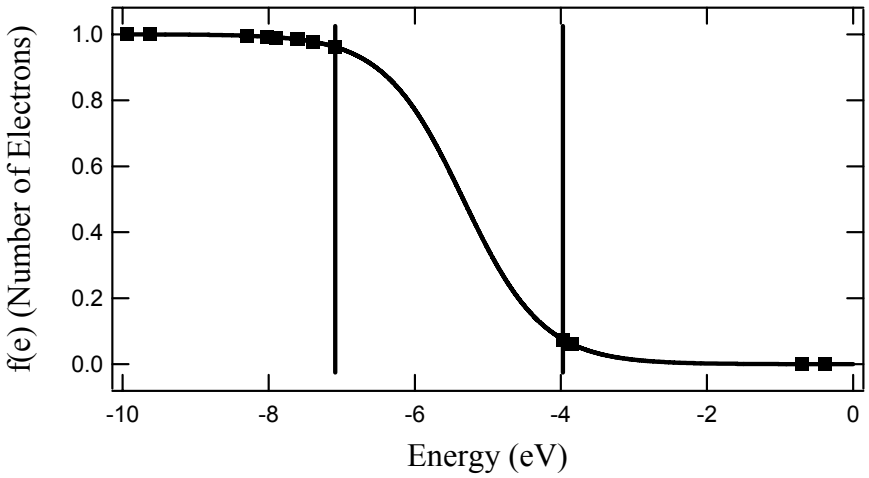

Figure 3. DFT calculated distribution of electrons in the vicinity of the Fermi energy for iridium oxide (markers) fit to the Fermi-Dirac distribution (solid). The two vertical lines denote the optical band gap.

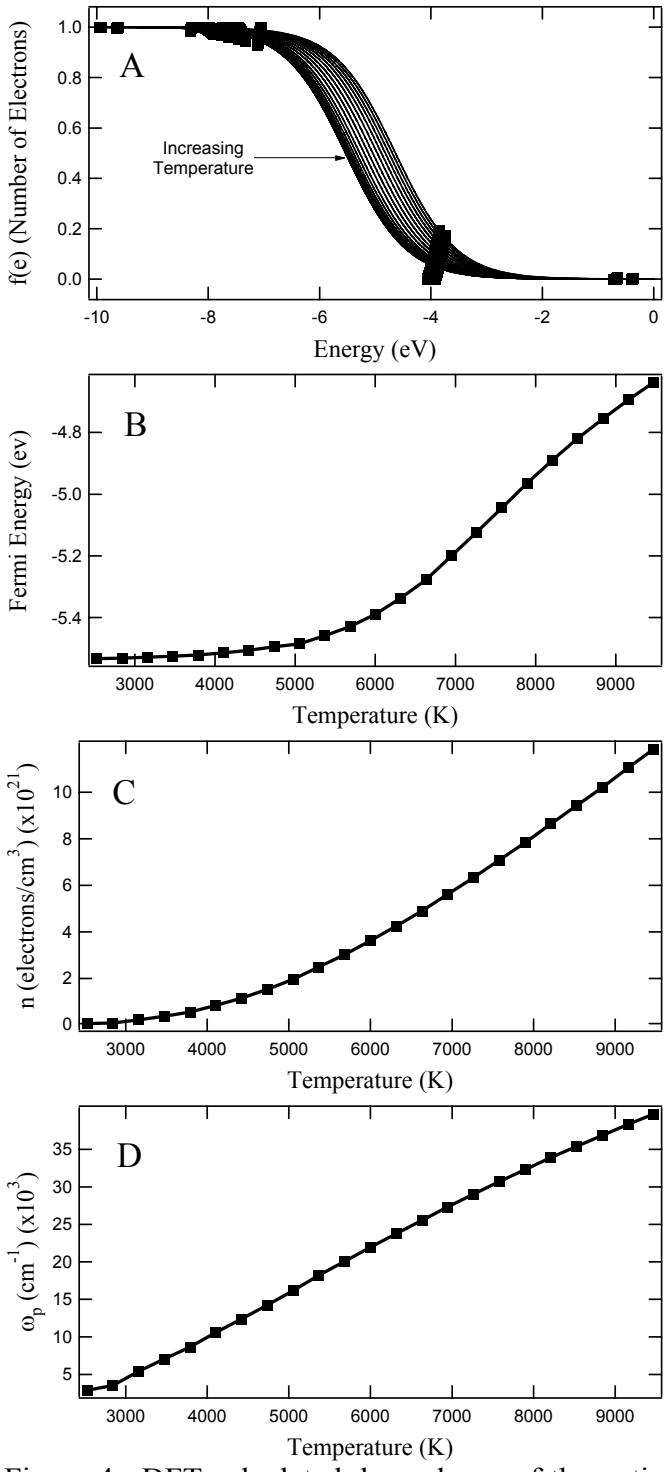

Figure 4. DFT calculated dependence of the optical band gap, Fermi energy, charge carrier concentration and plasma frequency of iridium oxide on temperature.

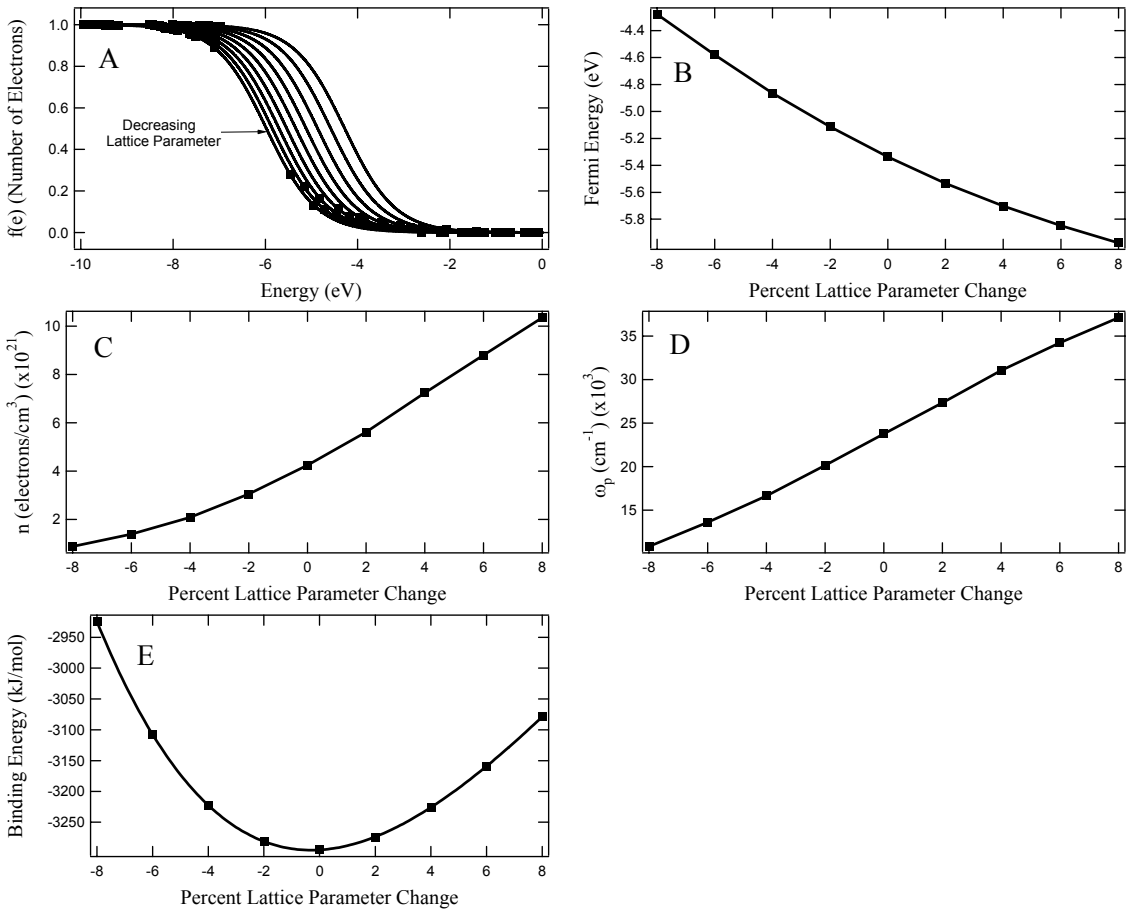

Figure 5. DFT calculated dependence of the optical band gap, Fermi energy, charge carrier concentration, plasma frequency and binding energy of iridium oxide on the compression or expansion of the unit cell of iridium oxide.

Chapter 10

A Quantitative Theory and Computational Approach for the Vibrational Stark Effect

Abstract

Density functional theory (DFT) has been used to calculate the vibrational Stark tuning rates of a variety of nitriles and carbonyls in quantitative agreement with experimental values with a correction factor of $f = 1.1$ for the local electric field. These calculations show that the vibrational Stark tuning rate has an anharmonic contribution and a contribution due to geometric distortions caused in the molecules due to the applied electric field. The anharmonic and geometric distortion components of the vibrational Stark tuning rate were calculated by the frequency dependence of the CN or CO stretching mode with varying applied electric fields by using the optimized structure in zero applied field or allowing the structure to optimize in the applied electric field, respectively. The changes in the calculated frequency of the CN or CO stretching mode, bond length and dipole moment of this bond with varying applied electric fields are shown. The transition polarizability and the difference polarizability were also calculated by DFT for comparison to the experimental data on nitriles and carbonyls. The DFT calculations suggest that the sign of the transition polarizability is negative and this result in turn has an effect on the experimental data analysis since the sign of the transition polarizability is not determined by experiment.

Introduction

The vibrational Stark effect is a new method for determining the local dielectric properties in polymers and proteins. [1-5] Quantitative correlation of the observed effect of an externally applied field on vibrational frequencies has application to the study of the electrostatic environment in complex dielectrics. The shift in the vibrational frequency due

to an externally applied field can be used to determine the difference dipole moment, which can be used to quantify frequency shifts due to local field effects in proteins. Local fields help to determine the reactivity of enzymes. For example, the electrostatic environment alters the acid dissociation constant (pKa), the strength of hydrogen bonds and the strength of nucleophiles. The internal fields responsible for these effects can be measured by studying the effect of environment on vibrational reporters such as carbonyls or nitriles within a protein. [1-4] The comparison of the frequency shifts of environmental reporters such as nitriles buried in proteins can be calibrated by comparison of the effect of applied external fields on those reporters. The vibrational Stark effect has been measured for a number of carbonyls and nitriles to aid in understanding the strength of internal fields. [3,6] A quantitive analysis of the difference dipole moment is needed in order to apply these studies to the study of reporter groups in complex systems such as proteins or polymer matrices.

The origin of the vibrational Stark effect has been the subject of theoretical investigation for nearly 30 years. [4,7-19] The effect of an externally applied electric field provides an experimental approach that can be quantified in terms of molecular parameters, the dipole moment (μ_0), difference dipole moment ($\Delta\mu$) and the difference polarizability ($\Delta\alpha$) [1-3]. Experimental signals can be decomposed into derivatives. A zeroth derivative line shape change implies a change in the transition moment, M in the applied electric field that arises from the transition moment polarizability, A. A second derivative line shape change arises from $\Delta\mu$. A first derivative line shape arises due to $\Delta\alpha$ and the cross term involving $\Delta\mu$ and A. For a static geometry, within the harmonic approximation, there is no change in dipole moment, $\Delta\mu$ since the expectation value for nuclear position is independent of the

vibrational eigenstate. For this reason, the initial treatment of the vibrational Stark effect focused only on changes in molecular structure in the applied field [7,8]. Later, anharmonicity was investigated as the origin of the vibrational Stark effect [15]. Anharmonic contributions have been separated as either mechanical or electrical anharmonicity. Mechanical anharmonicity is due to cubic or other odd powered anharmonic terms will give rise to a change in the dipole moment as a function of the eigenstate due to the asymmetry of the potential energy surface. However, these theories have failed to fit the vibrational Stark data, because the predicted electric field effect due to (mechanical) anharmonicity is less than half of the magnitude of the experimental data. [4] A resolution to this discrepancy was proposed some time ago by combination of both a geometric and anharmonicity contribution to the vibrational Stark effect [9]. However, the quantitative application of the complete theory requires intensive use of electronic structure calculations.

The method presented in this paper builds on the concept of a combined geometric and anharmonicity contribution. Figure 1 shows the absolute requirement for an equilibrium bond length change that is inherent in the interaction of a molecule with an applied electric field. Although the change in nuclear geometry is expected to be small, a change in internuclear distance is an essential component of the Stark tuning rate (i.e. a change in dipole moment in an applied field). The molecular geometry is not at equilibrium in an applied electric field until the molecule has readjusted its nuclear coordinates in response to the field. Moreover, the harmonic potential surface at zero field has a cubic term in the applied field. This contribution to the shift in vibrational frequency is known as mechanical anharmonicity [7,8,19]. Fortunately, the systems chosen for study are carbonyls and nitriles

that permit a relatively simple interpretation of the potential energy surface in terms of bond length changes in analogy with Figure 1. In this study, we demonstrate an approach that accounts quantitatively for the vibrational Stark effect using a combination of anharmonic level shifts (also known as electrical anharmonicity) and changes in molecular geometry (also known as mechanical anharmonicity). The DFT calculations are complemented with a simple intuitive theory based on classical expressions for the potential energy surfaces such as those given in Figure 1. The DFT approach also permits the calculation of the transition polarizability and difference polarizability.

Methods

The density functional theory (DFT) calculations were performed using the MSI (Molecular Simulations, Inc.) *ab initio* quantum chemical software program DMol3. [20] DMol3 was used for geometry optimization, single point energy and frequency calculations of the various carbonyl and nitrile containing molecules. These calculations used the double numerical plus polarization (DNP) basis set and the generalized gradient approximation (GGA) functional[21] in the gas phase. Eigenvector projections were carried out as described elsewhere.[22] The Accelrys software InsightII was used to build the models and to visualize the eigenvector projections calculated by DMol3. Although the geometric contribution was calculated here for convenience using a vibrational frequency calculation at each value of the applied electric field, the method can also be applied using only projections along the potential energy surface as performed elsewhere [12-14]. The DFT calculations were performed at the North Carolina Supercomputing Center (NCSC) on the IBM RS/6000 SP.

Normal coordinate analysis was performed using FCART01 [23] to calculate the potential energy distributions (PED) of the nitrile or carbonyl stretching normal mode. The intrinsic mode anharmonicities were determined by calculating potential energy surfaces (PES) along the nitrile or carbonyl stretching normal mode formed by calculating the energy at displacements along the eigenvector from the optimized geometry. A fourth order polynomial ($U(Q)=a_0Q+b_0Q^2+c_0Q^3+d_0Q^4$) was used to fit the PES and these parameters were used in the Numerov-Cooley [24,25] method to calculate the energies and wavefunctions for the first five vibrational levels for this normal mode. The Numerov-Cooley method is an iterative numerical algorithm that determines the bound-state eigenvalues and eigenfunctions of the Schrödinger equation (Eqn. 1) for an arbitrary potential energy surface:

$$\frac{\partial^2 \psi}{\partial r^2} + [E - V(r)]\psi = 0 \qquad (1)$$

where ψ is the radial wavefunction, E is the iterative energy guess and V(r) is an arbitrary potential energy surface. The numerical wavefunction is constructed from the initial guess, E in the classically forbidden region and propagated from either side into the allowed region. The criterion for convergence is that the left-propagated and right-propagated wave functions should meet in the allowed region to within a specified tolerance. In this study, V(r) is the potential energy surface along the given normal mode vibrational eigenfunction determined using DFT. The algorithm was tested with harmonic potential energy surfaces to verify that the numerical solutions agreed with the analytical solution of the harmonic oscillator (Hermite polynomials multiplied by Gaussians). Anharmonicity arises due to a deviation of the potential energy surface from a pure quadratic form as verified in test calculations. The

intrinsic mode anharmonicity was then calculated from the average energy (cm^{-1}) spacing difference between ν_1-ν_0 and ν_2-ν_1, ν_3-ν_2, and ν_4-ν_3 transitions (see Supporting Information (Appendix 4)).[26]

The Stark tuning rate (cm^{-1}/(MV/cm)), $\Delta\mu$, was calculated as shown in Eqn 2:

$$\Delta\mu = \frac{E_+ - E_-}{F_+ - F_-} = \frac{\Delta E}{\Delta F} \qquad (2)$$

where E_+ and E_- correspond to the vibrational frequency (cm^{-1}) of the CN or CO stretching normal mode with a positive and negative applied electric field, respectively and F_+ and F_- correspond to the positive and negative applied electric field, respectively. Therefore ΔE corresponds to the effect on the vibrational transition energy in response to an applied electric field. The electric field term in the hamiltonian was applied parallel to the CN or CO bond. The Stark tuning rate was calculated for the models with or without allowing the nitriles or carbonyls to optimize in the applied electric field, referred to as fixed and reoptimized geometries, respectively. The frequency of the CN or CO stretching vibrations for both the fixed and the reoptimized geometries was calculated within the harmonic approximation by finite difference. The overall Stark tuning rate ($\Delta\mu_{tot}$) was calculated by the sum of the geometry distortion ($\Delta\mu_{geom}$) and anharmonic ($\Delta\mu_{anharm}$) components as shown in Eqn. 3:

$$\Delta\mu_{tot} = \Delta\mu_{geom} + \Delta\mu_{anharm} \qquad (3)$$

where $\Delta\mu_{geom}$ and $\Delta\mu_{anharm}$ were calculated using Eqn. 2 for the reoptimized and fixed geometries, respectively. The labels geom and anharm are equivalent to mechanical and electrical anharmonicity, respectively.

The anharmonicity of the CN and CO stretching vibrations was also examined by determining the shift in the expectation value x (normal coordinate (bond length) displacement), $\langle x \rangle$, for the nitrile or carbonyl group in the ground (ν_0) and first vibrational wavefunction (ν_1) calculated from the PES of these normal modes. The expectation value of x was calculated as shown in Eqn. 4:

$$\Delta x_{\nu_1-\nu_0} = \langle x \rangle_{\nu_1} - \langle x \rangle_{\nu_0} \qquad (4)$$

The expectation value was converted into angstroms by determining the conversion factor between normal coordinate displacement and the change in bond distance of the nitrile or carbonyl bond in angstroms for each of the molecules (see Supporting Information (Appendix 4)).[26]

The transition moment polarizability (D/(MV/cm)), A, is defined in Eqn. 5:

$$M(F) = M + AF \qquad (5)$$

where M is the transition moment and F is the electric field. Therefore the transition moment, M must be determined at multiple applied electric fields. To account for anharmonic contributions to the transition moment, each vibrational wavefunction (χ) is considered as the sum of multiple vibrational wavefunctions with appropriate coefficients as shown in Eqn. 6:

$$\left|\chi_j^{'}\right\rangle = \sum_{n=0}^{\infty} a_{nj} \left|\chi_n\right\rangle \qquad (6)$$

where a_{nj} are the variational coefficients. The general expression for the transition moment is then shown in Eqn. 7:

$$M = \left(\frac{\partial \mu}{\partial Q}\right)\left\langle \chi_0^{'} \middle| Q \middle| \chi_1^{'} \right\rangle = \left(\frac{\partial \mu}{\partial Q}\right)\sum_{n=1}^{\infty}\sum_{m=1}^{\infty} a_{n0}a_{m1}\left\langle \chi_n \middle| Q \middle| \chi_m \right\rangle \qquad (7)$$

When the harmonic oscillator selection rules are included the corrected transition moment is (Eqn. 8):

$$M = \left(\frac{\partial \mu}{\partial Q}\right)\left(a_{00}a_{11}\left\langle \chi_0 \middle| Q \middle| \chi_1 \right\rangle + a_{10}a_{21}\left\langle \chi_1 \middle| Q \middle| \chi_2 \right\rangle + a_{20}a_{31}\left\langle \chi_2 \middle| Q \middle| \chi_3 \right\rangle + ...\right) \qquad (8)$$

or in the general case (Eqn. 9)

$$M = \left(\frac{\partial \mu}{\partial Q}\right)\sum_{n=0}^{\infty} a_{n0}a_{n+1,1}\left\langle \chi_n \middle| Q \middle| \chi_{n+1} \right\rangle = \left(\frac{\partial \mu}{\partial Q}\right)\sum_{n=0}^{\infty} a_{n0}a_{n+1,1}\sqrt{\frac{n+1}{2\alpha}} \qquad (9)$$

The calculated anharmonic contribution to the transition moment was found to be negligible (≤0.7%) at zero applied electric field. This is evident from the the small a_{n0} and $a_{n+1,1}$ coefficients relative to a_{00} and a_{11} (see Supporting Information (Appendix 4)).[26] The largest correction corresponded to HCN (0.7%) that had the largest calculated anharmonicity by the Numerov-Cooley method. The correction to the transition moment was determined at one positive and negative field along with the zero field correction. The corrections in an applied electric field were also found to be negligible (see Supporting Information (Appendix 4)).[26] Therefore the transition moment can be simply expressed as follows (Eqns. 10 - 12):

$$M = \left(\frac{\partial \mu}{\partial Q}\right)\left\langle \chi_0 | Q | \chi_1 \right\rangle \qquad (10)$$

where

$$\langle \chi_0 | Q | \chi_1 \rangle = \sqrt{\frac{1}{2\alpha}} \qquad (11) \qquad \text{and} \qquad \alpha = \frac{\mu\omega}{\hbar} \qquad (12)$$

where $\frac{\partial \mu}{\partial Q}$ is the change in the dipole moment with respect to the normal coordinate, Q, χ is the vibrational wavefunctions where the 0 and 1 subscripts refer to the first and second vibrational levels, respectively, μ is the reduced mass, and ω is the angular frequency of the normal mode vibration. The term $\frac{\partial \mu}{\partial Q}$ was calculated from the slope of a plot of the dipole moment as a function of eigenvector projections along the carbonyl or nitrile stretching normal coordinate. Therefore the transition moment polarizability can be calculated as shown in Eqn. 13:

$$|A| = \frac{1}{2}\left(\left| \frac{|M_{1F+}|\langle \chi_{0F+} | Q | \chi_{1F+} \rangle - |M_1|\langle \chi_0 | Q | \chi_1 \rangle}{F_+} \right| + \left| \frac{|M_{1F-}|\langle \chi_{0F-} | Q | \chi_{1F-} \rangle - |M_1|\langle \chi_0 | Q | \chi_1 \rangle}{F_-} \right| \right) \qquad (13)$$

where F is the magnitude of the applied electric field parallel to the CO or CN bond and + and – refer to positive and negative applied electric fields, respectively. This method averages the transition moment polarizability for positive and negative applied fields. The same value for A can be determined from the slope of a plot of M vs. F. Experimentally the transition polarizability governs the change in intensity of a normal mode vibrational intensity in the presence of an applied electric field compared to the absence of the field. However since the intensity of the normal mode is dependent on the square of the transition moment (M) the sign of the transition moment polarizability cannot be determined from a Stark effect measurement. The transition moment polarizability enters in the zeroth derivative term as the square, hence its sign is not known from the Stark effect measurement.

The difference polarizability ($cm^{-1}/(MV/cm)^2$), $\Delta\alpha$, was calculated from Eqn. 14:

$$\tilde{\nu}(F) = \tilde{\nu}_o + \Delta\mu F + \frac{1}{2}\Delta\alpha F^2 \qquad (14)$$

where $\tilde{\nu}$ is the energy (cm^{-1}) of the normal mode vibration, $\Delta\mu$ is the Stark tuning rate, and F is the applied electric field. Therefore twice the polynomial coefficient from a second order polynomial fit of a plot of $\tilde{\nu}$ vs. F yields the difference polarizability. The linear term represent the Stark tuning rate (Eqn. 2.).

Results and Discussion

The calculated values of the frequency, cubic anharmonicity, bond length and ground state dipole moment are listed in Table 1 for zero applied electric field. Overall the agreement with the experimental values is quite good. The frequencies tend to be higher than the experimental values as expected since they are calculated within the harmonic approximation. Anharmonic corrections for CO and CN stretching modes are all cubic terms that reduce the frequency and bring it closer to experiment. For example, ν(CO) = 2159 cm^{-1}, but when the anharmonicity of 13 cm^{-1} is included the frequency is 2146 cm^{-1} in close agreement with the experimental value of 2143 cm^{-1}. The anharmonic energy levels and wavefunctions were determined using the Numerov-Cooley algorithm. [24,25] A representative potential energy surface with vibrational wavefunctions is presented for CO in Figure 2.

The correlation shown in Figure 3 demonstrates that DFT gives quantitative agreement with the available vibrational Stark data when applied to a molecule with

inclusion of both anharmonic and geometry distortion terms. The line fit to the experimental data for 14 compounds given in Table 2 has a slope of 1.1, which is in agreement with estimates for the local field correction in a glycerol glass or polymer matrix at 80 K. [27] The average difference between the calculated (inclusion of both anharmonic and geometry distortion terms) and the experimental vibrational Stark data (given in Table 2) is ~9%. The values of the normal mode frequency of the carbonyl and nitrile stretch in different applied electric fields are listed in the Supporting Information (Appendix 4).[26] The local field correction arises due to solvent polarization in an applied electric field. It is usually included as a factor f that amplifies the applied field [28,29] due to reorientation of solvent dipoles that align in the applied field, $\Delta E_{expmt} = \Delta\mu_{expmt} \cdot fF$. In the spherical cavity approximation $f = 3\varepsilon/(2\varepsilon+1)$, where ε is the solvent dielectric constant. In a frozen matrix the solvent dielectric constant is approximately equal to the high frequency dielectric constant $\varepsilon_\infty = n^2$, where n is the index of refraction. For H_2O n = 1.33 giving $f = 1.16$. The DFT calculation is a vacuum calculation and thus $\Delta E_{calc} = \Delta\mu_{calc} \cdot F$. Equating the experimental and calculated field-dependent energy shifts, $\Delta E_{expmt} = \Delta E_{calc}$ we find $\Delta\mu_{expmt} = \Delta\mu_{calc} f$ in agreement with the comparison shown in Figure 3.

Within a fixed geometry model the observed Stark tuning rate can result only from a change in the dipole moment between the vibrational ground and excited states. The molecular geometry is fixed within the harmonic approximation, and the cubic anharmonic term permits a change in molecular geometry between the vibrational ground and excited state. However, it has been recognized that the anharmonicity alone is too small to account

for the observed vibrational Stark signals [17]. A bond polarization term has been advanced as a second contribution within the fixed geometry approximation. [4]

The main conclusion of the present study is a change molecular geometry in an applied electric field can give rise to a geometric distortion contribution to the harmonic approximation. The correlation of the force constant with the bond length known as Badger's rule suggests that vibrational frequency shifts will be observed due to changes in the molecular geometry. [30] This can be seen from a simple model for the potential energy surface in an applied electric field similar to previous work. [12] Within the Born-Oppenheimer approximation the electronic Schrodinger equation can be solved parametrically as a function of the nuclear coordinate, Q. The resulting potential energy surface at zero applied field is U(Q). In an applied electric field, the perturbation to the potential is a linear term that depends on the ground state dipole moment for the bond as given in Eqn. 15 up to the linear term is:

$$\mu(Q) = \mu_o + \left(\frac{\partial \mu}{\partial Q}\right)(Q - Q_o) + \ldots \qquad (15)$$

Up to cubic anharmonicity the potential energy surface is:

$$U(Q) - \mu(Q)F = a_0(Q - Q_0)^2 + b_0(Q - Q_0)^3 - (\mu_o F + \frac{\partial \mu}{\partial Q}(Q - Q_o)F) \qquad (16)$$

However, the addition of the linear term due to the applied electric field means that the system is no longer at equilibrium. We consider the simplest case where the equilibrium geometry is altered in response to the applied field. The molecular potential in the applied field is:

$$U_F(Q) = a_F(Q - Q_F)^2 + b_F(Q - Q_F)^3 - (\mu_o F + \frac{\partial \mu}{\partial Q}(Q_F - Q_0)F) \qquad (17)$$

The difference dipole offset arises due to the fact that the system moves to lower energy in the applied field. The energy difference is given by the difference dipole moment. However, the second order term a_F that is proportional to the force constant is also altered in the field. Expanding Eqns. 16 and 17 in powers of Q leads to a non-linear system of equations. We use the approximation that

$$x_F = x_0(1 + \varepsilon) \qquad (18)$$

All powers of ε higher than the first are ignored to linearize this system of equations. Equating like powers leads to the following result for this simple model.

$$b_F = b_0$$

$$a_F = \frac{a_0 + \frac{\partial \mu}{\partial Q}\frac{F}{2}(\frac{1}{x_0} - 3\frac{b_0}{a_0})}{1 - \frac{\partial \mu}{\partial Q}\frac{F}{2a_0 x_0}} \qquad (19)$$

$$x_F = x_0 - \frac{\partial \mu}{\partial Q}\frac{F}{2a_0}$$

Higher powers of x can be included in this model. In general, the highest power term will not show any field dependence. Thus, the cubic case treated here shows no field dependence, i.e. $b_F = b_0$. However, in the current level of approximation there is a field-dependent quadratic term. This simple model predicts a shift in the bond length for a typical nitrile that can be calculated using the relation $a_0 = \mu\omega^2/2 = 2\pi^2\mu c^2\nu^2$ where the wavenumber $\nu = 2250$ cm^{-1} and $\mu = m_C m_N/(m_C + m_N)$, $m_C = 12$ a.m.u. and $m_N = 14$ a.m.u. For a C-N bond this

simple model predicts a position shift of 8 x 10^{-5} Å/MV/cm in reasonable agreement with the calculated position shift of 5 x 10^{-5} Å/MV/cm for the ten nitriles listed in Table 1. For a CO bond with m_O = 16 a.m.u. and ν = 1700 cm^{-1} the model predicts a bond length shift of 1.4 x 10^{-4} Å/MV/cm, which is in exact agreement with acetone and methyl vinyl ketone (Table 1). The model also predicts a Stark tuning rate of 0.35 cm^{-1}/(MV/cm), which is quite close to the average of 0.4 cm^{-1}/(MV/cm) calculated using the DFT method for ten nitriles given in Table 2. For a carbonyl group the predicted Stark tuning rate is 0.42 cm^{-1}/(MV/cm) compared to DFT calculated values of 0.69 cm^{-1}/(MV/cm) and 0.61 cm^{-1}/(MV/cm) for acetone and MVK, respectively. Both the sign and the magnitude of the effects predicted by the very simple model in Eqns. 19 are in reasonable agreement with DFT and experimental values.

Although the geometric distortion term is the largest contribution to the vibrational Stark effect, the correlation is significantly improved by simultaneous inclusion of both geometry distortion and anharmonic terms. In other words, the present model is similar to that advanced by Andrews and Boxer [4] except that the bond polarization term is replaced with a geometric term. In both models, the anharmonicity accounts for less than half of the observed Stark tuning rate.

Figure 4 shows the comparison of the DFT calculated and experimental values for the transition moment polarizability, A, showing reasonable agreement between the experimental and calculated values for small molecule nitriles. The DFT calculated values for |A| for nitriles and carbonyls are compared to the available experimental values in Table 3. The values are reported as the absolute value since the transition polarizability appears as the square in the zeroth derivative Stark term and hence its sign is not determined by experiment.

[3] The calculated sign of the transition moment polarizability is negative for the entire series of molecules studied. Figure 4 illustrates the ability of density functional theory to calculate the transition polarizability. The slope of the line in Figure 4 is 0.965 with an intercept of 7.8 $D(MV/cm)^{-2}$ for the plot of experimental versus DFT calculated transition polarizabilities. Table 3 shows that the value for the transition polarizability is nearly unaffected by geometry optimization. A plot of the transition moment polarizabilities for a fixed nuclear geometry is indistinguishable from the comparison shown in Figure 4. The invariance of A to geometry optimization is expected due to the strong dependence of A on the electrical anharmonicity relative to its dependence on the mechanical anharmonicity. [12-14,19]

A comparison of the DFT calculated and experimental difference polarizabilities is shown in Table 4 for molecular geometries optimized in the absence or presence of an applied electric field. The models that were optimized in the presence of an applied electric field produced generally larger values of $\Delta\alpha$ than did the fixed geometry models. However, the difference polarizability results in a small shift of the observed normal mode vibrational energy, always less than 9% of the shift due to the difference dipole moment (i.e. the Stark tuning rate). Experimental measurements of $\Delta\alpha$ have an inherently large error because the first derivative term contains contributions from $\Delta\alpha$ and from cross terms that include contributions from the transition polarizability, A and Stark tuning rate, $\Delta\mu$. [3] Since the sign of A is not defined by the experiment there is an intrinsic uncertainty in the magnitude of $\Delta\alpha$ when A is not negligible as is the case for the collection of molecules studied here.

Conclusion

A complete theory of the vibrational Stark effect includes both the deformation of the bond length in response to the applied electric field and the anharmonicity of the vibrational mode. The present approach follows most previous treatments of the vibrational Stark effect [7-14,16-19] and allows geometrical distortions of a molecule in an applied electric field. The approach is both simple and accurate for the calculation of the vibrational Stark effect in 14 molecules given in Table 2 and shown in Figure 3. The DFT approach for the linear electric field effect of nitriles and carbonyls agrees quantitatively with the experimentally measured Stark tuning rates (assuming a local field correction value of 1.1 in frozen glycerol buffer matrices). The anharmonic contribution was due to the cubic anharmonicity of the CO or CN stretching normal mode as shown in the potential energy surfaces formed from the displacement along this normal mode. The Numerov-Cooley method for calculation of the anharmonicity is introduced here for application to the vibrational Stark effect. The geometric distortions were shown by changes in the calculated CO or CN bond length with varying applied electric fields. The DFT approach was further applied to transition polarizabilities and reasonable agreement was obtained with experimental data. Although an average deviation from experimental results of 9 and 29 % were obtained in the DFT calculated values of the Stark tuning rate and the transition polarizability, this method allows for the ability to determine these vibrational Stark properties of large molecules. The application of a classical model provides a theoretical basis for the hypothesis that the bond length change is a central feature of the vibrational Stark effect.

Acknowledgements

This work was done in collaboration with Stefan Franzen (NCSU) and is the subject of a publication, Brewer, S. H.; Franzen, S. *Journal of Chemical Physics* **2003**, 119 (2), 851-858. SB was supported by NIH Biotechnology Training Grant T32-GM08776. SF gratefully acknowledges support by NSF grant MCB-9874895. Support and computational facilities were provided by the North Carolina Supercomputing Center. We thank Dr. H. F. Franzen and Dr. R. Leacock of Iowa State University for helpful comments.

References

(1) Park, E. S.; Andrews, S. S.; Hu, R. B.; Boxer, S. G. *J. Phys. Chem. B* **1999**, *103*, 9813-9817.

(2) Park, E. S.; Thomas, M. R.; Boxer, S. G. *J. Am. Chem. Soc.* **2000**, *122*, 12297-12303.

(3) Andrews, S. S.; Boxer, S. G. *Journal of Physical Chemistry a* **2000**, *104*, 11853-11863.

(4) Andrews, S. S.; Boxer, S. G. *Journal of Physical Chemistry a* **2002**, *106*, 469-477.

(5) Hughes, J. M.; Hutter, M. C.; Reimers, J. R.; Hush, N. S. *Journal of the American Chemical Society* **2001**, *123*, 8550-8563.

(6) Park, E. S.; Boxer, S. G. *submitted* **2002**.

(7) Hush, N. S.; Williams, M. L. *Journal of Molecular Spectroscopy* **1974**, *50*, 349-368.

(8) Gready, J. E.; Bacskay, G. B.; Hush, N. S. *Chemical Physics* **1978**, *31*, 467-483.

(9) Bauschlicher, C. W. *Chemical Physics Letters* **1985**, *118*, 307-310.

(10) Andres, J. L.; Duran, M.; Lledos, A.; Bertran, J. *Chemical Physics* **1991**, *151*, 37-43.

(11) Hermansson, K.; Tepper, H. *Molecular Physics* **1996**, *89*, 1291-1299.

(12) Hush, N. S.; Reimers, J. R. *J. Phys. Chem.* **1995**, *99*, 15798-15805.

(13) Reimers, J. R.; Zeng, J.; Hush, N. S. *Journal of Physical Chemistry* **1996**, *100*, 1498-1504.

(14) Reimers, J. R.; Hush, N. S. *J. Phys. Chem. A* **1999**, *103*, 10580-10587.

(15) Lambert, D. K. *Solid State Communications* **1984**, *51*, 297-300.

(16) Lambert, D. K. *Journal of Chemical Physics* **1988**, *89*, 3847-3860.

(17) Lambert, D. K. *Electrochimica Acta* **1996**, *41*, 623-630.

(18) Dykstra, C. E. *Journal of Chemical Education* **1988**, *65*, 198-200.

(19) Marti, J.; Bishop, D. M. *Journal of Chemical Physics* **1993**, *99*, 3860-3864.

(20) Delley, B. *J. Chem. Phys.* **1990**, *92*, 508-517.

(21) Perdew, J. P.; Chevary, J. A.; Vosko, S. H.; Jackson, K. A.; Pederson, M. R.; Singh, D. J.; Fiolhais, C. *Phys. Rev. B* **1992**, *46*, 6671-6687.

(22) Lappi, S. E.; Collier, W.; Franzen, S. *J. Phys. Chem. A* **2002**, *106*, 11446-11455.

(23) Collier, W. B. *Quantum Chemistry Program Exchange Bulletin* **1993**, *13*, 19.

(24) Cashion, J. K. *Journal of Chemical Physics* **1963**, *39*, 1872-1877.

(25) Malik, D. J.; Eccles, J.; Secrest, D. *Journal of Computational Physics* **1980**, *38*, 157-184.

(26) See EPAPS Document No. for Supporting Information (Appendix 4). This document may be retrieved via the EPAPS homepage (http://www.aip.org/pubservs/epaps.html) or from ftp.aip.org in the directory /epaps/. See the EPAPS homepage for more information.

(27) Franzen, S.; Boxer, S. G. *J. Phys. Chem.* **1993**, *97*, 6304-6318.

(28) Bublitz, G. U.; Boxer, S. G. *Annual Review of Physical Chemistry* **1997**, *48*, 213-242.

(29) Wortmann, R.; Bishop, D. M. *Journal of Chemical Physics* **1998**, *108*, 1001-1007.

(30) Badger, R. M. *J. Chem. Phys.* **1934**, *2*, 128-131.

Tables

Table 1. Experimental (recorded at liquid nitrogen temperatures) and calculated values of the CN or CO stretching frequency, cubic anharmonicity, bond length and ground state dipole moment in zero applied electric field.

Molecule	ν (cm^{-1}) (expmt.)[a]	ν (cm^{-1}) (calc.)	PED[c]	x (cm^{-1}) (calc.)	R (Å) (calc.)	R(F)[d] (Å/MV/cm)	μ (D)
Acetone	1711.0	1739.1	93	8	1.2225	1.4×10^{-4}	3.0258
CO	2143.0	2159.5	100	13	1.1403	6.3×10^{-5}	0.1252
CN^-	2080.0[b]	2056.8	100	12	1.1903	3.1×10^{-5}	0.3567
HCN	2072.4	2142.4	94	10	1.1612	3.0×10^{-6}	2.9940
CAN	2247.5	2289.6	91	6	1.1653	2.9×10^{-5}	4.0423
BCN	2227.8	2259.1	88	6	1.1686	4.4×10^{-5}	4.6573
MVK	1676.0	1719.3	77	3	1.2267	1.4×10^{-4}	2.8260
NMP	1685.0	1713.4	89	5	1.2010	2.4×10^{-4}	4.0992
4-ClBCN	2230.6	2259.4	88	6	1.1686	5.9×10^{-5}	3.3184
3-ClBCN	2232.7	2262.6	88	6	1.1682	4.1×10^{-5}	4.0145
2-ClBCN	2232.1	2260.7	88	6	1.1669	1.4×10^{-5}	5.0942
4-MeOBCN	2223.5	2250.1	87	6	1.1680	6.3×10^{-5}	6.1256
Propionitrile	2243.5	2282.6	89	7	1.1656	2.9×10^{-5}	4.1353
Butyronitrile	2247.0	2282.3	89	7	1.1659	3.5×10^{-5}	4.2881
Valeronitrile	2239.2	2282.0	89	7	1.1658	7.8×10^{-5}	4.4073
Hexanenitrile	2243.2	2281.4	89	7	1.1659	1.0×10^{-4}	4.4418

a. literature experimental values[3,6,14]

b. recorded at room temperature

c. % (CN or CO stretch)

d. field-dependent bond length

Table 2. Calculated Stark tuning rates using the anharmonic and geometry distortion approaches compared with the experimentally measured values.

Molecule	Stark Tuning Rate Calculated[A] (cm^{-1}/(MV/cm)	Stark Tuning Rate Calculated[B] (cm^{-1}/(MV/cm)	Stark Tuning Rate A + B	Stark Tuning Rate Experimental (cm^{-1}/(MV/cm)[C]
Acetone	0.253	0.437	0.690	0.756
CO	0.010	0.457	0.467	0.429[D]
CN^-	0.019	0.204	0.223	-----
HCN	0.049	0.049	0.098	-----[E]
CAN	0.068	0.272	0.340	0.433
BCN	0.097	0.418	0.515	0.606
MVK	0.214	0.398	0.612	0.823
NMP	0.262	0.706	0.968	1.142
4-chlorobenzonitrile	0.126	0.554	0.680	0.584
3-chlorobenzonitrile	0.097	0.408	0.505	0.534
2-chlorobenzonitrile	0.097	0.359	0.456	0.514
4-methoxybenzonitrile	0.146	0.603	0.749	0.835
Propionitrile	0.078	0.321	0.399	0.465
Butyronitrile	0.097	0.340	0.437	0.475
Valeronitrile	0.088	0.321	0.409	0.448
Hexanenitrile	0.097	0.369	0.466	0.470

A. The models were not allowed to optimize in the applied electric field. The coordinates calculated in the absence of an applied electric field were used. (Anharmonic contribution) B. The models were allowed to optimize in the presence of the applied electric field. (Geometry distortion term) C. Literature experimental values. [3,6,14] D. Two experimental values for the Stark Tuning Rate are in the literature 0.429 and 0.672 cm^{-1}/(MV/cm). [1,14] E. Variation in the experimental Stark tuning rate for HCN occurred due to different concentration of HCN in 2-MeTHF because of hydrogen bonding. [3] Therefore no literature value is reported here.

Table 3. Calculated transition moment polarizabilities compared to experimental values.

Molecule	$\|A\|$ ($x10^{-4}$) (D/(MV/cm)) [I]	$\|A\|$ ($x10^{-4}$) (D/(MV/cm)) [II]	$\|A\|$ ($x10^{-4}$) (literature values) (D/(MV/cm) [III]
Acetone	2.81	2.05	-----
CO	16.05	16.60	-----
CN^-	37.45	37.46	-----
HCN	5.81	5.90	-----[IV]
CAN	6.61	6.63	17.7
BCN	17.01	17.01	33.4
MVK	4.20	1.33	-----
NMP	2.50	2.30	-----
4-chlorobenzonitrile	20.91	21.28	32.3
3-chlorobenzonitrile	18.26	18.43	27.4
2-chlorobenzonitrile	15.40	15.38	29.0
4-methoxybenzonitrile	21.31	21.85	16.3
Propionitrile	7.28	7.29	17.3
Butyronitrile	8.04	8.04	17.7
Valeronitrile	8.54	8.54	7.67
Hexanenitrile	8.86	8.86	8.34

where A is the transition polarizability (defined in Eqn. 13).

I. The models were not allowed to optimize in the applied electric field. The coordinates calculated in the absence of an applied electric field were used. (Anharmonic contribution) II. The models were allowed to optimize in the presence of the applied electric field. (Geometry distortion term) III. Literature experimental values. [3] IV. Variation in the literature transition polarizability for HCN occurred due to different concentration of HCN in 2-MeTHF because of hydrogen bonding. [3] Therefore no literature value is reported here.

Table 4. Calculated difference polarizabilities compared to experimental values.

Molecule	$\Delta\alpha$ ($x10^{-3}$) ($cm^{-1}/(MV/cm)^2$) [I]	$\Delta\alpha$ ($x10^{-3}$) ($cm^{-1}/(MV/cm)^2$) [II]	$\Delta\alpha$ ($x10^{-3}$) (literature values) ($cm^{-1}/(MV/cm)^2$) [III]
Acetone	2.17	-7.56	-----
CO	-2.16	-8.65	-----
CN^-	-2.17	15.1	-----
HCN	2.16	4.32	-----[IV]
CAN	-2.16	-10.1	-45.4
BCN	-2.16	15.1	-36.4
MVK	2.16	-2.16	-----
NMP	-4.32	13.0	-----
4-chlorobenzonitrile	-4.32	-2.15	-14.6
3-chlorobenzonitrile	-2.15	-10.8	-12.9
2-chlorobenzonitrile	0.00	-3.78	-19.6
4-methoxybenzonitrile	-4.32	-6.49	-1.12
Propionitrile	-0.01	-4.33	-39.8
Butyronitrile	0.00	-4.32	-26.9
Valeronitrile	-2.16	-7.57	7.84
Hexanenitrile	-2.16	-2.15	-29.2

where $\Delta\alpha$ is the difference polarizability (defined in Eqn. 14).

I. The models were not allowed to optimize in the applied electric field. The coordinates calculated in the absence of an applied electric field were used. (Anharmonic contribution) II. The models were allowed to optimize in the presence of the applied electric field. (Geometry distortion term) III. Literature experimental values. [3] IV. Variation in the literature transition polarizability for HCN occurred due to different concentration of HCN in 2-MeTHF because of hydrogen bonding. [3] Therefore no literature value is reported here.

Figures

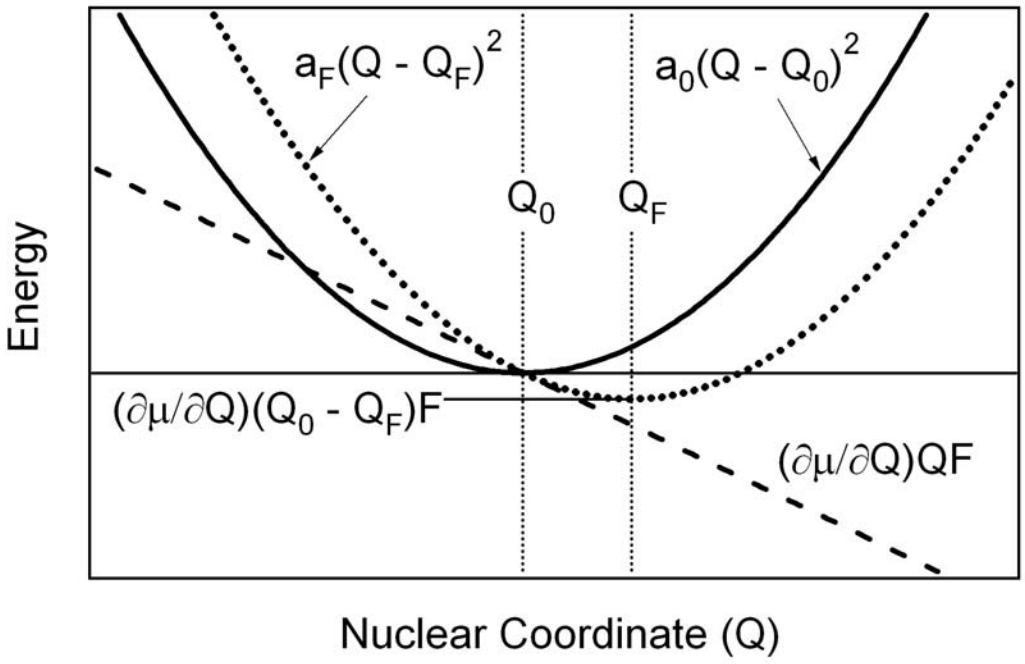

Figure 1. Potential surface at zero field (—) and in an applied electric field (···). The electric field perturbation is linear (– – –). The potential energy surface in an applied field is the linear combination of the PES at zero field and the linear perturbation. The position of the zero field potential and the electric field shifted potential surfaces are shown as Q_0 and Q_F, respectively. The energy offset $(\partial\mu/\partial Q)(Q_0 - Q_F)F$ is shown for the perturbed surface.

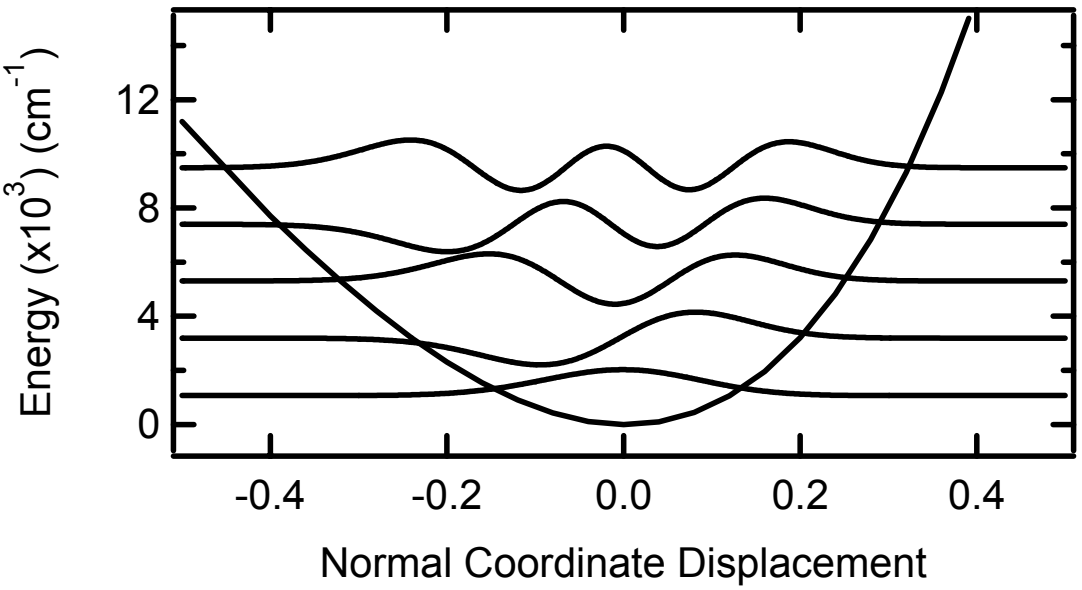

Figure 2. Potential energy surface formed by displacing along the CO stretching normal mode in carbon monoxide and the first five vibrational energy levels calculated by the Numerov-Cooley method.

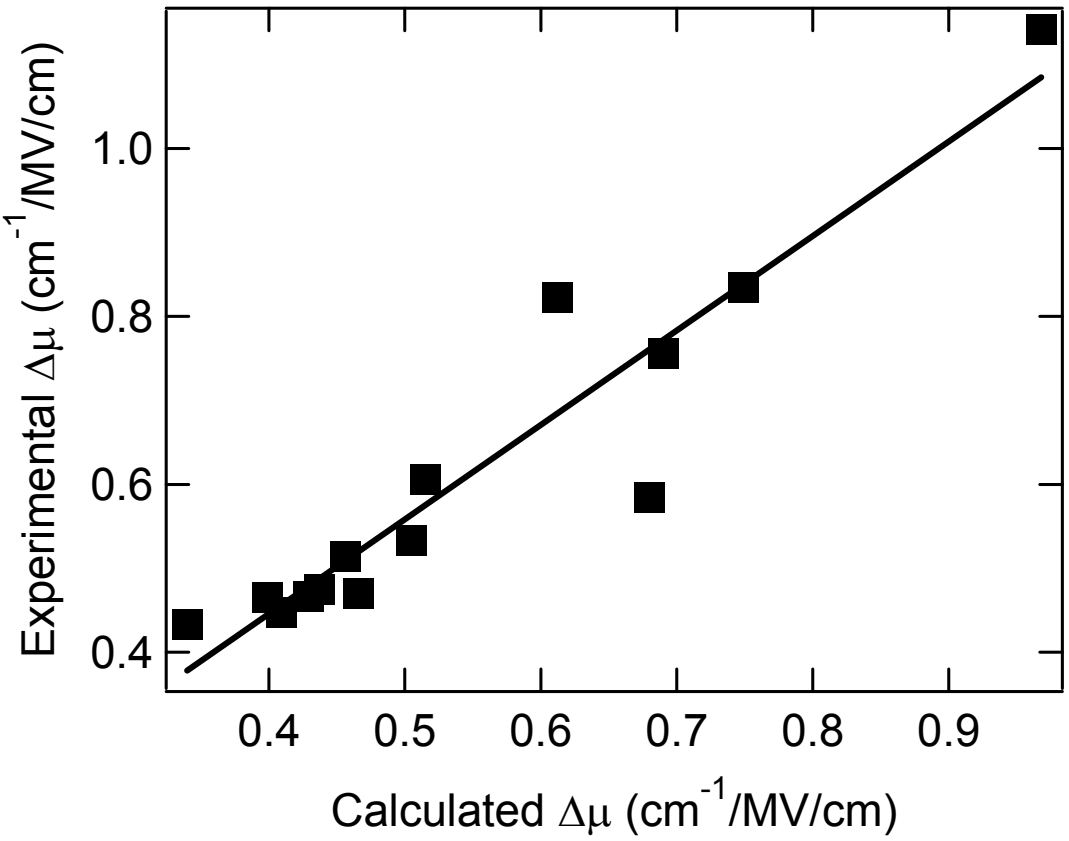

Figure 3. Plot of the experimental versus the DFT calculated vibrational Stark tuning rates for nitriles and carbonyls fit to a line with a slope of 1.1.

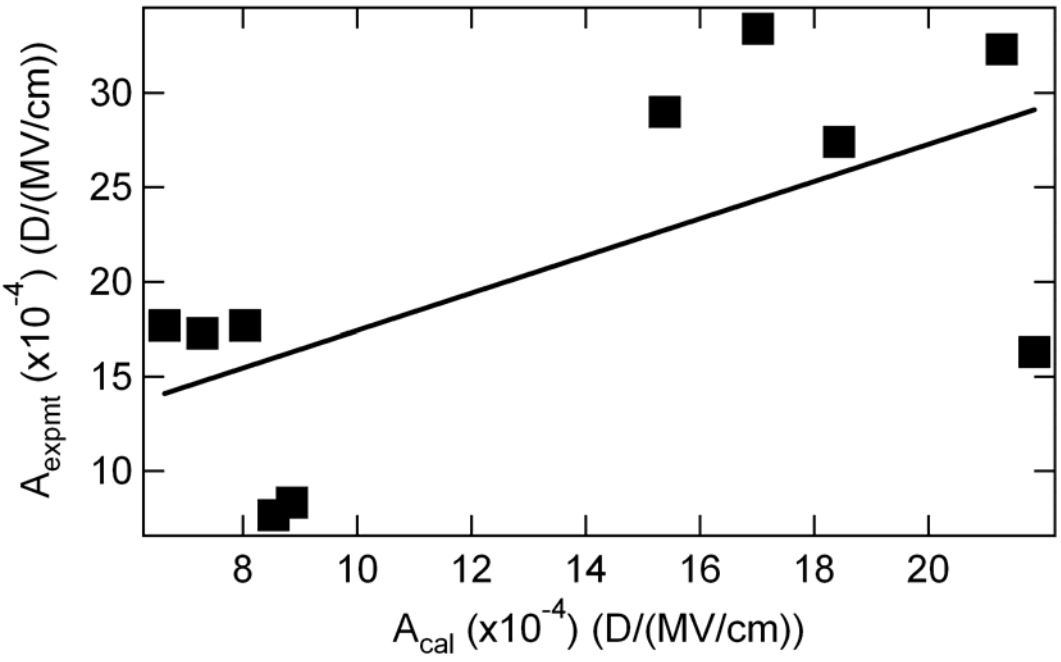

Figure 4. Plot of the experimental versus the DFT calculated transition polarizability for nitriles using optimized molecular geometries in the presence of an applied electric field. The plot for the molecular geometries obtained in the absence of an applied electric field is nearly identical.

Chapter 11

Probing BSA Binding to Citrate Coated Gold Nanoparticles and Surfaces

Gold nanoparticles have been widely used as drug delivery vectors [1-9] and in bio-assays such as in the detection of DNA hybridization [10,11] to take advantage of their unique optical and electronic properties. Citrate is a common electrostatic stabilizing agent for gold nanoparticles since the particles are typically synthesized through a citric acid reduction reaction. [12-14] Electrostatic stabilization arises from mutual repulsion between neighboring gold nanoparticles owing to the negative surface charge of the citrate layer. For drug delivery applications, gold nanoparticles have been modified with bovine serum albumin (BSA). Bovine serum albumin (BSA) appears to bind spontaneously to the surface of citrate coated gold nanoparticles, however, the mechanism of its binding has not yet been determined. BSA can be conjugated to other proteins and peptides utilizing the large number of surface lysine residues of BSA as a scaffolding for chemical attachment. [1-4] The use of gold nanoparticles allows for tracking of the bio-conjugate (nanoparticle plus coating) in different cellular compartments, such as differentiating between cytosol delivery, nuclear delivery and adsorption to the external cell surface by use of optical microscopy and TEM. [1-9]

During the formation of an adsorbed layer on a surface, each adsorbing molecule must pass through the following steps: 1) transport toward the surface, 2) attachment to the surface, and 3) spreading on the surface. [15] These steps suggest that there are two possible hypotheses for the interaction between BSA and a citrate-coated gold surface or nanoparticle. The first is the electrostatic binding hypothesis and the second is the displacement hypothesis. Spreading or structural changes in the adsorbing protein on the surface lower the free energy of the system could be a component of both hypotheses. The electrostatic binding hypothesis states that the attraction between the positive surface residues (at basic

pH values) of BSA and the negative charge from the citrate are responsible for the strong binding of BSA to citrate-coated gold nanoparticles. In this hypothesis, the protein attaches itself to the passivating layer on the gold surface, with little direct interaction between BSA and the gold surface. The displacement hypothesis states that citrate is displaced by BSA upon adsorption, with functional groups derived from lysine (amine) and cysteine (thiol) among others interact directly with the gold surface. The denaturation hypothesis (for unmodified surfaces) states that the protein unfolds near the surface and exposes hydrophobic residues as well as presenting specific functional groups that interact with the gold surface. Dispersive and van der Waal's forces must play some role in all of the above mechanisms as well.

To better understand citrate and BSA modified gold nanoparticles and surfaces, we use a quartz crystal microbalance with an extra feature for the measurement of dissipation (QCM-D) to monitor citrate and BSA binding to gold surfaces, and zeta potential measurements to compare the pH dependence of the surface charge of citrate (Mallinckrodt Chemical) and BSA (Sigma-Aldrich) coated 10 nm gold nanoparticles (BBInternational). QCM-D monitors both the frequency change upon binding to a gold surface and the dissipation change (the frictional and viscoelastic energy losses in system) upon binding. This technique will be able to study the binding of BSA to citrate coated gold slides as a function of the concentration of protein to obtain binding isotherms. Kasemo and co-workers have pioneered the use of QCM-D for studying biological surface science related processes in liquids [16] including protein adsorption on pure [17,18] and phospholipid-coated [19] surfaces, adsorption of transmembrane protein containing supported phospholipid bilayers on silica, [20]

intact vesicle adsorption and supported biomembrane formation from vesicles in solution, [21] and cell adhesion on supported lipid bilayers. [22] Comparative studies on protein adsorption using QCM-D and optical techniques such as ellipsometry, surface plasmon resonance (SPR) and optical waveguide lightmode spectroscopy (OWL) have shown that the values measured by QCM-D are generally higher in terms of mass than the corresponding optical techniques because the frequency change in liquid QCM-D is sensitive to both protein adsorption and water molecules that bind or hydrodynamically couple to the protein adlayer. [17,18] However this technique is complementary to these optical techniques by providing insight about the mechanical/structural properties of the adlayer such as viscoelasticity through the analysis of the energy dissipation in the adlayer and its magnitude in relation to the frequency shift (due to adsorbed mass). The zeta potential measurements will allow the surface charge of the particles between citrate and BSA stabilized particles to be compared as a function of pH. Both of these techniques have the advantage of not requiring the use of modified proteins such as luminescent or radioactive labeled proteins in the detection strategy as these labels could alter the structure and function of the protein.

Figure 1A shows representative QCM-D (Q-Sense (Gothenburg, Sweden)) results in the change of the 35 MHz seventh overtone of the fundamental frequency (5 MHz), and the dissipation change upon the sequential addition of citrate (10 mM in water) and BSA (100 μM in 10 mM citrate in water) to a gold coated quartz crystal. These results (normalized by dividing by a factor of 7 corresponding to the number of the harmonic) show a decrease in the frequency of approximately 3.4 Hz and 23.7 Hz and a change in the dissipation of 0.5 and 2.0 for the addition of citrate and BSA, respectively. This dissipation change is indicative of

the formation of a non-rigid layer on the gold surface. Formation of a viscoelastic layer results in a change in the dissipated energy, as it dampens the oscillation. These changes in the frequency and dissipation are due to the binding of citrate and BSA to the gold surface, sequentially. Figure 2B shows the BSA concentration dependence (1 – 100 μM) of the frequency change in response to the binding of BSA to a citrate coated gold surface. The QCM-D measurements for each concentration of BSA were performed on separate gold coated quartz crystals to determine the resulting surface coverage of BSA corresponding to each solution concentration. The change in frequency was converted to an approximate surface coverage of BSA using the Sauerbrey equation (Eqn. 2): [23]

$$\Delta m = -\frac{C\Delta f}{n} \qquad \text{(Eqn. 1)}$$

were Δm is the change in mass, n is the number of the harmonic of the fundamental resonance frequency used in the experiment, Δf is the change in frequency and C has a value of 17.8 $ngcm^{-2}Hz^{-1}$ for the crystals used in these experiments. The Sauerbrey equation was used since the dissipated energy was less than 10^{-6} per 5 Hz frequency change similar to previous studies. [17,18] The mass calculated from the frequency change is only an approximation since the frequency change is due to bound protein and any trapped or associated water molecules as well. The resulting surface coverage values as a function of BSA concentration in Figure 2B were subsequently fitted to a Langmuir adsorption isotherm given in Eqn. 2: [24]

$$\Gamma_{BSA} = \frac{\Gamma_{\max} K_L [S]_{free}}{1 + K_L [S]_{free}} \qquad \text{(Eqn. 2)}$$

where Γ_{BSA} is the surface coverage of BSA, Γ_{max} is the maximum coverage of BSA and K_L is a constant that is the inverse of the BSA solution concentration required to obtain one half of Γ_{max}. The fit gave the values of $3.8x10^{12}$ molecules/cm^2 for Γ_{max} and 0.8 μM^{-1} for K_L. Figure 2B shows that the binding of BSA exhibits a high affinity binding isotherm common for biopolymers and other macromolecules. These experiments confirm that BSA does bind to citrate coated gold surfaces.

Parallel QCM-D binding studies of BSA to citrate or non-citrate modified gold surfaces were performed where the same crystal was used and the concentrations of BSA were added sequentially from low to high concentration. These results are shown in Figure 2. The change in frequency and surface coverage of BSA for the citrate (solid squares) and non-citrate (hollow squares) coated gold surfaces are plotted as a function of BSA concentration, and fitted to a Langmuir adsorption isotherm. These fits yielded values of $3.0x10^{12}$ molecules/cm^2 and $9.4x10^{12}$ molecules/cm^2 for Γ_{max}, while K_L was found to be 0.05 μM^{-1} and 0.02 μM^{-1} for the citrate or non-citrate coated gold surface, respectively. This figure (Figure 2) shows that the presence of citrate on the gold surface limits the amount of adsorption of BSA onto the gold surface suggesting that BSA does not completely displace the citrate upon binding to the surface and that binding to a citrate coated surface by BSA proceeds predominately by an electrostatic mechanism. The interaction between BSA and the surface is critical for further modification of BSA with targeting peptides, oligonucleotides, or drug molecules.

Figure 3 shows the zeta potential (ZetaSizer 3000, Malvern Instruments) resulting from a pH titration of 10 nm gold nanoparticles ($4.18x10^{12}$ particles/ml) stabilized by citrate

(solid squares) or BSA (hollow squares). The BSA stabilized particles exhibited an isoelectric point (zeta potential is zero) at pH 4.6 as determined by a sigmoid fit (solid curve) to the data of the BSA modified nanoparticles. The commercially available citrate stabilized gold nanoparticles (BBInternational) were used as received and the BSA modified particles were obtained by mixing a solution of BSA and gold nanoparticles in a ratio of 2000 BSA molecules to one gold nanoparticle for 16 hours. Zeta potential measurements could not be performed on this concentration of BSA alone. Only in the presence of gold nanoparticles could the zeta potential be determined. The pH titration of the citrate stabilized particles was stopped at pH 5 due to the onset of particle aggregation. BSA modified particles were more stable with respect to pH and thus allowed the isoelectric point shown in Figure 3 of the BSA modified gold nanoparticles to be measured. The zeta potential data show that BSA imparts stability to the gold nanoparticles with respect to aggregation by both electrostatic (depending on the pH) forces and steric interactions. The stability imparted by steric interactions (bulky protein on the surface preventing neighboring gold nanoparticles from getting in close enough proximity to interact and aggregate) is illustrated by the BSA coated gold nanoparticles remaining stable at the isoelectric point of the colloid when electrostatic repulsion is at a minimum. The citrate stabilized gold nanoparticles had a slightly more negative zeta potential than BSA modified particles in the pH range studied. The zeta potential of the citrate particles remained nearly constant in the pH 5 to 12 range unlike the BSA modified particles. The BSA modified gold nanoparticles illustrated a strong pH dependence in its zeta potential. Hence depending on the pH of the system, the zeta potential of the BSA modified particles could be negative or positive. For targeted chemotherapy

applications, the relevant pH range will be between pH 7.4 and 6.8, which represents the normal blood pH and the pH in the vicinity of a tumor, respectively. Thus, it is important that the stabilizing and targeting properties of the delivery vector are functional and known within this pH range.

These experiments show that BSA binding to gold nanoparticles and gold surfaces occurs by an electrostatic mechanism. The binding as measured by QCM-D was found to be a function of BSA concentration and the resulting binding isotherm could be fit to a Langmuir adsorption isotherm. The binding of BSA was found to decrease when the gold surface was first exposed to citrate relative to a clean surface. Hence the nature of the surface modification can impact the binding of proteins such as BSA to the surface thereby suggesting an electrostatic mechanism of BSA binding to a citrate coated gold surface. BSA modified particles were found to be more stable with respect to pH relative to citrate stabilized gold nanoparticles and showed an isoelectric point of pH 4.6. The stability of the BSA coated gold nanoparitlces was found from zeta potential measurements as a function of pH to be from electrostatic forces and steric interactions. This study offers the foundation for the future investigation of various modified metal nanoparticles with a variety of stabilizing agents and the subsequent binding of biomolecules such as potential drug candidates to these particles.

Acknowledgements

This work was done in collaboration with Wilhelm R. Glomm (NTNU), Marcus C. Johnson (NCSU), Magne K. Knag (NTNU) and Stefan Franzen (NCSU). This research was financially supported by the National Science Foundation.

References

(1) Tkachenko, A. G.; Xie, H.; Coleman, D.; Glomm, W.; Ryan, J.; Anderson, M. F.; Franzen, S.; Feldheim, D. L. *J. Am. Chem. Soc.* **2003**, *125*, 4700-4701.

(2) Tkachenko, A. G.; Xie, H.; Liu, Y. L.; Coleman, D.; Ryan, J.; Glomm, W. R.; Shipton, M. K.; Franzen, S.; Feldheim, D. L. *Bioconjugate Chem.* **2004**, *15*, 482-490.

(3) Tkachenko, A. G.; Xie, H.; Ryan, J.; Glomm, W. R.; Franzen, S.; Feldheim, D. L. In *Bionanotechnology Protocols*; Rosenthal, S., Wright, D., Eds.; Humana Press, Inc.: New York, In Press.

(4) Xie, H.; Tkachenko, A. G.; Glomm, W. R.; Ryan, J. A.; Brennaman, M. K.; Papanikolas, J. M.; Franzen, S.; Feldheim, D. L. *Anal. Chem.* **2003**, *75*, 5797-5805.

(5) Feldherr, C. M.; Akin, D. *J. Cell Biol.* **1990**, *111*, 1-8.

(6) Feldherr, C. M.; Lanford, R. E.; Akin, D. *Proc. Natl. Acad. Sci. U. S. A.* **1992**, *89*, 11002-11005.

(7) Feldherr, C. M.; Akin, D. *Exp. Cell Res.* **1994**, *215*, 206-210.

(8) Feldherr, C.; Akin, D. *Mol. Biol. Cell* **1998**, *9*, 188A-188A.

(9) Feldherr, C. M.; Akin, D. *J. Cell Sci.* **1999**, *112*, 2043-2048.

(10) Demers, L. M.; Mirkin, C. A.; Mucic, R. C.; Reynolds, R. A.; Letsinger, R. L.; Elghanian, R.; Viswanadham, G. *Anal. Chem.* **2000**, *72*, 5535-5541.

(11) Taton, T. A.; Mirkin, C. A.; Letsinger, R. L. *Science* **2000**, *289*, 1757-1760.

(12) Turkevich, J.; Stevenson, P. C.; Hillier, J. *Discussions of the Faraday Society* **1951**, 55-&.

(13) Turkevich, J.; Stevenson, P. C.; Hillier, J. *J. Phys. Chem.* **1953**, *57*, 670-673.

(14) Turkevich, J.; Garton, G.; Stevenson, P. C. *J. Colloid Sci.* **1954**, *9*, S26-S35.

(15) Malmsten, M., Ed. *Biopolymers at Interfaces*; 2nd ed.; Marcel Dekker, Inc.: New York, 2003; Vol. 110.

(16) Kasemo, B. *Surf. Sci.* **2002**, *500*, 656-677.

(17) Hook, F.; Kasemo, B.; Nylander, T.; Fant, C.; Sott, K.; Elwing, H. *Anal. Chem.* **2001**, *73*, 5796-5804.

(18) Hook, F.; Voros, J.; Rodahl, M.; Kurrat, R.; Boni, P.; Ramsden, J. J.; Textor, M.; Spencer, N. D.; Tengvall, P.; Gold, J.; Kasemo, B. *Colloid Surf. B-Biointerfaces* **2002**, *24*, 155-170.

(19) Glasmastar, K.; Larsson, C.; Hook, F.; Kasemo, B. *J. Colloid Interface Sci.* **2002**, *246*, 40-47.

(20) Graneli, A.; Rydstrom, J.; Kasemo, B.; Hook, F. *Langmuir* **2003**, *19*, 842-850.

(21) Reimhult, E.; Hook, F.; Kasemo, B. *Langmuir* **2003**, *19*, 1681-1691.

(22) Andersson, A. S.; Glasmastar, K.; Sutherland, D.; Lidberg, U.; Kasemo, B. *J. Biomed. Mater. Res. Part A* **2003**, *64A*, 622-629.

(23) Sauerbrey, G. *Zeitschrift Fur Physik* **1959**, *155*, 206-222.

(24) Kirk, J. S.; Bohn, P. W. *Journal of the American Chemical Society* **2004**, *126*, 5920-5926.

Figures

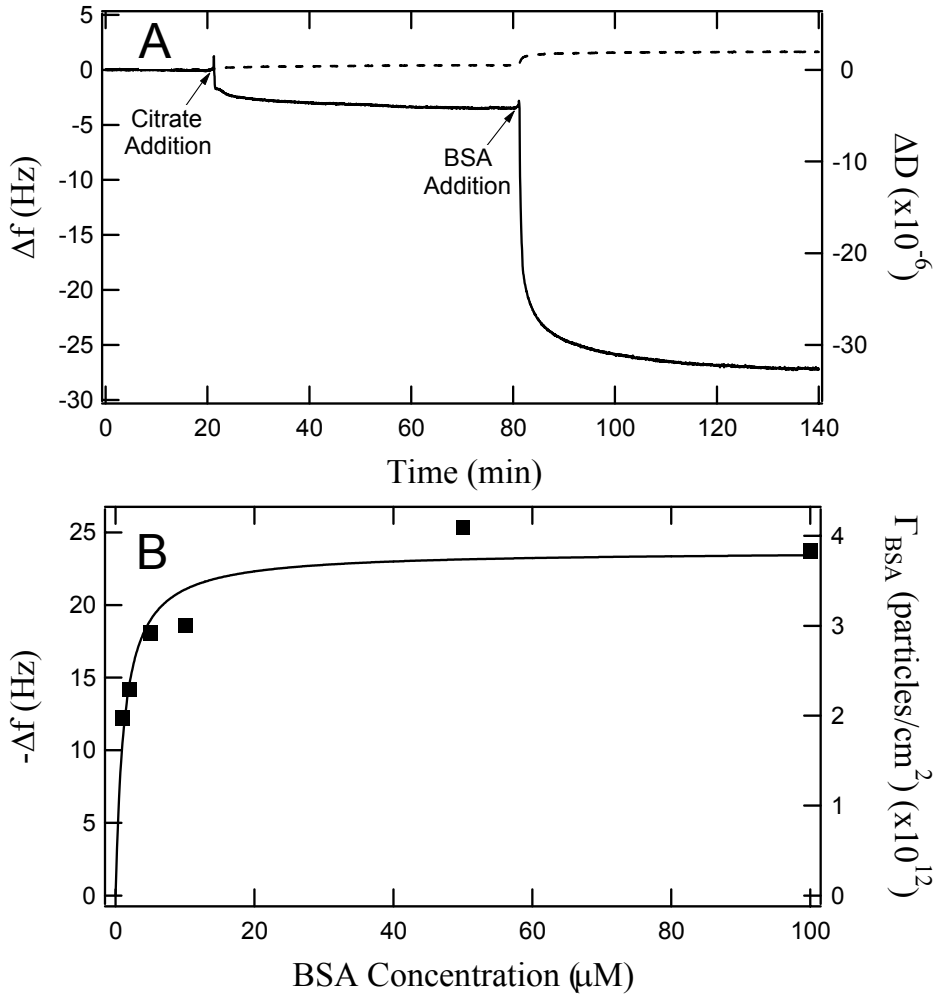

Figure 1. A. Representative QCM-D measured change in frequency of the 35 MHz seventh harmonic of the fundamental frequency and dissipation change upon binding of citrate (10 mM in water) and the subsequent binding of BSA (100 μM in 10 mM citrate in water) to a gold coated quartz crystal as a function of time at 25.7±0.1°C. The data is divided by seven to normalize for the harmonic used. B. The change in frequency and the corresponding change in surface coverage of BSA as a function of concentration onto a gold surface fit to a Langmuir adsorption isotherm (Eqn. 2).

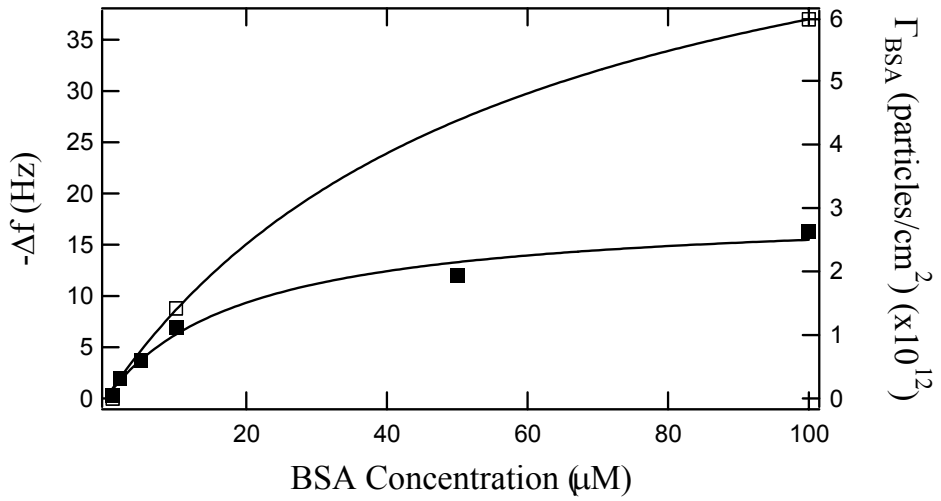

Figure 2. The change in the frequency of the 35 MHz seventh harmonic of the fundamental frequency of a gold coated quartz crystal as a function of BSA concentration coated with (solid squares) or without (hollow squares) citrate fit to a Langmuir adsorption isotherm (solid) (Eqn. 2) measured at 25.7±0.1°C.

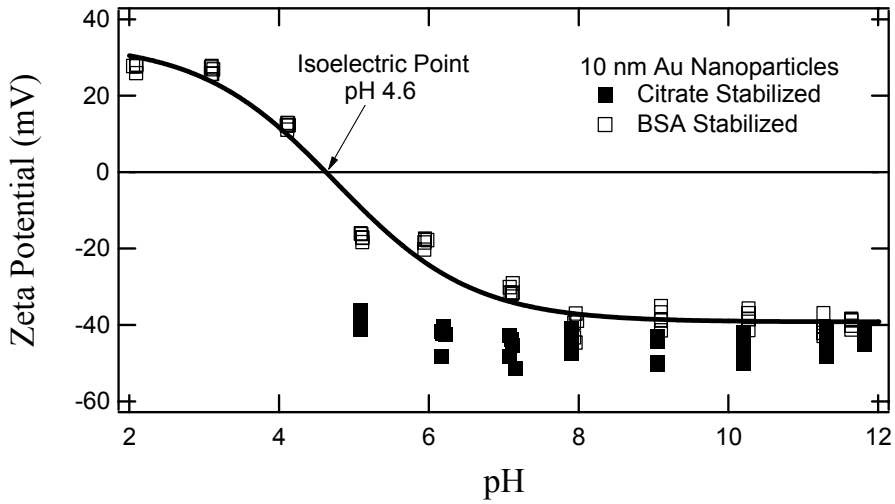

Figure 3. Zeta potential of 10 nm gold nanoparticles recorded as a function of stabilizing agent (citrate or BSA) and pH.

Chapter 12

Infrared Temperature Jump Investigation of the Folding Kinetics of the Villin Headpiece Subdomain

Abstract

Equilibrium FTIR and T-jump IR spectroscopic techniques were utilized to study the thermodynamic processes of unfolding and folding of a three-α-helix bundle protein known as the villin headpiece subdomain (HP36) and a double phenylalanine mutant (HP36F4751L) that destabilizes the hydrophobic core of this protein. The temperature dependence of the equilibrium FTIR absorbance spectra in the Amide I' region were analyzed by singular value decomposition (SVD) to determine the thermodynamic parameters of unfolding and to extract the spectral components indicative of unfolding for these proteins. Gaussian global fitting was utilized to confirm the SVD results by fitting the temperature dependent difference FTIR spectra formed by subtracting the lowest temperature absorbance spectrum from the higher temperature spectra in the Amide I' region to multiple Gaussian bands simultaneously for HP36. The relaxation kinetics following a T-jump perturbation to the system equilibrium was studied for both HP36 and HP36F4751L. These proteins exhibited biphasic kinetics due to the helix-coil transition and the formation of tertiary contacts. Based on the equilibrium FTIR data and the observed relaxation rates the microscopic folding and unfolding rates were determined.

Introduction

The kinetic study of protein folding mechanisms using nanosecond temperature-jump methods has progressed from studies of single alpha helical and beta hairpin peptides to small domains. The folding time scale for α helixes has been established to be ~100 – 300 ns [1-4] while the folding time scale for β hairpins has been shown to be ~ 6 μs. [5] Recently the

study of the kinetics of the folding of small three-α-helix bundle proteins has increased due to their relatively small size and short folding times. For instance, the relatively small size and fast folding times of the engrailed homeodomain, B domain of protein A (BdpA) and the villin headpiece (HP36) are good systems for molecular dynamic simulations. [6-11] However, more extensive experimental studies in the sub-microsecond regime need to be performed to test the proposed microscopic mechanisms and folding rates of these proteins by MD simulations. [6,7,12-15]

Protein folding studies provide information on how the linear sequence of amino acids folds into a unique structure. [16] Since protein function is also defined by the structure, these studies provide an essential step in the interpretation of genetic information. Protein folding or misfolding has been associated with several diseases including Alzheimer's disease due to the formation or β amyloid aggregates and prion diseases such as sheep scrapie, mad cow disease and Creutzfeldt-Jakob disease in humans possibly due to the initial misfolding of the prion protein which leads to further misfolding of native prion proteins. [17,18] In order to take advantage of the genomic information available, the protein folding problem needs to be solved. Many theoretical and experimental studies have been aimed at answering specific aspects of the folding problem. Significant experimental progress has been achieved through the use of NMR line shape analysis and T-jump IR, UV resonance Raman and fluorescence spectroscopy to investigate folding and unfolding in peptide and protein systems on the nanosecond to millisecond time regime. [1-5,12,14-16,19-23]

The villin headpiece subdomain is a 36 residue monomer, three-α-helix bundle protein (shown in Figure 1) from the larger 76 amino acid chicken villin actin bundling

protein that is one of the fastest folding proteins known. [15,24] Several MD simulations on the villin headpiece subdomain have been performed. [9-11,25-28] These simulations have used explicit [10,25] or implicit [9,11,26] solvent utilizing parallel computing [10,25] and worldwide distributed computing processing [11] to model this protein to study this protein that folds in the few microsecond [14,15] time regime. These simulations have suggested α-helix formation and the burial of some hydrophobic residues to be early events in folding. [9-11,25] Most of these theoretical studies suggest a two-state model of folding, [9,11] while one study has proposed the existence of a possible intermediate in the folding process. [10] One study has predicted a folding time of 5 μs, in good agreement with experimental studies. [11] However, experimental investigations are needed to test the calculated microscopic folding mechanisms.

Previous experimental studies on the villin headpiece subdomain have included NMR line shape analysis in the microsecond time regime suggesting that HP36 folds on the 10 μs time scale. [15] However recent T-jump fluorescence experiments on two villin headpiece mutants have shown the existence of biphasic relaxation kinetics. [14] The fast phase (70 ns at 300K) was proposed to be the helix – coil transition while the kinetics were modeled with a two-state system based on the slow (5 μs at 300K) relaxation time that follows the global folding of this protein. [14] In this study, the wild type villin headpiece subdomain (HP36) and a double mutant that replaces F47 and F51 in the hydrophobic core [29] with leucine residues (HP36F451L) were investigated. These two proteins were studied by equilibrium FTIR spectroscopy and T-jump infrared spectroscopy.

Materials and Methods

Protein Sample Preparation. The wild type villin headpiece (HP36) and double mutant (HP36F4751L) were expressed and purified from *Escherichi coli* BL21 (DE3)-pLysS strain as described previously. [24] The proteins were lyophilized from D_2O (Cambridge Isotope laboratories) to allow deuterium-hydrogen exchange of the amide protons to occur. The proteins were dissolved in a buffer containing 10 mM sodium phosphate and 150 mM sodium chloride at a pH^* of 5.3 in D_2O. The pH^* is the uncorrected (for D_2O) pH-meter reading at 25°C. The protein solutions were filtered to remove any aggregates present and used without any further purification. The protein solutions for the IR experiments had a concentration of 1 – 2 mM.

Equilibrium FTIR Temperature Dependent Measurements. The equilibrium protein FTIR T-dependent spectra were recorded on a Bio-Rad FTS-40A FTIR spectrometer equipped with a liquid nitrogen cooled MCT detector. The spectra were the result of 512 scans recorded at a resolution of 2 cm^{-1}. The proteins were dissolved in D_2O (instead of H_2O) to remove solvent interference in the Amide I' region (the prime indicates that D_2O is the solvent). A split IR cell composed of CaF_2 windows was utilized with a path length of 100 μm to record the spectrum of both the reference (buffer in D_2O) and the sample (protein in the buffer in D_2O) side of the IR transmission cell under identical conditions at each temperature. The temperature of the IR cell was controlled by a water bath while the sample temperature was measured by a thermocouple attached to the cell. The absorbance spectra of the proteins were determined from the negative logarithm of the ratio of the single beam spectrum of the sample to the reference side of the IR split cell at each temperature. The

absorbance spectra were baseline corrected using a single point at 1750 cm^{-1} by subtracting the absorbance at this wavenumber from the rest of the absorbance values at each temperature. The equilibrium thermal unfolding of the proteins was found to be reversible (absence of aggregation).

Time-Resolved Temperature Jump (T-Jump) IR Kinetic Measurements. The time resolved T-jump apparatus used to measure protein relaxation kinetics in this study has been described previously. [19] The method is a pump-probe experiment where 1.91 μm radiation is the pump beam that initiates a rapid T-jump in the sample perturbing the system equilibrium while an IR diode is used to probe structural changes in the sample as the sample relaxes back to a new equilibrium at the final temperature after the T-jump. The 1.91 μm (10 ns fwhm Gaussian pulse width, ~ 23 mJ/pulse) pump radiation is obtained from a H_2 filled Raman shifter (1 stokes shift) pumped by a 10 ns pulsed 10 Hz repetition rate Q-switched DCR-4 Nd:YAG laser (Spectra Physics, Mountain View, CA) and is absorbed by weak combination bands in deuterium oxide (ε = 6 cm^{-1} at 1.91 μm). This absorption results in a thermally equilibrated T-jump in the pump volume within 20 ns since thermal equilibration in deuterium oxide occurs in the sub-nanosecond time scale. This pump radiation was chosen due to its transmission properties (87 % pump radiation transmitted through 100 μm path length sample cell) that allows for nearly uniform heating in the pump-probe overlap region and because most peptides and proteins do not absorb at this wavenumber. The same split cell used for the equilibrium FTIR experiments was used for the kinetic measurements. The reference D_2O compartment serves as an internal thermometer in these experiments to determine the magnitude of the T-jump.

The probe is a CW lead salt IR diode laser (Laser Components Instrument Group, Wilmington, MA) that is tunable in the 1600 – 1700 cm^{-1} region. A fast (50 MHz) photovoltaic (PV) mercury cadmium telluride (MCT) detector (Kolmar Technologies, Newburyport, MA) measured the changes in transmission of the IR probe beam and a Tektronix digitizer (7612D, Beaverton, OR) was used to digitize the signal. The probe beam was focused to 50 μm at the center of the heated volume to ensure uniform temperature distribution in the probe volume to eliminate effects from the temperature gradients produced by the wings of the Gaussian pump beam (1 mm beam diameter). The T-jump apparatus has a response time of ~ 23 ns due to sample heating and the detector rise time. The transient kinetic traces in response to a T-jump of both the sample and reference side were recorded under identical conditions and were the average of 2000 laser perturbations. The initial temperature (before the T-jump) was controlled and measured the same as for the equilibrium FTIR measurements. The resulting T-jumps ranged in temperature from 5 – 15°C. The relaxation kinetics of the protein was extracted from the kinetic traces by subtracting the change in absorbance of the reference (D_2O buffer) from the sample (protein in D_2O buffer). The transient kinetic traces were recorded from the nanosecond to tens of milliseconds time regime with the thermal energy diffusing from the pump-probe interaction volume in about 20 ms.

Analysis of Equilibrium and Kinetic Data. The protein equilibrium (static) temperature dependent FTIR spectra were analyzed by singular value decomposition (SVD) and/or Gaussian global fitting. The SVD analysis is based upon Eqn. 1:

$$U \times W \times V^T = A \qquad (1)$$

where the A matrix is comprised of the absorbance at each wavenumber and temperature in the data set that is decomposed into spectral components (the U matrix) and the corresponding temperature profiles (the V^T matrix) of these spectral components while the weighting coefficients for each of these components is found along the diagonal of the W matrix. Gaussian global fitting was performed on the difference FTIR spectra formed by subtracting the lowest temperature spectrum from the higher temperature spectra. These temperature dependent spectra were fit to multiple Gaussian peaks where the parameters for each Gaussian band for all of the temperatures were minimized by a global chi square value. Both of these techniques allow for the temperature dependences of multiple processes to be extracted from the data if present.

The protein relaxation kinetic traces were fit to a bi-exponential function given in Eqn. 2:

$$y(t) = A_0 + A_1 \exp(-k_1 t) + A_2 \exp(-k_2 t) \qquad (2)$$

where A_0 is an offset, A_1 and A_2 are pre-exponential factors, k_1 and k_2 are the rates and t is the time. The relaxation time (τ) is determined from the inverse of the rate ($\tau = 1/k$). The change is absorbance of D_2O (ΔA) as a function of temperature was determined by static (equilibrium) IR measurements using Eqn. 3:

$$\Delta A = -\log\left(\frac{I_o + \Delta I}{I_o}\right) \qquad (3)$$

where I_o is the IR intensity at the lowest temperature and ΔI is the change in IR intensity at a given temperature relative to I_o. This data formed the calibration curve that was used to determine the magnitude of the T-jumps by the transient change in absorbance of D_2O after

the laser pulse perturbation of the system. The data analysis was performed in IGOR Pro (Wavemetrics Inc.) or Excel (Microsoft Corporation).

Results and Discussion

Structure of the Villin Headpiece Subdomain (PDB 1VII)

The structure of the wild type chicken villin headpiece subdomain (HP36) protein is shown in Figure 1. The peptide backbone of the protein is shown with ribbons to illustrate the three α helices that comprise this three-helix bundle protein. The sequence of the protein is: MLSDEDFKAVFGMTRSAFANLPLWKQQNLKKEKGLF. The protein has two small α-helices at the N-terminus consisting of five and four amino acid residues, respectively with a longer (ten amino acid residues) α-helix at the C-terminus. The three phenyalanine (F) residues (47, 51 and 58) that help stabilize the hydrophobic core of this protein are shown in Figure 1 since F47 and F51 were replaced by leucine (L) to form the HP36F4751L double mutant that is investigated here along with the wild type.

Equilibrium FTIR Spectroscopy

Infrared spectroscopy in the Amide I' region was utilized to study the equilibrium stability of HP36 and HP36F4751L as a function of temperature. Amide I' is comprised primarily of carbonyl (C=O) stretching of the peptide backbone. The energy of this vibration is sensitive to the secondary and tertiary structure of the protein. For instance, the position of this vibrational mode is dependent upon hydrogen bonding and its local dielectric environment (hydrophilic (solvent exposed) versus hydrophobic).

HP36

The equilibrium FTIR absorbance spectrum of HP36 is shown in Figure 2A in the 1550 – 1750 cm^{-1} region as a function of temperature from 3 – 93°C in ~ 5°C increments. The Amide I' band is centered at 1645 cm^{-1} at 3°C. This energy corresponds to an α-helical protein consistent with the known structure of HP36. As the temperature is increased, this band begins to decrease in intensity at its maximum and begins to shift to higher frequency. This shift is due to the melting or unfolding of the protein since disordered structures absorb at higher energies arising from a change in hydrogen bonding and the local dielectric environment of the peptide backbone carbonyl groups.

The Amide I' band is complex due to contributions from multiple carbonyl groups in different local environments and hydrogen bonding configurations. However, to identify sub-components of this band, difference FTIR spectra can be formed by subtracting the spectrum at the lowest temperature (3°C) from the rest of the spectra at higher temperatures. The resulting difference FTIR spectra are shown in Figure 2B. This figure (2B) shows a decrease in intensity in the region ~1600 – 1656 cm^{-1} (at higher temperatures) and an increase in intensity in the ~1656 – 1700 cm^{-1} region as the temperature is increased. The decrease in intensity is indicative of the loss of secondary and tertiary structure of the protein while an increase in intensity with increasing temperature results from the formation of more disordered regions of the protein. The decrease in intensity at 1674 cm^{-1} could be due to the presence of trifluoroacetic acid (TFA) from the purification of this protein, [2,24] from the melt of a turn region upon heating or due to two overlapping positive bands resulting in a negative

feature at 1674 cm^{-1}. These difference spectra do not show the presence of an isosbestic point suggesting that the unfolding of HP36 may not be a two-state process.

In order to analyze the temperature dependence FTIR data for HP36 in terms of the thermodynamic parameters of unfolding and to identify the various components involved in the unfolding process, singular value decomposition (SVD) and Gaussian global fitting were employed. The results from the SVD analysis of the temperature dependent FTIR absorbance spectra in the Amide I' spectral region are shown in Figure 3. Figure 3A shows the statistically significant spectral components identified by SVD while Figure 3B illustrates the temperature dependence of each of these spectral components. The SVD analysis identified three spectral components with the first component (solid spectrum) being essentially the average of all of the temperature dependent FTIR spectra in the Amide I' region with the second component (short dashed spectrum) and the third spectral component (long dashed spectrum) accounting for the deviation of the data from the first component. The second and third components were formed from a matrix rotation of the original two components determined by SVD to better account for the experimental data. These later two components account for the difference FTIR spectra shown in Figure 2B that do not show an isosbestic point suggestive of more than one process. The temperature dependence of the first component is essentially flat (squares) as expected whereas the second (triangles) and third (bowties) components show a temperature dependence as shown in Figure 3B. However the temperature dependence of the second component occurs at a lower temperature relative to the temperature dependence of the third spectral component. Three SVD components were expected given the lack of an isosbestic point in the difference FTIR

spectra (Figure 2B). This result suggests that the melt of HP36 is a three step process that involves an intermediate. NMR experiments[15] have shown a difference in the exchange rates based on line shape analysis from temperature dependent NMR experiments following F47 or F51 suggestive that the first N-terminus short helix possibly behaves differently from the rest of the protein.

In order to extract the thermodynamic parameters describing the thermal melt of the HP36 a two-state model of unfolding was employed focusing on the third component from the SVD analysis. The presence of three spectral components shows that the melt follows at least a three-state model of unfolding involving an intermediate; however, in this study only the transition represented by the third spectral component from the SVD analysis will be considered using a two-state model for simplicity due to the difficulty in determining the equilibrium constants for both steps in a three-state model. Based on a two-state model of folding given in Eqn. 4:

$$F \overset{K_{eq}}{\leftrightarrow} U \qquad (4)$$

where F and U represent the folded and unfolded ensemble, respectively and K_{eq} is the equilibrium constant relating these two states, the temperature dependence of the second spectral component from the SVD analysis can be fit (solid curve) to Eqn. 5:

$$A = \frac{A_f + K_{eq} * A_u}{1 + K_{eq}} \qquad (5)$$

where A, A_f and A_u represent the measured absorbance as a function of temperature, the absorbance of the folded ensemble and the absorbance of the unfolded ensemble, respectively. In this model, a linear temperature dependence of the absorbance

($A(T) = a + bT$) of the folded and unfolded ensembles was used for the fit of the temperature dependence of the third spectral component of HP36 determined by SVD. In Eqns. 4 and 5, the equilibrium constant is related to the change in the Gibbs free energy (ΔG) by Eqn. 6:

$$K_{eq} = \exp(-\Delta G / RT) \qquad (6)$$

where ΔG is given by Eqn. 7:

$$\Delta G = \Delta H_{T_m} + \Delta C_P (T - T_m) - T\left[\Delta S_{T_m} + \Delta C_P \ln\left(T / T_m\right)\right] \qquad (7)$$

where ΔH_{T_m} and ΔS_{T_m} are the enthalpy and entropy of unfolding at the melt temperature (T_m), respectively and ΔC_P is the change in the heat capacity of unfolding. The heat capacity takes into account the temperature dependence of the enthalpy and entropy of unfolding while Eqn. 7 assumes that the heat capacity is not temperature dependent in this temperature range. Using these equations, the temperature dependence of the third spectral component shown in Figure 3B of the thermal unfolding of HP36 (triangles) was fit (solid curve) to yield the thermodynamic parameters of the equilibrium melt of this protein given in Table 1A where the melt temperature was found to be 330K. These thermodynamic values illustrate that the thermal melt of this protein in enthalpically unfavorable but entropically favorable.

To confirm the results from the SVD analysis of the thermal unfolding of the villin headpiece subdomain, Gaussian global fitting was performed on the temperature dependent FTIR difference spectra shown in Figure 2B. Each spectrum was fit simultaneously to six Gaussian bands. The amplitude, width and position of these Gaussian bands were allowed to

vary simultaneously to achieve the best fit of the data. The number of Gaussian bands used to fit the data was determined by adding Gaussian bands until the fit did not significantly improve. A representative fit from the Gaussian global fitting of the temperature dependent FTIR difference spectra is given in Figure 4A for the difference spectrum formed from the subtraction of the absorbance spectrum measured at 64ºC from the absorbance spectrum recorded at 3ºC. In this figure (4A), the raw data (long dashed), the overall fit (solid) and the six individual Gaussian bands (short dashed) are shown. For this difference spectrum, the peak positions determined were 1614, 1629, 1645, 1663, 1680 and 1704 cm^{-1}. The Gaussian bands with negative features are due to structural elements that decrease as the protein melts and the positive modes account for the increase in disordered regions of the protein. Due to differences in hydrogen bonding and the local dielectric environment, the mode at 1629 cm^{-1} probably arises from carbonyl groups in the alpha helices that are solvent exposed, while the mode at 1645 cm^{-1} probably results from carbonyl groups in the alpha helices that are in solvent free areas such as the hydrophobic core in agreement with previous work. [13] The addition of hydrogen bonding with the aqueous solvent in addition to hydrogen bonding in the α-helix results in a lower energy for the carbonyl stretch of carbonyl groups in solvated regions of the alpha helices relative to carbonyl groups in buried regions of the protein. The temperature dependence of the areas of these Gaussian bands (with the exception of the band at 1704 cm^{-1}) is shown in Figure 4B. All of these curves show a temperature dependence similar to the third spectral component from the SVD analysis except for the temperature dependence of the area of the band at 1663 cm^{-1} that shows a similar profile to the second spectral component from the SVD analysis. Therefore, this analysis is in agreement with the

SVD analysis. The melt transition represented by the temperature dependence of the third spectral component is in agreement with previous studies on HP36. [14,15] All of the melt transitions (except the 1663 cm^{-1} curve) shown in Figure 4B were fit globally (solid curves) to Eqn. 5 to extrapolate the thermodynamic parameters of the thermal unfolding of HP36. Also, the individual curves for the areas of the bands at 1629 and 1645 cm^{-1} were fit separately. These values are listed in Table 1B. The thermodynamic parameters for the global fit show that there is an enthalpic barrier to unfolding but that unfolding is entropically favorable; however, the absolute values differ from the SVD results. The origin of these differences can be seen from the fit parameters for the temperature dependence of the 1629 and 1645 cm^{-1} band areas. The enthalpy, entropy and heat capacity values are all much larger for the melt of the 1645 cm^{-1} band relative to the melt of the 1629 cm^{-1} band because the melt transition is broader and more gradual for the 1629 cm^{-1} band relative to the 1645 cm^{-1} band although the melt temperatures (T_m) are nearly the same. Therefore, in the global fit the weighting of the individual Gaussian band areas will determine the final thermodynamic parameters. In the Gaussian fitting of the difference FTIR spectra, the mode at 1629 cm^{-1} is the largest component and therefore the fit parameters are lower than the values obtained from the SVD analysis. The Gaussian fitting of the difference spectra is more subjective than the SVD analysis and hence SVD is likely a better measure of the thermodynamic parameters for the thermal unfolding of HP36. In this study, the SVD analysis results from the melt of HP36 will be compared with the SVD analysis of the double mutant HP36F4751L of the villin headpiece subdomain to allow a direct comparison of these two proteins.

HP36F4751L

The same equilibrium infrared technique was used to investigate the unfolding of HP36F4751L as a function of temperature. Figure 5A shows the FTIR absorbance spectra of HP36F4751L as a function of temperature from 5 – 83°C in ~ 5°C increments in the 1550 – 1750 cm^{-1} region. These spectra show the Amide I' band centered at 1645 cm^{-1} for the lowest temperature spectrum. As the temperature is increased the band begins to decrease in intensity and shift to higher frequency similar to HP36. To determine the components of Amide I', difference FTIR spectra were made by subtracting the lowest temperature spectrum from the spectra at higher temperatures. The resulting difference spectra are shown in Figure 5B. As the temperature is increased the intensity in the region ~1600 – 1657 cm^{-1} decreased due to the loss of secondary and tertiary structure, while the intensity in the range from ~1657 – 1700 cm^{-1} increased due to increasing amounts of disordered regions of the protein. There is no decrease in intensity at 1674 cm^{-1} as the temperature was increased that could mean that no TFA is present, the turn region in HP36 that could be giving rise to this mode is not present in this double mutant or only one of the two bands in this region measured in HP36 is present in the double mutant. These difference spectra show an isosbestic point indicative of a two-state transition unlike HP36, however, this protein might melt by a three-state mechanism where the intermediate is never present in a high enough concentration to be measured.

The temperature dependence of the FTIR absorbance spectra of HP36F4751L shown in Figure 5A were analyzed by SVD. This analysis yielded two spectral components unlike the SVD analysis of the wild type FTIR data that yielded three spectral components. Figure

6A shows the first (solid) and second (dashed) spectral components for the melt of this double mutant of the villin headpiece subdomain. The temperature dependence of the first (squares) and second (triangles) spectral components are shown in Figure 6B. The first spectral component is essentially the average temperature dependent FTIR absorbance spectrum of the protein and therefore has minimal temperature dependence. However the second spectral component is the difference between the first spectral component and the rest of the temperature dependent FTIR absorbance spectra. Therefore the second spectral component resembles the temperature dependent difference FTIR spectra for HP36F4751L given in Figure 5B and the temperature dependence of this spectral component shows a transition indicative of the melt of this protein. The second spectral component was fit (solid curve) to Eqn. 5 and the results are given in Table 1A. The thermodynamic parameters along with the melt temperature are significantly lower than the corresponding values from the SVD analysis of the wild type data showing that this double mutant is significantly destabilized relative to the wild type protein. The smaller heat capacity relative to the wild type protein is indicative of the burial of less hydrophobic residues further indicative of a disrupted hydrophobic core in this double mutant. The unfolding of this double mutant is enthalpically unfavorable but entropically favorable however the absolute magnitude of these values is smaller than the corresponding values for the wild type protein. Therefore these thermodynamic values indicate that the double mutant is not as folded as the wild type protein.

One significant difference between the wild type and double mutant is that the double mutant only showed two spectral components compared to the three spectral components of

the wild type protein determined from the SVD analysis of the temperature dependent FTIR absorbance spectra. This result suggests that melt of HP36 occurs by at least a three-state mechanism, while the melt of HP36F4751L follows a two-state mechanism or a three-state mechanism where the intermediate is never present in sufficient concentration to be measured. This difference was expected from the difference FTIR spectra of these proteins since the double mutant showed an isosbestic point while the wild type protein does not.

Time Resolved T-Jump IR Spectroscopy

The relaxation kinetics of both wild type and the double Phe mutant of the villin headpiece subdomain were investigated in response to a rapid perturbation (T-jump) to the system equilibrium at various initial temperatures (as described in the Materials and Methods). These relaxation kinetics along with the equilibrium FTIR data allow the microscopic folding and unfolding rates of these proteins to be determined as a function of temperature. The relaxation kinetics of these systems were monitored at 1632 cm^{-1} and 1650 cm^{-1} to probe the solvated and buried helical components, respectively. as a function of temperature. The relaxation kinetics were monitored at 1632 and 1650 cm^{-1} instead of 1629 and 1645 cm^{-1} due to the lack of a good IR diode laser mode at the wavenumbers 1629 and 1645 cm^{-1}, which correspond to solvated and buried helical components, respectively. The T-jumps were typically 5 – 15°C. Representative relaxation kinetic traces for HP36 (A) and HP36F4751L (B) are given in Figure 7 (dashes) with a bi-exponential fit (solid). The relaxation times and relative amplitude percentages for these traces are given in Table 2. These traces show biphasic relaxation kinetics for both protein samples; however, the relative amplitudes of the two phases are protein and wavenumber dependent. The biphasic

relaxation kinetics suggest either a sequential three-state model of folding involving an intermediate whose composition is likely comprised predominately of solvated helices or a parallel folding scheme. The kinetics for the mutant are dominated by the fast phase unlike the wild type where both the fast and slow phase have significant amplitudes. The slow phase has a larger relative amplitude in the 1650 cm^{-1} data compared to 1632 cm^{-1} since this wavenumber follows the buried helical regions of the proteins while the fast phase has a larger amplitude in the 1632 cm^{-1} kinetic traces that follows the solvated helical regions of the proteins. However the bands for the buried and solvated helical regions of the alpha helices overlap resulting in the presence of the observation of both kinetic phases at each of these wavenumbers.

The relaxation kinetics were monitored in the temperature range of 28 – 73°C for HP36 with relaxation times of 100 – 66 ns and 4.47 – 1.19 μs for the fast and slow phase, respectively. The relaxation kinetics for HP36F4751L were monitored from 24.5 – 47.6°C because only the fast phase was observed outside of this temperature range. The relaxation times ranged from 65 – 57 ns and 3.12 – 1.13 μs for the fast and slow phase, respectively in this temperature range. Both relaxation phases were found to increase as the temperature increased. The relaxation times are generally shorter for the double mutant relative to the wild type protein. The fast ~ 100 ns relaxation time is likely indicative of the helix – coil transition based upon α helical peptide models showing relaxation times from 100 – 300 ns, [1-4] while the slow microsecond phase is likely following the formation of tertiary contacts required for the 3-D folded, native structure of these proteins. The relaxation kinetics of HP36F4751L were dominated by the helix – coil (~ 100 ns) relaxation phase further

suggesting a destabilized protein (less tertiary structure due to a destabilized hydrophobic core) relative to HP36.

The observed kinetics of the wild type and double mutant of the villin headpiece subdomain can be modeled by a two-state model of protein folding using the slow, microsecond phase that follows the formation of tertiary structure. Based upon the temperature dependent equilibrium constants determined from the SVD analysis of the temperature dependent FTIR spectra and the observed relaxation kinetics of the slow (microsecond) phase, the microscopic folding and unfolding rates for both of these proteins can be determined as a function of temperature. In the T-jump experiments, the equilibrium position is perturbed toward the unfolded state and the relaxation kinetics to equilibrium at this new (higher) temperature is monitored. Thus the two-state model used is $U \underset{k_u}{\overset{k_f}{\leftrightarrow}} F$ where U and F are the unfolded and folded ensembles, respectively and the k_f and k_u are the microscopic folding and unfolding rates, respectively. These microscopic rates are related to the observed relaxation rates by $k_{obs} = k_f + k_u$ where k_{obs} is the observed (microsecond) relaxation rate. The relaxation rates in this model use the microsecond (slow) observed relaxation rate that follows the formation of tertiary structure in the protein (global relaxation rate). These microscopic rates are related to the equilibrium constant for folding (K_f) (inverse of equilibrium value for unfolding) by $K_f = k_f / k_u$. Based on these two equations, the temperature dependent microscopic folding and unfolding rates can be determined. A plot of the natural log of these temperature dependent microscopic rates (s^{-1}) versus the

inverse of the temperature (K) can be plotted and fit to the Eyring equation (Eqn. 8) to give the thermodynamic parameters of activation for these proteins as shown below:

$$\ln k = \left(-\frac{\Delta G^{\ddagger}}{\mathrm{R}}\right)\left(\frac{1}{T}\right) + \ln(D) \qquad (8)$$

where $\Delta G^{\ddagger}$ is (Eqn. 9):

$$\Delta G^{\ddagger} = \Delta H^{\ddagger}_{T_m} + \Delta C^{\ddagger}_P\left(T - T_m\right) - T\left[\Delta S^{\ddagger}_{T_m} + \Delta C^{\ddagger}_P \ln\left(T/T_m\right)\right] \qquad (9)$$

and $\Delta H^{\ddagger}_{T_m}$, $\Delta S^{\ddagger}_{T_m}$ and $\Delta C^{\ddagger}_P$ are the enthalpy, entropy and heat capacity of activation relating the folded or unfolded states to the transition state.

Figure 8 shows the plot of the natural log of k_{obs}, k_f and k_u as a function of the inverse of temperature for HP36 calculated from a two-state model of folding described above where the temperature is the final temperature after the T-jump. The dependence of the folding and unfolding microscopic rates with respect to temperature are fit to the Eyring equation (Eqn. 8) (solid line) to determine the thermodynamic parameters of activation. The relaxation rates shown in Figure 8 were monitored at both 1632 cm^{-1} and 1650 cm^{-1}. The intersection of the fits for the microscopic rates occurs at the T_m of the protein. The activation thermodynamic parameters derived from these fits for HP36 are listed in Table 3. Figure 8 shows that both the folding and unfolding rate for HP36 are temperature dependent. These activation values describe the barrier required to go from either the folded or unfolded state to the transition state. These values show that the folding of HP36 is enthalpically favorable indicative of favorable interactions in the transition state (such as H-bonding in the α helix along with solvent H-bonding is stronger than just solvent H-bonding in the coil state) and entropically

unfavorable probably due to the loss of conformational entropy. The negative enthalpy of activation for the formation of α-helices in an α-helical peptide model has been observed previously. [4] Solvent re-organization in response to structural changes in the protein also affects the values of these parameters. The negative heat capacity value for folding is indicative of burial of hydrophobic residues upon folding. The heat capacity takes into account the temperature dependence of the enthalpy and entropy of activation. Table 3 also shows that the thermodynamic parameters of activation for unfolding of HP36 are enthalpically unfavorable and entropically favorable that is the opposite for the activation parameters for folding. The smaller temperature range that the slow, microsecond phase was observed for HP36F4751L prevented a robust fit of the temperature dependence of the microscopic folding and unfolding rates to the Eyring equation to be made. However a plot of the natural log of these rates along with the observed relaxation rate as a function of the inverse of the temperature for this double mutant are plotted in the Supporting Information (Appendix 5).

Table 4 shows the observed relaxation rate, folding rate and unfolding rate for HP36 and HP36F4751L at a similar final temperature after the T-jump based upon a two-state model of folding. These values allow a comparison of these rates between the wild type and double mutant of the villin headpiece subdomain to be made. Table 4 shows that the observed relaxation rate for the slow phase of HP36 and HP36F4751L are 3.87×10^5 s^{-1} and 6.63×10^5 s^{-1} at 45.6°C and 49.9°C, respectively. These rates show that the relaxation rate for the wild type is approximately 0.6 slower than the double mutant. At these temperatures, the folding rate for the wild type is approximately 1.2 faster than the double mutant and the

unfolding rate for the wild type is approximately 0.3 slower than the double mutant. These results show that the shorter relaxation time for the double mutant is due to the much slower unfolding time of the HP36 relative to the double mutant at these temperatures.

Conclusion

The equilibrium FTIR spectra of both HP36 and the double Phe mutant HP36F4751L showed an Amide I' band centered at 1645 cm^{-1} at low temperature (3 and 5°C, respectively) consistent with an α-helical protein. The difference FTIR spectra of these proteins in the Amide I' region showed decreases in absorbance due to the loss of secondary structure and increases corresponding to the formation of disordered regions of the proteins as the temperature increased. Singular value decomposition (SVD) and Gaussian global fitting showed that the wild type villin headpiece subdomain has two melt transitions. However the SVD analysis of the temperature dependent FTIR data of the double mutant resulted in a single unfolding transition. A comparison of the unfolding transitions illustrated by the SVD analyses of these proteins illustrated that the double mutant was significantly destabilized with respect to the wild type protein.

The observed relaxation times for both proteins following a T-jump measured at 1632 cm^{-1} and 1650 cm^{-1} consisted of two phases. The fast phase (~ 100 ns) corresponded to the helix – coil transition while the slow phase (few microseconds) was due to the formation of tertiary contacts. The biphasic relaxation kinetics are in agreement with previous experimental measurements, [14] while the overall folding time agree with previous theoretical studies. [11] A two-state model for folding based on the slow observed relaxation rate and the

temperature dependence of the third (HP36) or second (HP36F4751L) spectral component determined from SVD showed that the folding rates of the two proteins were similar while the unfolding time of HP36 is significantly slower than the double mutant HP36F4751L. The amplitude of the slow phase relative to the fast phase is significantly less for the double mutant as compared to the wild type. This difference in amplitude of the relaxation kinetics suggests that the extent of folding (association of the helices) is less for the double mutant compared to the wild type protein.

The experimental data shown here suggest that the villin headpiece subdomain folds by a three-state mechanism involving an intermediate. The biphasic relaxation kinetics of this protein could be explained by a sequential mechanism of folding involving the formation of alpha helices followed by the formation of tertiary structure. This type of mechanism would involve the formation of an intermediate that is comprised predominately of solvated alpha helices.

Acknowledgements

This work was done in collaboration with Dung M. Vu (LANL), Yuefeng Tang (State University of New York at Stony Brook), Daniel P. Raleigh (State University of New York at Stony Brook), R. Brian Dyer (LANL) and Stefan Franzen (NCSU). We thank Dr. Feng Gai (University of Pennsylvania) for helpful comments.

References

(1) Werner, J. H.; Dyer, R. B.; Fesinmeyer, R. M.; Andersen, N. H. *Journal of Physical Chemistry B* **2002**, *106*, 487-494.

(2) Williams, S.; Causgrove, T. P.; Gilmanshin, R.; Fang, K. S.; Callender, R. H.; Woodruff, W. H.; Dyer, R. B. *Biochemistry* **1996**, *35*, 691-697.

(3) Thompson, P. A.; Munoz, V.; Jas, G. S.; Henry, E. R.; Eaton, W. A.; Hofrichter, J. *Journal of Physical Chemistry B* **2000**, *104*, 378-389.

(4) Lednev, I. K.; Karnoup, A. S.; Sparrow, M. C.; Asher, S. A. *Journal of the American Chemical Society* **2001**, *123*, 2388-2392.

(5) Munoz, V.; Thompson, P. A.; Hofrichter, J.; Eaton, W. A. *Nature* **1997**, *390*, 196-199.

(6) Mayor, U.; Johnson, C. M.; Daggett, V.; Fersht, A. R. *Proceedings of the National Academy of Sciences of the United States of America* **2000**, *97*, 13518-13522.

(7) Mayor, U.; Guydosh, N. R.; Johnson, C. M.; Grossmann, J. G.; Sato, S.; Jas, G. S.; Freund, S. M. V.; Alonso, D. O. V.; Daggett, V.; Fersht, A. R. *Nature* **2003**, *421*, 863-867.

(8) Islam, S. A.; Karplus, M.; Weaver, D. L. *Journal of Molecular Biology* **2002**, *318*, 199-215.

(9) Jang, S. M.; Kim, E.; Shin, S.; Pak, Y. *Journal of the American Chemical Society* **2003**, *125*, 14841-14846.

(10) Duan, Y.; Kollman, P. A. *Science* **1998**, *282*, 740-744.

(11) Zagrovic, B.; Snow, C. D.; Shirts, M. R.; Pande, V. S. *Journal of Molecular Biology* **2002**, *323*, 927-937.

(12) Myers, J. K.; Oas, T. G. *Nature Structural Biology* **2001**, *8*, 552-558.

(13) Vu, D. M.; Myers, J. K.; Oas, T. G.; Dyer, R. B. *Biochemistry* **2004**, *43*, 3582-3589.

(14) Kubelka, J.; Eaton, W. A.; Hofrichter, J. *Journal of Molecular Biology* **2003**, *329*, 625-630.

(15) Wang, M. H.; Tang, Y. F.; Sato, S. S.; Vugmeyster, L.; McKnight, C. J.; Raleigh, D. P. *Journal of the American Chemical Society* **2003**, *125*, 6032-6033.

(16) Callender, R. H.; Dyer, R. B.; Gilmanshin, R.; Woodruff, W. H. *Annual Review of Physical Chemistry* **1998**, *49*, 173-202.

(17) Caughey, B.; Lansbury, P. T. *Annual Review of Neuroscience* **2003**, *26*, 267-298.

(18) Taylor, J. P.; Hardy, J.; Fischbeck, K. H. *Science* **2002**, *296*, 1991-1995.

(19) Maness, S. J.; Franzen, S.; Gibbs, A. C.; Causgrove, T. P.; Dyer, R. B. *Biophysical Journal* **2003**, *84*, 3874-3882.

(20) Leeson, D. T.; Gai, F.; Rodriguez, H. M.; Gregoret, L. M.; Dyer, R. B. *Proceedings of the National Academy of Sciences of the United States of America* **2000**, *97*, 2527-2532.

(21) Dyer, R. B.; Gai, F.; Woodruff, W. H. *Accounts of Chemical Research* **1998**, *31*, 709-716.

(22) Thompson, P. A.; Eaton, W. A.; Hofrichter, J. *Biochemistry* **1997**, *36*, 9200-9210.

(23) Yang, W. Y.; Gruebele, M. *Nature* **2003**, *423*, 193-197.

(24) Vugmeyster, L.; Trott, O.; McKnight, C. J.; Raleigh, D. P.; Palmer, A. G. *Journal of Molecular Biology* **2002**, *320*, 841-854.

(25) Duan, Y.; Wang, L.; Kollman, P. A. *Proceedings of the National Academy of Sciences of the United States of America* **1998**, *95*, 9897-9902.

(26) Shen, M. Y.; Freed, K. F. *Proteins-Structure Function and Genetics* **2002**, *49*, 439-445.

(27) Sullivan, D. C.; Kuntz, I. D. *Journal of Physical Chemistry B* **2002**, *106*, 3255-3262.

(28) Fernandez, A.; Shen, M. Y.; Colubri, A.; Sosnick, T. R.; Berry, R. S.; Freed, K. F. *Biochemistry* **2003**, *42*, 664-671.

(29) Frank, B. S.; Vardar, D.; Buckley, D. A.; McKnight, C. J. *Protein Science* **2002**, *11*, 680-687.

Tables

Table 1A. Thermodynamic parameters for the unfolding of HP36 and HP36F4751L as determined from the SVD analysis of the temperature dependent equilibrium FTIR spectra based on a two-state model of unfolding.

$F \overset{K_{eq}}{\leftrightarrow} U$	SVD	
	HP36	HP36F4751L
ΔH_u (kJ·mol^{-1})	85.3	24.1
ΔS_u (J·mol^{-1}·K^{-1})	258	79.3
$\Delta C_{p,u}$ (J·mol^{-1}·K^{-1})	2353	289
T_m (K)	330	304

*The third (HP36) or second (HP36F4751L) SVD component temperature dependence was fit to obtain these thermodynamic parameters.

Table 1B. Thermodynamic parameters for the unfolding of HP36 as determined from the Gaussian global fitting analysis of the temperature dependent equilibrium FTIR difference spectra based on a two-state model of unfolding.

$F \overset{K_{eq}}{\leftrightarrow} U$	Gaussian Global Fitting		
HP36	Global Analysis[1]	1629 cm^{-1} band[2]	1645 cm^{-1} band[2]
ΔH_u (kJ·mol^{-1})	42.8	30.2	122.7
ΔS_u (J·mol^{-1}·K^{-1})	126	90.6	367
$\Delta C_{p,u}$ (J·mol^{-1}·K^{-1})	225	375	1935
T_m (K)	341	333	335

*The temperature dependence of the band areas of the Gaussian bands at 1614, 1629, 1645, and 1680 cm^{-1} were fit globally (1) or the temperature dependence of the band areas of the Gaussian bands at 1629 and 1645 cm^{-1} were fit individually (2) to Eqn. 5. (These band positions are approximate because the band positions were allowed to vary as a fit parameter for each temperature.)

Table 2. Representative relaxation rates, times and percent amplitudes of the total amplitude at a given temperature (T_f) after a T-jump determined from a bi-exponential fit to the measured kinetic relaxation traces.

	T_f (°C)	Fast Relaxation Rate, Time (Percent Amplitude)	Slow Relaxation Rate, Time (Percent Amplitude)
HP36			
1632 cm^{-1}	48.5	$9.63x10^6$ s^{-1}, 104 ns (56 %)	$3.96x10^5$ s^{-1}, 2.53 μs (44 %)
1650 cm^{-1}	45.6	$8.19x10^6$ s^{-1}, 122 ns (43 %)	$3.87x10^5$ s^{-1}, 2.58 μs (57 %)
HP36F4751L			
1632 cm^{-1}	47.6	$1.76x10^7$ s^{-1}, 57 ns (82 %)	$8.81x10^5$ s^{-1}, 1.13 μs (18 %)
1650 cm^{-1}	49.9	$1.03x10^7$ s^{-1}, 97 ns (79 %)	$6.63x10^5$ s^{-1}, 1.51 μs (21 %)

Table 3. Kinetic activation (‡) thermodynamic parameters obtained from a two-state model of folding for HP36 determined from the dependence of the microscopic folding and unfolding rates as a function of temperature. The microscopic rates were determined using the equilibrium constants obtained from the dependence of the third spectral component determined by SVD from the equilibrium melt of this protein.

	$\Delta H^{\ddagger}$ ($kJ \cdot mol^{-1}$)	$\Delta S^{\ddagger}$ ($J \cdot mol^{-1} \cdot K^{-1}$)	$\Delta C_p^{\ddagger}$ ($J \cdot mol^{-1} \cdot K^{-1}$)	T_m (K)
HP36 $U \leftrightarrow F$	-20.9	-63.3	-2117	330
HP36 $F \leftrightarrow U$	64.4	195	236	330

Table 4. The slow (microsecond) observed relaxation rate with the corresponding microscopic folding and unfolding rates for HP36 and HP36F4751L at 45.6 and 49.9°C, respectively using the equilibrium values determined from the SVD analysis of the temperature dependent equilibrium FTIR data for each protein.

$U \underset{k_u}{\overset{k_f}{\leftrightarrow}} F$	Slow Relaxation Rate, Time	Folding Rate, Time (k_f)	Unfolding Rate, Time (k_u)
HP36 (45.6°C)	3.87×10^5 s^{-1}, 2.58 μs	2.77×10^5 s^{-1}, 3.61 μs	1.10×10^5 s^{-1}, 9.05 μs
HP36F4751L (49.9°C)	6.63×10^5 s^{-1}, 1.51 μs	2.33×10^5 s^{-1}, 4.30 μs	4.31×10^5 s^{-1}, 2.32 μs

Figures

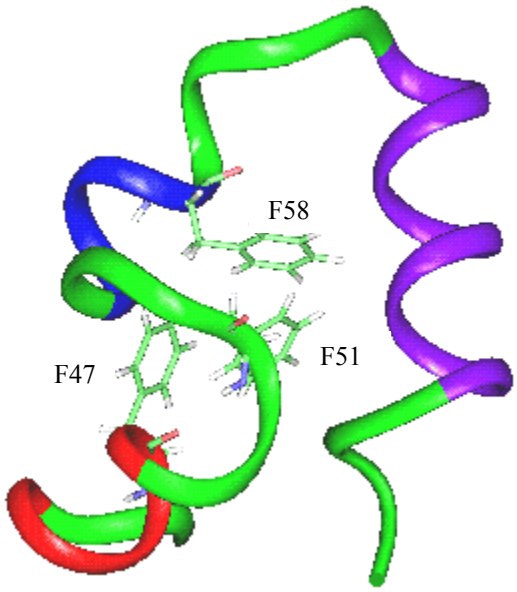

Figure 1. Structure of the wild type three-helix bundle protein villin headpiece subdomain (HP36) (Protein Data Bank Structure 1VII) illustrating the phenylalanine residues (F47, F51, F58) present in the hydrophobic core.

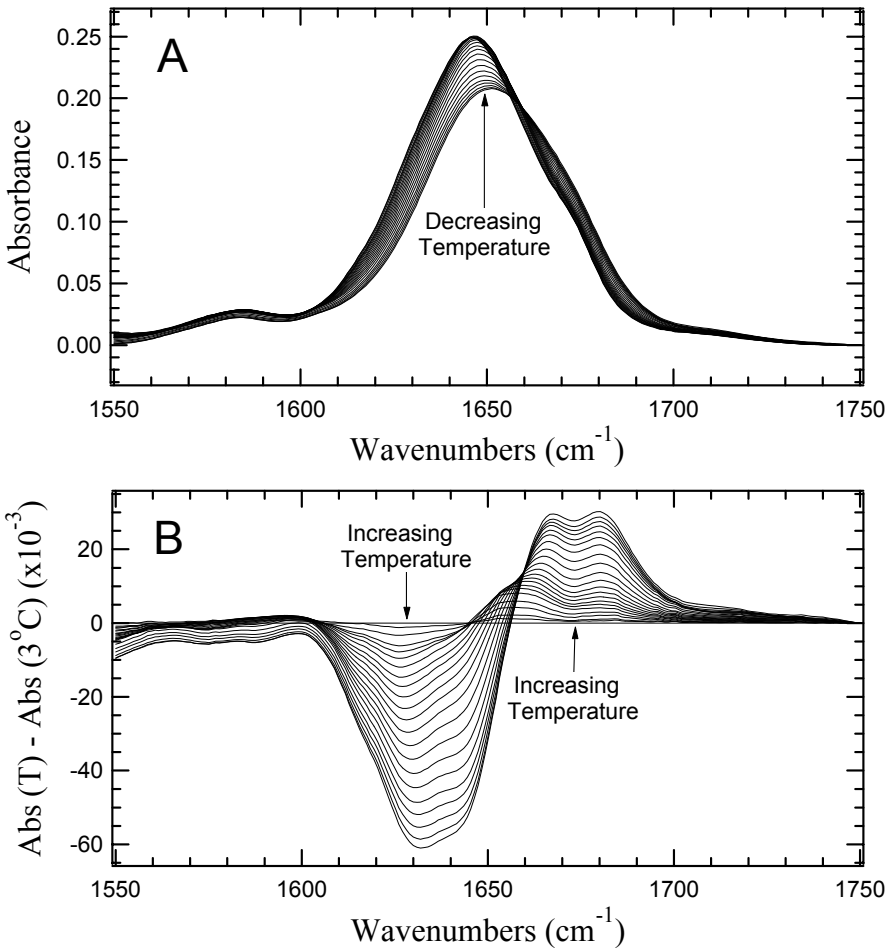

Figure 2. A. Equilibrium FTIR absorbance spectra of HP36 as a function of temperature in the range of 3 – 93°C in ~ 5°C increments in the 1550 – 1750 cm^{-1} region. B. Difference FTIR spectra of HP36 formed by subtracting the absorbance spectrum at 3°C from the spectra at the higher temperatures.

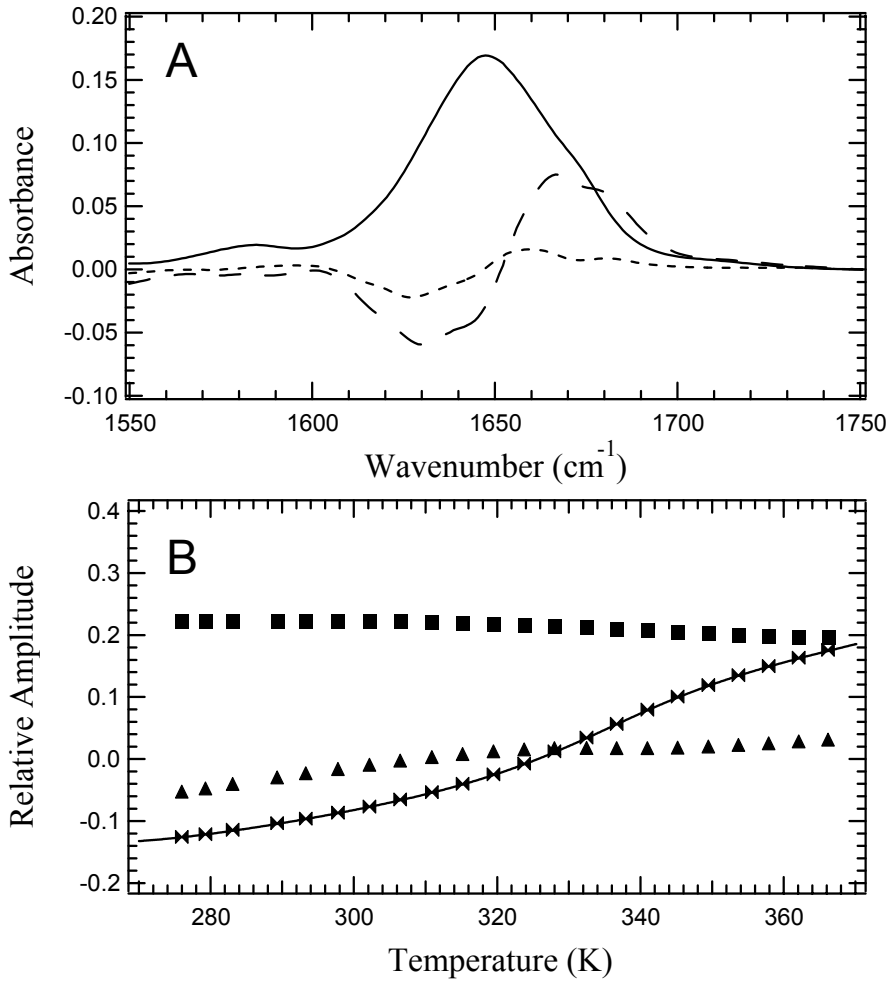

Figure 3. The first (solid), second (short dashed) and third (long dashed) spectral components (A) and the corresponding temperature dependence (B) of the first (squares), second (triangles) and third (bowties) spectral components as determined from the SVD analysis of the equilibrium FTIR temperature dependent data for HP36. The temperature dependence (B) of the third spectral component was fit (solid curve) to Eqn. 5.

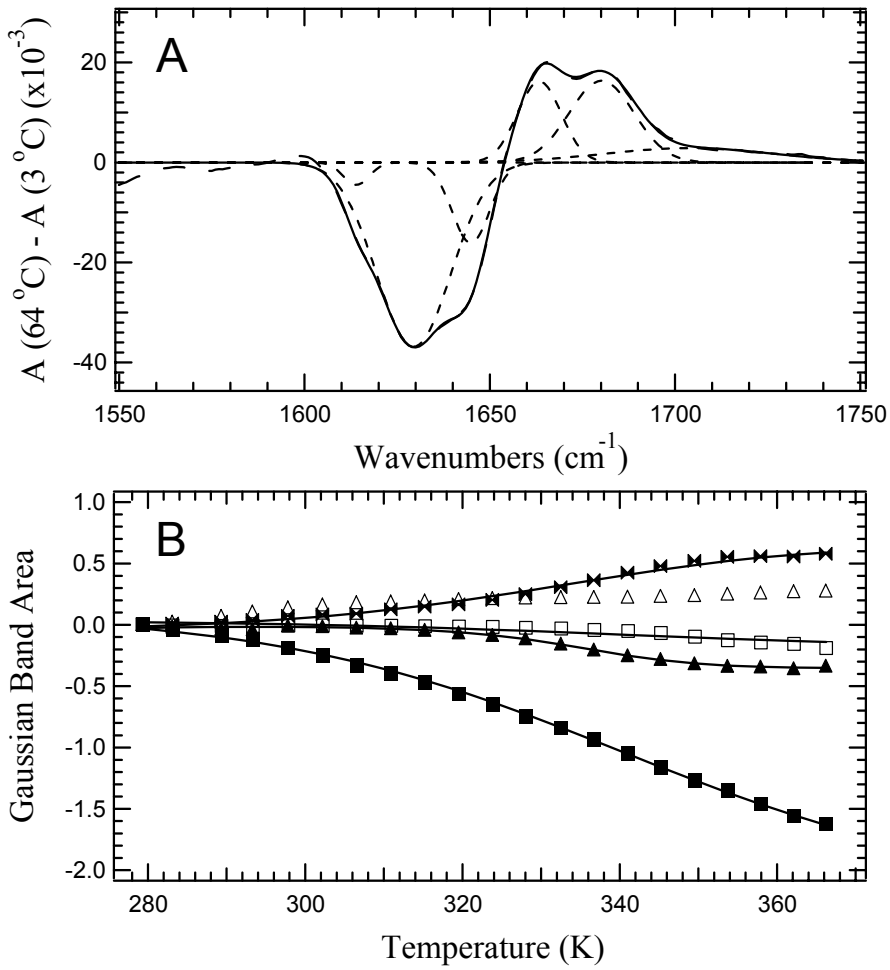

Figure 4. A. Representative Gaussian global fit of the temperature dependent equilibrium difference FTIR spectra of HP36 for the difference spectrum obtained by subtracting the FTIR absorbance spectrum measured at 4ºC from the spectrum recorded at 64ºC. The raw data (long dash) was fit to six Guassian bands. The individual bands (short dash) and the total Gaussian fit (solid) are shown. B. The temperature dependence of the areas of the 1614 (hollow squares), 1629 (black squares), 1645 (black triangles), 1663 (hollow triangles) and 1680 (bowties) cm^{-1} Gaussian bands as a function of temperature. The areas of the 1614, 1629, 1645, and 1680 cm^{-1} Gaussian bands were globally fit (solid) to Eqn. 5.

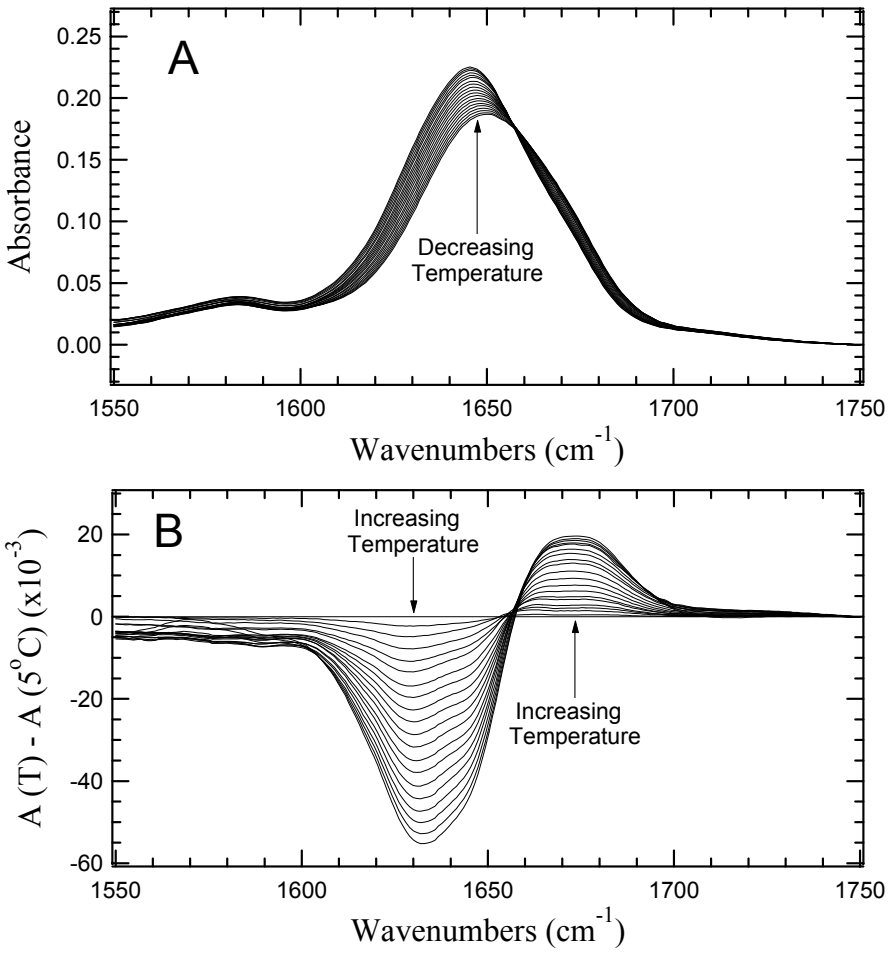

Figure 5. Equilibrium FTIR absorbance spectra of HP36F4751L as a function of temperature in the range of 5 – 83°C in ~ 5°C increments in the 1550 – 1750 cm^{-1} region (A) and the corresponding difference FTIR spectra formed by subtracting the absorbance spectrum at 5°C from the spectra at the higher temperatures (B).

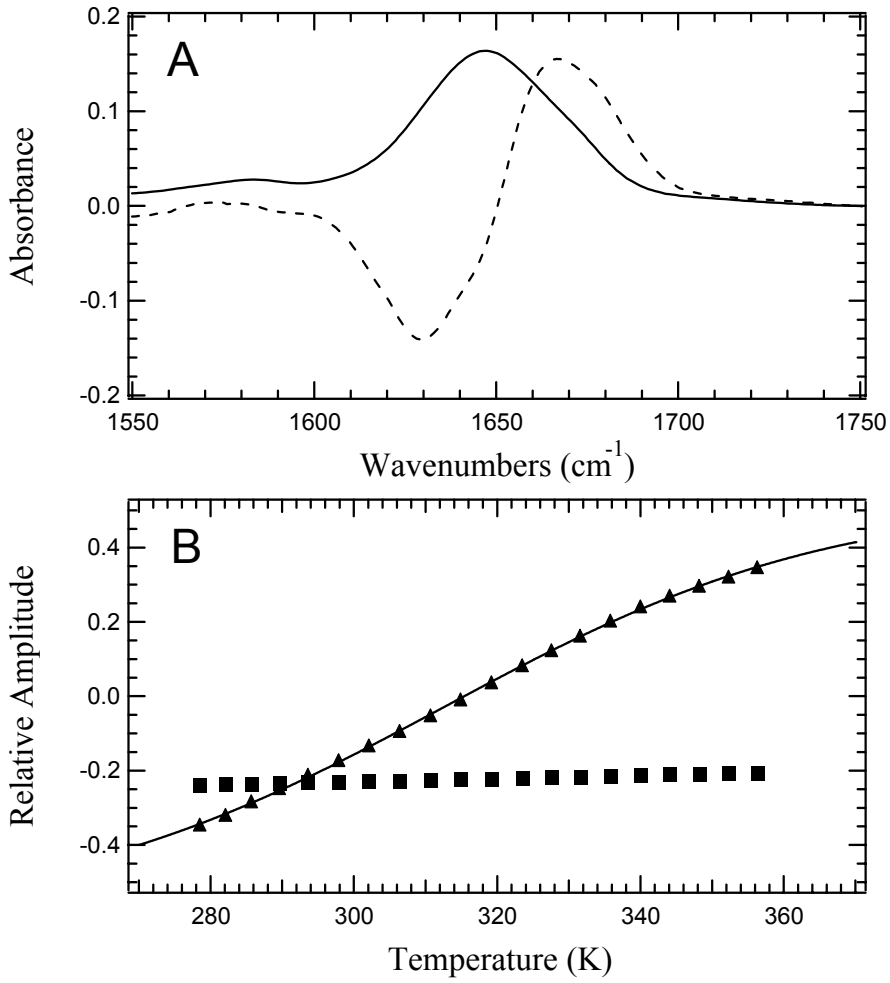

Figure 6. The first (solid) and second (dashed) spectral components (A) and the corresponding temperature dependence (B) of the first (squares) and second (triangles) spectral components as determined from the SVD analysis of the equilibrium FTIR temperature dependent data for HP36F4751L. The temperature dependence (B) of the second spectral component was fit (solid curve) to Eqn. 5.

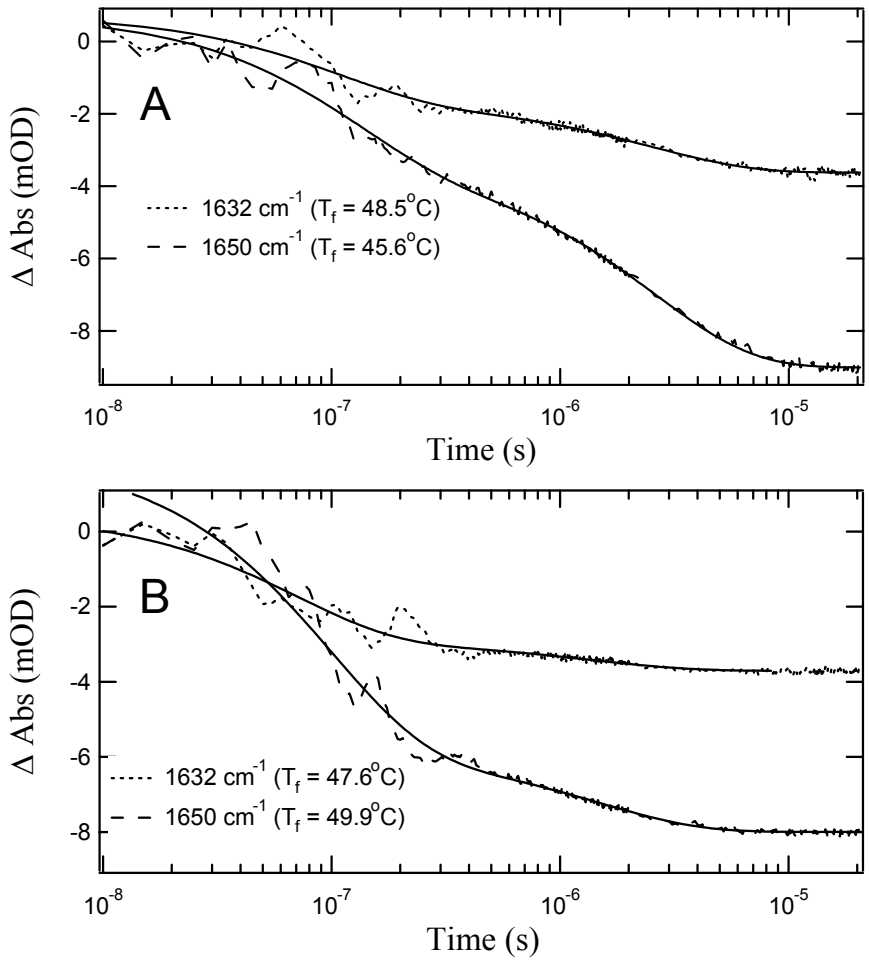

Figure 7. Representative kinetic traces of the relaxation kinetics of HP36 (A) and HP36F4751L (B) at 1632 cm^{-1} and 1650 cm^{-1} (dashed curves) fit to a bi-exponential function (solid curves). The temperature after the T-jump (T_f) is noted on the graph with temperature jumps ranging from 5 – 15°C.

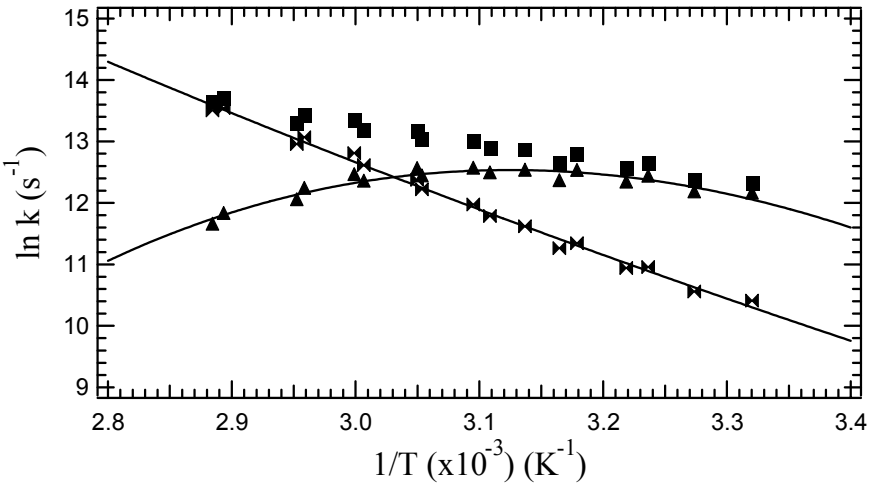

Figure 8. Plot of the natural log of the measured relaxation (square, slow phase), folding (k_f, triangles) and unfolding (k_u, bowties) rates as a function of the inverse of temperature for HP36 using a two-state model of folding. The dependence of the folding and unfolding rates on temperature was fit to Eqn. 8 (solid). The relaxation rates were measured at 1632 cm^{-1} and 1650 cm^{-1}.

Chapter 13

Time-Resolved Step-Scan FTIR Spectroscopy

Abstract

A time-resolved step-scan FTIR spectrometer was implemented with a time resolution of five microseconds. The system was validated by monitoring the recombination of CO to myoglobin as a function of time. The system is a pump-probe experiment where the pump is a laser flash and the probe is infrared radiation. This system has the advantage of probing the entire mid-IR spectral region simultaneously as a function of time to investigate reversible, photo-initiated events.

Introduction

The photo-dynamics of heme proteins[1-7] and protein folding[8-20] are two areas of active research. For instance, CO recombination to myoglobin is a well studied system[3,4] therefore this information can be applied to other heme proteins such as dehaloperoxidase.[21] Future studies on protein folding are important to understand how the amino acid sequence of a protein determines the three dimensional fold of a protein in addition to the kinetics and mechanism of this folding. As shown in the previous chapter, protein folding studies have been performed using T-jumps to perturb the protein away from equilibrium and the relaxation kinetics to equilibrium at the new temperature are monitored. The kinetics are typically monitored by an IR diode laser one wavenumber at a time. However, FTIR spectrometers have a multiplex advantage by sampling multiple wavenumbers simultaneously.[4] To be able to study either heme protein dynamics or protein folding using the multiplex advantage of FITR spectroscopy, a time-resolved step-scan FTIR spectrometer was implemented. This instrument has the advantages of FTIR spectroscopy, while being

able to probe the system of interest as a function of time with five microsecond temporal resolution. The details of the system implemented and the results of a test system validating the successful operation of the set-up are discussed below.

Materials and Methods

Protein Sample Preparation. Horse heart myoglobin (HH Mb) was obtained from Sigma-Aldrich and dissolved in 50 mM potassium phosphate buffer pH 7 in 75/25 percent glycerol / water (v/v) to a concentration of 20 mM. The protein was reduced with a molar excess of sodium dithionite and then carbon monoxide gas was added to the protein solution to bind CO to the iron of the heme prosthetic group of myoglobin to form the MbCO sample.

Time-Resolved Step-Scan FTIR Spectroscopy. The time-resolved step-scan FTIR spectrometer with the laser used for photolysis is shown in Figure 1. This technique is a pump-probe experiment where the laser flash is the pump that initiates a photochemical process and the probe is the FTIR spectrometer that probes the changes in the system upon the flash photolysis. Figure 1 illustrates how the timing of the laser flash and spectrometer collection are synchronized. In this figure, the FTIR spectrometer is operated in step-scan mode in which the moving mirror in the interferometer steps through the interferogram. This stepping involves the moving mirror going to one position along the path of the moving mirror in the interferometer and data is collected at this position. Then the moving mirror moves to the next position in the interferometer and data is again collected. This process continues until the entire interferogram in collected. One advantage of this method of collection is that at each point in the interferogram the spectrometer can collect data as a

function of time. Therefore a three dimensional interferogram can be collected with time being the third axis in addition to intensity and position of the moving mirror in the interferometer. In this setup, the instrument can digitize the response of the MCT detector at a time resolution of five microseconds. Therefore the system operates by the FTIR bench stepping to a new position and beginning data collection, then the laser flashes initiating the reversible event, while the bench is still collecting and then the moving mirror steps to a new position and the cycle is repeated. The appropriate time delay between the stepping of the FTIR bench, the flashing of the laser flashlamps and the opening of the Q-switch to emit the laser radiation is controlled by a four channel digital delay/pulse generator (Stanford Research Systems, Inc. model DG535). The interferograms are then Fourier transformed and a ratio is made with a background scan that lacks the laser photolysis. The results are time dependent difference FTIR spectra depicting the results of the laser photolysis. The timing of this instrument in the given configuration is controlled by the FTIR spectrometer and the TRS synchronizer is used to continue the laser flashing at 10 Hz while the moving mirror resets to begin data collection again.

The Digilab FTS 6000 FTIR spectrometer is equipped with a liquid nitrogen MCT detector, KBr beamsplitter and globar source. The protein sample is enclosed between two calcium fluoride windows (25x2 mm) with a 50 micron spacer (chlorotrifluoroethylene) in a temperature controlled copper sample holder by a Fisher Scientific Isotemp 1006S water bath (50/50 v/v ethylene glycol / water). The temperature of the sample block is measured with an omega thermocouple thermometer type E (Model 450 AET). The sample was maintained at a temperature of 20ºC. A UDR-4 filter was used to prevent scattered laser radiation from

reaching the detector and the FTIR instrument was placed on a vibration isolation table to stabilize the interferometer. The laser used to initiate to the photochemical event was a frequency doubled Nd:YAG Surelite (Continuum) laser emitting 532 nm laser radiation (10 Hz repetition rate, 10 ns wide Gaussian shaped laser pulses). The laser power used was 460 mW and was overlapped with the IR radiation at the sample cell through the use of an aperture. The time-resolved spectra were recorded at 4 cm^{-1} spectral resolution, 5 μs temporal resolution and were the result of the co-addition of 32 scans. Static measurements were made in rapid scan mode where the moving mirror in the interferometer moves at a constant speed at the same spectral resolution in the mid-IR spectral region. The static absorbance measurements were the result of the ratio of a single beam spectrum of the protein sample to a single beam spectrum of the calcium fluoride windows and were the result of the co-addition of 256 scans.

Results and Discussion

To verify that the time-resolved step-scan FTIR spectrometer was operating correctly, the dynamics of CO recombination to the iron of the heme prosthetic group of horse heart myoglobin were studied. The kinetics of CO recombination to myoglobin is a well studied photo-initiated event and the bimolecular recombination rate is in the appropriate time regime for this instrument.[3,4] The experiment is initiated by the 532 nm radiation of the laser photo-dissociating the iron – CO bond, then in bimolecular recombination the CO leaves the protein and then CO from the solution recombines with the protein to form the iron – CO bond again. This system is also ideal because the CO vibrational frequency is in a region that

is unobstructed from the solvent or other protein modes and can be used to follow the recombination of CO to myoglobin.

Figure 1A shows the static FTIR spectrum of 20 mM horse heart myoglobin with CO bound to the heme (HH MbCO). This spectrum shows the position of the CO vibrational mode to be at 1944 cm^{-1} when bound to the iron of the heme. Figure 1B shows the time dependent FTIR difference spectra of this system in response to a laser flash. At time zero, the laser flash occurs and the CO vibrational mode shows a decrease in intensity signifying CO has been photolyzed. However this mode begins to disappear to pre-laser flash levels in time due to bimolecular CO recombination to the heme of myoglobin. The time slices in Figure 1B are at five microsecond intervals and the spectra before time zero are before the laser flash has occurred. This figure therefore shows bimolecular CO recombination to heme through the disappearance of the negative CO vibrational mode at 1944 cm^{-1} since the difference spectra were formed from a ratio of the time dependent spectra recorded with the laser flash to spectra taken without the laser flash. The change in the absorbance of the CO vibrational mode in Figure 1B compared to the static absorbance of HH MbCO (Figure 1A) shows that ~63 % of the CO was photolyzed from the protein on the time scale used for these experiments. The recombination kinetics monitored here are in agreement with previous studies with the differences due to the concentration of CO used since the bimolecular recombination rate is dependent on the carbon monoxide concentration in solution.[3,4]

To further analyze the data, singular value decomposition (SVD) was used to extract the spectral components of the time dependent CO recombination to myoglobin along with the temporal dependence of these spectral components. Figure 2A shows the two spectral

components extracted from the data shown in Figure 1B. The first component (dashed curve) is essentially the average of the entire data set and therefore shows no time dependence as seen in Figure 2B (dashed curve). The second spectral component (solid curve) is indicative of differences in the data relative to the first spectral component. These two components were formed from a matrix rotation of the original SVD components to better account for the experimental data. The second spectral component is highly time dependent as shown in Figure 2B (solid curve). Before the laser flash, the absorbance is flat and then has a marked decrease due to CO photolysis. The change in absorbance then begins to approach the pre-laser flash baseline due to CO recombination. An expanded region up to 700 μs is shown in the inset of Figure 2B. This analysis shows the bimolecular recombination rate under these experimental conditions occurring on the microsecond time scale.

Conclusion

The time-resolved step-scan FTIR spectrometer with five microsecond temporal resolution was shown to operate correctly based upon the test system of CO recombination to myoglobin in response to the laser induced photolysis of CO from the iron of the heme prosthetic group of myoglobin. The data showed that the bimolecular recombination of CO to myoglobin was observed on the microsecond time scale under these experimental conditions. This time-resolved step-scan FTIR spectrometer is therefore ready to perform future studies investigating the photo-dynamics of heme proteins including dehaloperoxidase and possibly protein folding in response to a temperature jump of the solution with 5

microsecond time resolution. The T-jump could possibly be induced from heating of gold nanoparticles in solution with 532 nm radiation exciting the plasmon band of these particles or by pumping the combination bands of the aqueous solvent. The time resolution of the instrument is also being improved from 5 microsecond to 200 nanosecond time resolution.

Acknowledgements

This work was done in collaboration with Simon E. Lappi (NCSU) and Jennifer Belyea (NCSU) who helped implement the instrument and helped with the sample preparation, respectively.

References

(1) Balasubramanian, S.; Lambright, D. G.; Marden, M. C.; Boxer, S. G. *Biochemistry* **1993**, *32*, 2202-2212.

(2) Balasubramanian, S.; Lambright, D. G.; Simmons, J. H.; Gill, S. J.; Boxer, S. G. *Biochemistry* **1994**, *33*, 8355-8360.

(3) Causgrove, T. P.; Dyer, R. B. *Biochemistry* **1993**, *32*, 11985-11991.

(4) Plunkett, S. E.; Chao, J. L.; Tague, T. J.; Palmer, R. A. *Applied Spectroscopy* **1995**, *49*, 702-708.

(5) Hu, X. H.; Frei, H.; Spiro, T. G. *Biochemistry* **1996**, *35*, 13001-13005.

(6) Bailey, J. A.; Tomson, F. L.; Mecklenburg, S. L.; MacDonald, G. M.; Katsonouri, A.; Puustinen, A.; Gennis, R. B.; Woodruff, W. H.; Dyer, R. B. *Biochemistry* **2002**, *41*, 2675-2683.

(7) Franzen, S.; Bailey, J.; Dyer, R. B.; Woodruff, W. H.; Hu, R. B.; Thomas, M. R.; Boxer, S. G. *Biochemistry* **2001**, *40*, 5299-5305.

(8) Wang, M. H.; Tang, Y. F.; Sato, S. S.; Vugmeyster, L.; McKnight, C. J.; Raleigh, D. P. *Journal of the American Chemical Society* **2003**, *125*, 6032-6033.

(9) Myers, J. K.; Oas, T. G. *Nature Structural Biology* **2001**, *8*, 552-558.

(10) Werner, J. H.; Dyer, R. B.; Fesinmeyer, R. M.; Andersen, N. H. *Journal of Physical Chemistry B* **2002**, *106*, 487-494.

(11) Maness, S. J.; Franzen, S.; Gibbs, A. C.; Causgrove, T. P.; Dyer, R. B. *Biophysical Journal* **2003**, *84*, 3874-3882.

(12) Williams, S.; Causgrove, T. P.; Gilmanshin, R.; Fang, K. S.; Callender, R. H.; Woodruff, W. H.; Dyer, R. B. *Biochemistry* **1996**, *35*, 691-697.

(13) Leeson, D. T.; Gai, F.; Rodriguez, H. M.; Gregoret, L. M.; Dyer, R. B. *Proceedings of the National Academy of Sciences of the United States of America* **2000**, *97*, 2527-2532.

(14) Dyer, R. B.; Gai, F.; Woodruff, W. H. *Accounts of Chemical Research* **1998**, *31*, 709-716.

(15) Callender, R. H.; Dyer, R. B.; Gilmanshin, R.; Woodruff, W. H. *Annual Review of Physical Chemistry* **1998**, *49*, 173-202.

(16) Lednev, I. K.; Karnoup, A. S.; Sparrow, M. C.; Asher, S. A. *Journal of the American Chemical Society* **2001**, *123*, 2388-2392.

(17) Kubelka, J.; Eaton, W. A.; Hofrichter, J. *Journal of Molecular Biology* **2003**, *329*, 625-630.

(18) Thompson, P. A.; Eaton, W. A.; Hofrichter, J. *Biochemistry* **1997**, *36*, 9200-9210.

(19) Thompson, P. A.; Munoz, V.; Jas, G. S.; Henry, E. R.; Eaton, W. A.; Hofrichter, J. *Journal of Physical Chemistry B* **2000**, *104*, 378-389.

(20) Munoz, V.; Thompson, P. A.; Hofrichter, J.; Eaton, W. A. *Nature* **1997**, *390*, 196-199.

(21) Franzen, S.; Roach, M. P.; Chen, Y. P.; Dyer, R. B.; Woodruff, W. H.; Dawson, J. H. *Journal of the American Chemical Society* **1998**, *120*, 4658-4661.

Figures

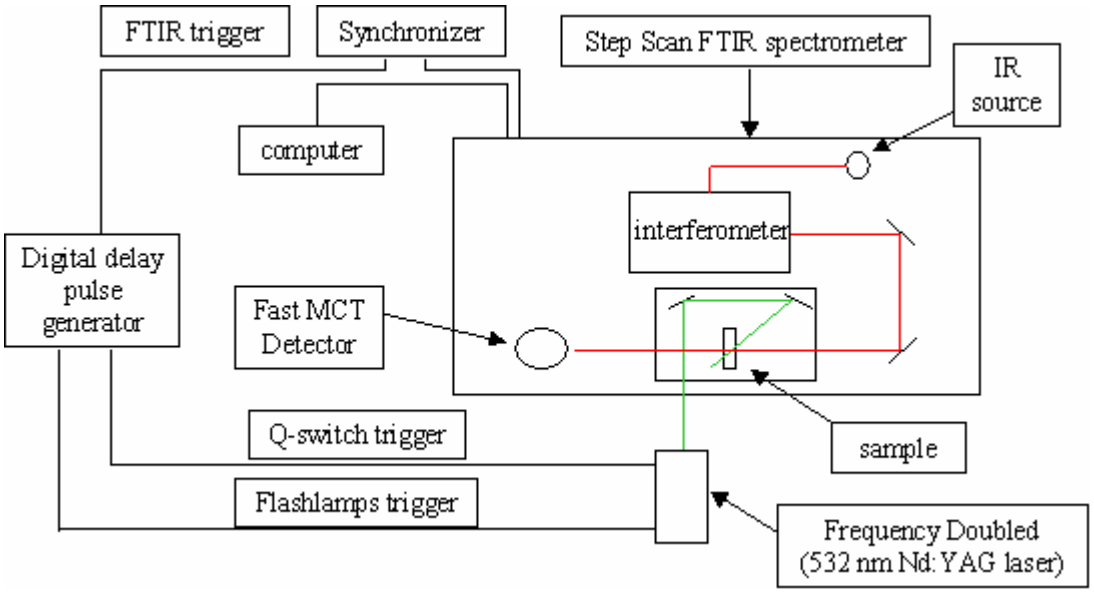

Figure 1. Schematic of the time-resolved step-scan FTIR spectrometer with 5 microscecond time resolution synchronized in time with a Nd:YAG laser.

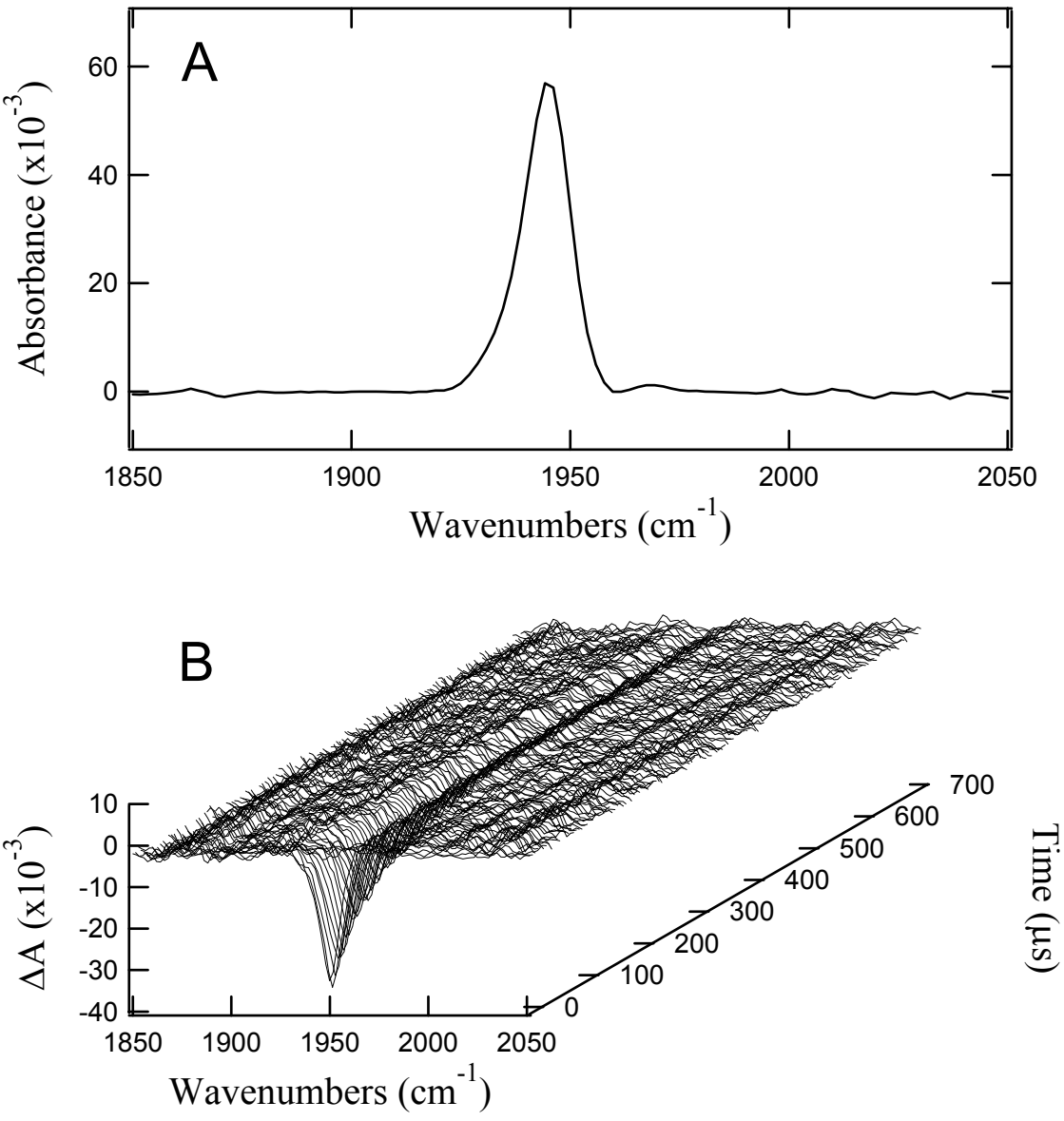

Figure 2. A. Baseline corrected static absorbance spectrum of 20 mM HH MbCO in 50 mM potassium phosphate buffer pH 7 in 75/25 percent glycerol / water (v/v). B. Time-resolved step-scan FTIR difference spectra of HH MbCO illustrating the bimolecular recombination of CO to myoglobin in response to a laser flash at 532 nm that photolyzed the iron – CO bond with 5 microsecond time resolution.

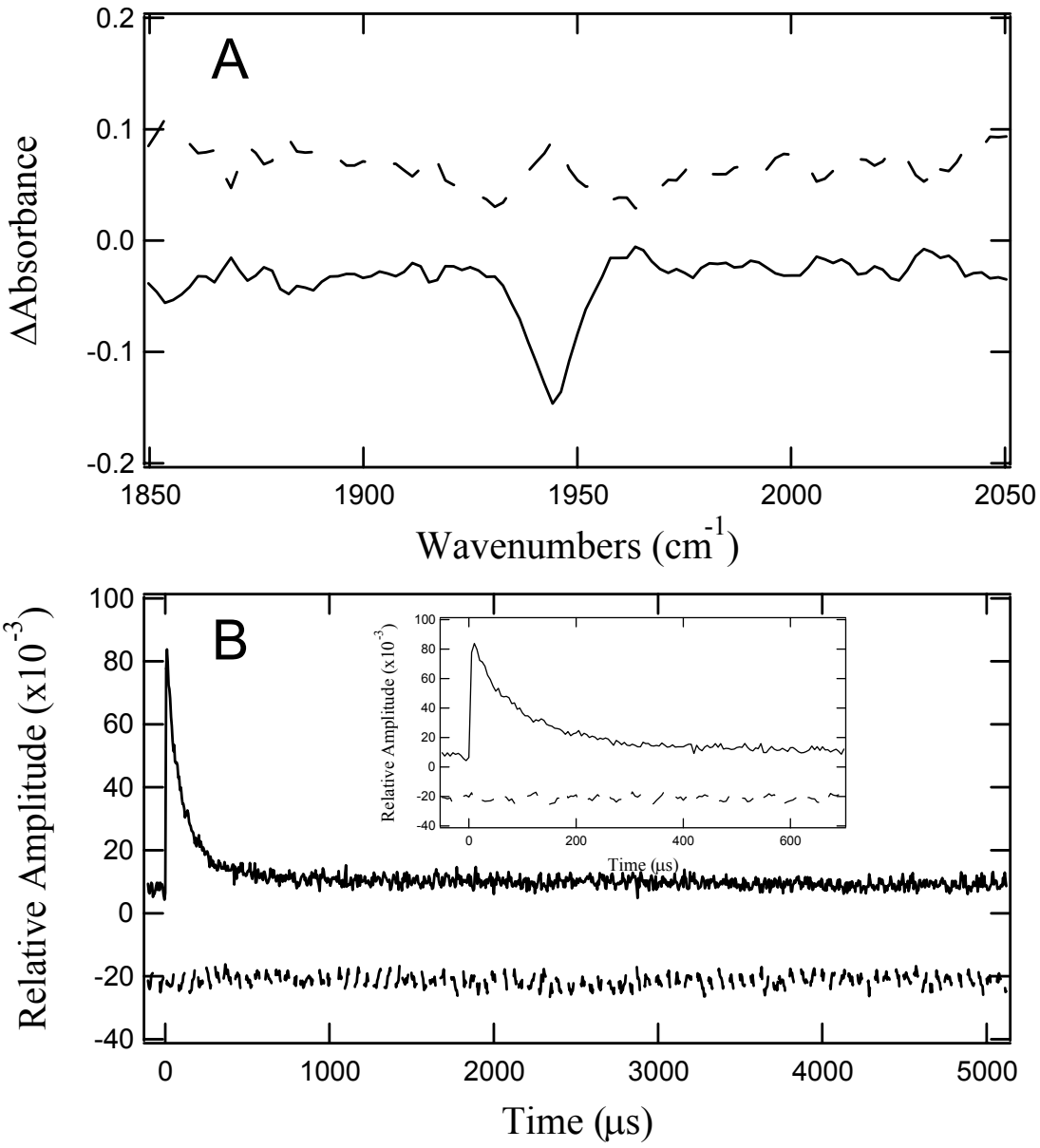

Figure 3. Singular value decomposition (SVD) of the time-resolved step-scan FTIR data showing the first (dashed) and second (solid) spectral components (A) with the corresponding time dependence (B) of the spectral components.

Appendix 1

Supplementary Material for Chapter 2

Supplementary Material

The following figures illustrate the eigenvectors of the individual DNA bases (adenine (A), thymine (T), guanine (G), cytosine (C)) and the corresponding complementary base pairs (AT, GC) used in the Results and Discussion section. These eigenvector projections primarily show the carbonyl stretch and the NH_2 bend of the bases. These eigenvector projections illustrate the red shift of the carbonyl stretch upon complementary base pair formation due to hydrogen bonding weakening the C=O force constant. These eigenvector projections also show the blue shift of the NH_2 bend upon complementary base pair formation due to increased constraint on the NH_2 group resulting from hydrogen bonding. Hydrogen bonding between complementary bases occurs between the oxygen of the C=O group and the hydrogens of the NH_2 group.

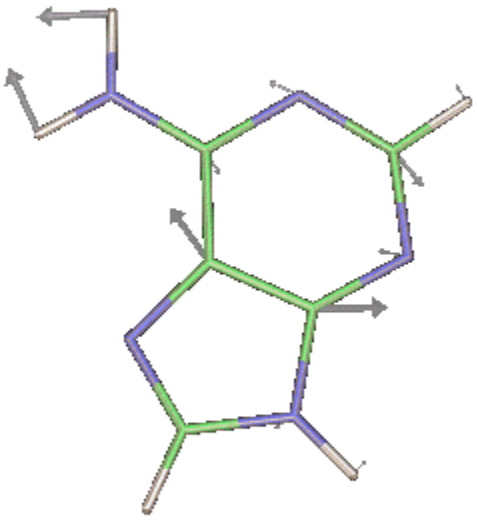

.

Figure 1. Eigenvector projection for the 1572 cm^{-1} vibrational mode of adenine comprised predominately of a NH_2 bend.

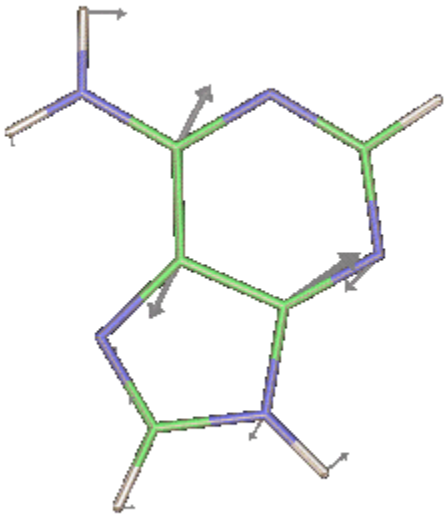

Figure 2. Eigenvector projection for the 1584 cm^{-1} vibrational mode of adenine comprised of a NH_2 bend and a C=N stretch.

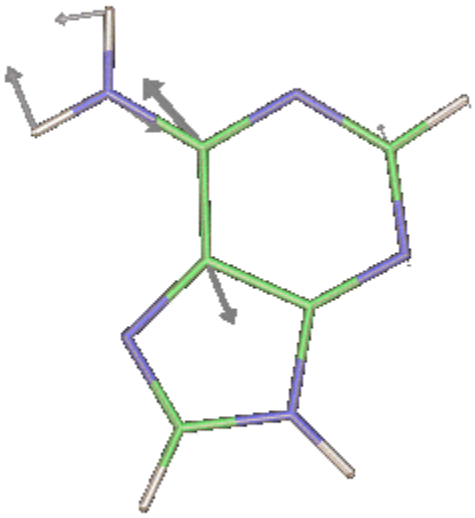

Figure 3. Eigenvector projection for the 1629 cm^{-1} vibrational mode of adenine comprised predominately of a NH_2 bend.

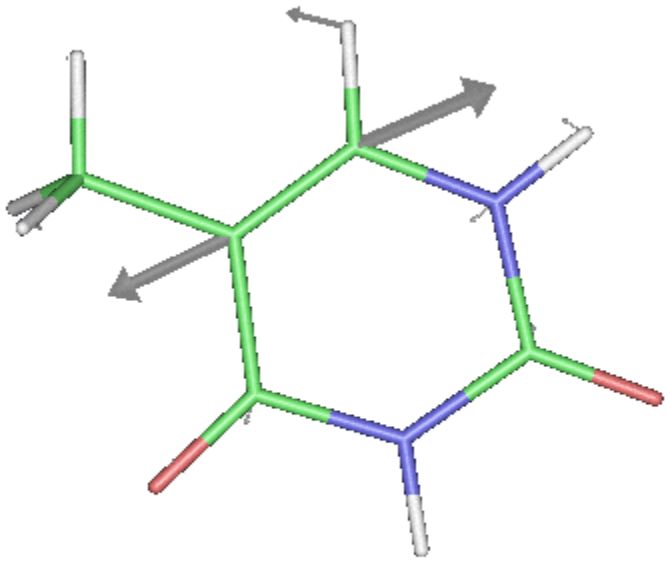

Figure 4. Eigenvector projection for the 1649 cm^{-1} vibrational mode of thymine comprised predominately of a C-C stretch.

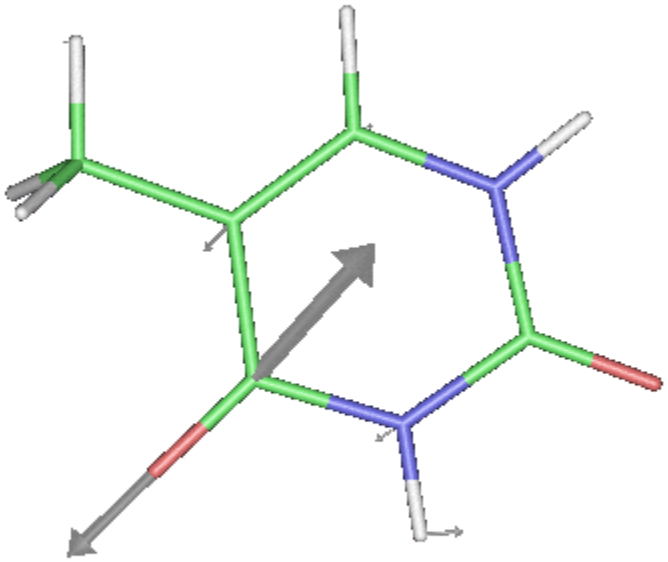

Figure 5. Eigenvector projection for the 1705 cm^{-1} vibrational mode of thymine comprised predominately of a carbonyl stretch.

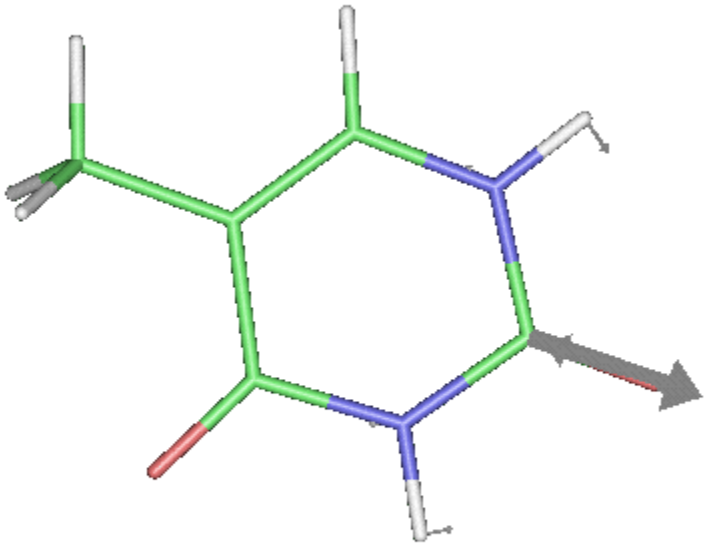

Figure 6. Eigenvector projection for the 1756 cm^{-1} vibrational mode of thymine comprised predominately of a carbonyl stretch.

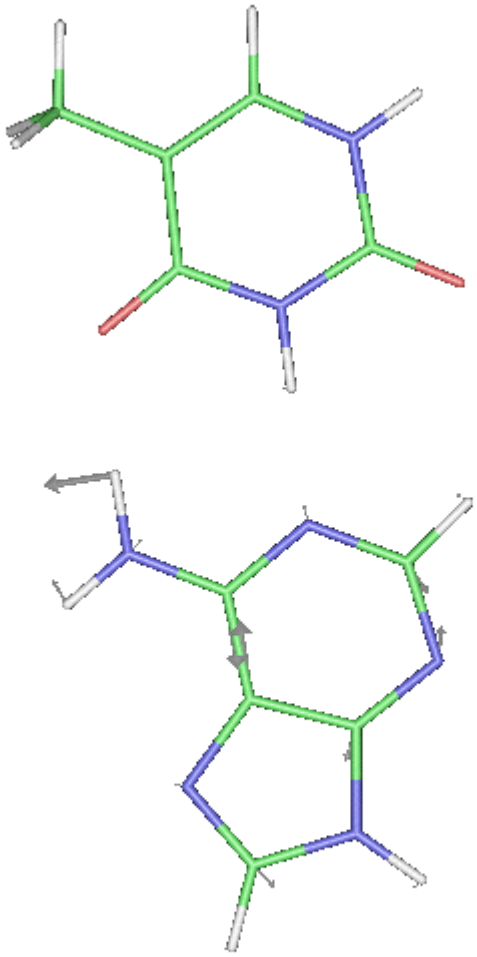

Figure 7. Eigenvector projection for the 1605 cm^{-1} vibrational mode of the adenine-thymine (AT) base pair comprised predominately of a NH_2 bend.

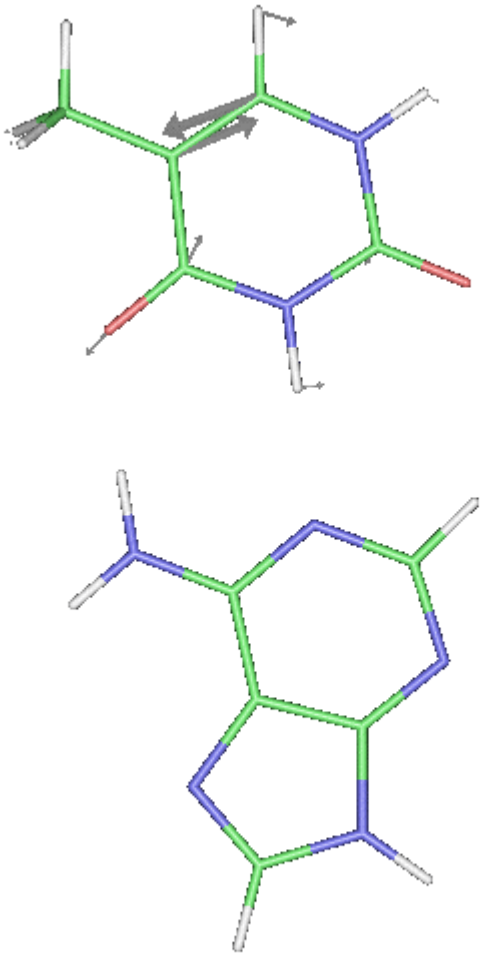

Figure 8. Eigenvector projection for the 1642 cm^{-1} vibrational mode of the adenine-thymine (AT) base pair comprised predominately of ring deformation.

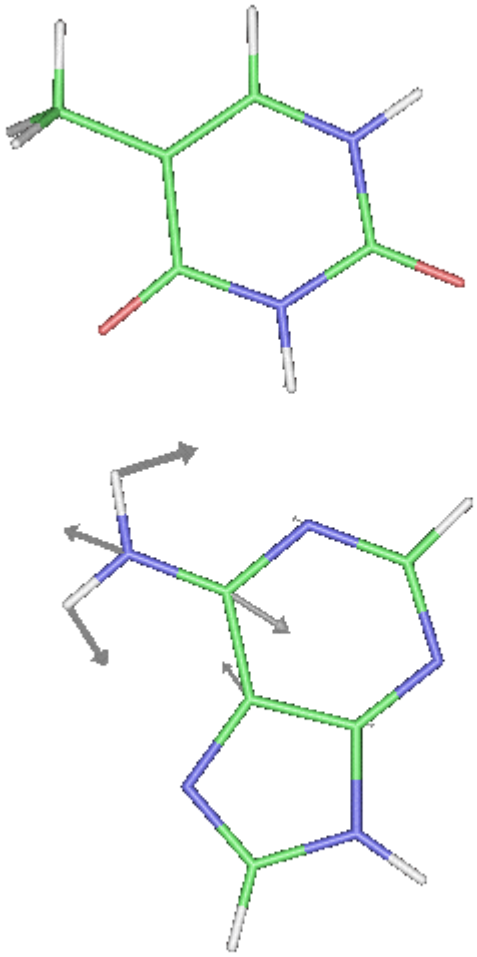

Figure 9. Eigenvector projection for the 1655 cm^{-1} vibrational mode of the adenine-thymine (AT) base pair comprised of a NH_2 bend and a C=N stretch.

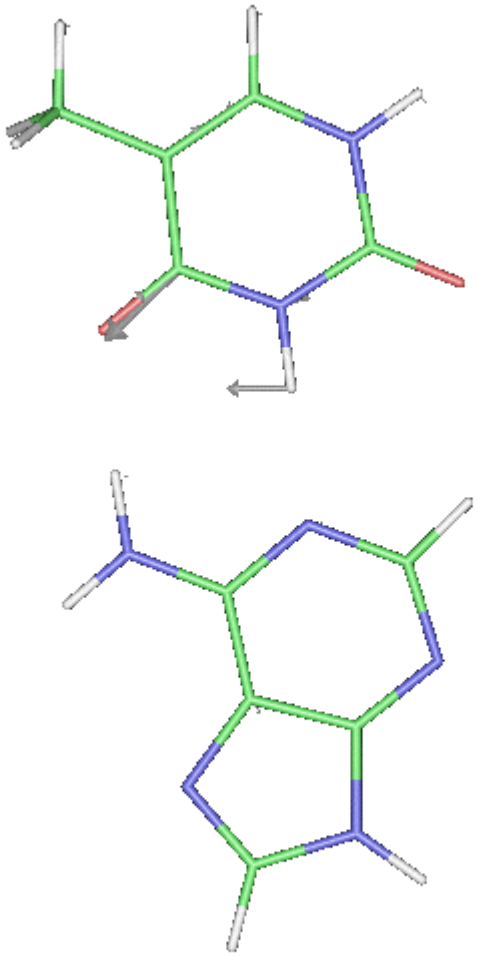

Figure 10. Eigenvector projection for the 1676 cm^{-1} vibrational mode of the adenine-thymine (AT) base pair comprised of a carbonyl stretch and a N-H bend.

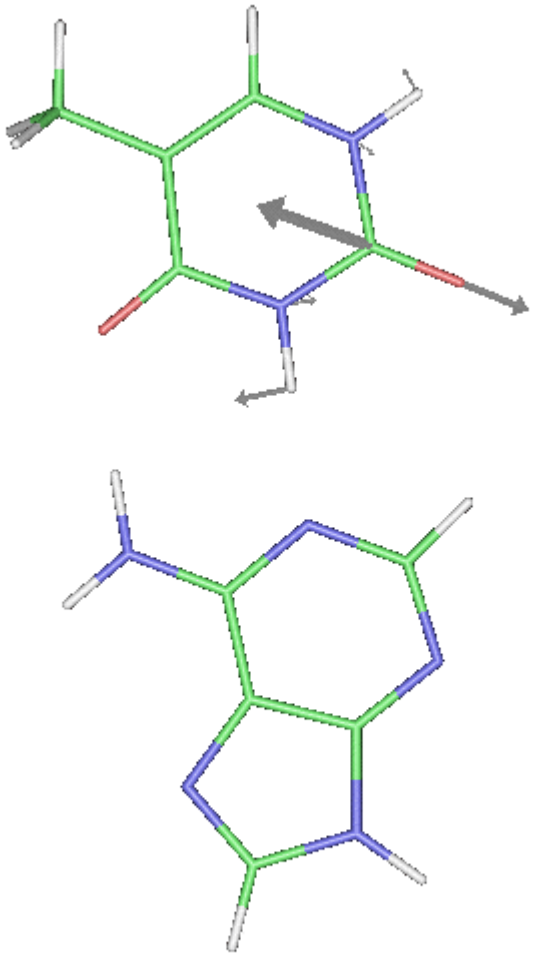

Figure 11. Eigenvector projection for the 1754 cm^{-1} vibrational mode of the adenine-thymine (AT) base pair comprised predominately of a carbonyl stretch.

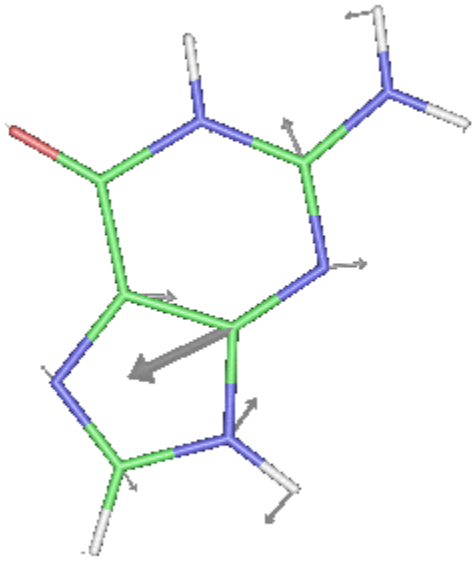

Figure 12. Eigenvector projection for the 1557 cm^{-1} vibrational mode of guanine comprised predominately of a C=N stretch.

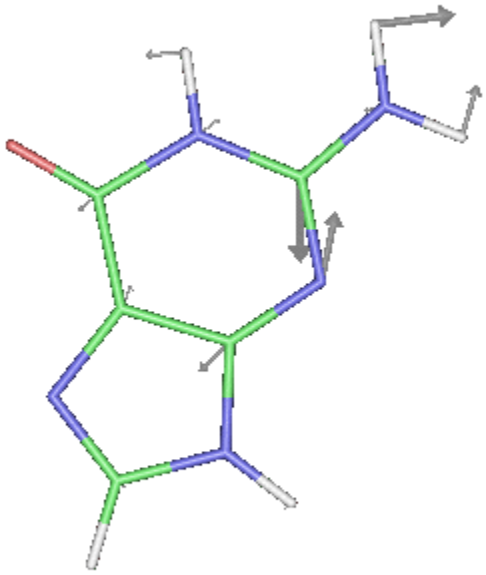

Figure 13. Eigenvector projection for the 1582 cm^{-1} vibrational mode of guanine comprised predominately of a NH_2 bend (and ring deformation).

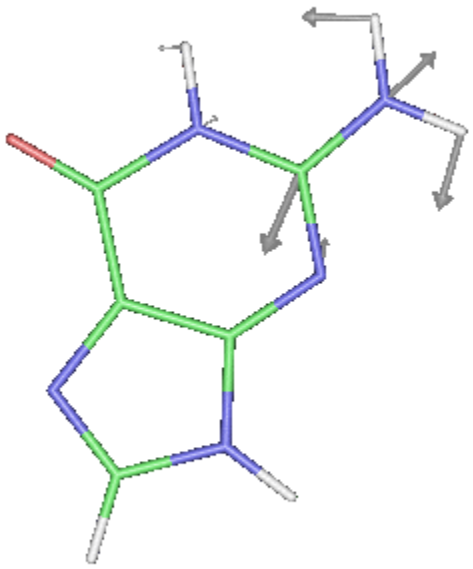

Figure 14. Eigenvector projection for the 1632 cm^{-1} vibrational mode of guanine comprised predominately of a NH_2 bend.

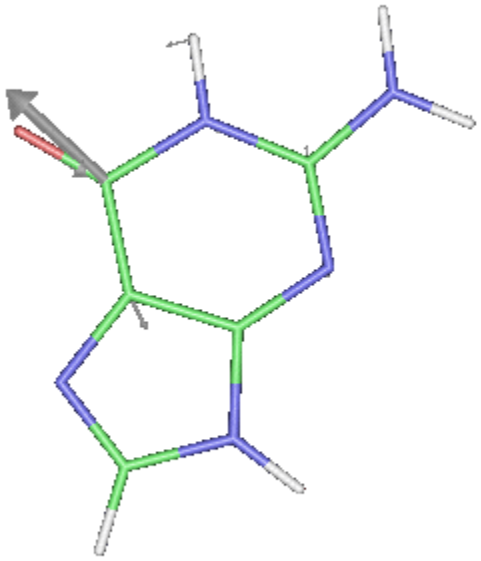

Figure 15. Eigenvector projection for the 1742 cm^{-1} vibrational mode of guanine comprised predominately of a carbonyl stretch.

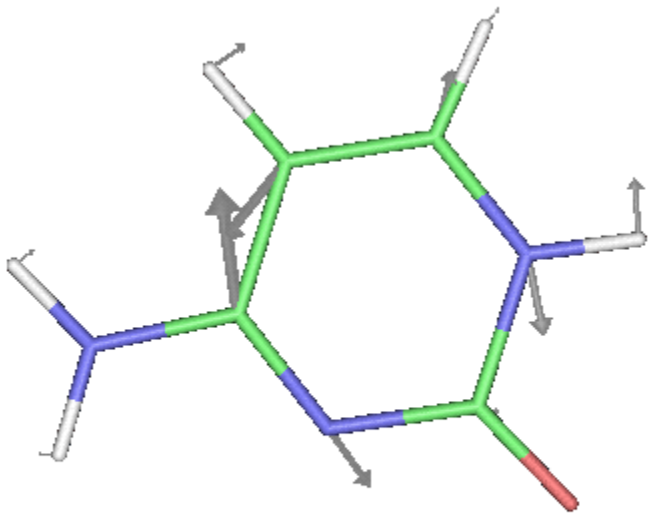

Figure 16. Eigenvector projection for the 1524 cm^{-1} vibrational mode of cytosine comprised predominately of a C=N stretch (and ring deformation).

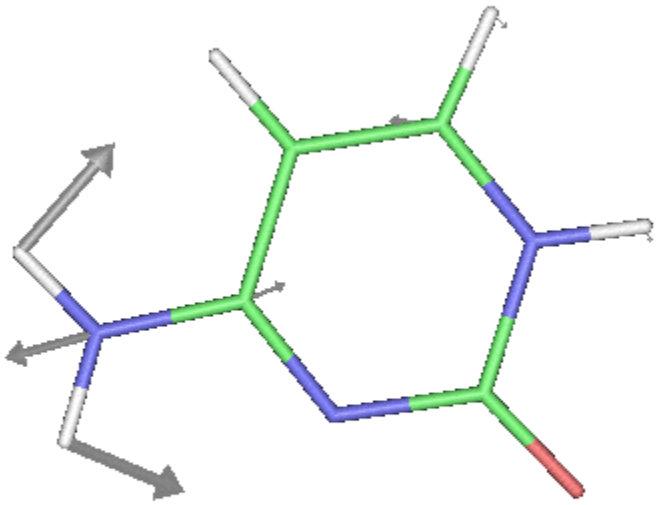

Figure 17. Eigenvector projection for the 1599 cm^{-1} vibrational mode of cytosine comprised predominately of a NH_2 bend.

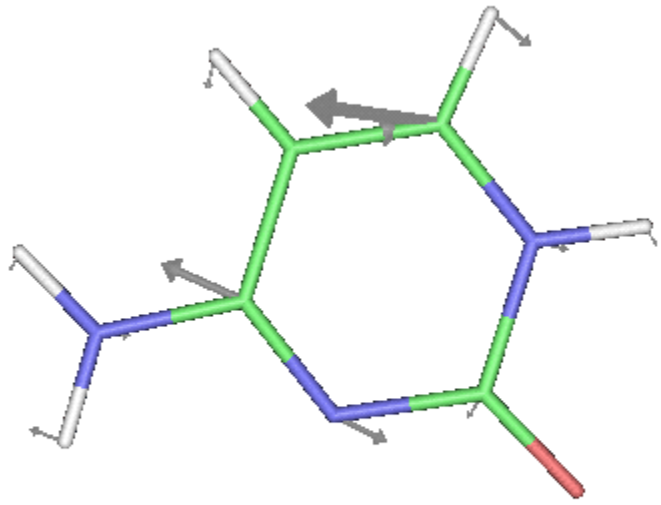

Figure 18. Eigenvector projection for the 1653 cm^{-1} vibrational mode of cytosine comprised a NH_2 bend and C=N stretch (and ring deformation).

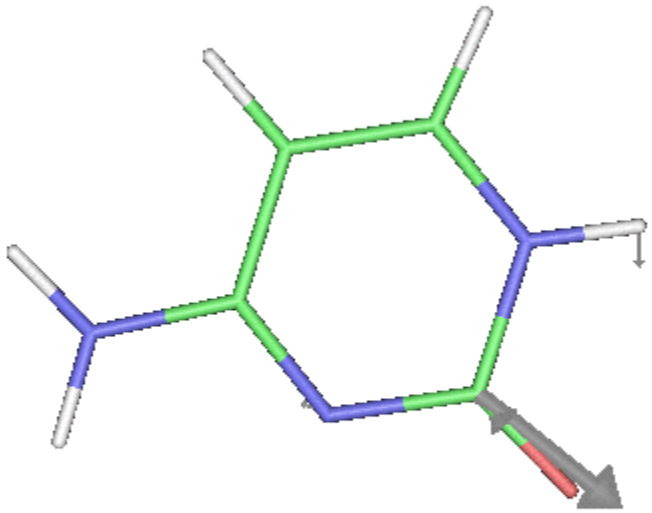

Figure 19. Eigenvector projection for the 1733 cm^{-1} vibrational mode of cytosine comprised predominately of a carbonyl stretch.

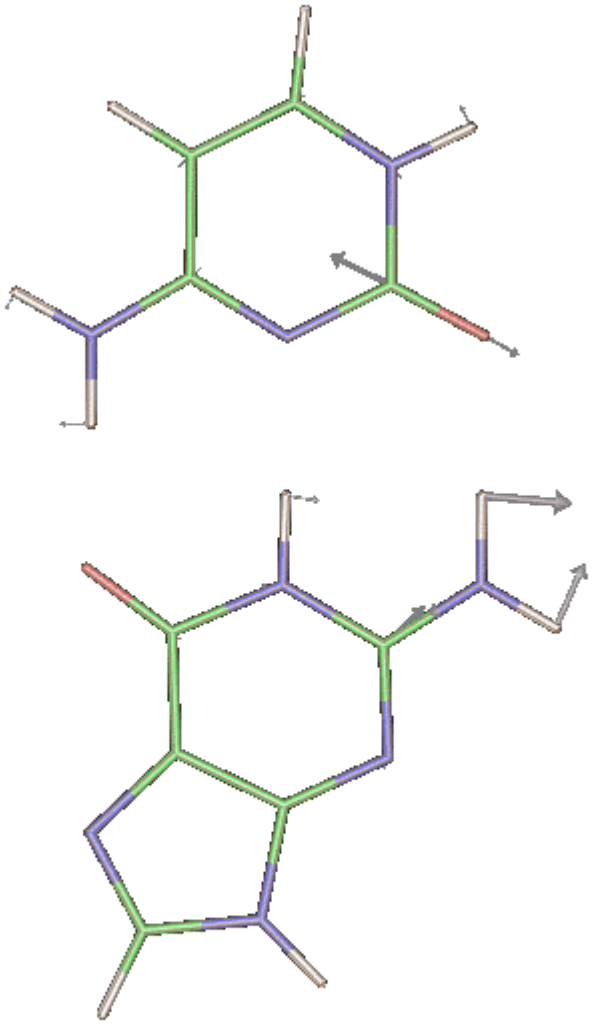

Figure 20. Eigenvector projection for the 1565 cm^{-1} vibrational mode of the guanine-cytosine (GC) base pair comprised of both a carbonyl stretch and a NH_2 bend.

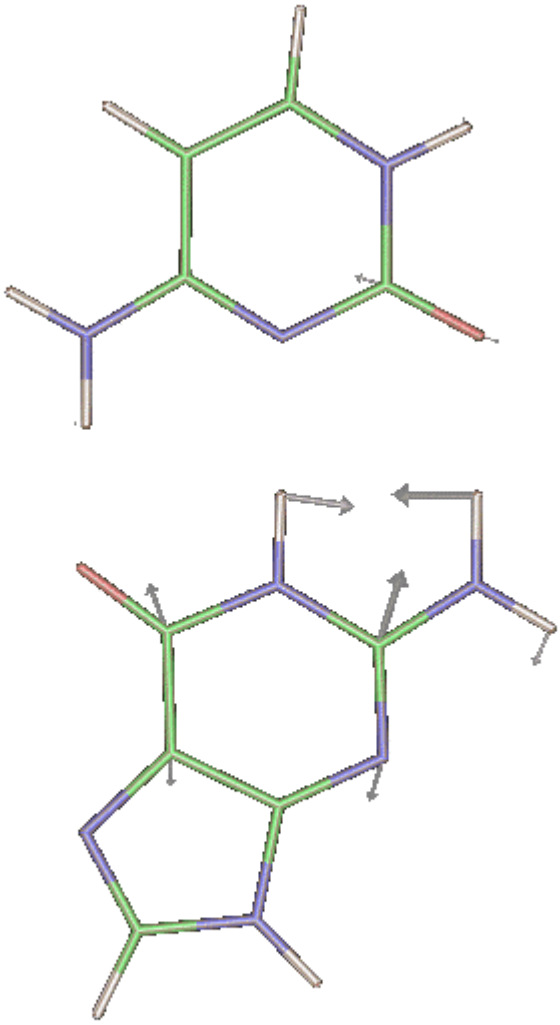

Figure 21. Eigenvector projection for the 1628 cm^{-1} vibrational mode of the guanine-cytosine (GC) base pair comprised of a carbonyl stretch, a NH_2 (and N-H) bend, and a C=N stretch (and ring deformation).

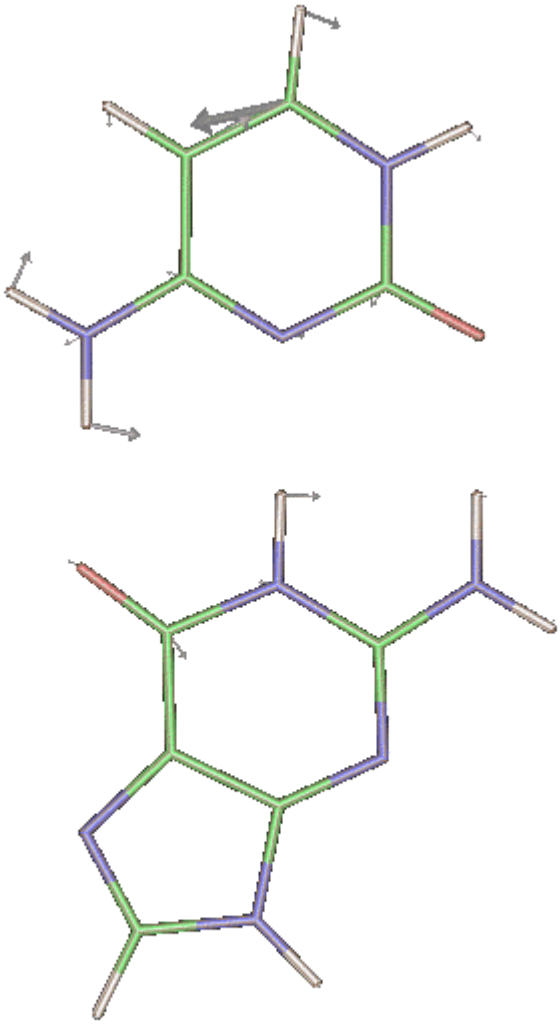

Figure 22. Eigenvector projection for the 1634 cm^{-1} vibrational mode of the guanine-cytosine (GC) base pair comprised of a carbonyl stretch and a NH_2 (and N-H) bend (and ring deformation).

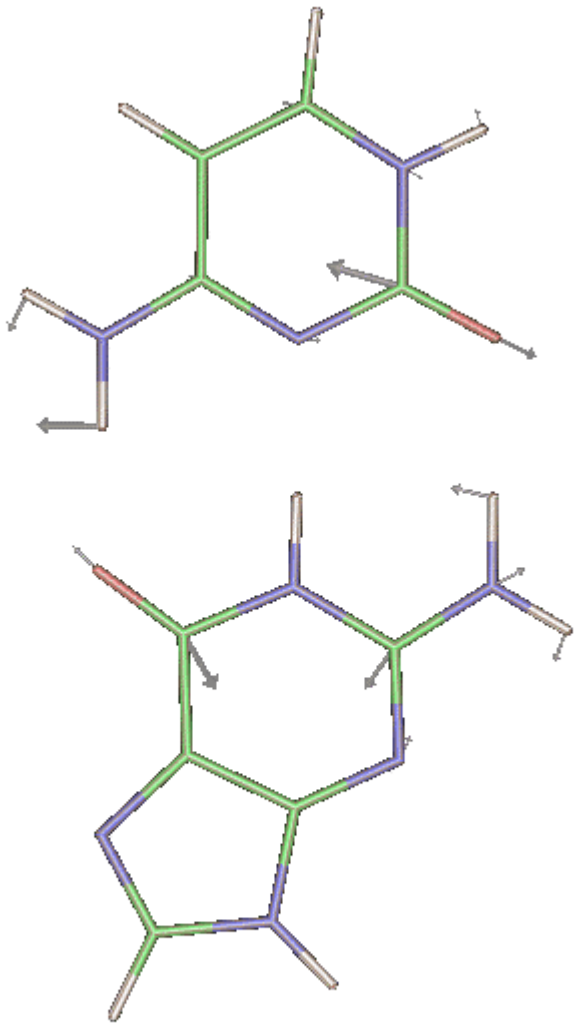

Figure 23. Eigenvector projection for the 1676 cm^{-1} vibrational mode of the guanine-cytosine (GC) base pair comprised of a carbonyl stretch and a NH_2 bend.

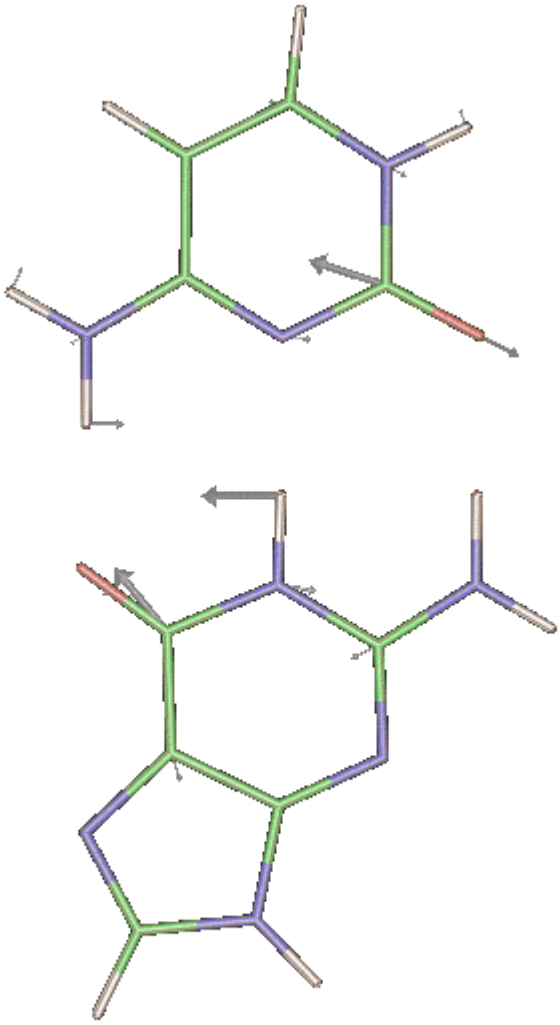

Figure 24. Eigenvector projection for the 1684 cm^{-1} vibrational mode of the guanine-cytosine (GC) base pair comprised of a carbonyl stretch and a N-H bend.

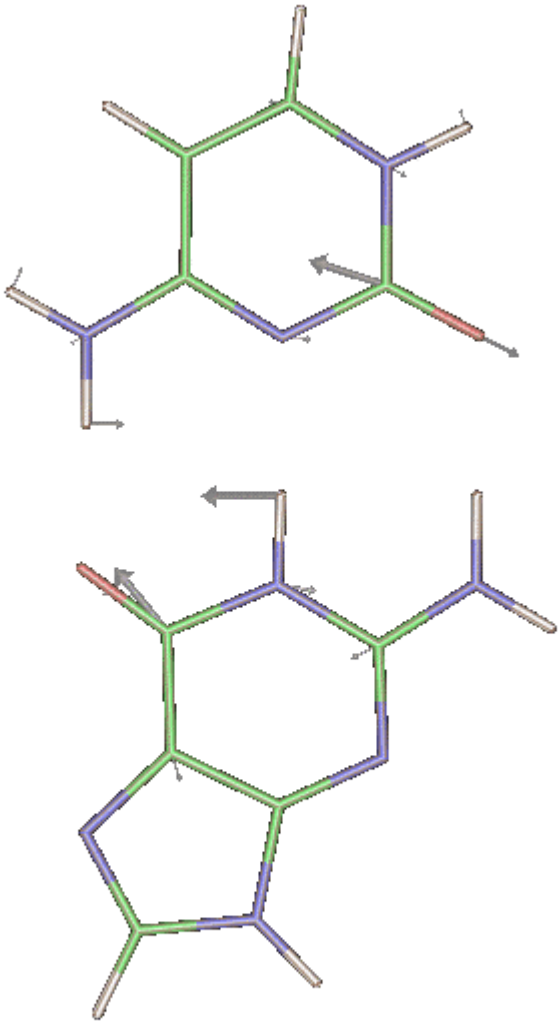

Figure 25. Eigenvector projection for the 1717 cm^{-1} vibrational mode of the guanine-cytosine (GC) base pair comprised of a carbonyl stretch and a N-H bend.

Appendix 2

Supporting Information for Chapter 3

Supporting Information

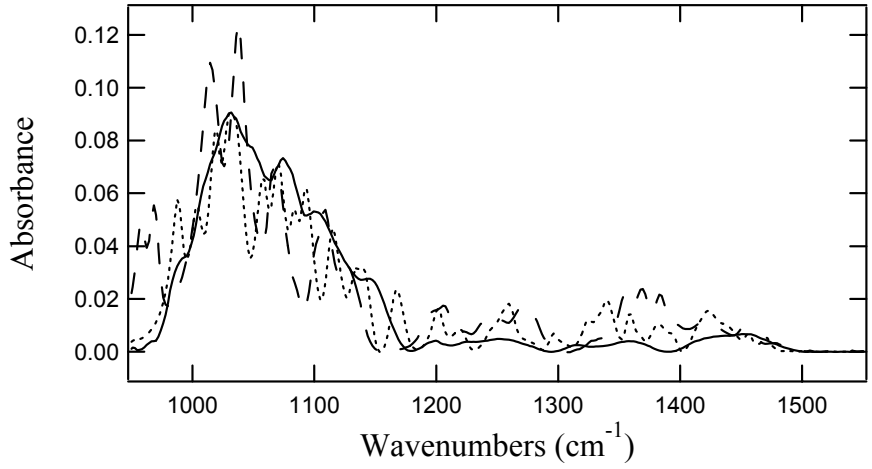

Figure 1. Single-pass ATR-FTIR spectra of a glucose (solid), mannose (long dashed) and lactose (short dashed).

To illustrate the formation of a PBA-SAM on a gold surface, a DFT model of this adlayer was constructed as shown in Figure 2. This model shows the DFT optimized structure of a PBA-SAM packed in a √3x√3R 30° lattice on a gold (111) surface in accord with previous literature reports concerning the packing of alkane thiols on gold. Figure 2 illustrates that these molecules can pack sterically into an ordered monolayer on a gold surface. However, instead of the typical straight alkane chains with a given tilt, the alkane chains in this model have a slight curvature due to the differently shaped phenylboronic acid head group of PBA.

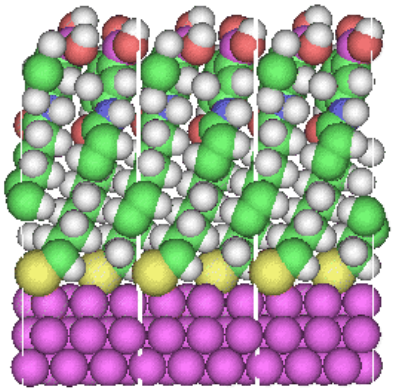

Figure 2. DFT optimized structure of a monolayer of PBA on a gold (111) surface. The PBA molecules were arranged in a √3x√3R 30° lattice pattern on the surface, typical for alkane thiols on a gold (111) surface.

Figures 3. DFT eigenvector projections of PBA with (B) and without (A) glucose bound with the corresponding calculated normal mode wavenumbers. These structures show the conversion of the boronic acid moiety of PBA to a boronate ester upon glucose binding.

A.

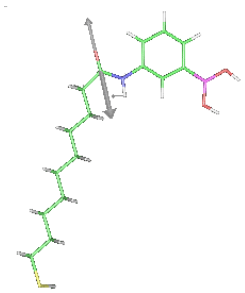

1664 cm^{-1}

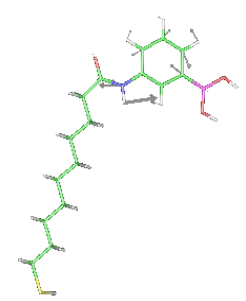

1534 cm^{-1}

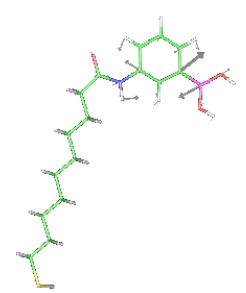

1412 cm^{-1}

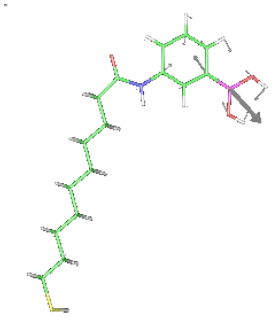

1362 cm^{-1}

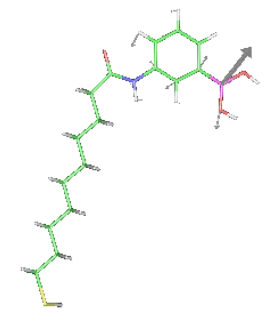

1344 cm^{-1}

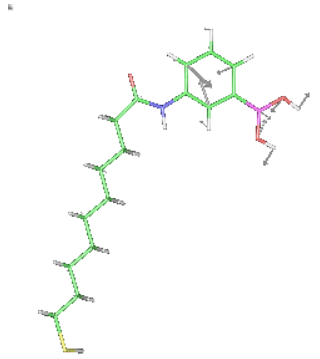

984 cm^{-1}

B.

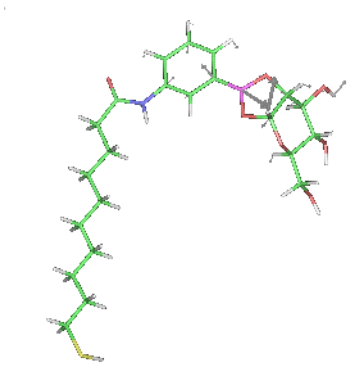

1341 cm^{-1}

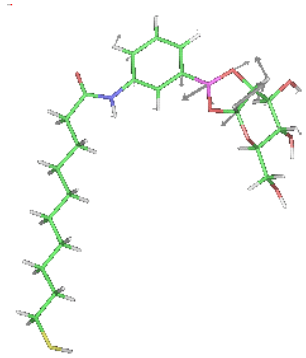

1339 cm^{-1}

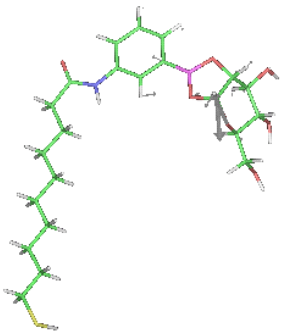

1131 cm^{-1}

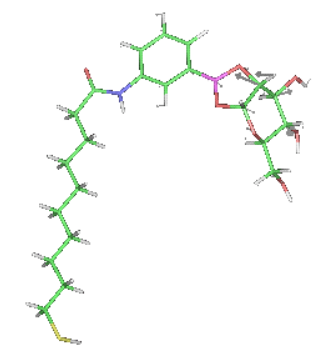

1051 cm^{-1}

Appendix 3

Supplementary Information for Chapter 6

Supplementary Information

Figure 1 shows the experimental reflectance FTIR spectra of ITO deposited on a fused quartz substrate for incident angles of 40, 60 and 80 degrees recorded with p-polarized IR radiation. The ITO film had a sheet resistance of 16.4 Ω/□. Figure 1 shows similar trends in the overall reflectivity as the ITO films on glass. The observed plasma frequency and the reflectance at wavenumbers just below the plasma frequency decreased as the incident angle decreased. The ITO also becomes more transparent at wavenumbers higher than the plasma frequency with the reflectance of 80 degrees being significantly higher than the other incident angles as expected from the Fresnel equations of reflection. Therefore the optical properties of ITO can be investigated on glass and quartz substrates using reflectance FTIR spectroscopy.

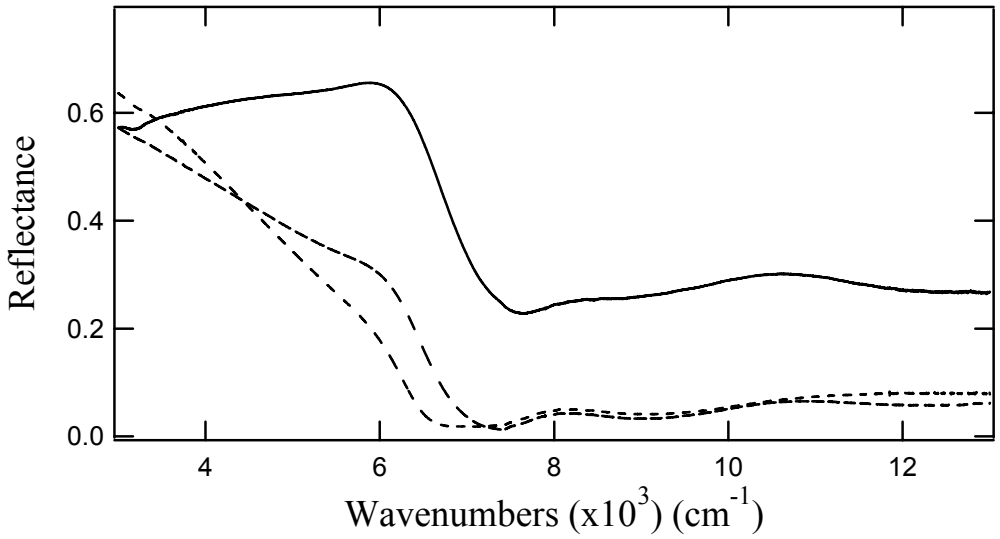

Figure 1. Experimental reflectance FTIR spectra for incident angles of 40 (short dashed), 60 (long dashed) and 80 (solid) degrees for ITO on a quartz substrate with a sheet resistance of 16.4 Ω/□ recorded with p-polarized radiation in the near-IR region (air/ITO sampling geometry).

Appendix 4

Supporting Information for Chapter 10

Supporting Information

Table 1. Calculated average anharmonicity values of nitrile and carbonyl functional groups for a variety of molecules.

Molecule	ν_1-ν_0	ν_2-ν_1	ν_3-ν_2	ν_4-ν_3	Average Anharmonicity (cm^{-1})
Acetone	1713	1705	1697	1690	8
CO	2124	2110	2096	2086	13
CN^-	2034	2021	2009	1997	12
HCN	2124	2114	2104	2095	10
ACN	2274	2268	2262	2257	6
BCN	2245	2238	2233	2227	6
MVK	1704	1701	1698	1696	3
NMP	1724	1718	1713	1709	5
4-chlorobenzonitrile	2244	2238	2231	2226	6
3-chlorobenzonitrile	2248	2241	2234	2229	6
2-chlorobenzonitrile	2249	2242	2236	2230	6
4-methoxybenzonitrile	2239	2232	2226	2220	6
Propionitrile	2265	2257	2251	2244	7
Butyronitrile	2264	2257	2250	2244	7
Valeronitrile	2264	2256	2250	2243	7
Hexanenitrile	2263	2256	2249	2243	7

Table 2. Calculated electric field effect on the frequency, bond length, and dipole magnitude of nitrile and carbonyl functional groups of a variety of molecules. Values were calculated by allowing the molecules to optimize in the applied electric.

Molecule	Electric Field (MV/cm)	Energy (cm^{-1})	Bond length (Å)	Dipole (Debye)
Acetone	-5.14257	1737.5	1.223156	3.1406
	-2.57129	1737.6	1.223005	3.0855
	0	1739.1	1.222582	3.0258
	2.57129	1740.6	1.222162	2.9679
	5.14257	1742.0	1.221751	2.9101
CO	-5.14257	2157.0	1.140698	0.0871
	-2.57129	2158.2	1.140534	0.1061
	0	2159.5	1.140355	0.1252
	2.57129	2160.6	1.140211	0.1441
	5.14257	2161.7	1.140052	0.1631
CN^-	-5.14257	2056.1	1.190461	0.2935
	-2.57129	2056.6	1.190377	0.3251
	0	2056.8	1.190349	0.3567
	2.57129	2057.7	1.190216	0.3883
	5.14257	2058.2	1.190139	0.4199
HCN	-5.14257	2142.7	1.161202	3.0504
	-2.57129	2142.5	1.161217	3.0222
	0	2142.4	1.161225	2.9940
	2.57129	2142.3	1.161226	2.9659
	5.14257	2142.2	1.161236	2.9376
ACN	-5.14257	2292.3	1.165377	4.1407
	-2.57129	2293.1	1.165296	4.0914
	0	2289.6	1.165264	4.0423
	2.57129	2294.5	1.165147	3.9929
	5.14257	2295.1	1.165082	3.9437
BCN	-5.14257	2257.2	1.168764	4.9674
	-2.57129	2258.3	1.168650	4.8125
	0	2259.1	1.168552	4.6573
	2.57129	2260.2	1.168440	4.5020
	5.14257	2261.5	1.168300	4.3467

Table 2 continued				
MVK	-5.14257	1717.2	1.227483	2.9571
	-2.57129	1718.2	1.227110	2.8915
	0	1719.3	1.226741	2.8260
	2.57129	1720.3	1.226368	2.7607
	5.14257	1721.3	1.226001	2.6954
NMP	-5.14257	1709.9	1.202203	4.2786
	-2.57129	1711.5	1.201586	4.1890
	0	1713.4	1.200956	4.0992
	2.57129	1715.3	1.200337	4.0095
	5.14257	1717.2	1.199721	3.9203
4-chlorobenzonitrile	-5.14257	2256.6	1.168925	3.7458
	-2.57129	2258.4	1.168720	3.5321
	0	2259.4	1.168620	3.3184
	2.57129	2260.7	1.168474	3.1054
	5.14257	2262.3	1.168295	2.8928
3-chlorobenzonitrile	-5.14257	2260.4	1.168399	4.3429
	-2.57129	2261.6	1.168283	4.1781
	0	2262.6	1.168174	4.0145
	2.57129	2263.7	1.168067	3.8521
	5.14257	2264.6	1.167973	3.6912
2-chlorobenzonitrile	-5.14257	2258.8	1.166801	5.4293
	-2.57129	2259.6	1.166998	5.2620
	0	2260.7	1.166887	5.0942
	2.57129	2261.6	1.166801	4.9268
	5.14257	2262.5	1.166718	4.7596
4-methoxybenzonitrile	-5.14257	2246.9	1.168382	6.5697
	-2.57129	2248.5	1.168210	6.3471
	0	2250.1	1.168045	6.1256
	2.57129	2251.6	1.167888	5.9051
	5.14257	2253.1	1.167739	5.6856
Propionitrile	-5.14257	2280.9	1.165795	4.2663
	-2.57129	2281.8	1.165716	4.2008
	0	2282.6	1.165640	4.1353
	2.57129	2283.4	1.165566	4.0699
	5.14257	2284.2	1.165496	4.0044

Table 2 continued				
Butyronitrile	-5.14257	2280.5	1.166042	4.4606
	-2.57129	2281.4	1.165944	4.3743
	0	2282.3	1.165854	4.2881
	2.57129	2283.2	1.165767	4.2020
	5.14257	2284.0	1.165683	4.1159
Valeronitrile	-5.14257	2280.0	1.166494	4.6136
	-2.57129	2281.0	1.165919	4.5104
	0	2282.0	1.165827	4.4073
	2.57129	2282.9	1.165734	4.3043
	5.14257	2283.3	1.165590	4.2030
Hexanenitrile	-5.14257	2279.5	1.166099	4.6907
	-2.57129	2280.5	1.166000	4.5662
	0	2281.4	1.165904	4.4418
	2.57129	2282.4	1.165811	4.3176
	5.14257	2283.3	1.164913	4.1934

Table 3. Calculated electric field effect on the frequency and dipole magnitude of nitrile and carbonyl functional groups of a variety of molecules. These parameters were calculated using the optimized coordinates obtained in the absence of an applied electric field.

Molecule	Electric Field (MV/cm)	Energy (cm^{-1})	Dipole (Debye)
Acetone	-5.14257	1740.4	3.1359
	-2.57129	1739.7	3.0809
	0	1739.1	3.0258
	2.57129	1738.4	2.9706
	5.14257	1737.8	2.9155
CO	-5.14257	2159.4	0.0883
	-2.57129	2159.4	0.1067
	0	2159.5	0.1251
	2.57129	2159.5	0.1436
	5.14257	2159.5	0.1620
CN^-	-5.14257	2056.9	0.2937
	-2.57129	2056.9	0.3252
	0	2056.8	0.3567
	2.57129	2056.8	0.3882
	5.14257	2056.7	0.4197
HCN	-5.14257	2142.2	3.0502
	-2.57129	2142.1	3.0221
	0	2141.9	2.9941
	2.57129	2141.8	2.9660
	5.14257	2141.7	2.9379
ACN	-5.14257	2290.0	4.1401
	-2.57129	2290.2	4.0910
	0	2290.4	4.0419
	2.57129	2290.5	3.9929
	5.14257	2290.7	3.9439
BCN	-5.14257	2259.2	4.9665
	-2.57129	2259.5	4.8121
	0	2259.7	4.6576
	2.57129	2260.0	4.5032
	5.14257	2260.2	4.3488

Table 3 continued			
MVK	-5.14257	1720.4	2.9500
	-2.57129	1719.8	2.8880
	0	1719.3	2.8260
	2.57129	1718.7	2.7641
	5.14257	1718.2	2.7023
NMP	-5.14257	1714.7	4.2660
	-2.57129	1714.1	4.1824
	0	1713.4	4.0992
	2.57129	1712.7	4.0163
	5.14257	1712.0	3.9337
4-chlorobenzonitrile	-5.14257	2258.7	3.7324
	-2.57129	2259.1	3.5253
	0	2259.4	3.3184
	2.57129	2259.7	3.1119
	5.14257	2260.0	2.9056
3-chlorobenzonitrile	-5.14257	2262.1	4.3395
	-2.57129	2262.4	4.1765
	0	2262.6	4.0145
	2.57129	2262.9	3.8537
	5.14257	2263.1	3.6941
2-chlorobenzonitrile	-5.14257	2260.2	5.4263
	-2.57129	2260.5	5.2602
	0	2260.7	5.0942
	2.57129	2260.9	4.9283
	5.14257	2261.2	4.7624
4-methoxybenzonitrile	-5.14257	2249.3	6.5342
	-2.57129	2249.7	6.3296
	0	2250.1	6.1256
	2.57129	2250.5	5.9223
	5.14257	2250.8	5.7198
Propionitrile	-5.14257	2282.2	4.2648
	-2.57129	2282.4	4.2001
	0	2282.6	4.1353
	2.57129	2282.8	4.0705
	5.14257	2283.0	4.0058

Table 3 continued			
Butyronitrile	-5.14257	2281.8	4.4590
	-2.57129	2282.1	4.3735
	0	2282.3	4.2881
	2.57129	2282.5	4.2027
	5.14257	2282.8	4.1174
Valeronitrile	-5.14257	2281.5	4.6116
	-2.57129	2281.7	4.5094
	0	2282.0	4.4073
	2.57129	2282.2	4.3053
	5.14257	2282.4	4.2032
Hexanenitrile	-5.14257	2280.9	4.6887
	-2.57129	2281.2	4.5652
	0	2281.4	4.4418
	2.57129	2281.7	4.3185
	5.14257	2281.9	4.1953

Table 4. Experimental and calculated wavenumbers for nitrile and carbonyl stretches for a variety of molecules.

Molecule	Frequency (cm^{-1}) (experimental)	Frequency (cm^{-1}) (calculated)	Potential Energy Distribution (PED) % (CN or CO stretch)
Acetone	1711.0	1739.1	93
CO	2143.0	2159.5	100
CN^-	2080.0	2056.8	100
HCN	2072.4	2142.4	94
ACN	2247.5	2289.6	91
BCN	2227.8	2259.1	88
MVK	1676.0	1719.3	77
NMP	1685.0	1713.4	89
4-chlorobenzonitrile	2230.6	2259.4	88
3-chlorobenzonitrile	2232.7	2262.6	88
2-chlorobenzonitrile	2232.1	2260.7	88
4-methoxybenzonitrile	2223.5	2250.1	87
Propionitrile	2243.5	2282.6	89
Butyronitrile	2247.0	2282.3	89
Valeronitrile	2239.2	2282.0	89
Hexanenitrile	2243.2	2281.4	89

Table 5. Literature difference dipole moment values for a variety of nitrile and carbonyl containing molecules.

Molecule	$\langle x \rangle \nu_1 - \langle x \rangle \nu_0$ (Å)	q (D/Å)	$\Delta\mu_{anharm}$ (D) (% of $\Delta\mu_{lit}$)	$\Delta\mu_{lit}$ (D)
Acetone	0.002880	2.4749	0.0071 (16)	0.045
CO	0.004233	0.1098	0.0005 (1)	0.04
CN^-	0.004306	0.2997	0.0013	-----
HCN	0.003408	2.5782	0.0088	-----
ACN	0.003197	3.4690	0.0111 (43)	0.0258
BCN	0.003200	3.9855	0.0128 (35)	0.0361
MVK	0.003071	2.3037	0.0071 (14)	0.049
NMP	0.003829	3.4133	0.0131(19)	0.068
4-chlorobenzonitrile	0.003279	2.8397	0.0093 (27)	0.0348
3-chlorobenzonitrile	0.003284	3.4366	0.0113 (35)	0.0318
2-chlorobenzonitrile	0.003264	4.3656	0.0143 (47)	0.0306
4-methoxybenzonitrile	0.003279	5.2443	0.0172 (35)	0.0497
Propionitrile	0.003316	3.5477	0.0118 (42)	0.0277
Butyronitrile	0.003320	3.6781	0.0122 (43)	0.0283
valeronitrile	0.003319	3.7804	0.0125 (47)	0.0267
hexanenitrile	0.003320	3.8097	0.0127 (45)	0.028

Table 6. PES polynomial coefficients for the nitrile or carbonyl stretching normal mode at zero applied electric field.

	Potential Energy Surface Polynomial Coefficients*				
	a_0	a_1	a_2	a_3	a_4
acetone	0.0	-680.58	43221	35564	20107
CO	0.0	-376.69	67451	65270	37116
CN^-	0.0	-264.10	61879	56525	30216
HCN	0.0	-319.58	67267	54314	26048
ACN	0.0	-222.03	77039	59216	34762
BCN	0.0	-167.53	75098	57162	33417
MVK	0.0	292.51	43028	-27005	14829
NMP	0.0	-438.55	44005	33305	19545
4-chlorobenzonitrile	0.0	332.76	74934	-58466	34253
3-chlorobenzonitrile	0.0	-342.21	75138	58740	34295
2-chlorobenzonitrile	0.0	-344.47	75222	58588	34192
4-methoxybenzonitrile	0.0	-330.00	74539	58067	34067
propionitrile	0.0	-293.81	76389	60603	34876
butyronitrile	0.0	286.06	76355	-60595	34899
valeronitrile	0.0	-291.27	76326	60539	34847
hexanenitrile	0.0	-292.78	76293	60550	34871

*$E(Q)=a_0+a_1Q+a_2Q^2+a_3Q^3+a_4Q^4$: where E is energy (cm^{-1}) and Q is the normal coordinate displacement of the nitrile or carbonyl stretching normal mode. The potential energy surfaces were offset to zero in the energy axis.

Table 7. PES polynomial coefficients for the nitrile or carbonyl stretching normal mode at 5.14257 MV/cm applied electric field.

	Potential Energy Surface Polynomial Coefficients*				
	a_0	a_1	a_2	a_3	a_4
acetone	0.0	-446.52	44251	36112	20321
CO	0.0	-391.47	67602	65566	37222
CN^-	0.0	-255.18	61956	56718	30303
HCN	0.0	262.58	67115	-54317	26587
ACN	0.0	-208.02	77035	58976	34291
BCN	0.0	181.14	75227	-57139	33345
MVK	0.0	-316.18	43427	26124	14304
NMP	0.0	432.26	43696	-32689	19426
4-chlorobenzonitrile	0.0	430.91	76480	-58485	29452
3-chlorobenzonitrile	0.0	-342.88	75276	58812	34321
2-chlorobenzonitrile	0.0	-342.15	75323	58622	34196
4-methoxybenzonitrile	0.0	-329.25	74711	58168	34079
propionitrile	0.0	-294.61	76500	60643	34891
butyronitrile	0.0	287.74	76458	-60617	34903
valeronitrile	0.0	-295.20	76458	60603	34880
hexanenitrile	0.0	293.61	76426	-60605	34892

* $E(Q)=a_0+a_1Q+a_2Q^2+a_3Q^3+a_4Q^4$: where E is energy (cm^{-1}) and Q is the normal coordinate displacement of the nitrile or carbonyl stretching normal mode. The potential energy surfaces were offset to zero in the energy axis.

Table 8. Difference in the PES polynomial coefficients for the nitrile or carbonyl stretching normal mode between zero and 5.14257 MV/cm applied electric field.

	Potential Energy Surface Polynomial Coefficients*				
	$\|\Delta a_0\|$ (%)	$\|\Delta a_1\|$ (%)	$\|\Delta a_2\|$ (%)	$\|\Delta a_3\|$ (%)	$\|\Delta a_4\|$ (%)
acetone	0.0 (0.0)	234.06 (34.4)	1030 (2.4)	548 (1.5)	214 (1.1)
CO	0.0 (0.0)	14.78 (3.9)	151 (0.2)	296 (0.5)	106 (0.3)
CN^-	0.0 (0.0)	8.92 (3.4)	77 (0.1)	193 (0.3)	87 (0.3)
HCN	0.0 (0.0)	57.00 (17.8)	152 (0.2)	3 (0.0)	539 (2.1)
ACN	0.0 (0.0)	14.01 (6.3)	4 (0.0)	240 (0.4)	471 (1.4)
BCN	0.0 (0.0)	13.61 (8.1)	129 (0.2)	23 (0.0)	72 (0.2)
MVK	0.0 (0.0)	23.67 (8.1)	399 (0.9)	881 (3.3)	525 (3.5)
NMP	0.0 (0.0)	6.29 (1.4)	309 (0.7)	616 (1.8)	119 (0.6)
4-chlorobenzonitrile	0.0 (0.0)	98.15 (29.5)	1546 (2.1)	19 (0.0)	4801 (14.0)
3-chlorobenzonitrile	0.0 (0.0)	0.67 (0.2)	138 (0.2)	72 (0.1)	26 (0.1)
2-chlorobenzonitrile	0.0 (0.0)	2.32 (0.7)	101 (0.1)	34 (0.1)	4 (0.0)
4-methoxybenzonitrile	0.0 (0.0)	0.75 (0.2)	172 (0.2)	101 (0.2)	12 (0.0)
propionitrile	0.0 (0.0)	0.80 (0.3)	111 (0.1)	40 (0.1)	15 (0.0)
butyronitrile	0.0 (0.0)	1.68 (0.6)	103 (0.1)	22 (0.0)	4 (0.0)
valeronitrile	0.0 (0.0)	3.93 (1.3)	132 (0.2)	64 (0.1)	33 (0.1)
hexanenitrile	0.0 (0.0)	0.83 (0.3)	133 (0.2)	55 (0.1)	21 (0.1)

* $E(Q)=a_0+a_1Q+a_2Q^2+a_3Q^3+a_4Q^4$: where E is energy (cm^{-1}) and Q is the normal coordinate displacement of the nitrile or carbonyl stretching normal mode. The potential energy surfaces were offset to zero in the energy axis.

Table 9. Single point energies of the nitriles or carbonyls at –5.14257, 0.0, and 5.14257 MV/cm applied electric fields.

	Single Point Energy (cm^{-1})		
	–5.14257 MV/cm	0.0 MV/cm	5.14257 MV/cm
acetone	-355004	-354737	-354479
CO	-96639	-96648	-96660
CN^-	-96886	-96914	-96948
HCN	-114076	-113780	-113559
ACN	-222522	-223036	-223223
BCN	-573320	-572904	-572515
MVK	-403198	-402964	-402742
NMP	-565517	-565095	-564689
4-chlorobenzonitrile	-567259	-566955	-566689
3-chlorobenzonitrile	-565436	-565091	-564776
2-chlorobenzonitrile	-565069	-564613	-564186
4-methoxybenzonitrile	-713156	-712702	-712283
propionitrile	-327232	-326868	-326514
butyronitrile	-432701	-432325	-431962
valeronitrile	-537786	-537395	-537022
hexanenitrile	-642801	-642408	-642035

Note: Whether the single point energy at ±5.14257 MV/cm is higher or lower than at zero applied electric field is dependent on the orientation of the CN or CO bond along the axis of the applied electric field. For instance, a negative applied electric field along the C-N or C-O bond results in a lower calculated energy of the molecule relative to zero applied electric field and vice versa.

Table 10. Coefficients for the anharmonic contributions to the transition moment at zero applied electric field.

ACN

N	a_{n0}	$a_{n+1,1}$	$a_{n0}a_{n+1,1}$	$a_{n0}a_{n+1,1}\sqrt{n+1}$
0	1	1	1	1
1	-0.023	-0.091	0.0021	0.0036
2	-0.039	-0.0225	0.00087	0.0019
3	-0.0033	-0.0068	2.3E-05	6.0E-05
4	-0.0018	0.0016	-2.9E-06	-8.6E-06

Total zero field correction = 0.0056

HCN

n	a_{n0}	$a_{n+1,1}$	$a_{n0}a_{n+1,1}$	$a_{n0}a_{n+1,1}\sqrt{n+1}$
0	1	1	1	1
1	-0.019	-0.090	0.0017	0.0029
2	-0.035	-0.057	0.0020	0.0044
3	-0.0037	-0.0030	1.1E-05	3.0E-05
4	0.00068	0.0066	4.5E-06	1.3E-05

Total zero field correction = 0.0073

CO

n	a_{n0}	$a_{n+1,1}$	$a_{n0}a_{n+1,1}$	$a_{n0}a_{n+1,1}\sqrt{n+1}$
0	1	1	1	1
1	-0.023	-0.10	0.0024	0.0041
2	-0.036	-0.023	0.00082	0.0018
3	-0.0043	-0.0076	3.3E-05	8.7E-05
4	0.0008	0.0022	1.7E-06	5.2E-06

Total zero field correction = 0.0061

Acetone

n	a_{n0}	$a_{n+1,1}$	$a_{n0}a_{n+1,1}$	$a_{n0}a_{n+1,1}\sqrt{n+1}$
0	1	1	1	1
1	0.014	-0.032	-0.00046	-0.0008
2	0.015	0.038	0.00058	0.0013
3	-0.0045	-0.0082	3.7E-05	9.7E-05
4	-3.7E-05	0.0029	-1.1E-07	-3.2E-07

Total zero field correction = 0.00058

Table 11. Coefficients for the anharmonic corrections to the transition moment for CO at -5.14257, 0 and 5.14257 MV/cm applied electric field.

	v = 0 F = 0	v = 1 F = 0	v = 0 F = -5.14257 MV/cm	v = 1 F = -5.14257 MV/cm	v = 0 F = +5.14257 MV/cm	v = 1 F = +5.14257 MV/cm
Energy (cm^{-1})	1066.78	3192.05	1065.71	3197.7	1068.18	3186.35
n=0	1	0	1	0	1	0
n=1	-0.023	1	-0.022	1	-0.022	1
n=2	-0.038	-0.10	-0.03722	-0.11	-0.038	-0.11
n=3	-0.0043	-0.13	-0.00434	-0.024	-0.0043	-0.024
n=4	0.00086	0.0088	0.000841	-0.0082	0.00087	-0.0081
n=5	0.00043	0.031	0.00043	0.0022	-0.00044	0.0023

Table 12. List of basis set used for carbonyl models.

Atomic cutoff radius 10.39 au
Hydrogen nbas= 1 z= 1. 3 radial functions, e_ref= -.0413196Ha
n=1 L=0 occ= 1.00 e= -.240212Ha -6.5365eV
n=1 L=0 occ= .00 e= -.845000Ha -22.9936eV
n=2 L=1 occ= .00 e= -2.000000Ha -54.4228eV
Carbon nbas= 2 z= 6. 7 radial functions, e_ref= -.0462554Ha
n=1 L=0 occ= 2.00 e= -10.052779Ha -273.5502eV
n=2 L=0 occ= 2.00 e= -.505759Ha -13.7624eV
n=2 L=1 occ= 2.00 e= -.195589Ha -5.3223eV
n=2 L=0 occ= .00 e= -1.485570Ha -40.4244eV
n=2 L=1 occ= .00 e= -1.170076Ha -31.8394eV
n=3 L=2 occ= .00 e= -2.722222Ha -74.0755eV
n=3 L=2 occ= .00 e= -1.388886Ha -37.7935eV eliminated
Oxygen nbas= 3 z= 8. 7 radial functions, e_ref= -.0560029Ha
n=1 L=0 occ= 2.00 e= -18.913267Ha -514.6564eV
n=2 L=0 occ= 2.00 e= -.880420Ha -23.9575eV
n=2 L=1 occ= 4.00 e= -.334992Ha -9.1156eV
n=2 L=0 occ= .00 e= -2.144815Ha -58.3634eV
n=2 L=1 occ= .00 e= -1.593916Ha -43.3727eV
n=3 L=2 occ= .00 e= -2.722222Ha -74.0755eV
n=3 L=2 occ= .00 e= -1.388886Ha -37.7935eV eliminated

Table 13. List of basis set used for the nitrile models.

Atomic cutoff radius 10.39 au
Hydrogen nbas= 1 z= 1. 3 radial functions, e_ref= -.0413196Ha
n=1 L=0 occ= 1.00 e= -.240212Ha -6.5365eV
n=1 L=0 occ= .00 e= -.845000Ha -22.9936eV
n=2 L=1 occ= .00 e= -2.000000Ha -54.4228eV
Carbon nbas= 2 z= 6. 7 radial functions, e_ref= -.0462554Ha
n=1 L=0 occ= 2.00 e= -10.052779Ha -273.5502eV
n=2 L=0 occ= 2.00 e= -.505759Ha -13.7624eV
n=2 L=1 occ= 2.00 e= -.195589Ha -5.3223eV
n=2 L=0 occ= .00 e= -1.485570Ha -40.4244eV
n=2 L=1 occ= .00 e= -1.170076Ha -31.8394eV
n=3 L=2 occ= .00 e= -2.722222Ha -74.0755eV
n=3 L=2 occ= .00 e= -1.388886Ha -37.7935eV eliminated
Nitrogen nbas= 3 z= 7. 7 radial functions, e_ref= -.1158319Ha
n=1 L=0 occ= 2.00 e= -14.142069Ha -384.8254eV
n=2 L=0 occ= 2.00 e= -.683372Ha -18.5955eV
n=2 L=1 occ= 3.00 e= -.262986Ha -7.1562eV
n=2 L=0 occ= .00 e= -1.808113Ha -49.2013eV
n=2 L=1 occ= .00 e= -1.382598Ha -37.6224eV
n=3 L=2 occ= .00 e= -2.722222Ha -74.0755eV
n=3 L=2 occ= .00 e= -1.388886Ha -37.7935eV eliminated

Figure 1. Potential energy surfaces and Numerov-Cooley vibrational wavefunctions.

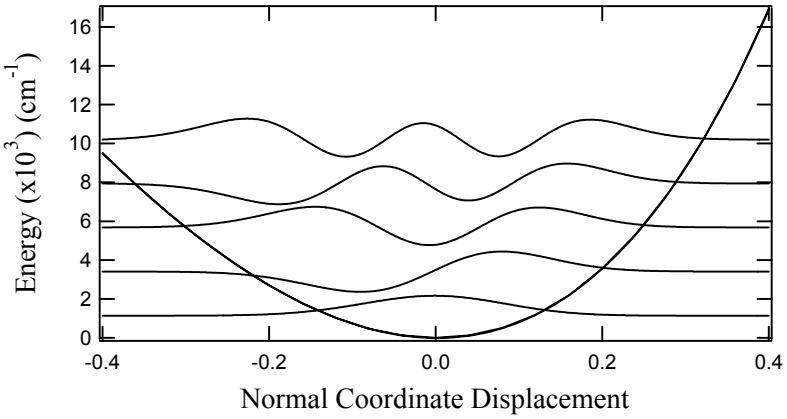

ACN

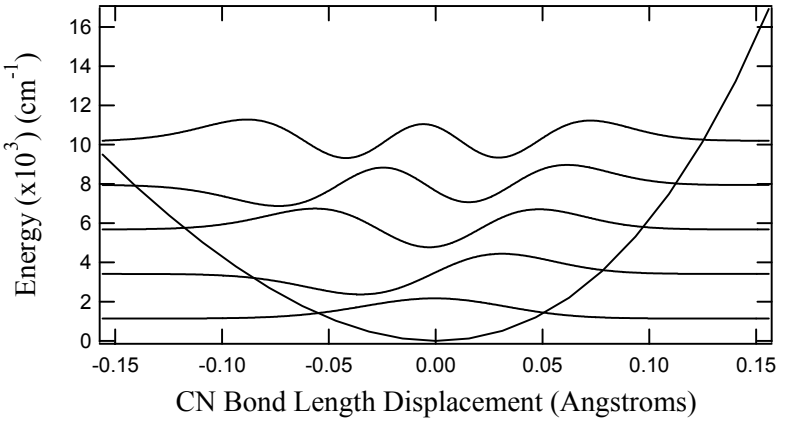

ACN

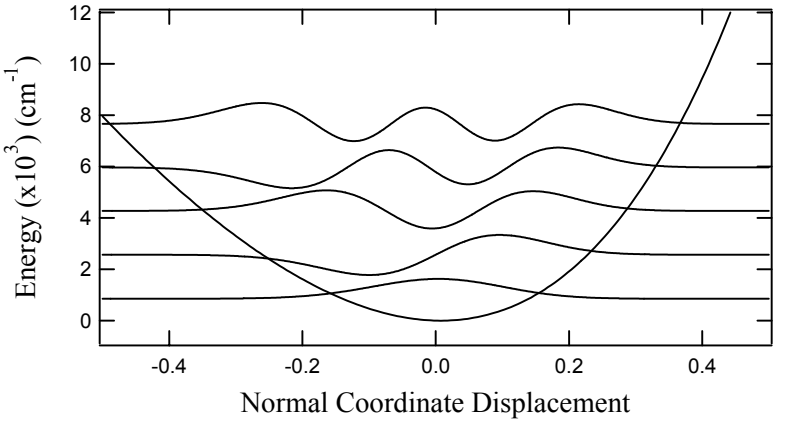

acetone

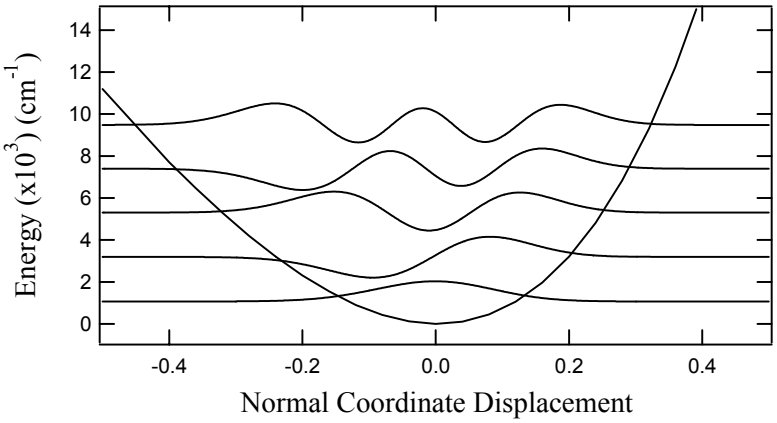
Energy (x10^3) (cm^{-1})
14
12
10
8
6
4
2
0
-0.4
-0.2
0.0
0.2
0.4
Normal Coordinate Displacement

CO

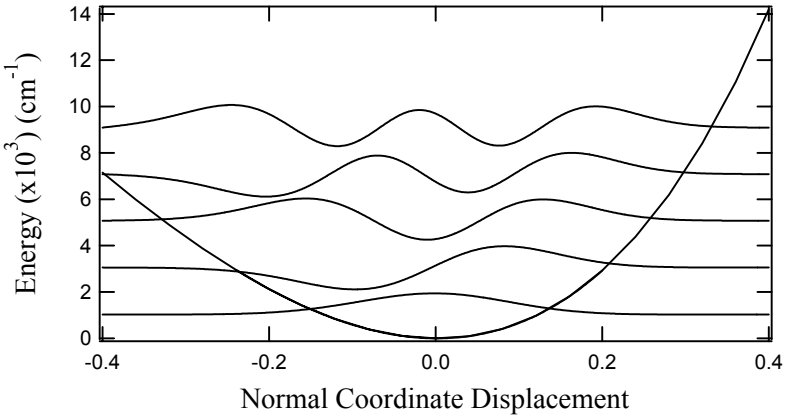
Energy (x10^3) (cm^{-1})
14
12
10
8
6
4
2
0
-0.4
-0.2
0.0
0.2
0.4
Normal Coordinate Displacement

CN^-

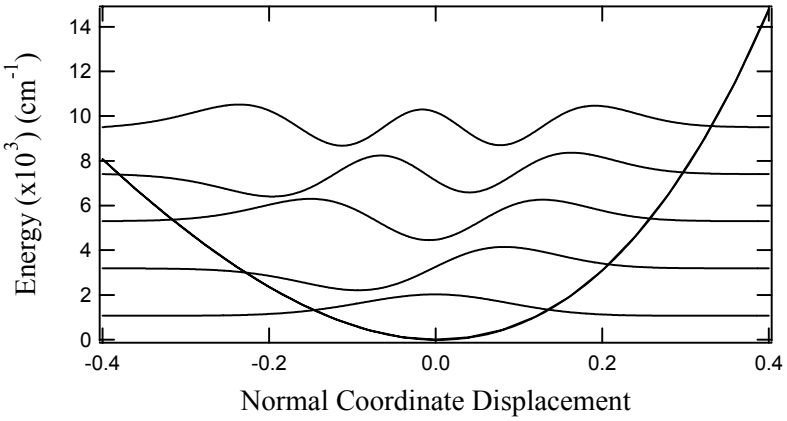
Energy (x10^3) (cm^{-1})
14
12
10
8
6
4
2
0
-0.4
-0.2
0.0
0.2
0.4
Normal Coordinate Displacement

HCN

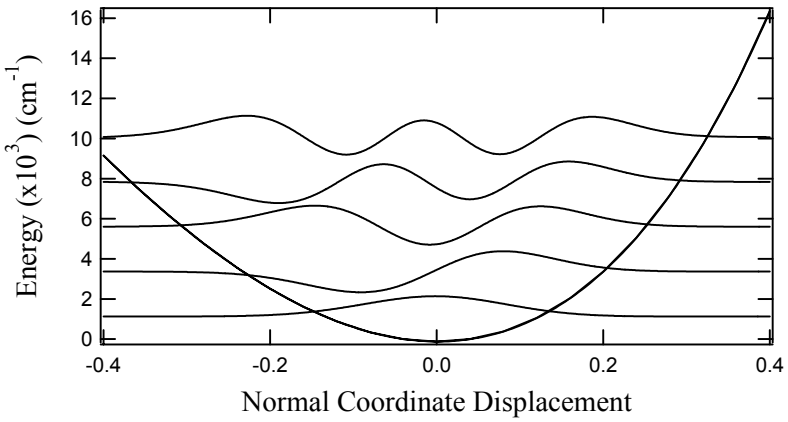
Energy (x10^3) (cm^{-1})
16
14
12
10
8
6
4
2
0
-0.4
-0.2
0.0
0.2
0.4
Normal Coordinate Displacement

BCN

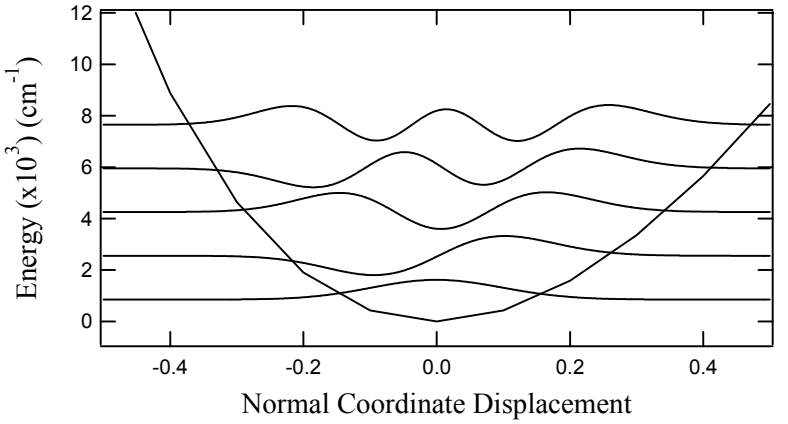
Energy (x10^3) (cm^{-1})
12
10
8
6
4
2
0
-0.4
-0.2
0.0
0.2
0.4
Normal Coordinate Displacement

MVK

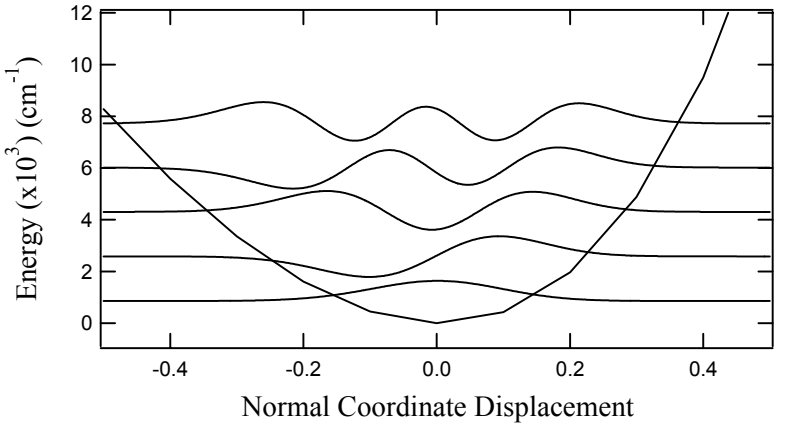
Energy (x10^3) (cm^{-1})
12
10
8
6
4
2
0
-0.4
-0.2
0.0
0.2
0.4
Normal Coordinate Displacement

NMP

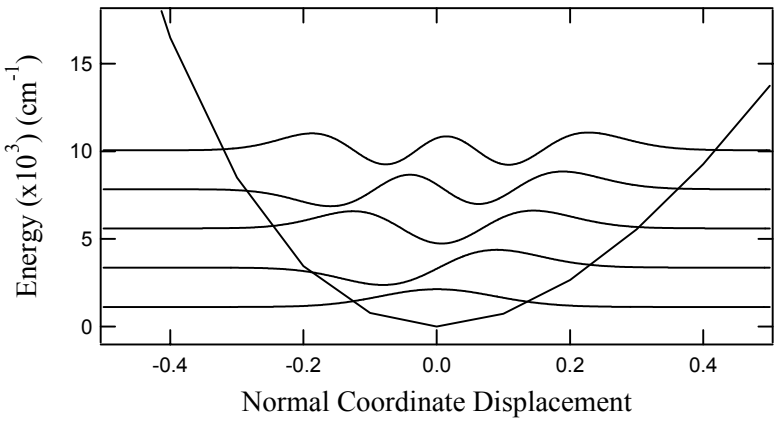

4-chlorobenzonitrile

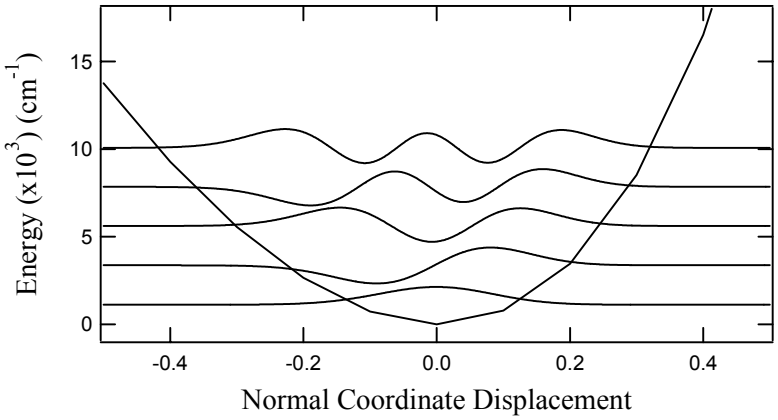

3-chlorobenzonitrile

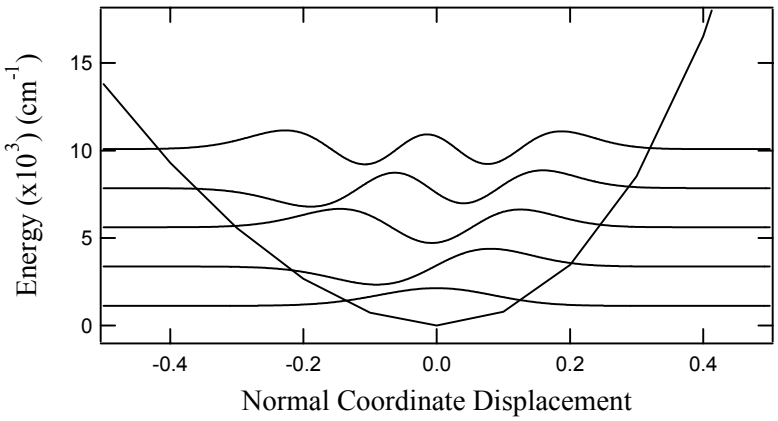

2-chlorobenzonitrile

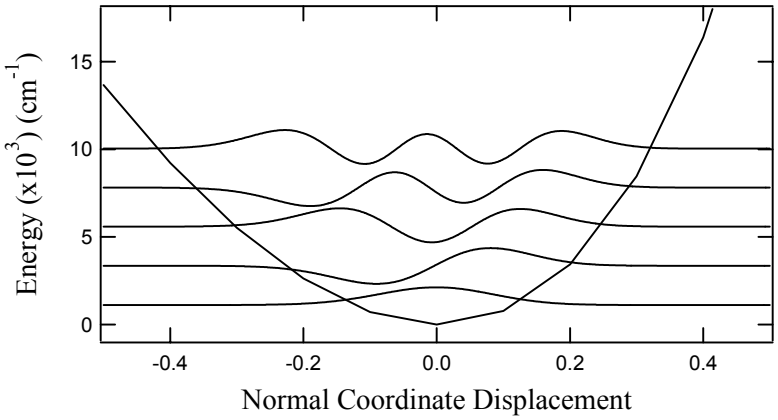

4-methoxybenzonitrile

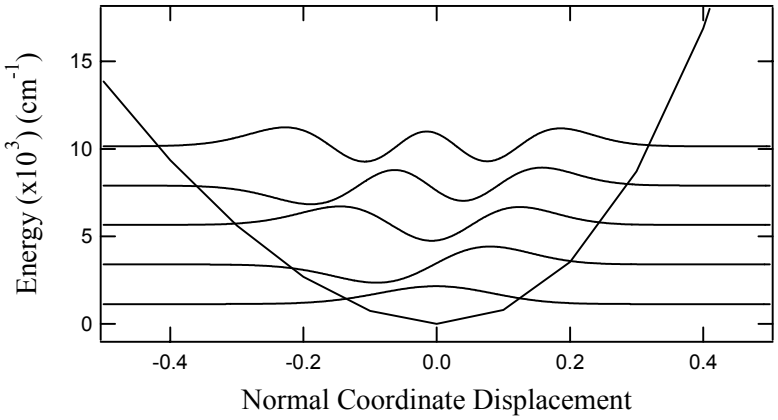

propionitrile

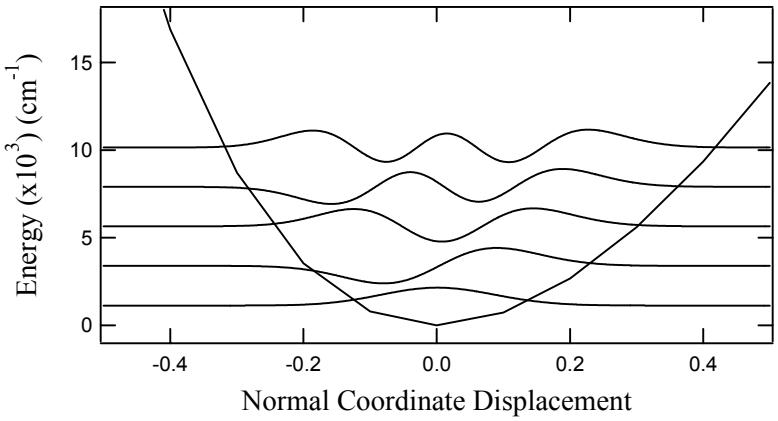

butyronitrile

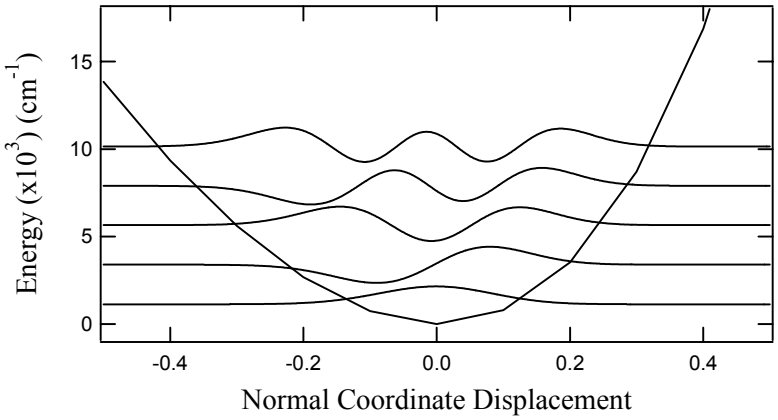

valeronitrile

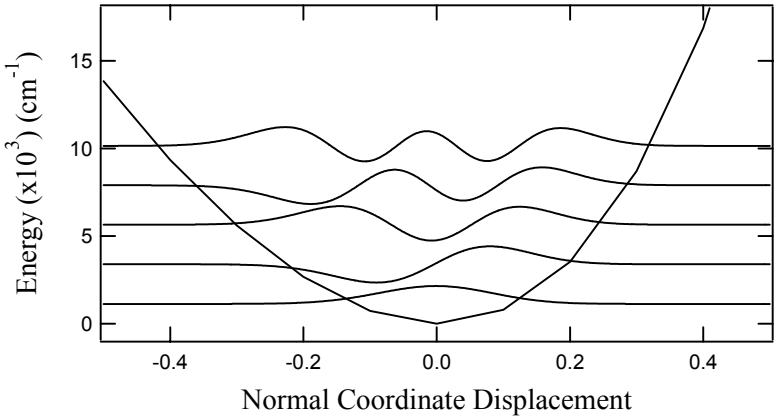

hexanenitrile

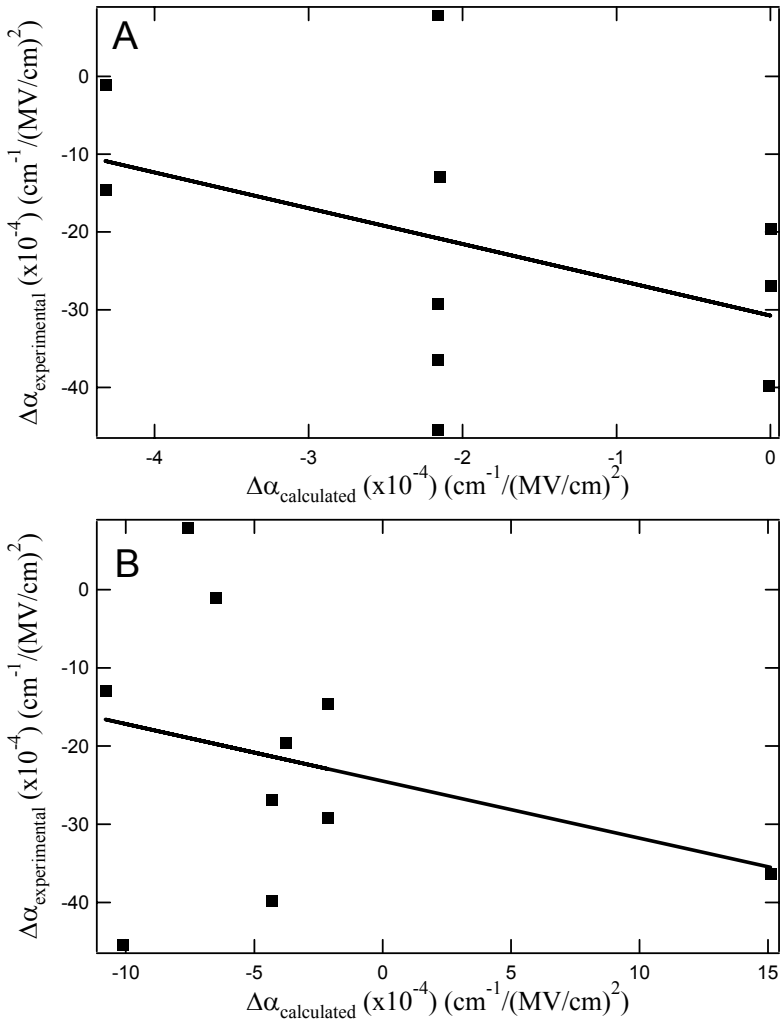

Figure 2. Plot of the experimental versus the DFT calculated difference polarizability for nitriles using optimized molecular geometries in the absence (A) or presence of an applied electric field.

Figure 3. Optimized CO and CN containing molecules in zero applied electric field.

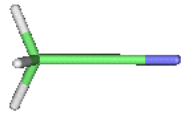

ACN

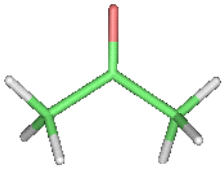

acetone



CO



CN^-



HCN

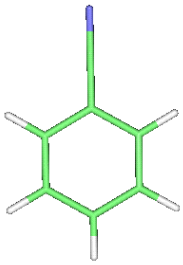

BCN

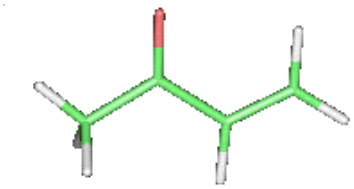

MVK

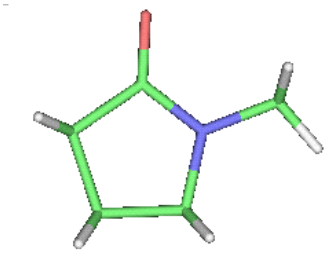

NMP

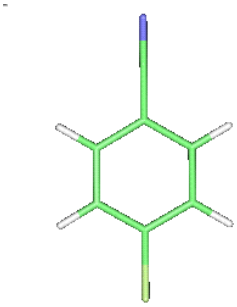

4-chlorobenzonitrile

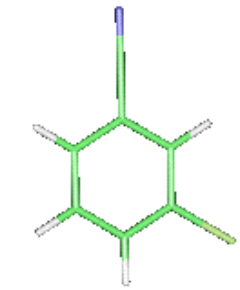

3-chlorobenzonitrile

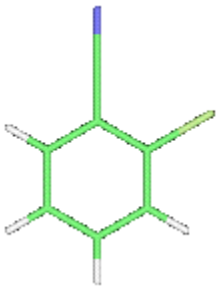

2-chlorobenzonitrile

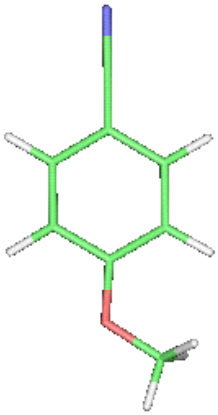

4-methoxybenzonitrile

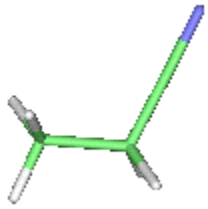

propionitrile

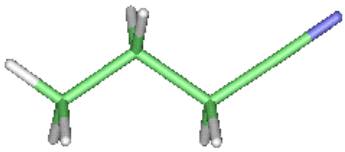

butyronitrile

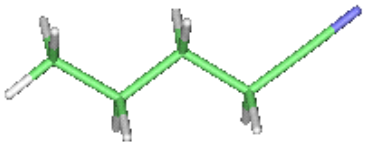

valeronitrile

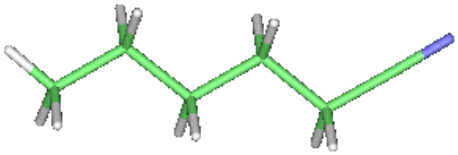

hexanenitrile

Appendix 5

Supporting Information for Chapter 12

Supporting Information

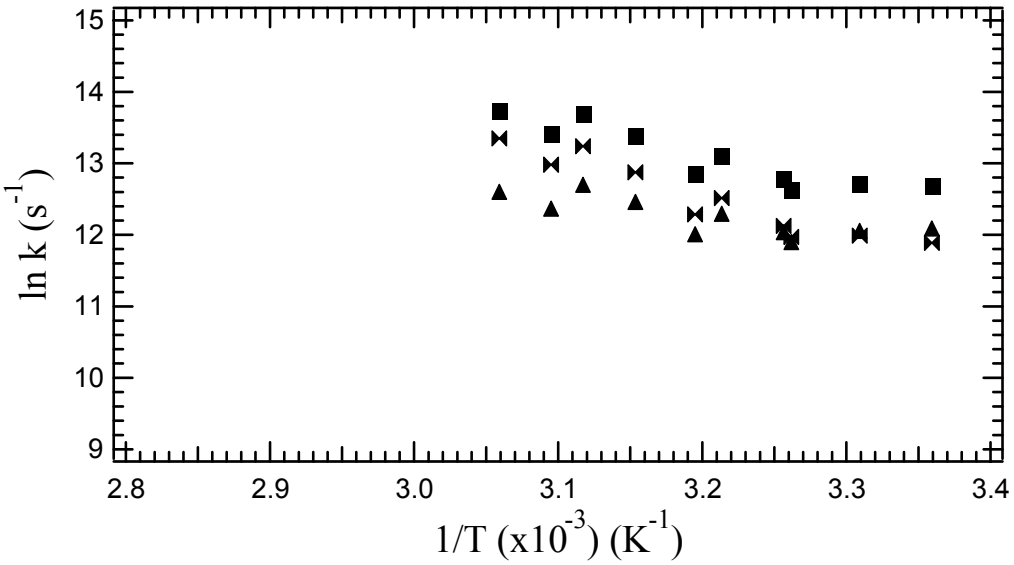

Figure 1. Plot of the natural log of the measured relaxation (square, slow phase), folding (k_f, triangles) and unfolding (k_u, bowties) rates as a function of the inverse of temperature for HP36F4751L using a two-state model of folding. The relaxation rates were measured at 1632 cm^{-1} and 1650 cm^{-1}.